Universitat Politècnica de Catalunya

Doctoral Thesis

A Parallel Algorithm for Deformable Contact Problems

Matías Ignacio Rivero

Advisor:
Dr. Mariano Vázquez

Tutor:
Dr. José María Cela Espín

Doctoral Program in Civil Engineering
Escola Tècnica Superior d'Enginyers de Camins, Canals i Ports de Barcelona

Barcelona, Spain
February 2018

To Anita and Pepe,
for being my teachers of life.

Abstract

In the field of nonlinear computational solid mechanics, contact problems deal with the deformation of separate bodies that interact when they come in touch. Usually, they are formulated as constrained minimization problems that may be solved using optimization techniques such as penalty method, Lagrange multipliers, Augmented Lagrangian method, etc. This classical approach is based on node connectivities between the contacting bodies. These connectivities are created through the construction of contact elements introduced for the discretization of the contact interface, which incorporate the contact constraints in the global weak form. These methods are well known and widely used in the resolution of contact problems in engineering and science.

As parallel computing platforms are nowadays widely available, solving large engineering problems on high performance computers is a concrete possibility for any engineer or researcher. Due to the memory and compute power that contact problems require and consume, they are good candidates for parallel computation. Industrial and scientific realistic contact problems involve different physical domains and a large number of degrees of freedom, so algorithms designed to run efficiently on high performance computers are needed. Nevertheless, the parallelization of the numerical solution methods which arises from the classical optimization techniques and discretization approaches presents some drawbacks that must be considered. Mainly, for general contact cases where sliding occurs, the introduction of contact elements requires the update of the mesh graph in a fixed number of time steps. From the point of view of the domain decomposition approach for parallel resolution of numerical problems, this is a significant drawback due to its computational expensiveness since dynamic repartitioning must be done to redistribute the updated mesh graph to the different processors. On the other hand, some of the optimization techniques modify the number of degrees of freedom in the problem dynamically, by introducing Lagrange multipliers as unknowns.

In this work we introduce a Dirichlet-Neumann type parallel algorithm for the numerical solution of nonlinear frictional contact problems, putting a strong focus on its computational implementation. Among its main characteristics, it can be highlighted that there is no need to update the mesh graph during the simulation, as no contact elements are used. Also, no additional degrees of freedom are introduced into the system, since no Lagrange multipliers are required. In this algorithm, the bodies in contact are treated separately, in a segregated way. The coupling between the contacting bodies is performed through boundary conditions transfer at the contact zone. From a computational point of view, this feature allows using a multicode approach. Furthermore, the algorithm can be interpreted as a black-box method as it allows to solve each body separately even with different computational codes. We describe the parallel implementation of the proposed algorithm and analyze its parallel behaviour and performance in both validation and realistic test cases executed in HPC machines using several processors.

Resumen

En el ámbito de la mecánica de contacto computacional, los problemas de contacto tratan con la deformación que sufren cuerpos separados cuando interactúan entre ellos. Comunmente, estos problemas son formulados como problemas de minimización con restricciones, que pueden ser resueltos utilizando técnicas de optimización como el penalty, los multiplicadores de Lagrange, el Lagrangiano Aumentado, etc. Este enfoque clásico está basado en la conectividad de nodos entre los cuerpos, que se realiza a través de la construccion de los elementos de contacto que surgen de la discretización de la interfaz de contacto, los cuales, a su vez, incorporan las restricciones de contacto en forma débil.

Debido al consumo de memoria y a los requerimientos de potencia computacional que los problemas de contacto requieren, resultan ser muy buenos candidatos para la paralelización computacional. Sin embargo, la paralelización de los métodos numéricos que surgen de las técnicas clásicas de optimización y los distintos enfoques para su discretización presentan algunas desventajas que deben ser consideradas. Principalmente, en los problemas más generales de la mecánica de contacto ocurre un deslizamiento entre cuerpos. Por este motivo, la introducción de los elementos de contacto vuelve necesaria una actualización del grafo de la malla cada cierto número de pasos de tiempo. Desde el punto de vista del método de descomposición de dominios utilizado en la resolución paralela de problemas numéricos, esto es una gran desventaja debido a su coste computacional, ya que un reparticionamiento dinámico debe ser realizado para redistribuir el grafo actualizado de la malla entre los diferentes procesadores. Por otro lado, algunas técnicas de optimización modifican dinámicamente el número de grados de libertad del problema al introducir multiplicadores de Lagrange como incógnitas del problema.

En este trabajo presentamos un algoritmo paralelo del tipo Dirichlet-Neumann para la resolución numérica de problemas de contacto con fricción no lineales, poniendo un especial énfasis en su implementación computacional. Entre sus principales características se puede destacar la no necesidad de actualizar el grafo de la malla durante la simulación, ya que en este algoritmo los elementos de contacto no son utilizados. Adicionalmente, ningún grado de libertad extra es introducido al sistema, ya que los multipliadores de Lagrange no son requeridos. En este algoritmo los cuerpos en contacto son tratados de forma separada, de una manera segregada. El acople entre estos cuerpos es realizado a través del intercambio de condiciones de contorno en la interfaz de contacto. Desde un punto de vista computacional, esta característica permite el uso de un enfoque multicódigo. Además, este algoritmo puede ser interpretado como un método del tipo *black-box* ya que permite resolver cada cuerpo por separado, aun utilizando distintos códigos computacionales. En este trabajo describimos la implementación paralela del algoritmo propuesto y analizamos su comportamiento y performance paralela tanto en casos de validación como reales, ejecutados en computadores de alta performance utilizando varios procesadores.

Acknowledgements

In the first place, I would like to thank my advisor, Mariano Vázquez. Thank you, Mariano, for giving me the opportunity to come to the Barcelona Supercomputing Center as a PhD student, for always keeping the door of your office open and for your willingness to hear everything I had to say. I also want to thank Guillaume Houzeaux, for his enthusiasm and readiness to help.

I am deeply indebted to Miguel Zavala for his selfless and invaluable help, and for the fruitful discussions. Miguel, there are no words to express my gratitude for all the time you invested. I have enjoyed working with you. I am also indebted to Gerard Guillamet for all his comments, suggestions and, especially, for all his last-minute help. Gerard, it would have been nice to have you here from the very beginning of my thesis. A very special thanks goes to my other colleagues of the *solidz team* at BSC and UdG: Adrià Quintanas, Guido Giuntoli and Eva Casoni, for their ideas and their problem-solving attitude.

I have to thank other people who indirectly contributed to this thesis by giving me moral and emotional support. I want to express my gratitude to Alex Ferrer and Matías Avila for lending me their ears everytime I needed, for all the talks we had and all the advice they gave me. A big thanks also goes to Mariña López, Jordi Barcons and María Coto for their support, understanding and active encouragement. I also want to thank Alex Martí, Dani Mira, Mónica de Mier, Abel Gargallo and Ruth Arís, for their help at precise moments which made an important difference to me.

I am also grateful to my colleagues of the CASE department at BSC who have contributed to my day-to-day life and who have made my experience at BSC pleasant. Although the list of these people is too long to be given in totality, I would especially like to mention: Alfonso Santiago, Edgar Olivares, María Cristina Marinescu, Simon Carrignon, Paula Córdoba, Sergio Mendoza, Dani Pastrana, Xevi Roca, Diana Fernández, Hadrien Calmet, Herbert Owen, Ricard Borell, Guille Marín, Juan Carlos Cajas, Bea Eguzkitza, Albert Coca, Stephan Mohr, Rogeli Grima and Jazmín Aguado.

Gracias al Juancho, mi *little* brother, por ser mis ojos a la distancia y por aguantar los trapos, aún más en los momentos difíciles. Te quiero mucho hermano. Y gracias al Cholo, porque el esfuerzo no se negocia, y porque sólo en el diccionario éxito está antes que trabajo.

Finally, I would like to thank you Agus, my wife. Thank you for all the sacrifices you did by staying by my side all those years, and by letting my dream became our dream. Thank you for all your support, understanding, patience, tolerance and for believing in me ten times more than I do. Without you, all this journey would not have made any sense.

This work has been done with the support of the grant SEV-2011-0067 and fellowship BES-2012-052278 of Severo Ochoa Programme, awarded by the Spanish Government.

Contents

1 Introduction **1**

1.1 Motivation . . . 1

1.2 Background . . . 3

1.2.1 Classical and modern theoretical works . . . 3

1.2.2 Numerical treatment of contact problems . . . 4

1.2.2.1 Domain decomposition approaches . . . 5

1.2.2.2 Parallel computational contact mechanics . . . 6

1.3 Objectives . . . 6

1.4 Outline . . . 8

2 Governing Equations for Large Deformation Contact **11**

2.1 Initial/Boundary value problems for the finite strain case . . . 11

2.1.1 Problem formulation . . . 11

2.1.2 The weak form in finite strains . . . 13

2.2 Two-body contact problem definition . . . 13

2.2.1 Contact constraints in large deformation . . . 15

2.2.1.1 Frictional conditions . . . 16

2.2.2 Weak form of the large deformation contact problem . . . 18

2.2.2.1 Contact virtual work: the contact integral . . . 20

2.3 Discretization aspects . . . 20

2.3.1 Contact surface discretization . . . 21

3 Analysis of Existing Computational Methods **25**

3.1 Key concepts for parallel computing. A crash introduction . . . 25

3.1.1 Parallel computational models . . . 25

3.1.1.1 Message passing interface (MPI) . . . 27

3.1.2 Domain decomposition . . . 28

3.1.3 Mesh partitioning . . . 30

3.1.4 Sparse storage . . . 31

3.2 Contact mechanics: methods of constraint enforcement . . . 33

3.2.1 Unconstrained system . . . 33

3.2.2 Constrained system . . . 34

3.2.2.1 Penalty method . . . 35

3.2.2.2 Lagrange multipliers method . . . 36

3.2.2.2.1 Mortar method for contact problems . . . 38
3.2.2.3 Augmented Lagrangian method . . . 38
3.3 Domain decomposition and constraint enforcement methods . . . 40
3.3.1 Sliding . . . 41
3.4 Standard methods and the parallel world . . . 44
3.5 Design basis of the proposed algorithm . . . 45

4 A Parallel Method for Unilateral Contact Simulation 47
4.1 Introduction . . . 47
4.2 Formulation of unilateral contact problems . . . 48
4.2.1 Unilateral normal contact . . . 48
4.2.2 Balance of momentum including contact . . . 49
4.2.3 Interpretation of contact Hertz-Signorini-Moreau conditions . . . 50
4.2.4 Interpretation of frictional condition . . . 51
4.3 Method of partial Dirichlet-Neumann boundary conditions . . . 52
4.3.1 Frictionless case . . . 53
4.3.2 Frictional case . . . 54
4.4 Computational implementation . . . 56
4.4.1 Contact searching and communication: the PLE++ tool . . . 57
4.4.1.1 Parallel location and exchange algorithm . . . 57
4.4.1.1.1 Global searching . . . 59
4.4.1.1.2 Local searching . . . 62
4.4.1.2 Exchange . . . 64
4.4.2 Implementation issues . . . 65
4.4.2.1 MPC enforcement . . . 71
4.4.2.2 Friction enforcement . . . 73
4.4.2.3 Nodes release . . . 74
4.5 Numerical examples . . . 75
4.5.1 Computational framework . . . 75
4.5.2 Test cases . . . 76
4.5.2.1 Signorini problem: cylinder on a rigid foundation - 2D . . . 77
4.5.2.2 Indentation parallel benchmark - 2D . . . 80
4.5.2.3 Frictional case: uniaxial compression test - 2D . . . 84
4.5.2.4 Hertzian contact: sphere on a flat rigid plate - 3D . . . 86
4.5.2.5 Indentation parallel benchmark - 3D . . . 89
4.5.2.6 Frictional case: sliding of a cube on a rigid plane - 3D . . . 95
4.5.2.7 Expansion of a tube and a rounded frame - 3D . . . 98

5 A Parallel Method for the Two-Body Contact Problem 101
5.1 Introduction . . . 101
5.2 Contact algorithm of Dirichlet-Neumann type . . . 103
5.2.1 Nonlinear parallel extension . . . 104

5.2.2 Fixed-point solver analogy - convergence issues . . . 106
5.2.2.1 Fixed relaxation parameter . . . 107
5.2.2.2 Aitken dynamic relaxation . . . 107
5.2.2.3 Quasi-Newton algorithms . . . 108
5.3 Computational implementation . . . 108
5.3.1 Interpolation of contact tractions. Load transference. . . . 110
5.4 Numerical examples . . . 112
5.4.1 Computational framework . . . 112
5.4.2 Test cases . . . 114
5.4.2.1 Hertz contact between two hemispheres - 2D . . . 114
5.4.2.2 Indentation parallel benchmark - 2D . . . 118
5.4.2.3 Bouncing ball - 2D . . . 122
5.4.2.4 Ironing example - 3D . . . 124
5.4.2.5 Impact problem - 3D . . . 128

6 Conclusions and Outlook **131**
6.1 Summary . . . 131
6.2 Contributions . . . 132
6.3 Future research perspectives . . . 133

A Computational Environment **137**
A.1 Alya . . . 137
A.1.1 Numerical issues - solid mechanics module . . . 138
A.2 Ostero . . . 140
A.2.1 Description . . . 140
A.2.2 How to get Ostero . . . 142

B Physical Interpretation of the Newton's Method Residual **143**

C Load Transference Analysis **147**

Bibliography **149**

Chapter 1

Introduction

In this first chapter we intend to give a general context and overview of this thesis. We start by describing from a general viewpoint the context where this thesis is situated and the main aspects that motivate this work. Then, we give a more detailed description of the scientific background which is used as the theorethical frame for the developments included here. Finally, we present the objectives of this work and the outline which shows the structure followed in this manuscript.

1.1 Motivation

Contact is a complex phenomena which can be analyzed from the atomistic perspective to the macroscopic viewpoint, and from a high-speed impact to a quasi-static interaction. The level of detail in this analysis depends on the context, which basically responds to the problem in hand, related to an specific area of research. However, for most contact applications in solid and structural mechanics, a purely macroscopic viewpoint based on classical continuum formulations is sufficient. Throughout this thesis, this is the approach that will be followed.

The kind of contact problems which will be considered in this thesis are those which deal with the deformation of separate bodies that interact when they come in touch. Since decades ago, contact problems have taken an important place in the computational mechanics. Because of their relevance and complexity, many numerical procedures have been proposed in engineering literature. What makes improved contact simulation approaches promising is the fact that the resulting numerical algorithm can be typically employed in a very wide range of scientific and technical areas. This allows not only to reduce costs in product development and testing but also to a better understanding of complex systems influenced by contact phenomena.

Due to the characteristics of the contact boundary conditions, this type of problems are formulated as constrained minimization problems which may be solved using different optimization techniques such as penalty method, Lagrange multipliers, Augmented Lagrangian method and others. From the discretization of the continuum setting, those approaches result in a monolithic system of linear equations which includes all the unknowns for all the geometries of the

mechanical system. Furthermore, the discretization of contact problems using implicit solvers requires the construction of contact elements, contact tangent matrices and contact residual vectors which incorporate the contact constraints in the global weak form. In almost all contact problems where the contact zone is a priori unknown, the use of contact elements requires the update of the mesh graph in a fixed number of time steps. On the other hand, some of the optimization techniques used in contact problems increase the number of degrees of freedom in the problem, by introducing Lagrange multipliers as unknowns. Since the number of Lagrange multipliers depends on the active contact surface at each time step, the total unknowns of the system can vary as the problem evolves.

As parallel computing platforms are nowadays widely available, solving large engineering problems on high perfomance computers is a concrete possibility for any engineer or researcher. Due to the memory and compute power that contact problems require and consume, they are good candidates for parallel computation. Industrial and scientific realistic contact problems involve different physical domains and a large number of degrees of freedom, so algorithms designed to run efficiently in high performance computers are needed. Nevertheless, the parallelization of the solution methods which arises from the classical optimization techniques and discretization approaches presents some drawbacks that must be considered. In the finite element formulation the contact element matrices are assembled in the global structural matrix of the system. This presents some disadvantages when sliding between meshes occurs, as classical formulations are based on nodes connectivities. Sliding is a very frequent phenomena in contact problems which requires the modification of node connectivities between the nodes at the boundary contact zone. Since the contact area changes during an incremental solution procedure, the data structure for the exchange of data between processors (i.e. the mesh graph) has also to be modified. The use of Lagrange multipliers also affects the parallel data structure, since the size of the linear equation system changes dynamically as the problem evolves. As consequence, mesh graph updating and Lagrange multipliers usage has a strong and direct impact on the performance of a parallel solution procedure for contact problems. Under a parallel approach, the modification of the contacting area during execution time requires a mesh repartitioning at least every time the node connectivity of the contact elements changes. This is a computationally expensive and inefficient task.

According to what was explained in the previous paragraphs, it can thus be advantageous to construct an algorithm for solving contact problems that employs a strategy in which the bodies involved in the contact problem are treated separately, in a segregated way, in order to avoid mesh graph updating issues. Also it would be advantageous if the algorithm doesn't need to rely on optimization techniques and Lagrange multipliers. Yet, such segregated algorithms must be numerical robust, accurate, efficient and flexible. As will be seen in Sec. 1.2, there exists a gap in scientific research where those issues are not covered thoroughly, in a unified manner. The lack of an intensive analysis regarding the parallelization of traditional contact algorithms, and new alternatives that are best suitable for the numerical resolution of contact problems in high performance computing environments, are the main motivation of this thesis.

1.2 Background

This section is intended to give a brief overview of some historical remarks and the state-of-the-art in computational contact mechanics. For a more comprehensive analysis of this topic the reader is referred to [88, 109, 112, 142], among others.

1.2.1 Classical and modern theoretical works

The birthmark of classical contact mechanics is linked to the early work conducted by Hertz [62] on pressure distributions between contacting spheres. He developed an analytical solution by assuming that bodies are elastic with small deformation, frictionless and that the area of contact is elliptic.

After Hertz's work many researchers continued studying contact problems between elastic bodies of different shapes, with or without friction, looking for possible analytical solutions. Nevertheless, only a few solutions restricted to a simple geometry of the bodies, a linear elastic material and small deformations have been found. In these solutions, the shape of the bodies is usually rectangular or circular, axisymmetric or two-dimensional. They are summarized in [53, 76, 77, 66].

In opposition to the classical approach, non-classical contact mechanics can be defined as mechanics of unilateral contacts with threshold friction, adhesion or lubrication between geometrical complicated bodies undergoing large deformations, made of elastic, viscuous or plastic materials. As the Hertz work for the classical approach, the formulation derived by Signorini [122] for the equilibrium of a linear elastic body in frictionless contact with a rigid foundation can be regarded as a milestone in modern contact mechanics. The generalization and theoretical structure of the friction law was stablished by Moreau [99].

The next important step in modern contact mechanics was made by the application of variational methods to contact and friction formulations. Because of the nature of the contact boundary conditions, the contact problem can be mathematically interpreted as a physical system subjected to a governing variational inequality [41, 79]. An important characteristic of such variational inequalities is that the solution and variation spaces are constrained by the physical constraints, which depend on the unknown solution. Consequently, the mathematical structure of the contact problem is very different from a typical initial/boundary value problem that only includes Dirichlet and/or Neumann boundary conditions. Additionally, the presence of friction adds significant mathematical complications [79, 28, 101, 102].

In previous references and others, the particular case of a linear elastic solid in frictional contact with a rigid obstacle (unilateral contact) has been extensively studied and can be considered to be well characterized mathematically. Nevertheless, extension to inelastic materials and large deformations is much more difficult and remains unsolved. Additionally, the replacement of the rigid obstacle by a second deformable body adds extra complications to the problem that affects its mathematical well-posedness. Those effects are still not completely understood.

1.2.2 Numerical treatment of contact problems

From previous section it becomes clear that classical and modern contact mechanics give response only to a small part of real industrial applications. For this reason, computational contact mechanics became a relevant field of research since 1970s and 1980s, where first contributions to the treatment of contact mechanics within the Finite Element Method can be traced back. Works by Francavilla and Zienkiewicz [48] and Hughes et al. [72] are considered the pioneers in this field, proposing a purely node-base approach, which requires node-matching meshes between contacting bodies and is restricted to small deformations.

As a satisfactory general methodology for formulating contact and friction inequalities still doesn't exist, further developments in computational contact mechanics have gone into two main directions. In the first direction, contact and friction conditions are stablished in the discrete form of the problem. Constraints and linearization of the nonlinear resultant equation are therefore limited to a particular type of discretization. Using this approach gradual progress in solving increasingly difficult problem was made, see [138, 125, 32, 106, 140]. Nevertheless further works in this direction have encountered serious obstacles as: limitations on the admissible incremental motions, restrictions to rigid obstacle problems and, as mentioned before, restriction to a particular discretization. This situation results from the lack of a continuum framework for the large deformation frictional contact problems.

The second direction intends to overcome these obstacles putting special effort in the development of a continuum formulation for contact problems, which intends to approach contact mechanics from the abstract and general continuum point of view. As mentioned in Sec. 1.2.1, the continuum formulation of contact problems includes variational inequalities leading to non-smooth constrained minimization problems that can not be directly tackled by the finite element method. First, they have to be expressed as variational equalities or unconstrained minimization problems. Variational inequalities can be reformulated into a variational equality problem with special contact terms under the assumption of knowing *a priori* the contact force. The form of the contact terms depends on the method chosen to enforce the contact constraints. For constraint enforcement, a wide range of techniques from the optimization literature exist [92, 52]. Among them, the most used methods for constraint enforcement in the numerical treatment of contact problems are: the penalty method [100, 30, 57, 125, 32, 140] and the classical Lagrange multiplier method [8, 50]. Due to known drawbacks of the penalty method (see [92, 79]), Lagrange multiplier techniques have become relevant in the domain of constrained problems. Especially one of its extensions has gained importance in the field of computational contact mechanics: the Augmented Lagrangian method, which combines advantages of both penalty and Lagrange multipliers methods and has been applied successfully to frictionless and frictional contact (see [54, 139, 4, 123, 110]).

The implicit numerical resolution of contact problems with the Finite Element Method requires the construction of *contact elements*. Contact elements are used to link potentially interacting surfaces and to transfer efforts from one to another. The structure of the contact elements depends on the *contact discretization* method. The simplest is the *node-to-node* discretization [48]

which is valid only for matching meshes and does not allow sliding between contacting bodies or large deformations. The *node-to-segment* is a multipurpose discretization [73, 8, 17, 57, 88, 90, 123, 140] which is valid for non-conforming meshes, large deformation and sliding, therefore becoming the standard procedure in computational contact mechanics. But as it is, this discretization is not stable, fails contact patch test unless a two-pass scheme is used and is valid only for low order elements. A different discretization approach, called *contact domain method* and based on the node-to-segment approach has been proposed in [103, 59]. This method has been reported to be stable and passes the patch test, but its three dimensional implementation is not applicable for arbitrary discretizations. The last method that may be distinguished is the *segment-to-segment* discretization [125, 105, 144]. In contrast to the purely point-wise procedure (typical of the node-to-segment methods), the segment-to-segment approach is based on a subdivision of the contact surface into individual segments for numerical integration together with an independent approximation of the contact pressure.

1.2.2.1 Domain decomposition approaches

Mortar element methods, originally introduced as an abstract domain decomposition technique [18, 14], are characterized by an imposition of the occurring interface constraints in a weak sense and by the possibility to prove their mathematical optimality. In general terms, they allow for nonconforming decomposition of the computational domain into subregions and for the optimal coupling of different variational approximations in different subregions. In the context of contact analysis, this allows for a variationally consistent treatment of non-penetration and frictional sliding conditions despite the inevitably non-matching interface meshes for finite deformations and large sliding motions. Segment-to-segment discretization has been coupled with mortar methods and applied to contact problems in early works [15, 64, 96], though limited to small deformations. Restrictions on the mortar-based contact formulations regarding the nonlinear kinematics have been removed, leading to the implementations given in [46, 117, 131, 118, 113].

The *FETI* method is an iterative substructuring method for solving systems of linear equations using Lagrange multipliers. It was introduced in [43] and is based on the decomposition of the spatial domain into non-overlapping subdomains that are *glued* by Lagrange multipliers. The FETI method can be applied without any algorithmic changes for a mortar finite element discretization in non-matching meshes [126]. This has been reported in [39, 35] only for 3D frictionless contact problems in linear elasticity. A more comprehensive approach for mortar discretization and FETI methods i.e. frictional contact problems in large deformation for non-matching meshes, is still missing in the literature. Conversely, FETI method has been applied to elastic frictionless and frictional contact problems in matching grids for small [34, 36, 40, 37, 38] and large displacements [133].

Monotone Multigrid methods are algorithms for solving linear systems arising from the discretization of partial differential equations based on a sequence of meshes obtained by successive refinement, having a recursive structure [82]. Despite in the literature multigrid methods are sometimes defined as alternatives to domain decomposition methods, in the field of computational contact mechanics they are used as subdomain linear solvers. For unilateral contact prob-

lems, monotone multigrid methods yield globally convergent and efficient iterative solvers [83, 84]. However, these techniques cannot be applied directly to multibody contact problems because of the non-conforming situation at the interface of the contacting bodies. In [135] a new approach for the numerical simulation of multibody frictionless contact problems based on monotone multigrid techniques and mortar methods is presented.

Alternative domain decomposition approaches for contact problems are based on formulations that allow to solve problems for each body separately with certain boundary conditions at the natural interface. A Dirichlet-Neumann algorithm for solving frictional Signorini contact problems between two elastic bodies based on mortar elements and the monotone multigrid method has been proposed and studied in the discrete setting in [85]. This algorithm consists on solving in each iteration a linear Neumann problem for one body and a unilateral contact problem for the other by using essentially the contact interface as the boundary data transfer. The convergence of this algorithm in the continuous setting in its frictionless form has been proved in [10, 42] and considering friction in [12]. In [11] another improvement leading to a Neumann-Neumann approach was proposed, in which two Neumann sub-problems are solved in order to ensure the continuity of normal stresses and its convergence is proven in the continuous setting. Later in [60] the authors presented various numerical implementations of this approach. Finally, in [61] the Neumann-Neumann algorithm is extended to two-body elastic contact problems with Tresca friction.

The Dirichlet-Neumann approach presented in the previous paragraph is the main topic of this thesis and marks the point of origin of this work.

1.2.2.2 Parallel computational contact mechanics

Few works in the computational contact mechanics literature have been devoted to parallel methods. The main research interest in this topic was focused on static or transient explicit contact simulations due to its simplicity compared with implicit integrators. Several authors have reported on their effort to parallelize this kind of problems and specially the contact detection procedure [94, 108, 111, 7, 58].

1.3 Objectives

As mentioned in Secs. 1.1 and 1.2, computational algorithms for the solution of contact mechanics problems between deformable bodies present some particularities which can be considered as handicaps for their parallelization. Mainly, the following are the two most important issues:

- Penalty and Augmented Lagrangian based methods add explicit connectivities between contacting nodes, and
- Lagrange multiplier based methods increase dinamically the number of degrees of freedom of the resultant system matrix.

Traditional algorithms for computational contact mechanics are based on node connectivities for the transference of data related to the contact phenomena, through the contact elements created for such end. General contact problems involve sliding after contact i.e. relative movement of one body with respect to the other in a contacting situation. This implies that contact elements must be created and actualizated *on the fly* in each inner iteration and/or time step, what continously changes the graph of the system. This means that connectivities between contacting nodes are created and modified in execution time, and because of that, new contributions in the global tangent matrices will appear.

Parallel algorithms for distributed memory machines require the partitioning of the system graph, which is defined by the connectivities of the mesh. This is normally done as a preprocess task, as generally the mesh does not change. Nevertheless, for contact problems where the graph is continously being updated, this partitioning must be done in execution time everytime the graph changes. From the viewpoint of the computational resources, this is a very demanding procedure.

Motivated by the fact that standard contact algorithms are not a suitable alternative for efficient parallelization and by the lack of scientific literature regarding those issues, the main objective of this thesis is to introduce a novel contact algorithm based on domain decomposition methods that can run efficiently in High Performance Computing (HPC) based supercomputers, considering in a unified way: physical, numerical, algorithmic and computational aspects. This algorithm solves numerically a nonlinear contact problem between two deformable bodies. It is based on a nonlinear block Gauss-Seidel method as an iterative solver, which can be interpreted as a Dirichlet-Neumann algorithm for the nonlinear contact problem. The main aspect of the proposed algorithm is that the bodies in contact are treated separately, in a segregated way. Then, coupling is performed through boundary conditions transfer at the contact zone. As this approach solves each body separately, there is no need to increase the degrees of freedom of the problem or to redefine the mesh graph at different time steps, since no contact elements are used in the algorithm. The main advantages of the algorithm introduced in this thesis are summarized in the following list:

- General parallel contact algorithm.
- Do not restrict the mesh partitioner.
- Do not require dynamic partitioning.
- The number of unknowns remain constant during the simulation.
- Do not affect the system matrix (no connectivities are created).
- Is suitable for large scale problems (domain decomposition approach).
- Has individual scheme solution for each problem.
- Is robust.

- Black box. Can be coupled to any linear or nonlinear mechanics simulation code.
- Can be used with any material, damage and element model.
- Strongly favours a general computational framework of parallel multiphysics simulations for supercomputers.

As a complementary objective, all the algorithms presented in this thesis were implemented in *Alya*, the multiphysics, multiscale and massively parallel finite element code developed in-house at the Barcelona Supercomputing Center. For a detailed description of the Alya system, please see Appendix A, Sec. A.1.

1.4 Outline

Despite the main objective of this thesis is to present a novel algorithm for the parallel numerical resolution of contact problems, not less important are the fundaments which justify the necessity for the development of such algorithm. To reach a clear overview of the computational context that motivated this work has been an important and time-demanding stage during the elaboration of this thesis. This is why we designed its structure to give a strong technical basis of these fundaments before introducing the new developments. Thus, the rest of this thesis is organized as follows.

In Chapter 2, we outline the relevant governing equations of nonlinear solid mechanics and contact mechanics. Additionally, we review the basic concepts as contact problem definition, boundary conditions and weak formulation in a very general style. We cover also some discretization aspects. This chapter intends to set the minimal mathematical basis needed for a comprehensive development of the following chapters.

Chapter 3 is divided in two parts. The first part is devoted to an introduction of some basics concepts related to parallel computing. The second part, which is supported by the first part of this chapter, describes the context and enumerates the reasons which fundament this work. In this chapter we also introduce and enumerate the design basis for the novel algorithm proposed in this thesis.

In Chapter 4 we present a new methodology for solving parallel unilateral frictional contact problems in distributed memory computers. Here, we review in more detail the mathematical formulation of unilateral contact problems and enumerate the basics of the new proposed method. Then, we introduce the parallel strategy used for contact detection and communication and present a detailed description of the algorithm implementation in a parallel environment. Finally, we show some numerical experiments and present some performance studies.

In Chapter 5 we extend the methodology presented in the previous chapter to a two-body contact problem, i.e. bilateral contact problem. Following the same procedure from Chapter 4, we present the algorithm putting special emphasis in its parallel implementation, which is the more distinctive part of this work. To close, we present some numerical results that illustrates the efficiency and flexibility of our proposed method.

Finally, the conclusions and outlook in Chapter 6 summarize the most important results and achievements of this thesis. Also, it points out which aspects of the proposed algorithm still have room for improvement, establishing future lines of research.

Chapter 2

Governing Equations for Large Deformation Contact

By reviewing the basic concepts of continuum mechanics with an emphasis on the governing equations for solid dynamics and contact mechanics, the goal in this chapter is to establish a basic conceptual foundation that will serve as starting point for this thesis. Also, some discretization aspects are covered here. Previous work exists on the exact linearization of frictionless contact problems [138, 106] as well as two dimensional frictional problems [125, 140], but each case is limited to a particular discretization. The mathematical framework presented in this thesis is taken from [88, 90, 89], which includes the linearization in the continuum setting, such that no limitations exists. This general formulation and implementation of the frictional contact problem in a finite element setting has not been reported previously in the literature. For a more extensive review in the field of solid and computational contact mechanics, see also [87], [137], [142] and [16].

2.1 Initial/Boundary value problems for the finite strain case

2.1.1 Problem formulation

To formulate solid mechanic problems in finite strain it is necessary to distinguish between two distinct observer frames: the reference configuration Ω, which represents the domain occupied by all the material points $\boldsymbol{X}$ at time $t = 0$, and the current configuration at a time $t \in \mathbb{I}$, given by application of a configuration mapping $\boldsymbol{\varphi}_t$ to Ω. This current configuration describes the changed position $\boldsymbol{x}$ at a certain time t ($\boldsymbol{x} = \boldsymbol{\varphi}_t(\boldsymbol{X})$). The absolute displacement of a material point is then described as $\boldsymbol{u}(\boldsymbol{X}, t) = \boldsymbol{x}(\boldsymbol{X}, t) - \boldsymbol{X}$. A common Cartesian coordinate system is considered here for all configurations. The boundary $\partial\Omega$ of the open set Ω is decomposed into two nonoverlapping subdomains; one in which the motions are prescribed (Γ_u), and one in which the tractions are specified (Γ_σ), see Fig. 2.1. We assume that these regions obey:

$$\begin{aligned} \Gamma_u \cup \Gamma_\sigma &= \partial\Omega, \\ \Gamma_u \cap \Gamma_\sigma &= \emptyset. \end{aligned} \tag{2.1}$$

Points in the reference (or material) description are denoted $\boldsymbol{X}$, while points in the current (or spatial) configuration are denoted $\boldsymbol{x}$, such that $\boldsymbol{x} = \boldsymbol{\varphi}_t(\boldsymbol{X})$. Consistent with the most frequent choice in solid and structural mechanics, in the present section we aim to develop a Total Lagrangian description of the problem, such that the independent variable of interest will be the material points in the reference configuration $\boldsymbol{X}$, while the unknown in the problem to be solved will be $\boldsymbol{\varphi}_t$, for all $t \in \mathbb{I}$ (or equivalenty, the displacement vector $\boldsymbol{u}(\boldsymbol{X}, t)$).

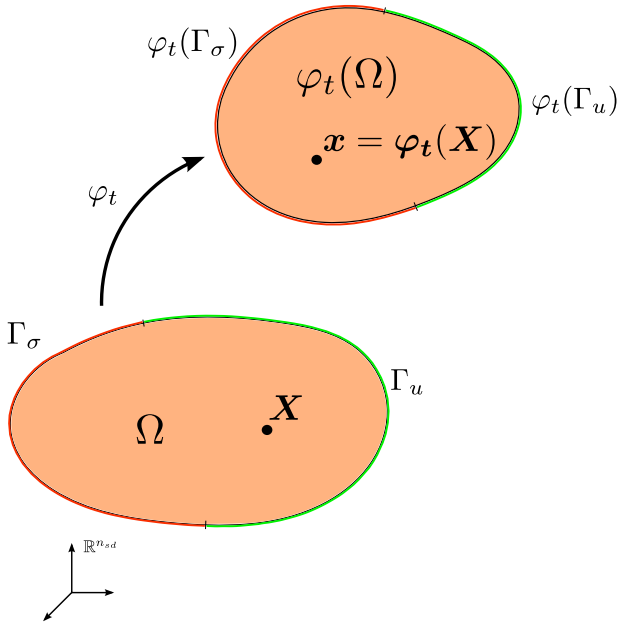

Figure 2.1: Basic notation for the finite strain boundary value problem.

Regardless of the constitutive law employed, the balance of linear momentum for a continuous medium considering finite strains may be specified as:

$$\nabla \cdot \boldsymbol{P} + \boldsymbol{F} = \rho_0 \boldsymbol{A} \quad \text{in} \quad \Omega, \tag{2.2}$$

where $\boldsymbol{P}$ is the first Piola-Kirchhoff stress tensor, which measures stress by referencing the force acting on areas to the magnitude of those areas in their undeformed configuration. $\boldsymbol{F}$ is the prescribed body force per unit *reference* volume in Ω, ρ_0 is the reference mass density and $\boldsymbol{A}$ is the material acceleration of the particle referred to spatial coordinates.

To complete the description of the problem, the boundary conditions and initial conditions must be given. The prescribed values are designated by a superposed bar. The boundary conditions are:

$$\begin{aligned} \boldsymbol{\varphi}_t &= \bar{\boldsymbol{\varphi}}_t \quad \text{on} \quad \Gamma_u, \\ \boldsymbol{P} \cdot \boldsymbol{N} &= \bar{\boldsymbol{T}} \quad \text{on} \quad \Gamma_\sigma, \end{aligned} \tag{2.3}$$

where $\boldsymbol{N}$ is the unit outward normal to $\partial\Omega$ in the reference configuration, $\bar{\boldsymbol{\varphi}}_t$ are the prescribed displacements and $\bar{\boldsymbol{T}}$ the prescribed tractions.

Since Eq. (2.2) is second order in time, two set of initial conditions are needed. Those are expressed in terms of the displacements and velocities:

$$\begin{aligned} \boldsymbol{\varphi}|_{t=0} &= \bar{\boldsymbol{\varphi}}_0 \quad \text{in} \quad \bar{\Omega}, \\ \dot{\boldsymbol{\varphi}}|_{t=0} &= \bar{\boldsymbol{V}}_0 \quad \text{in} \quad \bar{\Omega}, \end{aligned} \tag{2.4}$$

where $\bar{\boldsymbol{\varphi}}_0$ are the prescribed initial displacements, $\bar{\boldsymbol{V}}_0$ the prescribed initial velocities and $\bar{\Omega}$ denotes the closure, or inclusion of the boundary, of the open set Ω.

2.1.2 The weak form in finite strains

In the finite element method, the entity discretized is the weak form of the differential equation. To tacke the resolution of Eq. (2.2) using finite elements, we turn now to the development of a weak form for the finite strain problem. This can be done by considering weighting functions $\overset{*}{\boldsymbol{\varphi}}$, defined on $\bar{\Gamma}$, which are members of a weighting space $\mathcal{V}$ meeting the following definition:

$$\mathcal{V} = \{\overset{*}{\boldsymbol{\varphi}} : \bar{\Omega} \to \mathbb{R}^{n_{sd}} \,|\, \overset{*}{\boldsymbol{\varphi}} \in H^1(\Omega), \overset{*}{\boldsymbol{\varphi}} = 0 \text{ on } \Gamma_u\} \tag{2.5}$$

Additionally, we may define a solution space $\mathcal{U}_t$ for each $t \in \mathbb{I}$, according to the following:

$$\mathcal{U}_t = \{\boldsymbol{\varphi}_t : \bar{\Omega} \to \mathbb{R}^{n_{sd}} \,|\, \boldsymbol{\varphi}_t \in H^1(\Omega), \boldsymbol{\varphi}_t = \bar{\boldsymbol{\varphi}} \text{ on } \Gamma_u\} \tag{2.6}$$

With the solution and weighting spaces defined, the weak form is developed by dotting the governing differential Eq. (2.2) with an arbitrary $\overset{*}{\boldsymbol{\varphi}} \in \mathcal{V}$ and integrating over Ω. This operation gives:

$$\int_\Omega (\rho_0 \boldsymbol{A} - \nabla \cdot \boldsymbol{P} - \boldsymbol{F}) \overset{*}{\boldsymbol{\varphi}} \, d\Omega + \int_{\Gamma_\sigma} (\boldsymbol{P} \cdot \boldsymbol{N} - \bar{\boldsymbol{T}}) \overset{*}{\boldsymbol{\varphi}} \, d\Gamma = 0 \tag{2.7}$$

Rearrangement of Eq. (2.7), use of the fact that $\overset{*}{\boldsymbol{\varphi}} = 0$ on Γ_u and utilization of the boundary condition on Γ_σ gives rise to the weak form of the problem:

$$\text{For each } t \in \mathbb{I}, \text{ find } \boldsymbol{\varphi}_t \in \mathcal{U}_t \text{ such that } \delta \mathcal{W}_{sb} = 0 \text{ for all } \overset{*}{\boldsymbol{\varphi}} \in \mathcal{V},$$

where:

$$\begin{aligned} \delta \mathcal{W}_{sb}(\boldsymbol{\varphi}_t, \overset{*}{\boldsymbol{\varphi}}) := & \int_\Omega \left[\rho_0 \overset{*}{\boldsymbol{\varphi}} \cdot \boldsymbol{A} + \text{GRAD}(\overset{*}{\boldsymbol{\varphi}}) \colon \boldsymbol{P} \right] d\Omega \\ & - \int_\Omega \overset{*}{\boldsymbol{\varphi}} \cdot \boldsymbol{F} \, d\Omega - \int_{\Gamma_\sigma} \overset{*}{\boldsymbol{\varphi}} \cdot \bar{\boldsymbol{T}} \, d\Gamma. \end{aligned} \tag{2.8}$$

2.2 Two-body contact problem definition

The large deformation, large motion frictional contact problem involving two bodies is shown schematically in Fig. 2.2. The reference configurations of this two bodies are represented by $\Omega^{(1)}$ and $\Omega^{(2)}$. The bodies undergo motions, denoted $\boldsymbol{\varphi}^{(1)}$ and $\boldsymbol{\varphi}^{(2)}$, which cause them to contact and

produce interactive forces during some portion of the time interval $\mathbb{I} = [0, T]$. These motions can be expressed by the following mappings:

$$\boldsymbol{\varphi}^{(i)} : \bar{\Omega}^{(i)} \times \mathbb{I} \to \mathbb{R}^{n_{sd}},\ i = 1, 2. \tag{2.9}$$

For any time $t \in \mathbb{I}$, the configuration obtained by fixing the time argument of $\boldsymbol{\varphi}^{(i)}$ is denoted as $\boldsymbol{\varphi}_t^{(i)}$, $i = 1, 2$. Quantities defined on $\boldsymbol{\varphi}_t^{(i)}(\Omega^{(i)})$ are referred to as spatial objects, while quantities defined on the reference states $\Omega^{(i)}$ are referred to as material objects.

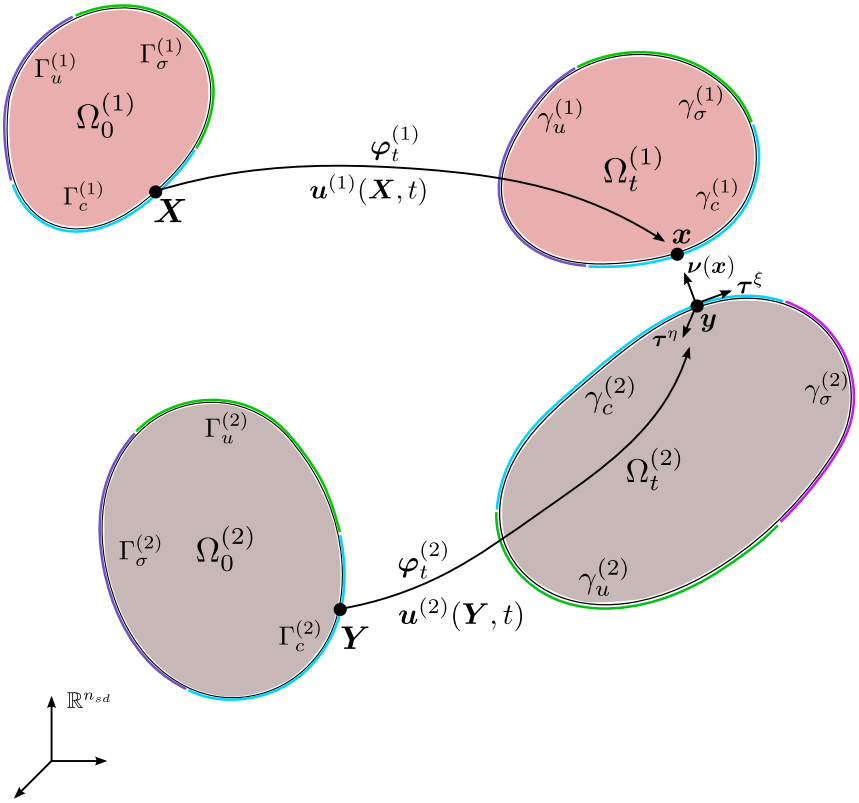

Figure 2.2: Basic notation for the two body large deformation contact problem.

Accordingly, material points of $\bar{\Omega}^{(1)}$ are denoted $\boldsymbol{X}$, while material points of $\bar{\Omega}^{(2)}$ are denoted $\boldsymbol{Y}$. Spatial counterparts are defined as $\boldsymbol{x}$ and $\boldsymbol{y}$, respectively. Considering the boundaries $\partial\Omega^{(i)}$ of $\Omega^{(i)}$, $i = 1, 2$, one may define subsets $\Gamma_c^{(i)} \subset \partial\Omega^{(i)}$ such that all points $\boldsymbol{X}$ (or $\boldsymbol{Y}$) where contact occurs are included. Spatial counterparts of these subsurfaces are designated as $\gamma_c^{(i)} = \boldsymbol{\varphi}_t^{(i)}(\Gamma_c^{(i)})$, $i = 1, 2$. It is over the surfaces $\Gamma_c^{(i)}$ that contact constraints are defined. The remainder of the surfaces $\partial\Omega^{(i)}$ are assumed to be divided between portions $\Gamma_u^{(i)}$ where motions are prescribed, and portions $\Gamma_\sigma^{(i)}$ where tractions are prescribed. Then, $\Gamma_c^{(i)}$, $\Gamma_u^{(i)}$ and $\Gamma_\sigma^{(i)}$ satisfy:

$$\begin{aligned} &\Gamma_\sigma^{(i)} \cup \Gamma_u^{(i)} \cup \Gamma_c^{(i)} = \partial\Omega^{(i)}, \text{ and} \\ &\Gamma_\sigma^{(i)} \cap \Gamma_u^{(i)} = \Gamma_\sigma^{(i)} \cap \Gamma_c^{(i)} = \Gamma_u^{(i)} \cap \Gamma_c^{(i)} = \emptyset \end{aligned} \tag{2.10}$$

for each of the bodies i.

Recalling Eq. (2.2), the momentum balance equation can be written for each body i via:

$$\nabla \cdot \boldsymbol{P}^{(i)} + \boldsymbol{F}^{(i)} = \rho_0^{(i)} \boldsymbol{A}^{(i)} \quad \text{in} \quad \Omega^{(i)}. \tag{2.11}$$

Relying on the previous summary of the finite strain problem in Sec. 2.1.1, the initial and boundary conditions imposed on each of the bodies i can be summarized as:

$$\begin{aligned} \boldsymbol{\varphi}_t^{(i)} &= \bar{\boldsymbol{\varphi}}_t{}^{(i)} \quad \text{on} \quad \Gamma_u^{(i)}, \\ \boldsymbol{P}^{(i)} \cdot \boldsymbol{N}^{(i)} &= \bar{\boldsymbol{T}}^{(i)} \quad \text{on} \quad \Gamma_\sigma^{(i)}, \\ \boldsymbol{\varphi}^{(i)}|_{t=0} &= \bar{\boldsymbol{\varphi}}_0{}^{(i)} \quad \text{in} \quad \bar{\Omega}^{(i)}, \\ \dot{\boldsymbol{\varphi}}^{(i)}|_{t=0} &= \bar{\boldsymbol{V}}_0{}^{(i)} \quad \text{in} \quad \bar{\Omega}^{(i)}. \end{aligned} \tag{2.12}$$

2.2.1 Contact constraints in large deformation

The final ingredient in the specification of a finite strain IBVP including contact is the definition of the contact conditions governing the response on $\Gamma_c^{(1)}$ (or, alternatively, $\Gamma_c^{(2)}$). In the approach followed here, the contact conditions are considered to be parametrized by $\boldsymbol{X} \in \Gamma_c^{(1)}$, with the opposing surface $\Gamma_c^{(2)}$ (and its current position $\gamma_c^{(2)}$) providing the additional geometric information necessary to complete the definitions. We consider any such point $\boldsymbol{X} \in \Gamma_c^{(1)}$, whose current position, for any time $t \in \mathbb{I}$, is given by $\boldsymbol{x} = \boldsymbol{\varphi}_t^{(1)}(\boldsymbol{X})$. The current position for any point $\boldsymbol{Y} \in \Gamma_c^{(2)}$ is similarly expressed as $\boldsymbol{y} = \boldsymbol{\varphi}_t^{(2)}(\boldsymbol{Y})$. The impenetrability constraint is defined for all $\boldsymbol{X}$, and for a given pair of motions $\boldsymbol{\varphi}^{(1)}(\cdot, t)$ and $\boldsymbol{\varphi}^{(2)}(\cdot, t)$ by first identifying a contact point $\bar{\boldsymbol{Y}}(\boldsymbol{X}, t)$ according to the following closest point projection in the spatial configuration:

$$\bar{\boldsymbol{Y}}(\boldsymbol{X}, t) = \arg \min_{\boldsymbol{Y} \in \Gamma_c^{(2)}} \|\boldsymbol{\varphi}_t^{(1)}(\boldsymbol{X}) - \boldsymbol{\varphi}_t^{(2)}(\boldsymbol{Y})\|. \tag{2.13}$$

The gap function $g(\boldsymbol{X}, t)$ may then be defined as:

$$g(\boldsymbol{X}, t) = -\boldsymbol{\nu} \cdot \left(\boldsymbol{\varphi}_t^{(1)}(\boldsymbol{X}) - \boldsymbol{\varphi}_t^{(2)}(\bar{\boldsymbol{Y}}) \right), \tag{2.14}$$

where $\boldsymbol{\nu}$ denotes the outward unit normal to $\gamma_{c_t}^{(2)}$ at $\bar{\boldsymbol{y}} = \boldsymbol{\varphi}_t^{(2)}(\bar{\boldsymbol{Y}})$ (see Fig. 2.3). Thus, for any time t, $g(\boldsymbol{X}, t)$ is defined in terms of the closest point projection (in an Euclidean sense) of $\boldsymbol{x} = \boldsymbol{\varphi}_t^{(1)}(\boldsymbol{X})$ onto the opposing surface $\gamma_c^{(2)}$. Of course g is a function of both $\boldsymbol{\varphi}^{(1)}$ and $\boldsymbol{\varphi}^{(2)}$, although for notational simplicity explicit indication of this dependence is omitted.

In considering the tractions $\boldsymbol{t}^{(i)}$ acting on the contacting regions of $\Gamma_c^{(i)}$, it is important to emphasize that Newton's laws require these to be equal and opposite, i.e.:

$$\boldsymbol{t}^{(1)}(\boldsymbol{X}) = -\boldsymbol{t}^{(2)}(\bar{\boldsymbol{Y}}(\boldsymbol{X})), \text{ for all } \boldsymbol{X} \in \Gamma_c^{(1)}. \tag{2.15}$$

Thus, we can now quantify the tractions on the interface in terms of one traction vector only, which we select here as $\boldsymbol{t}^{(1)}$. The contact pressure t_N acting at $\boldsymbol{X}$, assumed to be positive in compression, is defined by considering the component of this traction in the direction of $\boldsymbol{\nu}$:

$$t_N(\boldsymbol{X}) := \boldsymbol{t}^{(1)}(\boldsymbol{X}) \cdot \boldsymbol{\nu}. \tag{2.16}$$

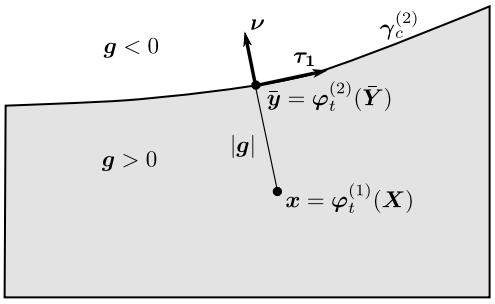

Figure 2.3: Gap definition and basis vectors. The interior of $\Omega^{(2)}$ is indicated by the shaded region.

Besides, contact pressure t_N can be recovered from the decomposition of the Piola traction $\boldsymbol{T}$ at $\boldsymbol{X}$ in normal and tangential (or frictional) components via:

$$\boldsymbol{T}(\boldsymbol{X},t) = \boldsymbol{P}(\boldsymbol{X},t)\boldsymbol{N}(\boldsymbol{X},t) = t_N\boldsymbol{\nu} - \boldsymbol{t}_{T_\alpha}\boldsymbol{\tau}^\alpha \tag{2.17}$$

The contact conditions interrelating t_N and g on the contact surface $\Gamma_c^{(1)}$ may now be stated in terms of *Kuhn-Tucker optimality conditions* (see, e.g., [79]):

$$t_N \geq 0, \tag{2.18a}$$
$$g \leq 0, \tag{2.18b}$$
$$t_N\, g = 0, \tag{2.18c}$$

which must hold for all $\boldsymbol{X} \in \Gamma_c^{(1)}$ and $t \in \mathbb{I}$.

Eq. (2.18a) refers to the fact that all contact interaction must be compressive, while Eq. (2.18b) states the impenetrability condition. The final condition, given by Eq. (2.18c) requires that compressive stress only be generated in the instance where contact is occuring, i.e. $g = 0$. When $g < 0$, this condition requires t_N to be zero, consistent with an out-of-contact condition. Fig. 2.4a gives a simple schematic representation of the admissible combinations of g and t_N corresponding to Eqs. (2.18). Fig. 2.4b shows all the possible combinations of t_N and g values for each possible situation: out-of-contact, non-admissible penetration and contact condition.

2.2.1.1 Frictional conditions

Contact conditions given by Eqs. (2.18) are valid for frictionless contact problem definition. We turn attention now to the introduction of frictional response into the problem description. The frictional modeling framework used in this thesis is based on the most common of frictional descriptions: the Coulomb friction law.

A Coulomb friction law can be stated by introducing the coefficient of friction μ, and by requiring the following conditions to be met for all $\boldsymbol{X} \in \Gamma_c^{(1)}$, in addition to the Kuhn-Tucker conditions summarized by Eqs. (2.18):

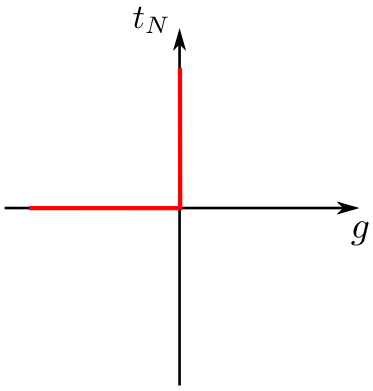

(a)

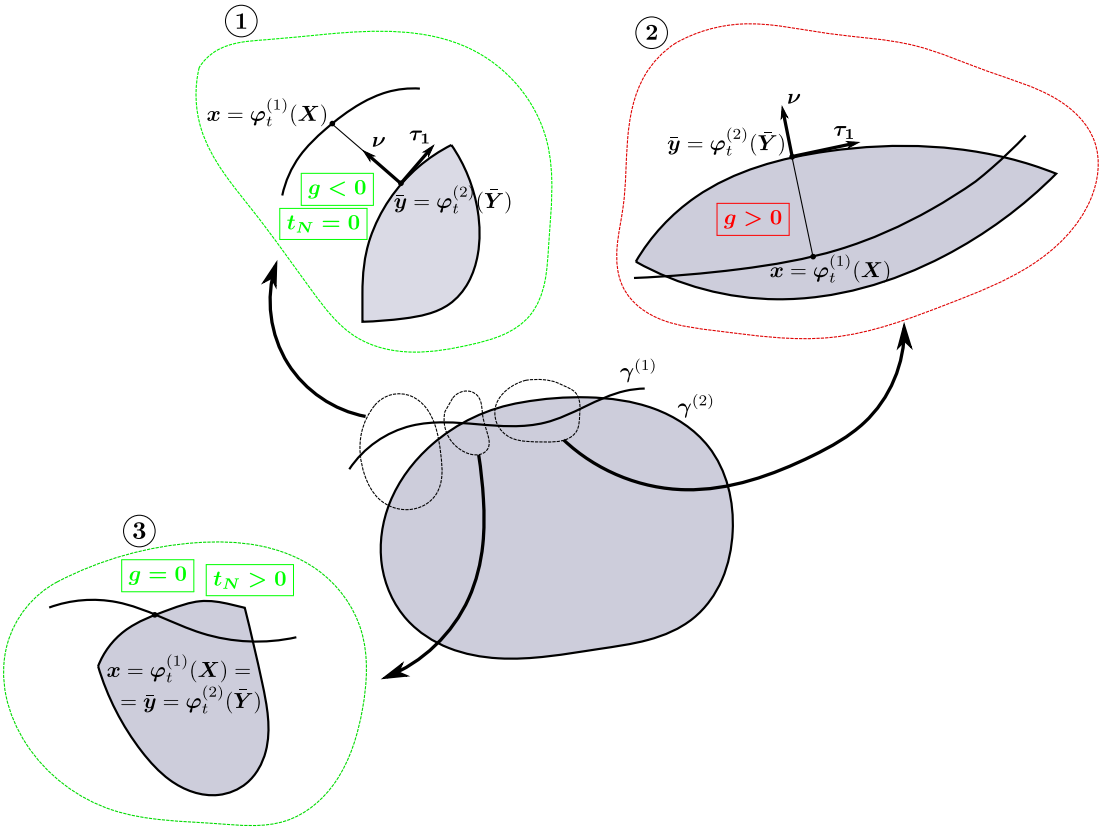

(b)

Figure 2.4: (a) Schematic illustration of the Kuhn-Tucker conditions governing the frictionless contact interaction. Bold line indicates admissible combinations of contact pressure t_N and gap g. (b) Illustrative example showing all the possible situations in a two body contact problem: 1- Out-of-contact (admissible); 2- Penetration (non-admissible); 3- Contact (admissible).

$$||\boldsymbol{t}_T|| \leq \mu\, t_N \tag{2.19}$$

and

$$\boldsymbol{u}_T = \lambda\, \boldsymbol{t}_T, \text{ where } \begin{cases} \lambda = 0, \text{ if } ||\boldsymbol{t}_T|| < \mu\, t_N, \\ \lambda \geq 0, \text{ if } ||\boldsymbol{t}_T|| = \mu\, t_N. \end{cases} \tag{2.20}$$

Eq. (2.19) requires that the magnitude of the tangential stress vector $\boldsymbol{t}_T$ does not exceed the coefficient of friction μ times the contact pressure t_N. Eq. (2.20), on the other hand, represents two important physical ideas associated with the Coulomb law: first, that the tangential slip $\boldsymbol{u}_T$ be identically zero when the tangential stress is less than the Coulomb limit; and second, that any tangential slip that does occur be colinear with the frictional stress exerted by the sliding point $\boldsymbol{X}$ on the opposing surface $\Gamma_c^{(2)}$. Fig. 2.5 graphically represents the concept in the case corresponding to one dimensional sliding. For a more detailed description about the frictional treatment in large deformation contact, see [87].

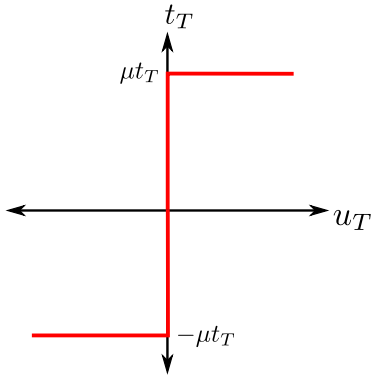

Figure 2.5: Schematic depiction of Coulomb friction law.

2.2.2 Weak form of the large deformation contact problem

We recall Sec. 2.1.2 and define solution and weighting spaces $\mathcal{U}_t^{(i)}$ and $\mathcal{V}^{(i)}$, consisting of potential solutions $\boldsymbol{\varphi}^{(i)}$ and admissible variations $\overset{*}{\boldsymbol{\varphi}}{}^{(i)}$ with respect to the reference configuration of body (i), according to:

$$\mathcal{U}_t^{(i)} = \{\boldsymbol{\varphi}_t^{(i)} : \bar{\Omega}^{(i)} \to \mathbb{R}^{n_{sd}} \,|\, \boldsymbol{\varphi}_t^{(i)} \in H^1(\Omega^{(i)}), \boldsymbol{\varphi}_t^{(i)} = \bar{\boldsymbol{\varphi}}^{(i)} \text{ on } \Gamma_u^{(i)}\} \tag{2.21}$$

and

$$\mathcal{V}^{(i)} = \{\overset{*}{\boldsymbol{\varphi}}{}^{(i)} : \bar{\Omega}^{(i)} \to \mathbb{R}^{n_{sd}} \,|\, \overset{*}{\boldsymbol{\varphi}}{}^{(i)} \in H^1(\Omega^{(i)}), \overset{*}{\boldsymbol{\varphi}}{}^{(i)} = 0 \text{ on } \Gamma_u^{(i)}\}. \tag{2.22}$$

Following the same arguments given in Sec. 2.1.2, the weak form of the momentum balance for each body (i) is given by:

$$\begin{aligned}\delta\mathcal{W}^{(i)}(\boldsymbol{\varphi}_t^{(i)}, \overset{*}{\boldsymbol{\varphi}}{}^{(i)}) := &\int_{\Omega^{(i)}} \left[\rho_0 \overset{*}{\boldsymbol{\varphi}}{}^{(i)} \cdot \boldsymbol{A}^{(i)} + \mathrm{GRAD}(\overset{*}{\boldsymbol{\varphi}}{}^{(i)}) \colon \boldsymbol{P}^{(i)}\right] d\Omega \\ &- \int_{\Omega^{(i)}} \overset{*}{\boldsymbol{\varphi}}{}^{(i)} \cdot \boldsymbol{F}^{(i)}\, d\Omega - \int_{\Gamma_\sigma^{(i)}} \overset{*}{\boldsymbol{\varphi}}{}^{(i)} \cdot \bar{\boldsymbol{T}}^{(i)}\, d\Gamma - \int_{\Gamma_c^{(i)}} \overset{*}{\boldsymbol{\varphi}}{}^{(i)} \cdot \bar{\boldsymbol{T}}^{(i)}\, d\Gamma = 0,\end{aligned} \tag{2.23}$$

which must hold for all $\overset{*}{\boldsymbol{\varphi}}{}^{(i)} \in \mathcal{V}^{(i)}$. The last two terms of Eq. (2.23) corresponds to the virtual work of the tractions, which are specified on $\Gamma_\sigma^{(i)}$ and subjected to contact restrictions on $\Gamma_c^{(i)}$. The last term in particular, corresponds to the contact virtual work on body (i).

A variational statement for the two body system is obtained by adding the two weak forms implied by Eq. (2.23). For notational convenience in what follows, we introduce the notations $\boldsymbol{\varphi}_t$ and $\overset{*}{\boldsymbol{\varphi}}$ to denote the collection of the respective mappings $\boldsymbol{\varphi}_t^{(i)}$ and $\overset{*}{\boldsymbol{\varphi}}{}^{(i)}$ for $i = 1, 2$. In other words,

$$\begin{aligned}\boldsymbol{\varphi}_t &: \bar{\Omega}^{(1)} \cup \bar{\Omega}^{(2)} \to \mathbb{R}^{n_{sd}}, \\ \overset{*}{\boldsymbol{\varphi}} &: \bar{\Omega}^{(1)} \cup \bar{\Omega}^{(2)} \to \mathbb{R}^{n_{sd}}.\end{aligned} \tag{2.24}$$

We utilize similar notations for the solution and variational spaces, such that $\mathcal{U}_t$ is the collection of $\mathcal{U}_t^{(i)}$ and $\mathcal{V}$ is the collection of $\mathcal{V}^{(i)}$. With these ideas, the variational principle for the entire system is expressed as:

$$\begin{aligned}\delta\mathcal{W}(\boldsymbol{\varphi}_t, \overset{*}{\boldsymbol{\varphi}}) &:= \sum_{i=1}^{2} \delta\mathcal{W}^{(i)}(\boldsymbol{\varphi}_t^{(i)}, \overset{*}{\boldsymbol{\varphi}}{}^{(i)}) \\ &= \sum_{i=1}^{2} \left\{ \int_{\Omega^{(i)}} \left[\rho_0 \overset{*}{\boldsymbol{\varphi}}{}^{(i)} \cdot \boldsymbol{A}^{(i)} + \mathrm{GRAD}(\overset{*}{\boldsymbol{\varphi}}{}^{(i)}) \colon \boldsymbol{P}^{(i)}\right] d\Omega \right. \\ &\quad \left. - \int_{\Omega^{(i)}} \overset{*}{\boldsymbol{\varphi}}{}^{(i)} \cdot \boldsymbol{F}^{(i)}\, d\Omega - \int_{\Gamma_\sigma^{(i)}} \overset{*}{\boldsymbol{\varphi}}{}^{(i)} \cdot \bar{\boldsymbol{T}}^{(i)}\, d\Gamma \right\} \\ &\quad - \sum_{i=1}^{2} \left\{ \int_{\Gamma_c^{(i)}} \overset{*}{\boldsymbol{\varphi}}{}^{(i)} \cdot \boldsymbol{T}_c^{(i)}\, d\Gamma \right\} = 0\end{aligned} \tag{2.25}$$

which must hold for all $\overset{*}{\boldsymbol{\varphi}} \in \mathcal{V}$. By means of Eq. (2.8) we can rewrite Ec. (2.25) to obtain the following expression:

$$\delta\mathcal{W}(\boldsymbol{\varphi}_t, \overset{*}{\boldsymbol{\varphi}}) := \sum_{i=1}^{2} \delta\mathcal{W}_{sb}^{(i)}(\boldsymbol{\varphi}_t^{(i)}, \overset{*}{\boldsymbol{\varphi}}{}^{(i)}) + \delta\mathcal{W}_c(\boldsymbol{\varphi}_t, \overset{*}{\boldsymbol{\varphi}}) = 0. \tag{2.26}$$

where the notation

$$\delta\mathcal{W}_c(\boldsymbol{\varphi}_t, \overset{*}{\boldsymbol{\varphi}}) := -\sum_{i=1}^{2} \left\{ \int_{\Gamma_c^{(i)}} \overset{*}{\boldsymbol{\varphi}}{}^{(i)} \cdot \boldsymbol{T}_c^{(i)}\, d\Gamma \right\} \tag{2.27}$$

represents the virtual work due to the contact forces.

Eq. (2.26) shows that the virtual work for the entire system can be expressed as a sum of the

contributions given by the virtual work of each independent body $\delta\mathcal{W}_{sb}^{(i)}$ due to internal stresses and applied loadings, plus the contribution given by the virtual work due to the contact forces $\delta\mathcal{W}_c$.

2.2.2.1 Contact virtual work: the contact integral

From Ec. (2.27) it can be seen that expression for $\delta\mathcal{W}_c$ includes two integrals, one over each contact surface. As all contact quantities can be parametrized by $\boldsymbol{X} \in \Gamma_c^{(1)}$, $\delta\mathcal{W}_c$ is now converted to an expression involving only an integral over $\Gamma_c^{(1)}$. This is achieved by enforcing linear momentum across the contact interface, by requiring that the differential contact force induced on body (2) at $\bar{\boldsymbol{Y}}$ be equal and opposite to that produced on body (1) at $\boldsymbol{X}$:

$$\boldsymbol{t}_t^{(2)}\left(\bar{\boldsymbol{Y}}(\boldsymbol{X})\right) d\Gamma_c^{(2)} = -\boldsymbol{t}_t^{(1)}\left(\boldsymbol{X}\right) d\Gamma_c^{(1)}. \tag{2.28}$$

Eq. (2.28) facilitates replacement of the contact contribution in Eq. (2.27) by:

$$\delta\mathcal{W}_c(\boldsymbol{\varphi}_t, \overset{*}{\boldsymbol{\varphi}}) := -\int_{\Gamma_c^{(1)}} \boldsymbol{t}_t^{(1)}(\boldsymbol{X}) \cdot \left[\overset{*}{\boldsymbol{\varphi}}^{(1)}(\boldsymbol{X}) - \overset{*}{\boldsymbol{\varphi}}^{(2)}(\bar{\boldsymbol{Y}}(\boldsymbol{X}))\right] d\Gamma. \tag{2.29}$$

Using the resolution of $\boldsymbol{t}^{(1)}(\boldsymbol{X})$ into normal and tangential (or frictional) components in Eq. (2.29), we obtain:

$$\delta\mathcal{W}_c(\boldsymbol{\varphi}_t, \overset{*}{\boldsymbol{\varphi}}) := -\int_{\Gamma_c^{(1)}} \underbrace{\left[t_N \boldsymbol{\nu} - t_{T_\alpha} \boldsymbol{\tau}^\alpha\right]}_{\boldsymbol{t}^{(1)}(\boldsymbol{X})} \cdot \left[\overset{*}{\boldsymbol{\varphi}}^{(1)}(\boldsymbol{X}) - \overset{*}{\boldsymbol{\varphi}}^{(2)}(\bar{\boldsymbol{Y}}(\boldsymbol{X}))\right] d\Gamma \tag{2.30}$$

Eq. (2.30) can be expressed even more compactly through consideration of appropriate linearized variations of the contact kinematics (for a detailed description of this topic see [87]):

$$\delta\mathcal{W}_c(\boldsymbol{\varphi}_t, \overset{*}{\boldsymbol{\varphi}}) := \int_{\Gamma_c^{(1)}} \left[t_N\, \delta g + t_{T_\alpha}\, \delta\bar{\xi}^\alpha\right] d\Gamma \tag{2.31}$$

where δg is the normal gap variation and $\delta\bar{\xi}^\alpha$ is the tangential gap variation.

2.3 Discretization aspects

In this section we will introduce some basics aspects of the finite element discretization of contact interaction. The reader can refer to [87, 137, 142] for a more detailed description of this topic.

In giving the discrete formulation of the contact problem, the idea is that one applies the spatial discretization (Fig. 2.6) to the weak form of the governing equations. The result is a nonlinear set of ordinary differential equations. To be more specific, one begins by considering $\boldsymbol{\varphi}^{(i)^h}$ and $\overset{*}{\boldsymbol{\varphi}}^{(i)^h}$, finite dimensional counterparts of $\boldsymbol{\varphi}^{(i)}$ and $\overset{*}{\boldsymbol{\varphi}}^{(i)}$. Substitution of these finite dimensional quantities into the global variational principle (Eq. (2.26)) gives a set of nonlinear ordinary diferential equations of the form:

$$\boldsymbol{M}\ddot{\boldsymbol{d}}(t) + \boldsymbol{f}_{\text{int}}(\boldsymbol{d}(t)) - \boldsymbol{f}_{\text{ext}}(t) + \boldsymbol{f}_{\text{c}}(\boldsymbol{d}(t)) = 0, \tag{2.32}$$

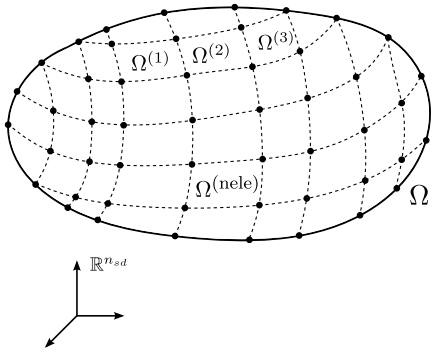

Figure 2.6: Finite element discretization of the computational domain.

subject to initial conditions on $\boldsymbol{d}$ and $\dot{\boldsymbol{d}}$. In Eq. (2.32), $\boldsymbol{M}$ is the mass matrix, $\boldsymbol{f}_{\text{int}}$ is the internal force vector, $\boldsymbol{f}_{\text{c}}$ is the contact force vector and $\boldsymbol{f}_{\text{ext}}$ is the external force vector, which is assumed to be known data. The vector $\boldsymbol{d}$ symbolically represents the solution vector, or a vector of nodal values of the motion $\boldsymbol{\varphi}^h$. Eq. (2.32) is in general highly nonlinear, mostly because of the terms $\boldsymbol{f}_{\text{int}}(\boldsymbol{d}(t))$ and $\boldsymbol{f}_{\text{c}}(\boldsymbol{d}(t))$. Its quasistatic equivalent is obtained by omission of the inertial term $\boldsymbol{M}\ddot{\boldsymbol{d}}(t)$. The contact stiffness, defined as $\boldsymbol{k}_c(\boldsymbol{d}) = \frac{\partial}{\partial \boldsymbol{d}} \boldsymbol{f}_{\text{c}}(\boldsymbol{d}(t))$ and the contact force vector $\boldsymbol{f}_{\text{c}}(\boldsymbol{d}(t))$ are needed to accomplish the desired result: the numerical solution of Eq. (2.32).

2.3.1 Contact surface discretization

For the discrete contact formulation developed in previous paragraph, all development depends only on the configurations and variations evaluated on the contact surfaces $\Gamma_c^{(i)}$, and not on the values in the interior of the bodies. Thus, in considering the discretization leading to the specification of $\boldsymbol{f}_{\text{c}}(\boldsymbol{d}(t))$, only the restrictions of $\boldsymbol{\varphi}^{(i)^h}$ and $\overset{*}{\boldsymbol{\varphi}}{}^{(i)^h}$ to $\Gamma_c^{(i)^h}$ need to be considered. These restrictions are considered to be collections of local mappings (denoted by superscript e), defined over individual element surfaces (see Fig. 2.7).

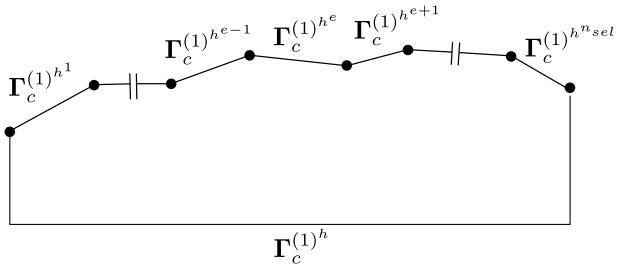

Figure 2.7: Discretization of the contact surface.

For example, $\boldsymbol{\varphi}^{(1)^{h^e}}(\boldsymbol{\eta})$, with $\boldsymbol{\eta} \in \mathcal{A}^{(1)^e}$, is expressed using the isoparametric interpolation as:

$$\boldsymbol{\varphi}^{(1)^{h^e}}(\boldsymbol{\eta}) = \sum_{a=1}^{n_{nes}} N_a(\boldsymbol{\eta}) \boldsymbol{d}_a^{(1)}(t), \tag{2.33}$$

where $\boldsymbol{d}_a^{(1)}(t)$ is a nodal value of $\boldsymbol{\varphi}^{(1)^h}$, and n_{nes} is the number of nodes per element surface.

$N_a(\boldsymbol{\eta})$ denotes a standard Lagrangian shape function, defined on the biunit square $\mathcal{A}^{(1)^e}$ for 3D problems and on $\mathcal{A}^{(1)^e} = [-1, 1]$ for 2D problems. The interpolation of $\overset{*}{\boldsymbol{\varphi}}{}^{(1)^h}(\boldsymbol{\eta})$ is similarly conceived, via:

$$\overset{*}{\boldsymbol{\varphi}}{}^{(1)^{h^e}}(\boldsymbol{\eta}) = \sum_{a=1}^{n_{nes}} N_a(\boldsymbol{\eta}) \boldsymbol{c}_a^{(1)}. \tag{2.34}$$

Using the isoparametric interpolation scheme, one also has:

$$\boldsymbol{X}^{h^e}(\boldsymbol{\eta}) = \sum_{a=1}^{n_{nes}} N_a(\boldsymbol{\eta}) \boldsymbol{X}_a. \tag{2.35}$$

Analogues of Eqns. (2.33)-(2.35) are assumed to hold for body (2):

$$\boldsymbol{\varphi}^{(2)^{h^e}}(\boldsymbol{\xi}) = \sum_{b=1}^{n_{nes}} N_b(\boldsymbol{\xi}) \boldsymbol{d}_b^{(2)}(t), \tag{2.36}$$

$$\overset{*}{\boldsymbol{\varphi}}{}^{(2)^{h^e}}(\boldsymbol{\xi}) = \sum_{b=1}^{n_{nes}} N_b(\boldsymbol{\xi}) \boldsymbol{c}_b^{(2)}, \tag{2.37}$$

and

$$\boldsymbol{Y}^{h^e}(\boldsymbol{\xi}) = \sum_{b=1}^{n_{nes}} N_b(\boldsymbol{\xi}) \boldsymbol{Y}_b, \tag{2.38}$$

defined over element surface parent domains $\mathcal{A}^{(2)^e}$. The contact virtual work in the discrete setting is now written by substitution of the above discrete fields into Eq. (2.31), as:

$$\delta\mathcal{W}_c(\boldsymbol{\varphi}_t^h, \overset{*}{\boldsymbol{\varphi}}{}^h) := \int_{\Gamma_c^{(1)^h}} [t_N^h \, \delta g^h + t_{T_\alpha^h} \, \delta\bar{\xi}^{\alpha^h}] \, d\Gamma. \tag{2.39}$$

Eq. (2.39) may be written as a sum of integrals over the n_{sel} elements surface of $\Gamma_c^{(1)^h}$ (see Fig. 2.7):

$$\delta\mathcal{W}_c(\boldsymbol{\varphi}_t^h, \overset{*}{\boldsymbol{\varphi}}{}^h) := \sum_{e=1}^{n_{sel}} \int_{\Gamma_c^{(1)^{h^e}}} [t_N^h \, \delta g^h + t_{T_\alpha^h} \, \delta\bar{\xi}^{\alpha^h}] \, d\Gamma, \tag{2.40}$$

where each subintegral of Eq. (2.40) is evaluated using quadrature.

Based on Eq. (2.40), the global contact force vector $\boldsymbol{f}_c$ can be expressed as:

$$\boldsymbol{f}_c = \mathop{\mathbf{A}}_{\tilde{k}=1}^{n_{sel} \cdot n_{int}} W^{\tilde{k}} \, j(\boldsymbol{\eta}^{\tilde{k}}) \, \left[t_N^h(\boldsymbol{\eta}^{\tilde{k}}) \, \delta g^h(\boldsymbol{\eta}^{\tilde{k}}) + t_{T_\alpha^h}(\boldsymbol{\eta}^{\tilde{k}}) \, \delta\bar{\xi}^{\alpha^h}(\boldsymbol{\eta}^{\tilde{k}}) \right] \tag{2.41}$$

where $\mathbf{A}$ is the standard finite element assembly operator, n_{int} is the number of integration points per element surface of $\Gamma_c^{(1)^h}$, W is the quadrature weight, j is the jacobian of the transformation and $\tilde{k}$ is a revised quadrature point index, which runs over all quadrature points in $\Gamma_c^{(1)^h}$.

The most relevant conclusion that can be extracted from Eq. (2.41) is that the global contact

force vector results from the assembly of elemental matrices which are constructed based on the position of contacting nodes between the two surfaces. In this way, one can think of new elements that are created between the connection of contacting nodes of both surfaces. The elemental matrices of such elements are assembled in the global system to obtain the global contact force. This elements are usually called *contact elements*.

Contact elements are kind of bridge elements between locally separated but potentially interacting surfaces. Each contact element contains components of both surfaces and the composition of these components depends upon the choice of the contact discretization. The most common and widely used contact discretization is the node-to-segment approach (see Fig. 2.8). Each contact element has its own vector of unknowns, residual and tangential matrix. Therefore, contact elements are assembled to the global system matrix, together with unknowns, residual and tangential matrices of ordinary structural elements.

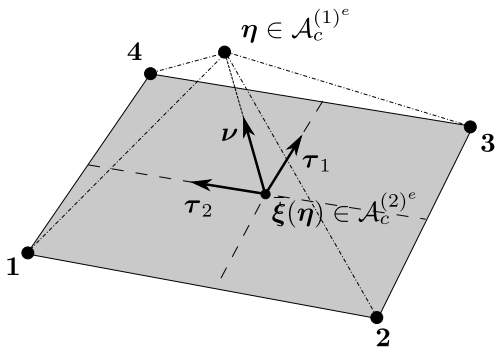

Figure 2.8: Contact element - Node-to-segment discretization.

The most important practical aspect of computing the contact force is the acquisition of the projection $\bar{\boldsymbol{y}} \in \gamma_c^{(2)^h}$ for a quadrature point currently at location $\boldsymbol{x} \in \gamma_c^{(1)^h}$, see Fig. 2.9. This projection is central to the definition of both the gap $\boldsymbol{g}$ and the tangential basis, needed for the frictional case. Calculation of the projection is often referred to as *contact detection* or *searching*.

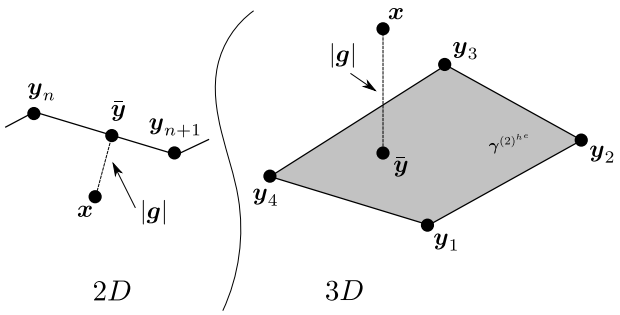

Figure 2.9: Projection of slave node to master segment/surface.

Chapter 3

Analysis of Existing Computational Methods

In this chapter we aim to expose the main drawbacks present in the parallelization of traditional contact mechanics algorithms and to provide a strong justification for the development of the parallel methodologies for the numerical solution of contact problems which are the main reason of this thesis. For such end, the chapter is divided in two parts. The first part is devoted to the introduction of some basic concepts related to parallel computing. The second part describes the current context of computational contact mechanics and enumerates the reasons which fundament this work. To conclude, we introduce and enumerate the design basis for the novel methodology proposed in this thesis.

3.1 Key concepts for parallel computing. A crash introduction

The aim of this section is to present some key concepts related to parallel computing and to the domain decomposition approach, which plays a relevant role in the motivation of this thesis.

3.1.1 Parallel computational models

Parallel computational models form a complicated structure. They can be differentiated along multiple axes: whether the memory is physically shared or distributed, how much communication is in hardware or software, what the unit of execution is, and so forth. The picture could be even more confusing by the fact that software provides an implementation of any computational model on any hardware. This section thus intends to define some terms to delimit our discussion and usage of the message-passing interface, which is a building block of this thesis.

Although parallelism occurs in many places and at many levels in a modern computer, one of the first cases it was made available to the programmer was in vector processors. Indeed, the vector machine began the current age of supercomputing. The vector machine's notion of operating on an array of similar data items in parallel during a single operation was extended to include the operation of whole programs on collections of data structures, as in SIMD (single-instruction, multiple-data) machines. At whatever level, the model remains the same: the parallelism comes

entirely from the data; the program itself looks very much like a sequential program. The partitioning of data that underlies this model may be done by a compiler. Nowadays, data parallelism has made a dramatic come back in the form of Graphical Processing Units, or GPUs.

Parallelism that is not determined implicitly by data independence but is explicitly specified by the programmer is control parallelism. One simple model of control parallelism is the shared memory model, in which each processor has access to all of a single, shared address space at the usual level of load and store operations (see Fig. 3.1). In a shared memory system, the processors usually communicate implicitly by accessing shared data structures. OpenMP [128] is probably the most well known and globally used application programming interface for multi-platform shared memory multiprocessing programming.

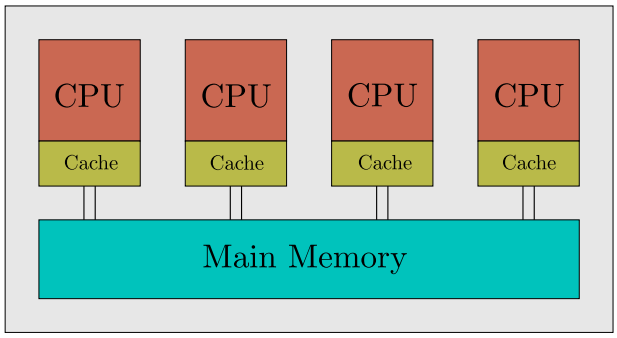

Figure 3.1: Shared memory architecture.

The message-passing model assumes that a set of processes that have only local memory can communicate with other processes by sending and receiving messages. It is a defining feature of the message-passing model that data transfer from the local memory of one process to the local memory of another requires communication operations to be performed by both processes. Message-passing is used widely on parallel computers with distributed memory (see Fig. 3.2). In a distributed memory system the memory is associated with individual processors, and a processor is only able to address its own memory. In this context, the message-passing model is suitable for the communication and data exchange amongst all the processors. The Message-Passing Interface (MPI) is a standardized and portable message-passing system designed by a group of researchers from academia and industry to function on a wide variety of parallel computing architectures [127]. The standard defines the syntax and semantics of a core of library routines useful to a wide range of users writing portable message-passing programs.

Current large-scale parallel computers are neither of the purely shared memory nor of the purely distributed memory type but a mixture of both, i.e., there are shared memory building blocks connected via a fast network. The concept has clear advantages regarding price vs. performance. The principal hardware issue is the cost of scaling the interconnection in a shared memory architecture. As we add processors to the communication bus amongst the CPUs, the chance that there will be conflicts over access to the bus increase dramatically, so buses are suitable for systems with only a few CPUs. On the other hand, distributed memory interconnects

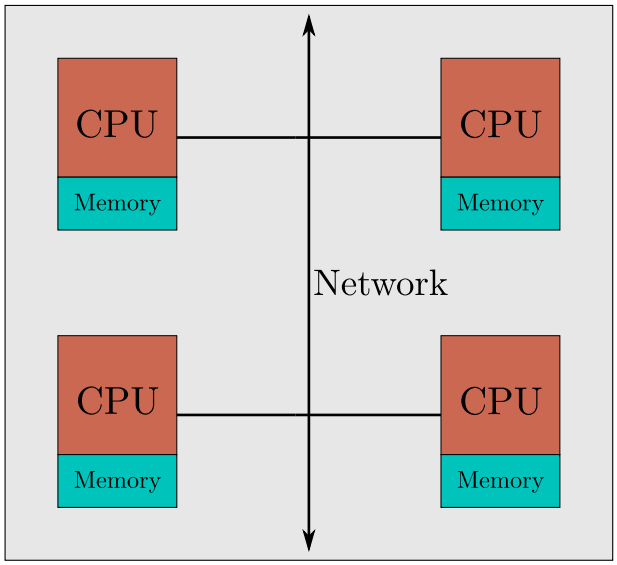

Figure 3.2: Distributed memory architecture.

are relatively inexpensive, and distributed memory systems with thousands of processors have been built. Thus, distributed memory systems are often better suited for problems requiring vast amounts of data or computation. Parallel computers with hierarchical structures as described above are also called hybrids. The concept is more generic and can also be used to categorize any system with a mixture of available programming paradigms on different hardware layers. For a more detailed description of parallel computational models, parallel architectures and parallel programming, see [55, 104, 56].

The aim of this thesis is the solution of mechanical contact problems in large scale systems, which involves a considerable number of processors. In this context, exclusively shared memory systems are not suitable for the purpose of this work, so distributed memory (or even hybrid) architectures must be used. The parallelization of the solution of mechanical contact problems is thus focused on distributed memory systems, where the MPI standard is the main tool used for all the implementations that appear in this thesis. The extension to hybrid systems is relatively straightforward since the parallelization at the shared memory level doesn't change the full workflow of the algorithm, as it only takes profit of finer grain parallelism of the workflow once stablished. In this work we will focus on the MPI layer of parallelism.

3.1.1.1 Message passing interface (MPI)

The Message Passing Interface (MPI) [127] is a standardized specification of a set of library subroutines for the portable and flexible development of efficient message-passing parallel programs. The standard defines the syntax and semantics of library routines and allows users to write portable programs in the main scientific programming languages. Since its release, the MPI specification has become the leading standard for message-passing libraries for parallel computers. Some key points are:

- The MPI Forum is in charge of the standardization (40 participating organizations, includ-

ing vendors, researchers, software library developers, and users).

- Revised several times, with the most recent specification being MPI-3. Actual implementations differ in the version/features of the standard they support.
- Is supported on virtually all HPC platforms. Several implementations are open source as OpenMPI or MPICH. Commercial implementations as Intel MPI are also available.
- Provides Fortran, C, and C++ bindings.
- Has a very broad standard with a huge number of library subroutines (over 440 in MPI-3). Fortunately, most applications merely require less than a dozen of them.

The way MPI programs are compiled and run is not fixed by the standard. Compiler and linker need special options that specify where modules and libraries can be found. There is a considerable variation in those locations among installations. Most MPI implementations provide compiler wrapper scripts (e.g., mpif90) that automatically supply the required options to the underlying native compiler. Typically a script called mpirun is provided to start a message-passing program: processor cores have to be allocated in advance. How exactly processes are created is entirely up to the implementation, and typically mpirun uses the batch system's infrastructure to launch processes.

An MPI message is defined as an array of elements of a particular MPI data type. MPI data types can be either basic or derived. MPI derived types created by calling appropriate MPI calls. MPI needs to know the data type of messages as it supports heterogeneous environments where it may be necessary to perform on-the-fly data conversions. The MPI data types on sender and receiver must match for messages to proceed.

MPI conforms the following rules:

- Single Program Multiple Data (SPMD) model: the same program runs on all processes. All processes taking part in a parallel calculation can be distinguished by a unique identifier called rank.
- The program is written in a sequential language like Fortran, C, C++ or Python. Data exchange is carried out via calls to MPI library subroutines.
- All variables in a process are local to this process.

3.1.2 Domain decomposition

The meaning of the term *domain decomposition* depends strongly on the context. It refers to the splitting of a partial differential equation, or to its numerical approximation, into coupled problems on smaller subdomains forming a partition of the original domain. This decomposition may enter at the continuous level, where different physical models may be used in different regions, or at the discretization level, where it may be convenient to employ different approximation methods in different regions, or in the solution of the algebraic systems arising from

the approximation of the partial differential equation. At first glance, these aspects seem to be rather independent. However, all have one central idea in common: the decomposition of the underlying global problem into suitable subproblems of smaller complexity. In general, a complete decoupling of the global problem into many independent subproblems, which are easy to solve, is not possible. Since the subproblems are very often coupled, there has to be communication between the different subproblems. For a comprehensive and more general overview of domain decomposition methods, see [136, 130, 120].

This thesis is entirely devoted to the third aspect of domain decomposition described in the previous paragraph, which is the solution of the algebraic systems arising from the approximation of the partial differential equation. In practical applications, finite element method or other discretizations reduce the problem to the solution of an often massive algebraic system of equations. Direct factorization of such systems might then not be a viable option and the use of basic iterative methods, such as the conjugate gradient algorithm, can result in very slow convergence. The basic idea of domain decomposition is that instead of solving one massive problem on a domain, it may be convenient (or necessary) to solve many smaller problems on single subdomains a certain number of times.

Domain decomposition methods aim at parallelizing the solution process by decomposing the computational domain in several subdomains. The problems on the subdomains are independent, which makes domain decomposition methods suitable for parallel computing. Regarding the computational aspects of domain decomposition, this thesis is devoted to parallelization in distributed memory machines, based on mesh partitioning and MPI processes. This implementation strategy proves to be especially well-suited for this type of applications.

The parallelization paradigm considered in this thesis is a sub-structuring method, were a Master-Worker interaction model between the CPUs is used. Sub-structuring methods consist essentially in distributing the work among the Workers, leaving the Master in charge of general tasks like I/O. In a Master-Worker interaction, the Master reads the mesh and performs the partition of the element graph. For the pure MPI strategy, each MPI process (the Workers) is in charge of each subdomain (i.e. the number of MPI processes equals the number of subdomains). The Workers build the local matrices and right-hand side and are in charge of the resulting system solution in parallel. In the assembly stage, very few communications are needed between Workers and the scalability only depends essentially on the load balancing.

For the sake of clarity, let's consider the example shown in Fig. 3.3. Here, a 2-dimensional discretized domain composed of 24 quadrilateral elements and 35 nodes is partitioned in 3 identical subdomains/MPI processes P_1, P_2 and P_3. In general, discretized domains can be split by elements or by nodes. For the finite element discretization, which is the one considered in this thesis, the partitioning of the domain throughout the elements is commonly the preferred choice (see [93]). Hence, the nodes used as a reference for the domain partitioning, called interface nodes, are repeated among contiguous subdomains. Going back to the example of Fig. 3.3, each of these subdomains are then conformed by 8 elements and 15 nodes each. Each MPI process handles local element and node identifiers. Suppose now that we want to solve the Poisson

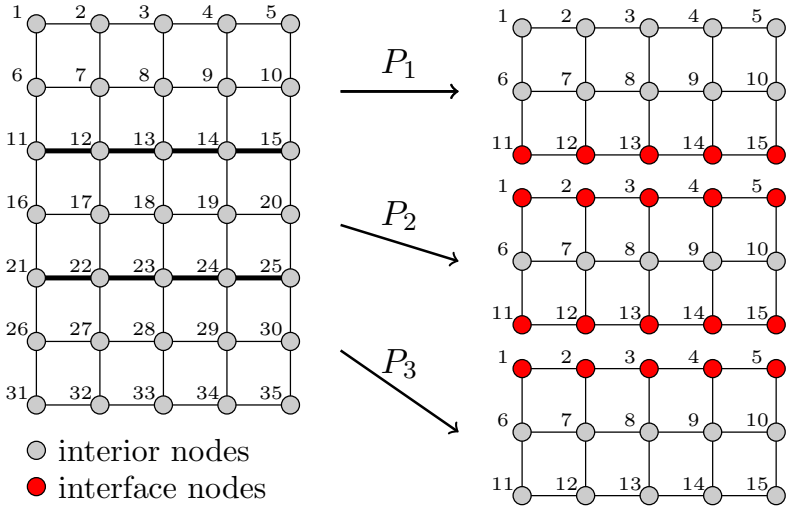

Figure 3.3: Mesh partitioning for domain decomposition approach.

equation using finite elements in parallel using the configuration shown in the previous example. In a Master-Worker interaction, each MPI process stores/assembles a local portion $\mathbf{A}_i$ and $\mathbf{f}_i$ ($i \doteq 1, 2, 3$) of the global matrix/vector $\mathbf{A}$ and $\mathbf{f}$ (i.e. the portion that belongs to its subdomain). Global matrices and vectors are never stored/assembled explicitly.

Parallel finite element assembly results in a sub-assembled (partially-summed) $\mathbf{A}_i$ and $\mathbf{f}_i$, the portion of $\mathbf{A}$ and $\mathbf{f}$ locally assembled by MPI process P_i. Sub-assembly means that for $\mathbf{A}_i$ and $\mathbf{f}_i$ the nodal contributions at interface nodes positions are partial because they don't take into account the contributions from neighbour nodes located in other subdomains. To compute a fully-summed solution (the correct solution) of the unknown vector $\mathbf{u}$, nodal contributions at interface nodes must be shared (and summed) amongst the subdomains (see Fig. 3.4).

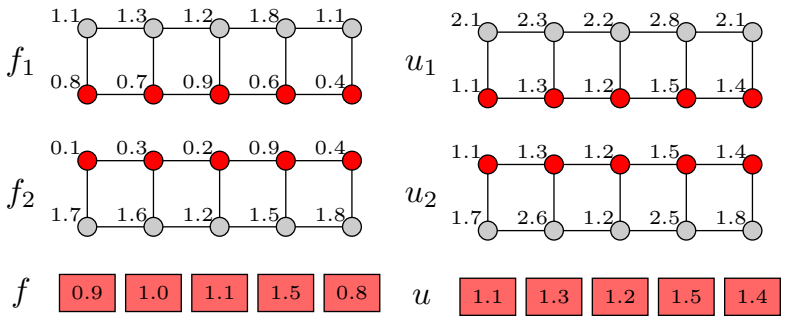

Figure 3.4: Parallel finite element assembly of RHS vector and solution vector.

3.1.3 Mesh partitioning

A great variety of methods for the numerical solution of any physical problem, such finite elements, finite volumes or finite differences, require a discretization of the physical domain into nodes and elements. This process is known as *meshing*. The main unknowns of the physical problem are then computed for each of the nodes of the *mesh*. The numerical resolution of real-

world engineering problems is a rather demanding task since meshes often have large numbers of elements. As a result, the numerical method is usually parallelised. For the solution of a, for instance, finite element problem in parallel using the domain decomposition method, the usual approach is to partition the mesh into subdomains. Each subdomain can then be mapped to each of the processors of the parallel machine allocated for the resolution of the problem. When assembling and solving the resultant linear system each processor is then responsible for the element matrices belonging to the elements that it owns. Furthermore, when the elements surrounding a particular node are owned by different processors some communication is required to obtain the global solution for the problem. Consequently, to achieve high parallel efficiency it is important that the mesh is partitioned in such a way that workloads are well balanced and interprocessor communication is minimised. This is achieved mainly by ensuring same node number in each subdomain and minimizing the number of nodes on the subdomains interfaces.

An important component in mesh partitioning is the well-known graph-partitioning problem (see Fig. 3.5). Unfortunately, this is an NP-hard optimisation problem, which makes it impossible to find optimum solutions in polynomial time. Consequently, heuristic approaches are normally used for mesh partitioning.

In the past two decades, graph partitioning methods have witnessed rapid development, giving rise to many graph partitioning software packages, such as METIS [97, 78], Zoltan [23], JOSTLE [134] and SCOTCH [121, 107]. Among these software packages the most representative one is METIS, which is a set of serial programs for partitioning graphs and finite element meshes. The algorithms implemented in METIS are based on the multi-level recursive-bisection, multi-level k-way, and multi-constraint partitioning schemes. The multi-level method reduces the size of the original graph, performs a partition on this and then finally uncoarsens the graph to find a partition for the original graph. It can be used as a suite of standalone partitioning applications or by linking a users own Fortran or C application to the software library. Comparing with other widely used partitioning algorithms, METIS is faster while providing high quality partitions [78].

3.1.4 Sparse storage

A sparse matrix is a matrix in which most of the elements are zero. Large sparse matrices often appear in scientific or engineering applications when solving partial differential equations. In particular, the matrices which result from the finite element discretization have the particularity of being considerably sparse. When storing and manipulating sparse matrices on a computer, it is beneficial and often necessary to use specialized algorithms and data structures that take advantage of the sparse structure of the matrix. Operations using standard dense-matrix structures and algorithms are slow and inefficient when applied to large sparse matrices as processing and memory are wasted on the zeroes. Sparse data is by nature more easily compressed and thus require significantly less storage. Very large sparse matrices are infeasible to manipulate using standard dense-matrix algorithms.

One method for storing sparse matrices is the compress sparse row (CSR) storage method [115]. The CSR storage method uses three arrays to store the non-zero elements of a sparse matrix. The

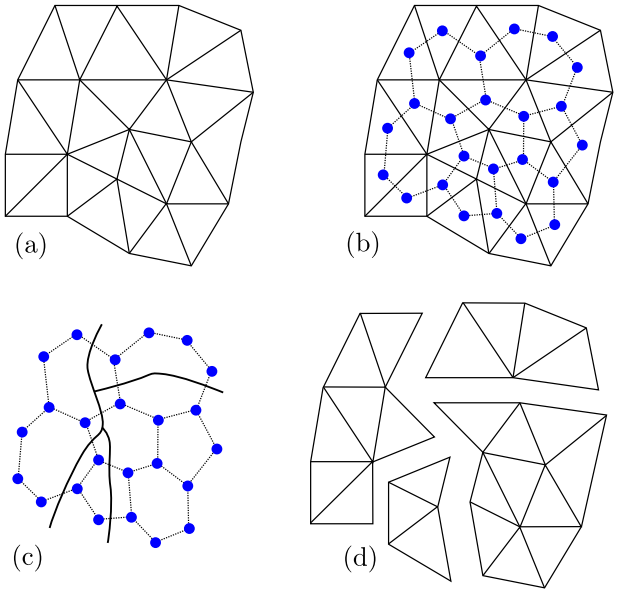

Figure 3.5: Mesh partitioning: (a) Sample mesh. (b) Mesh with induced graph. (c) Graph partitioning. (d) Partitioned mesh.

first array stores contiguously the non-zero elements in each row and is called Data array. The second array is of the same size as the Data array and stores the Column indices corresponding to the entries in the Data array. The third array is called Row pointer and stores the locations in the Data array that start a row.

This method of storing matrices is illustrated by a simple example. Fig. 3.6 shows a 1D mesh composed of 5 nodes, used to discretize the Poisson equation $\nabla^2\varphi = 0$. Fig. 3.7 shows the dense matrix which results from the finite element discretization and the arrays of the CSR format.

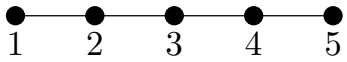

Figure 3.6: 1D mesh example.

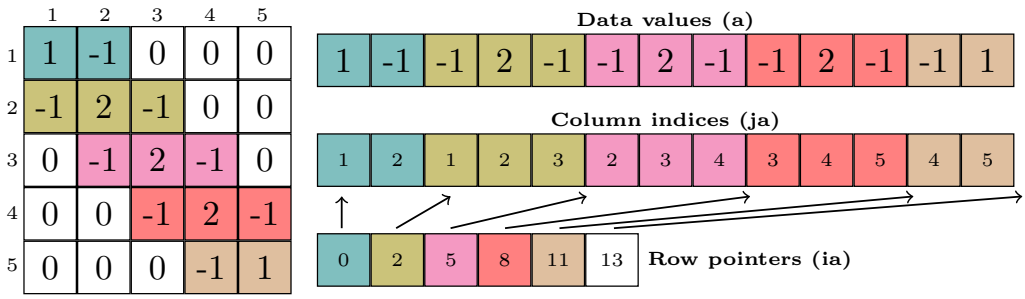

Figure 3.7: Example of matrix storage in compress sparse row (CSR) format.

In the example shown in Fig. 3.7, the dense matrix is first constructed and then, once the

zeroes location is known, used to build the CSR format arrays. In practice, computational codes which exploit the advantages of sparse storage never store the matrix in its dense form. On the contrary, they allocate only the required memory for the storage of the CSR format arrays by looking into the mesh connectivity, i.e. how the nodes of the mesh are connected. Mesh connectivity is what computational codes analyze to "predict" the location of zeroes without having to assemble the dense form of the system matrix.

3.2 Contact mechanics: methods of constraint enforcement

The variational inequality that results after the enforcement of the contact boundary conditions in the continumm equation is not appropriate for discretization. As remarked in Sec. 1.2, most of the numerical procedures for the resolution of contact problems are based on the so-called *variational equality*, which is easy to introduce in a finite element framework and can be easily adapted to pre-existent minimization techniques, as might be found generically in [92, 52]. This fact has been exploited historically to conceive the vast majority of the contact algorithms in common use today.

In this section we shall discuss the most common formulations that can be applied to incorporate the contact constraints into the variational formulation, Eq. (2.26). For the sake of simplicity we will consider here the frictionless form of the governing equations for contact mechanics. We present here the most popular and widely used methods for constraint enforcement applied in contact algorithms, which are: penalty, Augmented Lagrangian and Lagrange multipliers. We introduce them by means of practical example characterized by a 1D frictionless linear example of two beams, in a simplified way to facilitate a focus on the principal ideas, without diverting our intentions with more complex issues which are beyond our purpose. It is remarked that the ideas which emerge from the examples discussed below in this section are not limited to the linear elastic case. The interpretations of the ideas that follow, however, can be appropriately generalized to broader context.

3.2.1 Unconstrained system

We present a 1D frictionless linear example of two identical cantilever beams as shown in Fig. 3.8. Here, we consider an equilibrium situation of no contact, where the beams are initially separated by a gap g^* and a force of magnitude F is applied to node u_1^2.

In a non-contact situtation, as the one shown in Fig. 3.8, the last term of the governing equation for the contact problem, Eq. (2.26), vanishes. As in this case we do not need to impose the contact constraints, we define this configuration as an *unconstrained system*. This unconstrained system can be simply modelled by the sum of the momentum balance equation for each beam separately. From Eq. (2.26), and considering a linear example, we can write this expression in the following algebraic way:

$$\delta\mathcal{W} := \sum_{i=1}^{2} \delta\mathcal{W}_{sb}^{(i)} = \mathbf{K}\mathbf{u} - \mathbf{f} = 0, \tag{3.1}$$

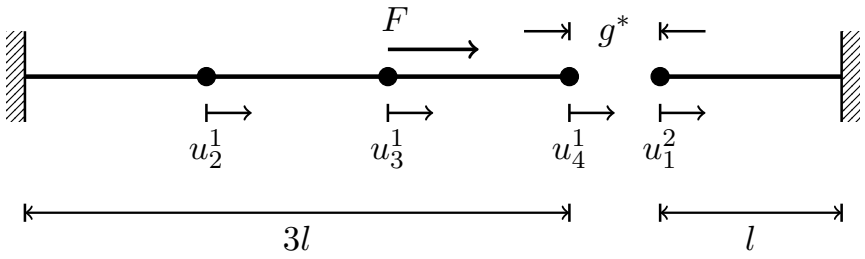

Figure 3.8: 1D FRICTIONLESS LINEAR EXAMPLE.

where $\mathbf{K}$ is the system matrix, $\mathbf{u}$ is the solution vector and $\mathbf{f}$ are the external forces. If we use the mesh of the Fig. 3.8 to discretize Eq. (3.1) using the finite element method, we obtain the following linear system of equations:

$$\frac{E\,A}{l}\left[\begin{array}{ccc|c} 2 & -1 & 0 & 0 \\ -1 & 2 & -1 & 0 \\ 0 & -1 & 1 & 0 \\ \hline 0 & 0 & 0 & 2 \end{array}\right]\left(\begin{array}{c} u_2^1 \\ u_3^1 \\ u_4^1 \\ \hline u_1^2 \end{array}\right) = \left(\begin{array}{c} 0 \\ F \\ 0 \\ \hline 0 \end{array}\right), \tag{3.2}$$

where E is the Young modulus of the material of the beams, A is the cross section of both beams, l is the characteristic length and F is the localized force applied to node u_3^1, as shown in Fig. 3.8.

Solving the linear system of equations given by Eq. (3.2), we obtain the following parametric solution vector for node displacements:

$$\mathbf{u}^T = \frac{Fl}{EA}\{1, 2, 2, 0\}^T. \tag{3.3}$$

Note that as the system is uncoupled due to the existence of the gap g^*, which is explained by the lack of relation between nodes u_4^1 and u_1^2. Thus, the displacement of node u_1^2 is equal to zero.

A contact situation will occur when the the gap is closed. From Eq. (3.3) we observe that this is equivalent to the following relation:

$$F > \frac{EA}{2}\frac{g^*}{l}. \tag{3.4}$$

When Eq. (3.4) is fullfiled, we must solve a constrained problem taking into account the contact boundary conditions, in order to properly model the contact between both beams. In the following sections, and based on this same example, we will introduce the different available and well-known methods in the literature of contact mechanics to solve this kind of problems.

3.2.2 Constrained system

Recalling Eq. (2.26), the virtual work for the entire system considering the contact forces can be written as follow:

$$\delta\mathcal{W} := \sum_{i=1}^{2} \delta\mathcal{W}_{sb}^{(i)} + \delta\mathcal{W}_c = 0. \tag{3.5}$$

From Eq. (2.30), we can express the last term of Eq. (3.5) in the following way:

$$\delta\mathcal{W}_c := \int_{\Gamma_c^{(1)}} [t_N\, \delta g + t_{T_\alpha}\, \delta\bar{\xi}^\alpha]\, d\Gamma. \tag{3.6}$$

As we are considering a frictionless example, then Eq. (3.6) simplifies to:

$$\delta\mathcal{W}_c := \int_{\Gamma_c^{(1)}} t_N\, \delta g\, d\Gamma. \tag{3.7}$$

Eq. (3.5) together with frictionless contact conditions (see Sec. 2.2.1):

$$t_N \geq 0, \tag{3.8a}$$
$$g \leq 0, \tag{3.8b}$$
$$t_N\, g = 0, \tag{3.8c}$$

define the boundary value problem with contact constraints.

On the other hand, the general formula for the gap g can be expressed as:

$$g = g^* - (u_4^1 - u_1^2), \tag{3.9}$$

where g^* is the initial gap and u_4^1 and u_1^2 are the displacement of the contacting nodes.

Finally, the variation of the gap g can be written as follow:

$$\delta g = \delta u_4^1 + \delta u_1^2. \tag{3.10}$$

3.2.2.1 Penalty method

In the penalty method the constrained optimization problem is converted into a unconstrained problem by introducing an artificial penalty for violating the constraint. Specifically, for the problem at hand, one obtains a penalty method for the frictionless contact problem by penalizing any penetration ($g > 0$), by the following relation:

$$t_N = \epsilon_N \langle g \rangle, \tag{3.11}$$

where $\epsilon_N > 0$ is defined as the penalty parameter and the notation $\langle \cdot \rangle$ denotes the *Macauley bracket*, which simply renders the positive part of its operand via:

$$\langle x \rangle := \begin{cases} x \ \text{ if } \ x \geq 0, \\ 0 \ \text{ if } \ x < 0. \end{cases} \tag{3.12}$$

Use of Eq. (3.11) in Eq (3.7) gives rise to the penalized form of the contact integral:

$$\delta \mathcal{W}_c := \int_{\Gamma_c^{(1)}} \epsilon_N \langle g \rangle \, \delta g \, d\Gamma. \tag{3.13}$$

Combining Eqs. (3.1) and (3.13) with Eq. (3.5) we obtain the penalized algebraic form of the contact problem:

$$\delta \mathcal{W} = \mathbf{K}_P \, \mathbf{u} - \mathbf{f}_P = 0. \tag{3.14}$$

where $\mathbf{K}_P$ is the penalized system matrix, $\mathbf{u}$ is the solution vector and $\mathbf{f}_P$ are the penalized external forces.

Going back to our base example, discretization of Eq. (3.14) for the geometry depicted in Fig. 3.8 via the finite element method gives the following linear system of equations:

$$\left[\begin{array}{ccc|c} 2\frac{EA}{l} & -1\frac{EA}{l} & 0 & 0 \\ -1\frac{EA}{l} & 2\frac{EA}{l} & -1\frac{EA}{l} & 0 \\ 0 & -1\frac{EA}{l} & 1\frac{EA}{l}+\epsilon_N & -\epsilon_N \\ \hline 0 & 0 & -\epsilon_N & 2\frac{EA}{l}+\epsilon_N \end{array}\right] \left(\begin{array}{c} u_2^1 \\ u_3^1 \\ u_4^1 \\ \hline u_1^2 \end{array}\right) = \left(\begin{array}{c} 0 \\ F \\ \epsilon_N \, g^* \\ \hline -\epsilon_N \, g^* \end{array}\right) \tag{3.15}$$

From Eq. (3.15) it can be seen that due to the contact constraints, nodes u_4^1 and u_1^2 are now coupled. Comparing with Eq. (3.2), this can be observed by the appearence of extra cross terms which include the penalty parameter on Eq. (3.15).

The coupling of nodes u_4^1 and u_1^2 can be physically interpreted by the introduction of a new structural element connecting both nodes, which appears due to the penalization (see Fig. 3.9). This element has the following elementary matrix:

$$\left[\begin{array}{cc} \epsilon_N & -\epsilon_N \\ -\epsilon_N & \epsilon_N \end{array}\right] \left(\begin{array}{c} u_4^1 \\ u_1^2 \end{array}\right) = \left(\begin{array}{c} \epsilon_N \, g^* \\ -\epsilon_N \, g^*. \end{array}\right) \tag{3.16}$$

To reinforce the previous idea, it can be observed that the assembly of the elementary matrix given by Eq. (3.16) in the unconstrained linear system given by Eq. (3.2) produces the coupled system defined by Eq. (3.15).

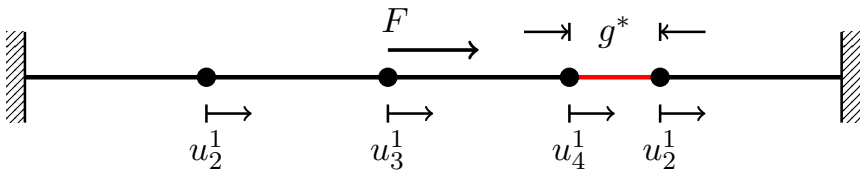

Figure 3.9: Additional structural element introduced by penalization.

3.2.2.2 Lagrange multipliers method

This method is used in optimization theory to find the extremum of a functional subjected to constraints. In a contact situation the idea is to minimize the functional $\mathcal{W}_{sb}$ from Eq. (2.8)

subjected to frictionless contact conditions given by Eq. (2.18). Thus, when contact is produced, we want to solve the following problem:

$$\min \mathcal{W}_{sb} \text{ subjected to } g = 0, \tag{3.17}$$

where g is the gap function. The basic idea of the Lagrange multipliers method is to expand the functional $\mathcal{W}_{sb}$ in the following way:

$$\mathcal{W}(\boldsymbol{u}, \lambda) := \mathcal{W}_{sb}(\boldsymbol{u}) + \mathcal{W}_{\lambda}(\boldsymbol{u}, \lambda), \tag{3.18}$$

where

$$\mathcal{W}_{\lambda}(\boldsymbol{u}, \lambda) := \int_{\Gamma_c^{(1)}} \lambda \, g \, d\Gamma. \tag{3.19}$$

Eq. (3.18) constitutes a *saddle problem*, whose solution is a maximum of $\mathcal{W}$ with respect to Lagrange multipliers λ but a minimum with respect to displacements $\boldsymbol{u}$. As Lagrange multipliers can be physically interpreted as the contact pressure, the solution of Eq. (3.18) satisfy not only the constraint $g = 0$ but also $t_N > 0$, as stated in Eq. (2.18):

Contrary to the penalty method explained in Sec. 3.2.2.1, where the resulting functional involves only one type of unknown, which are the displacements, the Lagrange multiplier method introduce extra unknowns to the system. The problem is then formulated as follows:

$$\delta\mathcal{W}_{sb}(\boldsymbol{u}, \delta\boldsymbol{u}) + \delta\mathcal{W}_{\lambda}(\delta\boldsymbol{u}, \lambda) = 0 \tag{3.20a}$$

$$\delta\mathcal{W}_{\lambda}(\boldsymbol{u}, \delta\lambda) = 0 \tag{3.20b}$$

The algebraic form of Eq. (3.20) can be written as:

$$\delta\mathcal{W} = \mathbf{K}_{lm}\, \mathbf{u}_{lm} - \mathbf{f}_{lm} = 0, \tag{3.21}$$

where $\mathbf{K}_{lm}$ is the augmented form of the system matrix, $\mathbf{u}_{lm}$ is the solution vector which includes displacements and Lagrange multipliers, and $\mathbf{f}_{lm}$ are the augmented external forces.

Returning to our base example (Fig. 3.8), discretization of Eq. (3.20) with the finite element method gives the following linear system of equations:

$$\frac{E\,A}{l}\begin{bmatrix} 2 & -1 & 0 & 0 & 0 \\ -1 & 2 & -1 & 0 & 0 \\ 0 & -1 & 1 & 0 & -1 \\ 0 & 0 & 0 & 2 & 1 \\ 0 & 0 & -1 & 1 & 0 \end{bmatrix} \begin{pmatrix} u_2^1 \\ u_3^1 \\ u_4^1 \\ u_1^2 \\ \lambda_N \end{pmatrix} = \begin{pmatrix} 0 \\ F \\ 0 \\ 0 \\ -g^* \end{pmatrix} \tag{3.22}$$

From the discretized linear system (Eq. (3.22)) it can be observed that the Lagrange multiplier act as intermediary for the transference of information between contacting nodes u_4^1 and u_1^2. From a geometrical viewpoint, the use of the Lagrange multiplier method is equivalent to the introduction of an extra node into the mesh which is connected to the contacting nodes. This

interpretation is schematically represented in Fig. 3.10.

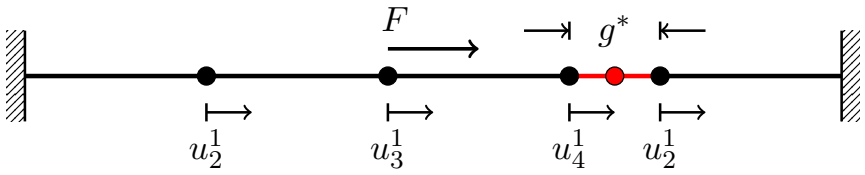

Figure 3.10: Additional node introduced by the Lagrange multipliers method.

It is worth mentioning that we have presented a very simplified case where only one Lagrange multiplier was needed. In a discrete system, the number of Lagrange multipliers depends on the number of contacting nodes which must be restricted from penetration. In more complex and realistic contact examples, the number of unknowns for the Lagrange multipliers not only can be considerably larger than one, but also its number can be time-dependent, as the contacting interfaces can evolve with time.

3.2.2.2.1 Mortar method for contact problems Recently, new methods, so-called mortar methods originally proposed in [18] for mesh tying, were designed for domain decomposition in which unstructured grids are connected within a parallel finite element solution. These methods has also been applied to finite element contact problems for two dimensional linear kinematics [15, 64, 96] and to large deformation kinematics for curved 3D surfaces [117, 118] when the nodes in the contact interface do not coincide. Contrary to the node-to-segment discretization, the mortar methods are based on a segment-to-segment apporach, and they do not lock since they are LBB stable [25]. As mortar methods for contact problems deal with the main numerical issues that affect the robustness of the node-to-segment approach (i.e. is valid only for low order elements, fails contact patch test unless a two-pass scheme is used and the stability test or inf-sup condition for Lagrange multipliers fails), they are currently the most general and well stablished methodology for numerical simulation of contact problems. As a general characteristic of this approach, mortar methods are based on the introduction of Lagrange multipliers to weakly enforce the contact constraints, thus increasing dynamically the number of degrees of freedom of the linear system to solve.

3.2.2.3 Augmented Lagrangian method

As shown in Sec 3.2.2.2 within the framework of the Lagrange multipliers method, contact conditions are exactly satisfied by the introduction of Lagrange multipliers, which increase the number of unknowns in the linear system. The additional unknowns that this method introduces require supplementary computational efforts. On the other hand, as seen on Sec. 3.2.2.1, the penalty method is simpler to implement and to interpret. Nevertheless, it presents the drawback that the contact conditions are fulfilled exactly only in the case of an infinite penalty parameter. This results in an ill-conditioning of the numerical problem.

The main idea of the Augmented Lagrangian method [63, 114] is to combine either the penalty method with the Lagrange multiplier method. It yields a fully unconstrained problem

without adding extra unknowns to the problem. Also, it enables exact fulfillment of the contact constraints while using a finite value of the penalty parameter to facilitate the iteration procedure. Thus, for the Augmented Lagrangian method, the contact integral for a frictionless approach (Ec. (3.7)) takes the following form:

$$\delta \mathcal{W}_c := \int_{\Gamma_c^{(1)}} \langle \lambda + \epsilon_N \, g \rangle \delta g \, d\Gamma \tag{3.23}$$

The most common technique used in mechanics for the solution of the Augmented Lagrangian problems is the method of multipliers, or Uzawa's method. This method relies on the following algorithm for a multiplier iteration (k) (see Fig. 3.11):

$$\lambda^{(k+1)} = \langle \lambda^{(k)} + \epsilon_N \, g^{(k)} \rangle. \tag{3.24}$$

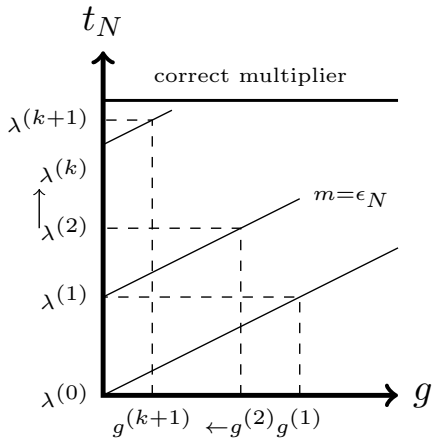

Figure 3.11: Augmented Lagrangian update process.

Replacing of Eq. (3.24) in Eq. (3.23) gives the following iterative procedure for the contact integral. This translates in an iterative procedure for the main unknown of the problem, i.e. the displacements:

$$\delta \mathcal{W}_c^{(k)} := \int_{\Gamma_c^{(1)}} \langle \lambda^{(k)} + \epsilon_N \, g^{(k)} \rangle \delta g \, d\Gamma. \tag{3.25}$$

Iterations on (k) continue until changes in the multipliers become small, or alternatively, until the constraints are satisfied within a tolerance range.

Expansion of the terms of Eq. (3.25) gives:

$$\delta \mathcal{W}_c^{(k)} := \int_{\Gamma_c^{(1)}} \lambda^{(k)} \, \delta g \, d\Gamma + \int_{\Gamma_c^{(1)}} \epsilon_N \langle g^{(k)} \rangle \delta g \, d\Gamma \tag{3.26}$$

It is worth mentioning that only the last term of Eq. (3.25) survives at the beginning of the iterative procedure (initial estimate $\lambda^{(0)} = 0$). Comparing with Eq. (3.13), it can be observed that this term represents the penalty method contribution to the Augmented Lagrangian method. As explained in Sec. 3.2.2.1, this term means, from a physical viewpoint, the introduction of a new

structural element which connects the contacting nodes, as depicted in Fig. 3.9. This physical meaning remains throughout the complete iterative procedure.

3.3 Domain decomposition and constraint enforcement methods

Let's suppose now that we want to solve the example of Fig. 3.8 in a memory distribuited system using a parallel finite element computational code (see Sec. 3.1). For the sake of simplicity, let's consider that we assign each element of the mesh to a different computational node. Firstly, let's assume a non-contact situation. As explained in Sec. 3.1.3, the normal procedure for any parallel finite element computational code is to perform the mesh partitioning as a preprocess stage, before the solution procedure. For the 1D example that we are considering, the result of the mesh partitioning procedure is schematically represented in Fig. 3.12.

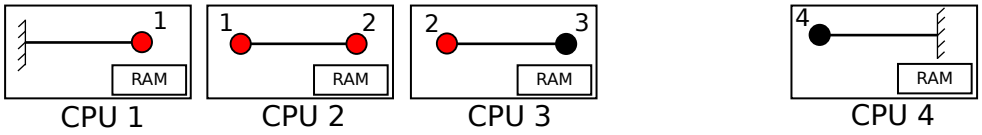

Figure 3.12: Domain decomposition of the 1D contact example - Non-contact situation.

Once the mesh partitioning finishes, the code enters into a numerical resolution stage. At this stage, the linear system of equations resultant from the chosen discretization method is solved using a domain decomposition approach (see Sec. 3.1.2).

Suppose now that during the solution procedure and due to an external input, the condition given by Eq. (3.4) is fullfiled. We must now solve a constrained problem by considering the contact boundary conditions, to properly model the contact between both beams. Suppose that we decide to use the penalty method to tackle the resolution of the constrained problem, in the way that was explained in Sec. 3.2.2.1. There, we showed that the physical interpretation of the penalty method for contact problems is the introduction of additional structural elements which aid to couple or relate contacting nodes, which originally were uncoupled. When this problem is being solved in a unique computational node, where all the information is gathered in the same memory unit, this situation doesn't present serious challenges. But if we consider the situation depicted in Fig. 3.13, the challenge that arises is how to deal with the new fictitious structural element, which is usually named *contact element*.

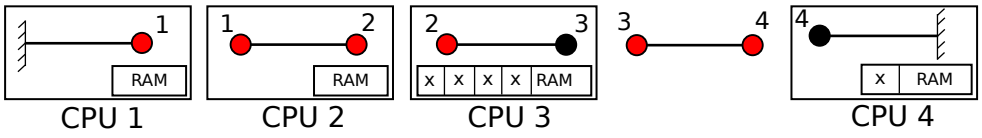

Figure 3.13: Domain decomposition of the 1D contact example - Contact element.

First, as we can not assign the contact element to a new computational node, we must decide to which existing computational node we should assign this element in order to maintain the

workload balance. The answer to this question seems obvious when we are dealing with only one contact element, but it is not straightforward when we handle bigger meshes and a considerable number of contacting nodes.

The second issue is the memory allocation and the sparse storage. As explained in Sec. 3.1.4, in any efficient finite element code the mesh connectivity is used to predict the zeros in the resultant system matrix. This information is used for memory allocation, which is required for the storage of the matrix components in compressed sparse formats. As the memory allocation is done in preprocess, the contact element components which appears in the middle of the simulation can not be stored, as there is no memory reserved for them.

The third, and not less important issue, is related to the subdomain connectiviy. As explained in Sec. 3.1.2, in a domain decomposition approach global matrices are never stored explicitly. On the contrary, the solution is obtained by means of the summation of the contributions of the interface nodes, which are shared between subdomains. For that reason, when the mesh is partitioned, the mesh splitting algorithm constructs a list which contains the interface nodes of each subdomain and also indicates to which of the rest of subdomains those nodes are shared with. The creation of contact elements adds new interface nodes to the subdomain to which they belong, thus altering the lists previously created by the mesh partitioner.

The drawbacks reported in the previous paragraphs were exemplified by using a penalty method example, but they are still valid for Augmented Lagrangian or Lagrange mutlipliers method. To avoid these drawbacks, the solution of contact problems in parallel environments requires to consider any possible contact situation before partitioning. By estimation of the probable contacting area, contact elements must be predicted (and created) before partitioning the mesh. For completeness sake, Fig. 3.14 shows the contribution of the contact element to the structural matrix in a 2D case for the *node-to-segment* (NTS) discretization. In this kind of contact discretization, which is the most widely used, nodes from one contacting surface exchange contact information (i.e. contact tractions) with boundary segments of the other contacting surface.

3.3.1 Sliding

In 1D contact problems, as the one described in previous sections (Fig. 3.8), is straightforward to identify the contact area or the contacting nodes before the contact interaction. But for 2D and 3D problems the situation is different. Consider, for example, the case illustrated in Fig. 3.15. Here we show a block-indenter configuration, where the rounded indenter impacts the square block. Without knowing extra information, in this problem is impossible to know *a priori* the location of the contact interface.

Yet, if one considers the kinematics of the problem, it is possible to estimate a possible area of contact. Once this area is predicted, the contact elements can be constructed (see Fig. 3.16). Just after this stage the mesh can be partitioned. Following this procedure, one avoids the drawbacks detailed in previous section (Sec. 3.3) for parallel contact problems.

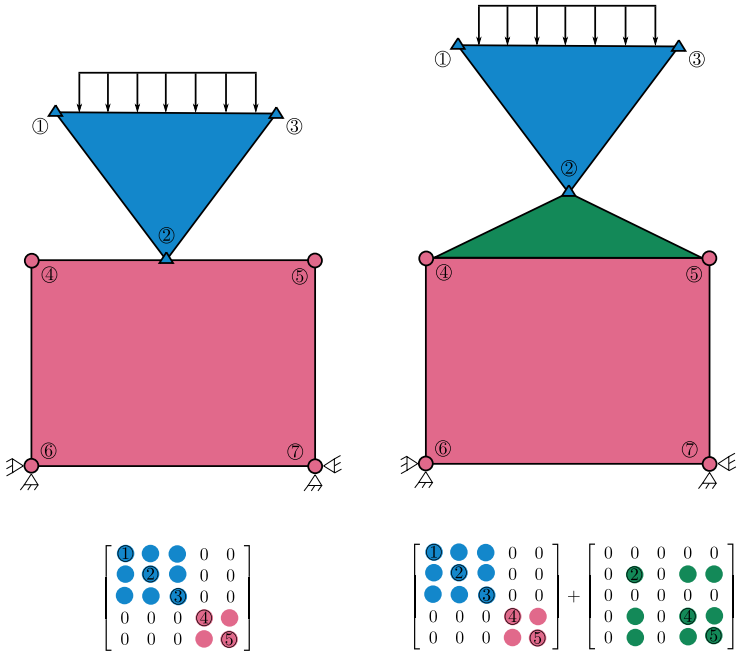

Figure 3.14: Contact element for a 2D case - NTS discretization.

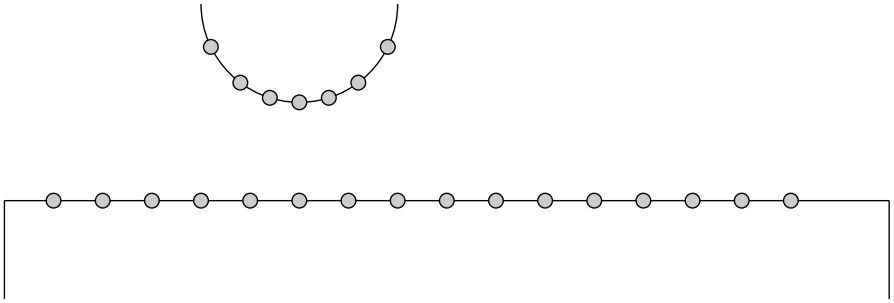

Figure 3.15: Block-indenter 2D example.

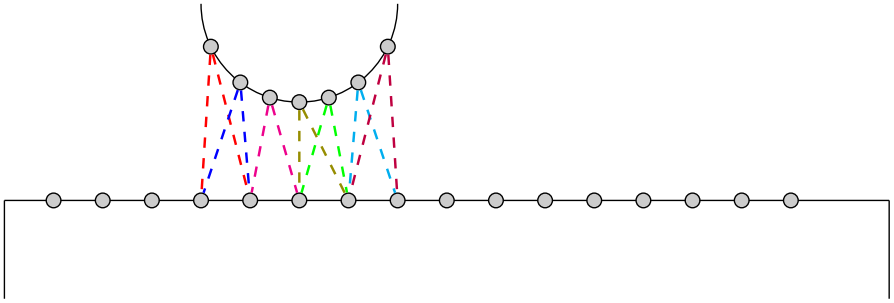

Figure 3.16: Block-indenter 2D example - contact prediction.

Nevertheless, the procedure described in previous paragraph does not consider the case of large sliding, i.e. the relative motion of contacting surfaces while they are in contact. Sliding is present in the majority of realistic 2D or 3D problems which are affected by finite deformations. If sliding occurs, one must update the contact elements *on the fly*, or in other words, during the

solution procedure. This update is required because the coupling nodes for the exchange of contact tractions are different than they were previously to the sliding, as will be further explained. In a parallel approach this situation presents a major drawback, which will be described next.

Consider the 2D example shown in Fig. 3.17. Contacting surfaces are identified with *slave* and *master* names, while their nodes are clearly identified in the figure. Fig. 3.17 shows the contact prediction, the contact elements and the mesh partitioning, where we have considered only two processors. In the figure one can observe which are the interior nodes that belong to processor 1, those interior nodes which belong to processor 2 and the interface nodes. A dashed line separates graphically both subdomains.

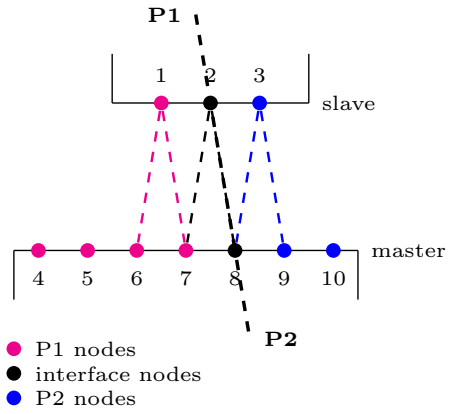

Figure 3.17: Contact elements before sliding.

Suppose now that a sliding between *slave* and *master* occurs. The sliding changes the location of the nodes which must be coupled for the exchange of contact tractions, which translates into a re-definition of the contact elements. This situation is as shown in Fig. 3.18.

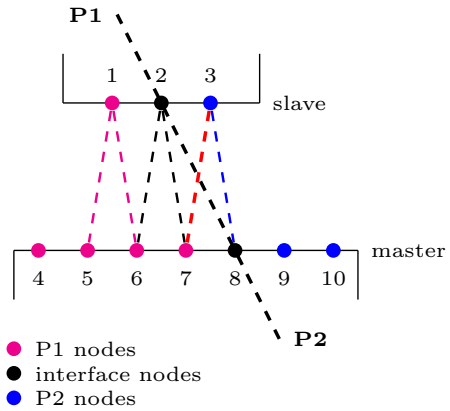

Figure 3.18: Contact elements after sliding.

Because of the sliding, contact elements should now be redefined during the solution process, and after the mesh partitioning. A feasible situation to deal with, is when new contact elements

lie inside the same subdomain than they where before sliding. An example of this situation is the contact element composed of nodes 1-6-7 before the sliding (see Fig. 3.17), which evolves to 1-5-6 after sliding (see Fig. 3.18). Nodes 1, 5, 6 and 7 are interior nodes of subdomain 1. Though, a more complex case can result. It could happen that, after sliding, new contact elements need to be defined as a connection between interior nodes of different subdomains. This is the case of the contact element composed of nodes 3-7-8 which appears after sliding, as can be observed in Fig. 3.18.

If due to the sliding any new contact element becomes defined by the connection of interior nodes, there is no other option than to perform a new mesh partitioning. A new mesh partitioning will split the mesh considering the new connectivities of the contact elements, avoiding the situation previously described. With a new partitioning the connected nodes would transform in interior nodes of an exclusive subdomain or, at least, in interface nodes. It is important to remark that the repartitioning needs to be done every time the configuration of the contact elements changes. This could occur even at each time step, which translates into a computationally high demanding and very expensive task.

A possible workaround for this drawback would be to associate the contacting interfaces to an specific group of processors. This would avoid repartitioning the mesh every time the contact elements configuration changes. Despite being an acceptable alternative, this strategy conditions the mesh partitioning algorithm, thus not ensuring the best workload balance and the minimal communication between computational nodes.

3.4 Standard methods and the parallel world

In this chapter we have analyzed the application of standard methods based on nodes connectivities for the resolution of contact problems in a parallel environment. The methods and discretizations reviewed here are well known and widely used in the resolution of contact problems in engineering and science. Yet, they are implemented in a serialized way in the majority of commercial and non-commercial codes, i.e.: Abaqus [1], ANSYS [5], ADINA [3], Code_Aster [31], FEAP [44], among others. During the past years, researchers have dedicated an extensive amount of work to their study. Because of that, their behaviour is well known and most of the scientific literature in contact mechanics is dedicated to them. The intention of this chapter is to evaluate the direct applicability of such methods to parallel resolution strategies based on domain decomposition approaches. This is motivated by the fact that parallel resolution strategies are a must in large scale problems. From the topics covered here, some conclusions can be obtained.

In this chapter we showed that penalty and Augmented Lagrangian method add explicit connections between contacting nodes, which present a serious drawback for parallel implementation. Also, Lagrange multipliers method (and the mortar approach) increases the number of unknowns of the system, as their number depend on the contacting nodes. Even more, as the contacting area may change with time, the number of unknowns may vary along the simulation. This situation is incompatible for problems were the mesh partitioning is done as a preprocessing task, thus requiring to perform dynamic partitioning during the simulation. Despite that some

drawbacks which arise when the mesh partitioning is done in preprocessing time can be solved by doing a contact prediction, the necessity of a dynamic partitioning becomes crucial when sliding between contacting surfaces occurs. Nevertheless, some workarounds may be proposed (see, for instance, [88]), but they are based on restricting the partitioning algorithm, which is not an efficient solution. This lead us to conclude that standard contact methods present serious disadvantages when they are extrapolated to parallel approaches based on domain decomposition methods, as in a general case dynamic repartitioning can not be avoided.

Some previous works exist on the field of large scale, parallel methods for the solution of large deformation contact problems [57, 95, 49], but they are limited to some particular applications such as unilateral contact or shell structures. To the author best knowledge, no previous work on general, bilateral parallel contact methods for 3D large deformation contact problems exist on scientific literature.

3.5 Design basis of the proposed algorithm

Based on the analysis made on the previous section, the main motivation of this thesis is to propose an alternative method for the numerical modelling of contact problems suitable for High Performance Computing (HPC). This method must fulfill some general requirements, which are adopted as the design basis for its development:

- it must be a general algorithm for the resolution of the two-body contact problem,
- it must not restrict the mesh partitioner,
- it must not require dynamic partitioning,
- it must not increase the number of unknowns of the system,
- it must not affect the system matrix, and
- it must be suitable for large scale problems.

The next two chapters (Chapters 4 and 5) are dedicated to the description of the proposed algorithm. In Chapter 4 we propose a parallel method for unilateral contact problems, which also serves as an intermediate step for the introduction of some concepts and ideas which are the basis of the general two-body contact algorithm described in Chapter 5. Our objective is to provide a comprehensive description by putting special emphasis not only on the detailed explanation of the algorithm but also on its parallel computational implementation.

Chapter 4

A Parallel Method for Unilateral Contact Simulation

In this chapter we present a new methodology for solving parallel unilateral frictional contact problems in distributed-memory HPC computers. Additionally, we describe its computational implementation, which is one of its distinctive characteristics. The presented methodology is based on the partial Dirichlet-Neumann method, first introduced in [141, 142]. The proposed method allows to solve the contact interaction as a coupled problem, in a staggered way. Furthermore, it can be interpreted as a black-box scheme that can be used with any parallel finite element code. In this method, the number of unknowns remains constant. Also, the mesh partitioning is only done at the beginning of the simulation, as a preprocess task, without restricting the partitioning algorithm. For those reasons, is a suitable methodology for the parallelization of the solution of unilateral contact problems using a domain decomposition approach. This chapter is also an intermediate step that serves to introduce some concepts and ideas which will be needed for the following chapter, where we present a general parallel two-body contact formulation. An important part of the general two-body algorithm is based on the ideas presented here.

In this method, each body is treated independently and the contact is solved throughout the exchange of boundary conditions at the contact interface. The contact detection is based on an Eulerian-Lagrangian system analogy. The geometry of the rigid body is used as reference (base mesh) for the detection of contact. As contact is a boundary phenomena, only the boundary nodes of the deformable body mesh are available for localization. These nodes take the role of particles that moves in the surroundings of the base mesh. The localization of at least one node of the deformable body mesh inside the base mesh is equivalent to detecting contact, which triggers the data exchange at the contact zone for the solution of the contact problem.

4.1 Introduction

In the engineering practice, a wide range of contact problems can be approximated by a unilateral contact. i.e. contact between a rigid surface and a deformable solid. In a contact scenario, forces

are transmitted through the common area of contact. These forces have commonly two components: a normal component which prevents interpenetration of the bodies, and the tangential component, created by friction. The normal contact forces are prescribed by the so-called *Hertz-Signorini-Moreau* conditions [137], which are geometrical boundary conditions which include inequalities related to frictionless contact and account for the non-interpenetration condition via variational form. With regard to the friction, the simplest and most popular frictional condition is given by the *Coulombian law* (see Sec. 2.2.1.1), which is in good harmony with practical experience.

A variational inequality characterizes the solution of unilateral contact problem. As mentioned in Sec. 3.2, variational inequalities can be reformulated into a variational equality problem with special contact terms under the assumption of knowing *a priori* the contact interface. The form of the contact terms depends on the method chosen to enforce the contact constraints. For constraint enforcement, a wide range of techniques exists in the optimization literature [92, 52]. Among them, the most used methods for constraint enforcement in the numerical treatment of contact problems are: the classical Lagrange multiplier method, the penalty method and the Augmented Lagrangian method.

An alternative methodology for the variational approach in the solution of unilateral contact problems is proposed in [141, 142]. This methodology is based on the equivalence of the geometrical constraints due to normal and frictional contact and a combination of partial Dirichlet and Neumann boundary conditions, prescribed in a specific way on the contact boundary. This approach simplifies the algorithm and provides an efficient framework for contact treatment on parallel computers.

On the other hand, in order to implement a parallel finite element calculation, the mesh is partitioned among the computational nodes to minimize interprocessor communications. Contact can occur between surfaces which are owned by different processors. Hence, in a parallel contact simulation, global searches across all computational nodes are required. This feature makes the contact detection one of the most important and complex parts in computational contact mechanics, and also, one of the major computational costs of contact algorithms.

4.2 Formulation of unilateral contact problems

4.2.1 Unilateral normal contact

Let a rigid plane be defined in a local coordinate system by $n = 0$, being n the normal axis of the plane, with unit external normal $\underline{\boldsymbol{\nu}} = \underline{\boldsymbol{e}}_n$. Being the plane in this position, the motion of any body in space is then restricted to $n \geq 0$ (see Fig. 4.1). We can represent this restriction by the following displacement contact constraint:

$$g(\underline{\boldsymbol{x}}) = \underline{\boldsymbol{x}} \cdot \underline{\boldsymbol{\nu}} \geq 0, \tag{4.1}$$

where $g(\underline{\boldsymbol{x}})$ is the gap between the current point $\underline{\boldsymbol{x}}$ of the body and the rigid plane. In other words, Eq. (4.1) states that any point of the body at any time can not penetrate the rigid plane.

Defining the displacement of any point of the body as $\underline{\boldsymbol{u}} = \underline{\boldsymbol{x}} - \underline{\boldsymbol{X}}$, we can express Eq. (4.1) as:

$$g(\underline{\boldsymbol{u}}) = \underline{\boldsymbol{u}} \cdot \underline{\boldsymbol{\nu}} + g_0 \geq 0, \tag{4.2}$$

where $g_0 = \underline{\boldsymbol{X}} \cdot \underline{\boldsymbol{\nu}}$ is the initial gap. If the body retains its integrity, the non-penetration condition given by Eq. (4.2) is applied only to the surface points $\partial\Omega$, precisely to the *potential contact zone* (Γ_c) in the actual configuration. Γ_c can be splitted into two nonintersecting sets: active contact zone $\bar{\Gamma}_c$ (points which are in contact) and inactive contact zone $\Gamma_c \backslash \bar{\Gamma}_c$ (points which are not in contact). The active contact zone in the actual configuration is defined by:

$$\underline{\boldsymbol{x}} \in \bar{\Gamma}_c \quad \text{if and only if} \quad g(\underline{\boldsymbol{x}}) = \underline{\boldsymbol{x}} \cdot \underline{\boldsymbol{\nu}} = 0, \tag{4.3}$$

while for the reference configuration, the active contact zone can be defined by:

$$\underline{\boldsymbol{X}} \in \bar{\Gamma}_c^0 \quad \text{if and only if} \quad \underline{\boldsymbol{X}} \cdot \underline{\boldsymbol{\nu}} = -\underline{\boldsymbol{u}} \cdot \underline{\boldsymbol{\nu}}. \tag{4.4}$$

From the definitions in Eq. (4.3) and Eq. (4.4) we observe that the active and inactive contact zones are a priori unknowns of the problem. Only in some specific problems, given the potential zone we can predict a priory the active contact zone at each instant of time.

When the contact between the body and the rigid plane is produced, a contact pressure appears in the active contact zone in order to prevent the penetration. This pressure should be non-negative, i.e. equal to zero in inactive and negative in active contact zone:

$$\sigma_n \leq 0 \quad \text{at} \quad \Gamma_c. \tag{4.5}$$

Combining the non-penetration condition in the active zone given by Eq. (4.3) and the definition of the contact pressure (Eq. (4.5)) we get the non-penetration-non-adhesion condition:

$$\sigma_n \, g(\underline{\boldsymbol{x}}) = 0 \quad \text{at} \quad \Gamma_c. \tag{4.6}$$

All together, the set of conditions expressed in Eq. (4.1), Eq. (4.5) and Eq. (4.6) form the Hertz-Signorini-Moreau law of unilateral normal contact:

$$g \geq 0, \;\; \sigma_n \leq 0, \;\; \sigma_n \, g = 0. \tag{4.7}$$

4.2.2 Balance of momentum including contact

The nonlinear contact problem can be written as a boundary value problem, given the following equilibrium condition in Ω and boundary conditions on $\partial\Omega$, which includes the Hertz-Signorini-Moreau law for normal contact:

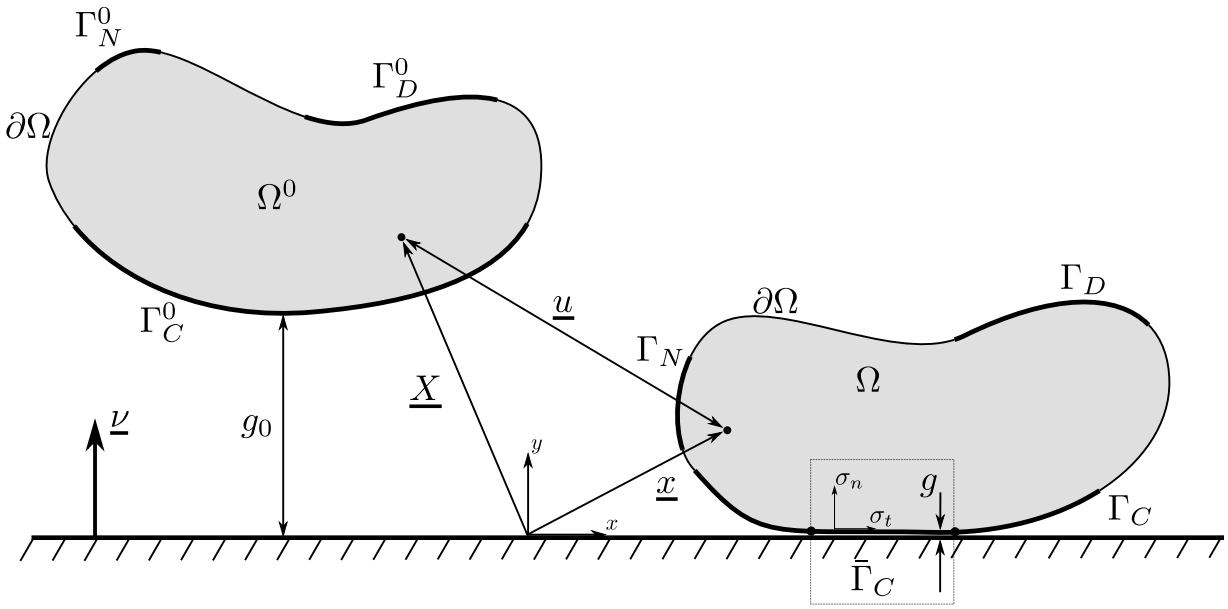

Figure 4.1: Reference (Ω_0) and actual (Ω) configurations of a deformable body in unilateral contact with a rigid plane.

$$
\begin{aligned}
&\nabla \cdot \underline{\underline{\boldsymbol{\sigma}}} + \underline{\boldsymbol{f}}_v = 0 \quad \text{in } \Omega \\
&\underline{\underline{\boldsymbol{\sigma}}} \cdot \underline{\boldsymbol{n}} = \underline{\boldsymbol{\sigma}}_0 \quad \text{on } \Gamma_N \\
&\underline{\boldsymbol{u}} = \underline{\boldsymbol{u}}_0 \quad \text{on } \Gamma_D \\
&g \geq 0,\ \sigma_n \leq 0,\ \sigma_n\, g = 0,\ \underline{\boldsymbol{\sigma}}_t = 0 \quad \text{on } \Gamma_C
\end{aligned}
\tag{4.8}
$$

being $\underline{\underline{\boldsymbol{\sigma}}}$ the Cauchy stress tensor, $\underline{\boldsymbol{f}}_v$ a vector of volumetric forces, $\underline{\boldsymbol{\sigma}}_0$ a set of prescribed tractions and $\underline{\boldsymbol{u}}_0$ a set of prescribed displacements. Over Γ_C we have imposed the contact boundary conditions: g represents the gap between contacting bodies, σ_n is the normal contact pressure and $\underline{\boldsymbol{\sigma}}_t$ is the tangential stress. For simplicity, on the balance of momentum given by Eq. (4.8) we have considered a frictionless case ($\underline{\boldsymbol{\sigma}}_t = 0$).

4.2.3 Interpretation of contact Hertz-Signorini-Moreau conditions

A contact problem can be directly interpreted as finding the active contact zone and the contact pressure which has to be applied in order to fulfill contact constraints. However, the problem can be also interpreted from another point of view: instead of prescribing the pressure at the active contact zone, we can impose a displacement according to the contact constraints. In what follows, and without loss of generality, we assume a frictionless case.

The set of normal contact conditions expressed by Eq. (4.7) can be separated into two parts for active $\bar{\Gamma}_c$ and inactive $\Gamma_c \backslash \bar{\Gamma}_c$ contact zones:

$$\begin{cases} g = 0,\ \sigma_n < 0,\ \underline{\boldsymbol{\sigma}}_t = 0 \ \text{ at } \ \bar{\Gamma}_c, & \text{(4.9a)} \\ g > 0,\ \sigma_n = 0,\ \underline{\boldsymbol{\sigma}}_t = 0 \ \text{ at } \ \Gamma_c \backslash \bar{\Gamma}_c. & \text{(4.9b)} \end{cases}$$

According to Eq. (4.2) and the definition of the active contact zone given by Eq. (4.4), the first term of Eq. (4.9a) can be written as follows:

$$g = 0 \iff \underline{\boldsymbol{\nu}} \cdot \underline{\boldsymbol{u}} = -g^0 \iff u_n = -g^0. \tag{4.10}$$

Eq. (4.10) shows that the no-penetration condition represented by Eq. (4.2) can be interpreted as a Dirichlet boundary condition. In contrast, the condition represented by Eq. (4.9b) can be interpreted as a singular Neumann boundary condition $\underline{\boldsymbol{\sigma}}_t = 0$ (free boundary) for the inactive zone. Considering the previous interpretations, we can rewrite the Hertz-Signorini-Moreau conditions of Eq. (4.9a) and Eq. (4.9b) as:

$$\begin{cases} u_n = -g^0,\ \underline{\boldsymbol{\sigma}}_t = 0 \ \text{ for } \ \underline{\boldsymbol{x}} \in \bar{\Gamma}_c, & \text{(4.11a)} \\ \underline{\boldsymbol{\sigma}} = 0 \ \text{ for } \ \underline{\boldsymbol{x}} \in \Gamma_c \backslash \bar{\Gamma}_c. & \text{(4.11b)} \end{cases}$$

Even more, we can rewrite Eq. (4.11a) using the condition given by Eq. (4.5) in the definition for the active zone:

$$u_n = -g^0,\ \underline{\boldsymbol{\sigma}}_t = 0 \ \text{ for } \ \{\underline{\boldsymbol{x}} \mid \underline{\boldsymbol{x}} \in \Gamma_c \ \text{ and } \ \sigma_n(\boldsymbol{x}) < 0\}. \tag{4.12}$$

In Eq. (4.11a) (and Eq. (4.12), which is equivalent) we have replaced the contact conditions on the active contact zone $\bar{\Gamma}_c$ by a partial Dirichlet boundary condition ($u_n = -g^0$) and a partial Neumann boundary condition ($\underline{\boldsymbol{\sigma}}_t = 0$). The non-linearity of the problem emerge because the active contact zone is, generally speaking, unknown a priori, and its specific location is part of the solution of the problem. On the contrary, in Eq. (4.11b) we have replaced the contact conditions in the inactive contact zone by prescribing a full singular Neumann boundary condition ($\underline{\boldsymbol{\sigma}} = 0$).

Writing Hertz-Signorini-Moreau law as expressed in Eq. (4.7) in the form of Eqs. (4.11a) and (4.11b) gives a better understanding of the normal contact boundary conditions for unilateral contact problems. From a numerical or computational mechanics approach, it is easier to prescribe in a given domain a given displacement and check for the sign of the contact pressure to determine the active contact zone, than to prescribe an unknown contact pressure in an unknown active contact zone, which is determined by a zero value of the normal gap.

4.2.4 Interpretation of frictional condition

This thesis is limited to the classical Coulomb's friction law for frictional problems, already introduced in Sec. 2.2.1.1. This friction law states that the value of the tangential stress depends only on the normal contact pressure $\underline{\boldsymbol{\sigma}}_t = \underline{\boldsymbol{\sigma}}_t(\sigma_n)$ by the following relation:

$$|\underline{\boldsymbol{\sigma}}_t| \leq \mu\, |\sigma_n|, \tag{4.13}$$

where μ is a coefficient of friction. So, in the case of frictional contact, the stress vector at the interface contains both normal and tangential components:

$$\underline{\boldsymbol{\sigma}} = \sigma_n \, \underline{\boldsymbol{n}} + \underline{\boldsymbol{\sigma}}_t(\sigma_n). \tag{4.14}$$

From Eq. (2.20) we can identify two different possible states which are allowed by the Coulomb's friction law: stick, that occurs when the tangential stress vector is smaller than the critical frictional stress:

$$\mu|\sigma_n| - |\underline{\boldsymbol{\sigma}}_t| > 0, \tag{4.15}$$

and slip, that occurs when the tangential force $\underline{\boldsymbol{\sigma}}_t$ reaches the threshold $\mu|\sigma_n|$ imposed by the Coulombian law:

$$\mu|\sigma_n| - |\underline{\boldsymbol{\sigma}}_t| = 0. \tag{4.16}$$

Similarly to the previous section, we can interpret frictional constraints. Thus, to take the frictional resistance into account, we must analyze the stress state. In the case of stick, the partial Dirichlet boundary conditions for normal contact must be replaced with full Dirichlet boundary conditions to reproduce the stick state. In the case of slip, the partial Dirichlet conditions for normal contact must be applied in combination with partial Neumann boundary conditions in order to reproduce the tangential frictional stress.

The interpretation of geometrical constraints due to frictional contact as partial Dirichlet-Neumann boundary conditions allows us to introduce a technique for the numerical resolution of unilateral contact problems using the Finite Element Method. This technique was first introduced in [141], and is called the *partial Dirichlet-Neumann (PDN) method*. Taking advantage of the reformulation of the geometrical contact constraints, this technique results very advantageous for the resolution of this kind of problems, because there is no need to evaluate residual vectors and tangent matrices. Coupled with a Lagrange multiplier method for the exchange of boundary conditions, this method results equivalent to a *mortar method*. But contrary to the mortar method, which increases dynamically the number of unknowns of the algebraic system, the PDN method maintains constant the number of unknowns.

4.3 Method of partial Dirichlet-Neumann boundary conditions

The main idea of this method is to replace the geometrical constraints due to normal and frictional contact by partial Dirichlet-Neumann boundary conditions in the case of unilateral contact with an arbitrary rigid surface. In particular, the geometrical constraints due to normal contact are imposed by means of Multi-Point Constraints (MPC) while friction is imposed in the form of a tangential force which is applied in the opposite direction of sliding of the node. From a geometrical point of view, MPC can be interpreted as Dirichlet boundary conditions which allow sliding of the contacting node only in the tangential plane. For the enforcement of MPC a chosen degree of freedom of each contacting node –*slave* dof u_s– is written as a linear combination of

the other dofs of the same node –*master* dofs u_m^i, $i = 1, \ldots, M$–:

$$u_s = \alpha_i u_m^i + \beta, \tag{4.17}$$

where α_i and β are scalar coefficients, and M is the total number of master dofs. The slave dof can be chosen arbitrarily for each contacting node but it is required that $\alpha_i < \infty$.

4.3.1 Frictionless case

Let $\underline{\boldsymbol{x}}^i$ be the coordinates of a contacting node over Γ_c in the i-th iteration. Then, the incremental displacement vector is given by:

$$\underline{\boldsymbol{u}}^i = \underline{\boldsymbol{x}}^i - \underline{\boldsymbol{x}}^{i-1}. \tag{4.18}$$

The incremental displacement of each degree of freedom is given by splitting the vector $\underline{\boldsymbol{u}}$ into the reference frame basis:

$$u_j^i = \underline{\boldsymbol{u}}^i \cdot \underline{\boldsymbol{e}}_j, \tag{4.19}$$

where $\underline{\boldsymbol{e}}_j$ is a set of basis vectors.

Otherwise, any rigid surface can be described by the parametric representation:

$$\underline{\mathbf{r}}(u, v) = x(u, v)\, \underline{\boldsymbol{e}}_1 + y(u, v)\, \underline{\boldsymbol{e}}_2 + z(u, v)\, \underline{\boldsymbol{e}}_3. \tag{4.20}$$

Without any loss of generality, let us suppose that locally exists a function f such that:

$$z = f(x, y), \tag{4.21}$$

where x, y and z are coordinates of the surface point in the chosen coordinate system:

$$x = x(u, v)\, \underline{\boldsymbol{e}}_1, \quad y = y(u, v)\, \underline{\boldsymbol{e}}_2, \quad z = z(u, v)\, \underline{\boldsymbol{e}}_3. \tag{4.22}$$

Then, using the definition given by Eq. (4.18), the geometrical constraint given by Eq. (4.1) can be written in the following way:

$$x_3^i \geq f(x_1^i, x_2^i) \iff u_3^i \geq f(x_1^{i-1} + u_1^i, x_2^{i-1} + u_2^i) - x_3^{i-1}. \tag{4.23}$$

We can compute the tangential plane at a given point $\{x^*, y^*\}$ on Γ_c by the following expression:

$$P : z = \left.\frac{\partial f}{\partial x}\right|_{\{x^*, y^*\}} (x - x^*) + \left.\frac{\partial f}{\partial y}\right|_{\{x^*, y^*\}} (y - y^*) + f(x^*, y^*). \tag{4.24}$$

Then, the multi-point constraint to be imposed to the point $\{x^*, y^*\}$ is given by:

$$u_3 = a u_1 + b u_2 + c - x_3^{i-1}, \tag{4.25}$$

where

$$a = \frac{\partial f}{\partial x}\Big|_{\{x^*,y^*\}}, \quad b = \frac{\partial f}{\partial y}\Big|_{\{x^*,y^*\}}, \quad c = f(x^*, y^*). \tag{4.26}$$

Fig. 4.2 shows an example of MPC boundary conditions for a 2D frictionless unilateral contact. The nodes of the deformable body which have penetrated the rigid body are identified and projected following an arbitrary direction to the rigid body surface. Then, a tangent line to the contact surface of the rigid body, which contains the projection point, is computed. This allows to determine the relation for the MPC boundary condition.

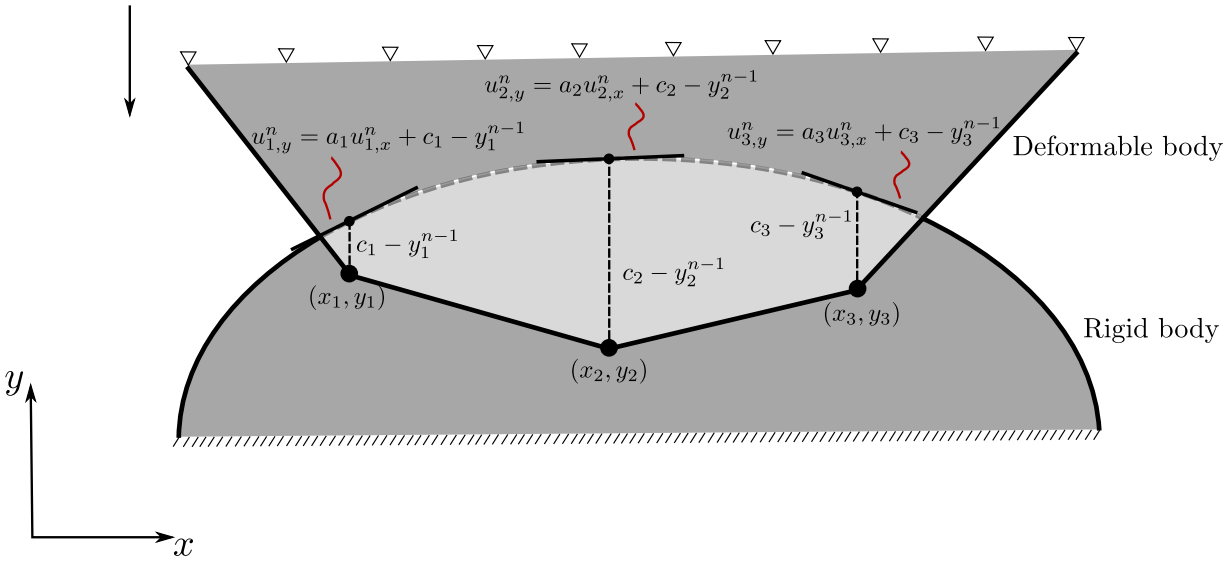

Figure 4.2: MPC BOUNDARY CONDITIONS FOR UNILATERAL FRICTIONLESS CONTACT.

In addition, is necessary to check that there are no artificial traction forces in the created contact interface. The reaction force $\underline{\mathbf{R}}$ appearing at the contacting nodes, where the MPC have been imposed, has to be checked: the normal contact force should point in the same direction as the normal to the rigid surface:

$$\underline{\mathbf{R}} \cdot \underline{\mathbf{n}} \geq 0. \tag{4.27}$$

Otherwise, the MPC imposed at the contacting node must be removed. Fig. 4.3 shows an example of an iterative process for the MPC update process. Once penetrated nodes are detected, MPC boundary conditions are imposed to such nodes. When equilibrium is reached, a search for non-physical adhesion nodes is performed. If adhesion nodes are detected, MPC boundary conditions are released for that nodes and the system is solved again. This procedure is repeated until no adhesion node is found.

4.3.2 Frictional case

The idea for this case consists of, first, replacing the MPC by full Dirichlet boundary conditions in order to fix the displacement of the node also in the tangential direction. That is, if a node $\underline{\boldsymbol{x}}$ penetrates the rigid surface, it should be returned to the penetration point $\underline{\boldsymbol{x}}^*$ by the enforcement

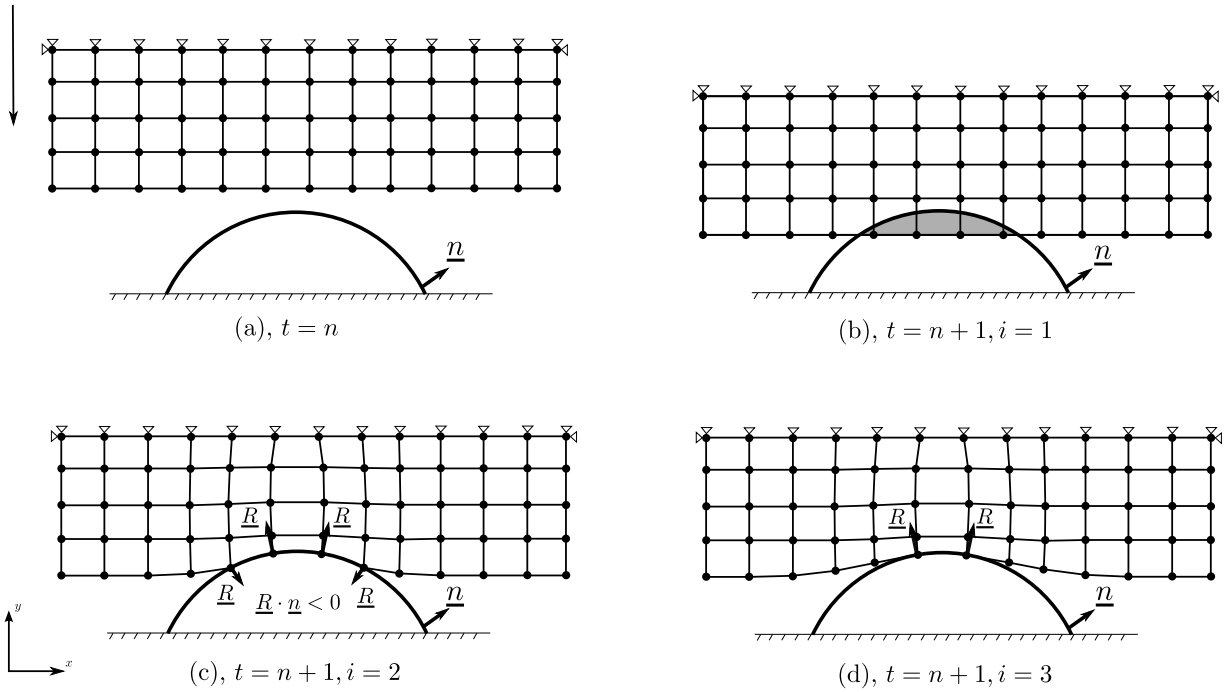

Figure 4.3: Iterative process for the MPC update process. (a) Initial configuration. (b) First iteration: four MPC boundary conditions are imposed at each of the four penetrated nodes. (c) Second iteration: after equilibrium is reached, two nodes are in adhesion to the surface of the rigid body. (d) In the third iteration, MPC boundary conditions are released for the adhesion nodes and equilibrium is recomputed.

of a full Dirichlet condition of the form:

$$\underline{\boldsymbol{u}} = \underline{\boldsymbol{x}}^* - \underline{\boldsymbol{x}}. \tag{4.28}$$

Afterwards, the reaction $\underline{\mathbf{R}}$ that appears at the node should be splitted into normal $\underline{\mathbf{R}}_n$ and tangential $\underline{\mathbf{R}}_t$ components, and the non-adhesion condition should be checked as well as the stick-slip condition:

$$\begin{cases} ||\underline{\mathbf{R}}_t|| < \mu ||\underline{\mathbf{R}}_n||, \text{ stick} \\ ||\underline{\mathbf{R}}_t|| \geq \mu ||\underline{\mathbf{R}}_n||, \text{ slip.} \end{cases} \tag{4.29}$$

In the case of slip, the full Dirichlet boundary condition has to be replaced by an MPC boundary condition to allow displacements on the tangent direction. In addition, an external force $\underline{\mathbf{F}}^e$ should be applied to the sliding node along the tangential direction, in the opposite direction to the tangential reaction $\underline{\mathbf{R}}_t$. How this force is applied to the sliding node together with the MPC is shown in Fig. 4.4. The magnitude of the external force $\underline{\mathbf{F}}^e$ is given by the Coulombian friction law, and is computed according to:

$$\underline{\mathbf{F}}^e = -\mu \, ||\underline{\mathbf{R}}_n|| \frac{\underline{\mathbf{R}}_t}{||\underline{\mathbf{R}}_t||}. \tag{4.30}$$

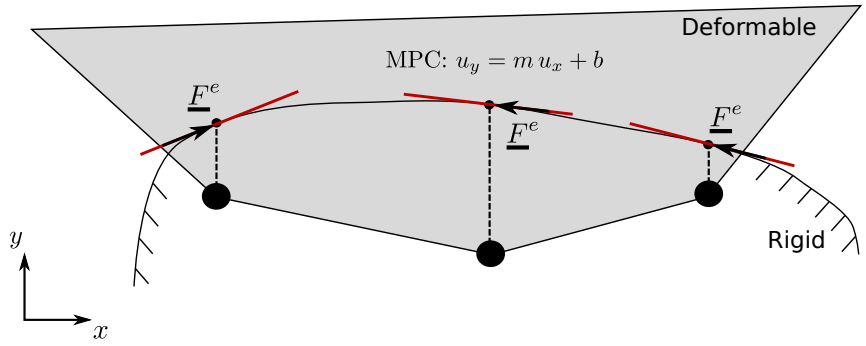

Figure 4.4: Representation of the external force for the frictional case.

4.4 Computational implementation

Based on the PDN method, we propose to solve the unilateral contact problem from a coupled point of view. In this approach, each body is treated separately, using one instance of the computational code for each body. The contact interaction is reproduced by means of the transference of Dirichlet boundary conditions at the contact interface. It is worth remarking that in the case of unilateral contact there is no need to solve the fully discretized system of equations for the rigid body; only the displacement of its boundary elements must be computed by the code instance devoted to this body. Nevertheless, its whole mesh is needed for contact detection purposes, as will be explained in the following section. In this chapter, however, we will consider a more general but equivalent case where the rigid body is assumed to be a deformable body which only experiences rigid body translations. Despite not being the most efficient way of solving a rigid body problem (since we are solving the fully discretized system of equations for the rigid body only to obtain rigid body motions instead of solving the Euler's equations for the rigid body dynamics) this idea allows us to present unilateral contact as the starting point of the bilateral formulation.

The usage of a parallel computational code allows to split each contacting body into several subdomains. In the methodology proposed in this thesis, each body is solved independently in one code instance. Thus, they can be treated as standalone problems with extra boundary conditions due to contact. As a consequence, the mesh is partitioned independently in both instances at preprocessing time, thus allowing to not restrict the mesh partitioner. The unilateral contact condition is enforced through the transference of information from the rigid to the deformable body. This algorithm can be treated as a black-box method, easily adaptable to any finite element computational code. As the solution procedure for the unilateral contact problem is performed through the exchange of boundary conditions, this algorithm can be plugged to any parallel computational code were the link is done by exchanging specific boundary information.

To better describe the computational implementation of this parallel method, we divide the current section into two main subsections, one for each main ingredient of the algorithm: (a) the contact searching and (b), the contact resolution. A contact situation is produced when the gap between the bodies is closed, so the first step of any contact algorithm is the contact detection.

This means to detect when interpenetration between contacting bodies occurs. Is at this point when the contact resolution is triggered, using the information obtained in the detection phase.

In a parallel environment, contacts can occur between surfaces which may be owned by different computational nodes, arbitrary defined by the mesh partitioner. As the surface geometries of the contacting bodies dynamically change in the general case, to find these contacts we require frequent global searches across all the computational nodes. These global searches require unstructured communication among the computational nodes in the parallel computer. These features make efficient parallel contact detection a very relevant topic in the field of contact mechanics [7].

4.4.1 Contact searching and communication: the PLE++ tool

For the localization of penetrated nodes and communication between different subdomains we use PLE++, which is an adaptation of the Parallel Location and Exchange (PLE) library [47], originally developed by Électricité de France (EDF) to couple the CFD code Code_Saturne and the heat transfer code Syrthes. PLE++ is a parallel 2D and 3D locator and communication tool, used here to detect interpenetration and to communicate and transfer information between subdomains. PLE++ is a C++ environmental library, with the capability of parallel localization of nodes in overlapping domains and communication between parallel applications in C, C++, Fortran or Python. In Fig. 4.5 we show an schematic representation of PLE++ localization functionality for a 2D case. PLE++ tool allows to detect those nodes of Ω_2 which have penetrated into Ω_1. As PLE++ is a parallel tool, it is possible to perform node localization even when the meshes are splitted into several subdomains. When this is the case, the localization is performed at the subdomain level. In the example shown in Fig. 4.5, each body represented by domains Ω_1 and Ω_2 is divided into two subdomains $\mathcal{S}1$ and $\mathcal{S}2$. PLE++ will identify those nodes of Ω_2 which have penetrated subdomain $\mathcal{S}1$ of Ω_1 (red) and those nodes which have penetrated subdomain $\mathcal{S}2$ of Ω_1 (blue). Despite it is not shown in the figure, PLE++ will also perform the inverse operation, identifying the nodes of Ω_1 which have penetrated into subdomain $\mathcal{S}1$ of Ω_2 and into subdomain $\mathcal{S}2$ of Ω_2. PLE++ also allows to communicate and transfer information between the subdomains involved in the localization process.

In the next section we will describe in more detail the strategy that PLE++ follows for localization and data exchange.

4.4.1.1 Parallel location and exchange algorithm

We will start setting the nomenclature that will be used for the description of the parallel location algorithm of PLE++. Generally speaking, any physical domain can be divided into independent *partitions*, each of them being characterized by particular type of *physics* i.e. fluid mechanics, solid mechanics, heat transfer, etc. The physics inside of each partition can be solved by any numerical technique such as finite elements, using different sets of *processors*. When using finite elements or any other numerical technique, the physical domain must be discretized. The domain discretization is the *mesh*, which is composed of *nodes* connected between them. Those nodal

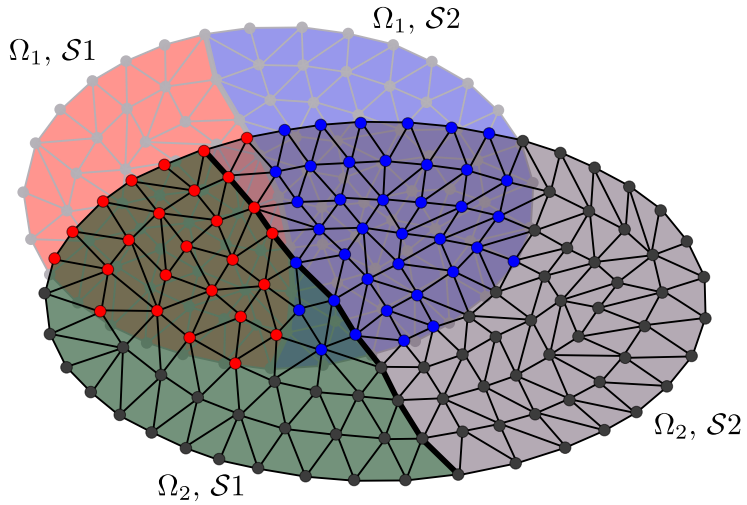

Figure 4.5: Schematic representation of PLE++ localization functionality. The PLE++ tool is used to localize those nodes of Ω_2 which have penetrated into Ω_1. Being a parallel locator, PLE++ can be used even when the meshes are divided into several subdomains.

connectivities define the *elements* of the *mesh*. For the parallel resolution of a numerical problem using domain decomposition, a mesh partitioning is done. Here, the mesh is splitted in small portions called *subdomains*. For the rest of this thesis we will consider only that each *subdomain* is associated to an unique *processor*, and that each *processor* is associated to an MPI task.

Let's now consider the 2D example shown in Fig. 4.6. Here we sketch a discretized physical domain formed by two non-conforming partitions Ω_a and Ω_b. A total of seven processors are used to solve the whole system, distribuited in the following way: three processors are assigned to Ω_a ($\{\Omega_a^1, \Omega_a^2, \Omega_a^3\}$) and four to Ω_b ($\{\Omega_b^1, \Omega_b^2, \Omega_b^3, \Omega_b^4\}$). As we can observe in Fig. 4.6, some boundary nodes of subdomain Ω_a^2 (processor 1) match with the interface boundary of subdomains Ω_b^1 (processor 3) and Ω_b^4 (processor 6). Thus, only processors 1, 3 and 6 are involved in the coupling between partitions Ω_a and Ω_b. Hence, a localization procedure must be followed in order to look for those matching nodes and to stablish a communication between the processors which own those nodes. This is of crucial necessity for solving coupled problems, which are based on the exchange of information between partitions at the boundary level.

When solving a coupled problem in a domain decomposition setting, each partition solver is executed by a different set of processors, i.e. each physics is solved in a specific partition by a defined set of processors. Any of these processors contain only a subdomain of such partition. As the subdomains are independent from each other, in a distribuited memory environment the node coordinates and its connectivities (i.e. the elements) are locally known in each subdomain but not amongst them.

In order to establish the connections needed for the resolution of a given coupled problem, each processor must know exactly which of its nodes (if any) are contained by any other subdomain. On the other hand, if a given processor contains external nodes (i.e. nodes owned by external processors), it must know the number and coordinates of those nodes. Also, that processor must

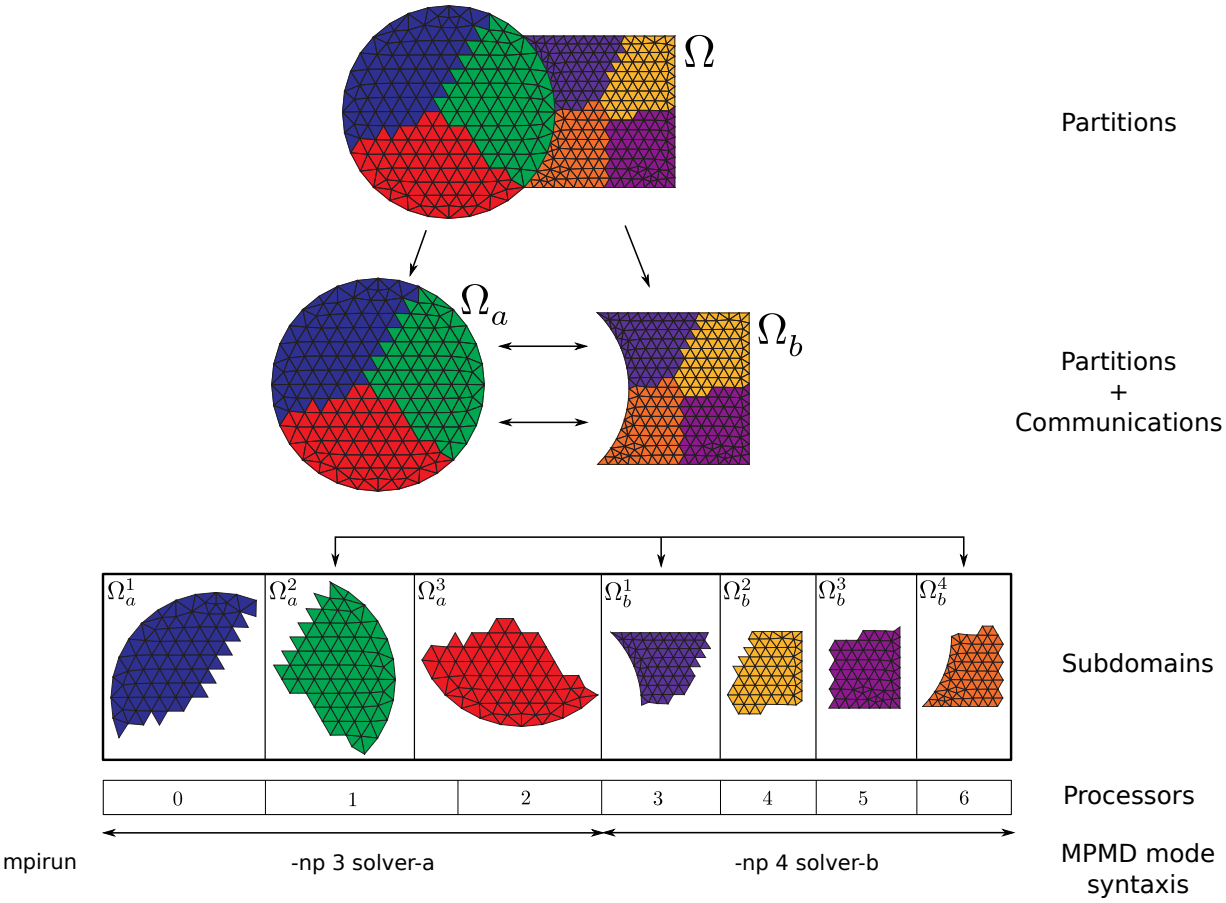

Figure 4.6: Example of a discretized physical domain formed by two non-conforming partitions Ω_a and Ω_b. Each partition is splitted in 3 and 4 subdomains respectively and each subdomain is assigned to one specific processor.

know which of its elements contains each of those external nodes and the processor to which those nodes belong. All this information is provided by PLE++.

The rest of this section is dedicated to describe the algorithm used by PLE++ for the localization of nodes and elements which participates in the coupling. This is, how PLE++ computes all the information described in the previous paragraph. This algorithm makes use of an hierarchical searching based on geometrical properties of the partitions.

4.4.1.1.1 Global searching The global searching process is the main part of the localization algorithm. Its aim is to provide the necessary information required for the coupling. A very important component of all coupled problems is the transference of information between all the subdomains which must be coupled. A crucial issue for the data exchange required in coupled problems is to know the relation between nodes and elements located in subdomains that are owned by different processors.

Without limiting the generality of the algorithm for the case of 3D geometries, let us suppose that each partition Ω_a and Ω_b is divided into subdomains $\mathbf{\Omega}_a^k = \{\Omega_a^1, \Omega_a^2, \Omega_a^3\}$ and $\mathbf{\Omega}_b^l = \{\Omega_b^1, \Omega_b^2, \Omega_b^3, \Omega_b^4\}$, and that each subdomain is assigned to a unique processor p_a and p_b respec-

tively, as shown in Fig. 4.6. We will have then as many processors as subdomains for each partition. Such processors or subdomains can be classified as *local* or *remote*. The *local* processors are those that belong to each subdomain of a given partition, while the *remote* processors belong to the rest of the subdomains of the other partitions.

For every local processor, the global searching algorithm seeks all the remote processors to which information related to the coupling must be exchanged. Specifically, in order to stablish the data tranference, the global searching algorithm computes for each local processor: (a) the number and identification of its own local nodes contained by each remote processor, (b) the number and the coordinates of the remote nodes that the local processor contains, (c) the identification of local elements which contain each of the remote nodes, and (d) the identification of the remote processor/processors to which those remote nodes belong.

This is done by using a Multiple Program Multiple Data (MPMD) model, where all the processors execute the Algorithm 1 *concurrently* (i.e. in parallel).

Without loss of generality, in the description of Algorithm 1 we will define as *local* subdomains those who belong to the partition Ω_a, while *remote* subdomains are those who belong to partition Ω_b.

Algorithm 1 Global search/localization

1: $Q_a^k = GetBox(\mathbf{\Omega}_a^k)$
2: **for** $l = \{1, 2, ..., p_b\}$ **do**
3: $\quad Q_b^l = SendRecv_l(Q_a^k)$
4: $\quad$ **if** $Q_{ab}^{kl} = Q_a^k \cap Q_b^l \neq \emptyset$ **then**
5: $\quad\quad \mathbf{Id}_a^k = WithinBox(\mathbf{R}_a^k, Q_a^k \cap Q_b^l)$
6: $\quad\quad \mathbf{r}_a^k = \mathbf{R}_a^k(\mathbf{Id}_a^k)$
7: $\quad\quad \mathbf{Id}_{a_c}^k = WithinBox(\mathbf{\Omega}_a^k, Q_a^k \cap Q_b^l)$
8: $\quad\quad \boldsymbol{\omega}_a^k = \mathbf{\Omega}_a^k(\mathbf{Id}_{a_c}^k)$
9: $\quad\quad \mathbf{r}_b^l = SendRecv_l(\mathbf{r}_a^k)$
10: $\quad\quad \mathbf{Id}_{a_c}^{\mathbf{r}_b} = LocateInCells(\mathbf{r}_b^l, \boldsymbol{\omega}_a^k)$
11: $\quad\quad \mathbf{Id}_{a_c}^{\mathbf{r}_a} = SendRecv_l(\mathbf{Id}_{a_c}^{\mathbf{r}_b})$
12: $\quad\quad \mathbf{ID}_a^k[l] = (\mathbf{Id}_a^k, \mathbf{Id}_{a_c}^{\mathbf{r}_a})$
13: $\quad$ **end if**
14: **end for**

For each subdomain in $\mathbf{\Omega}_a^k$ and $\mathbf{\Omega}_b^l$ we can define the following bounding boxes $Q_a^k = \{Q_a^1, Q_a^2, Q_a^3\}$ and $Q_b^l = \{Q_b^1, Q_b^2, Q_b^3, Q_b^4\}$ (line 1 of Algorithm 1), as shown in Fig. 4.7 for a 2D example. A bounding box is simply a rectangle in 2D or a box in 3D which encloses a given subdomain.

Suppose now that Algorithm 1 is being executed in a local processor. The first step of the algorithm is to share with all the remote processors (line 2) the geometric definition of each local bounding box Q_a^k (line 3).

As in reality Algorithm 1 is executed concurrently by *all* processors, due to the *SendRecv* instruction the remote subdomains $\mathbf{\Omega}_b^l$ also share its bounding boxes with local subdomains $\mathbf{\Omega}_a^k$. So, as a consecuence of the bi-directional *SendRecv* instruction, each local subdomain $\mathbf{\Omega}_a^k$ knowns

the definition of each bounding box of the remote subdomains $\mathbf{\Omega}_b^l$ (Q_b^l). The same occurs in the opposite way: each remote subdomain $\mathbf{\Omega}_b^l$ knows the position of the bounding boxes of the local subdomains $\mathbf{\Omega}_a^k$.

After this information is shared amongst all the subdomains, each local processor compares its bounding box with all the bounding boxes received from the remote processors (Fig. 4.7 (a)). Whether any pair of bounding boxes overlap $Q_{ab}^{kl} = Q_a^k \cap Q_b^l \neq \emptyset$ (Fig. 4.7 (b)), the processors associated to these subdomains are matched for coupling (line 4).

Once this matching is done, the next step is the searching of the *local* node coordinates $\mathbf{r}_a^k$ which lie inside the overlapping region Q_{ab}^{kl} (Fig. 4.7 (c)). This is done by identifying, from the list of coordinates of all local nodes $\mathbf{R}_a^k$, those who lie inside the overlapping region Q_{ab}^{kl}. The output of this step is a list of node identifiers $\mathbf{Id}_a^k$ (line 5). The coordinates list $\mathbf{r}_a^k$ are obtained by matching $\mathbf{Id}_a^k$ with $\mathbf{R}_a^k$ (line 6).

The elements identifier $\mathbf{Id}_{a_c}^k$ store those elements of the local subdomain $\mathbf{\Omega}_a^k$ which lie inside the overlapping region Q_{ab}^{kl} (line 7). The connectivities of those elements ($\boldsymbol{\omega}_a^k$) are given by matching the identifiers $\mathbf{Id}_{a_c}^k$ with the list of all the connectivities of the local subdomain $\mathbf{\Omega}_a^k$ (line 8).

Afterwards, the sub-set of local nodes $\mathbf{r}_a^k$ is shared with all the remote processors of those subdomains which fulfill the condition $Q_a^k \cap Q_b^l \neq \emptyset$ (line 9). At this point and due to the *SendRecv* instruction, each local processor also knowns the coordinates of those nodes from all the remote subdomains which are inside the overapped region Q_{ab}^{kl} ($\mathbf{r}_b^l$).

The next step of the algorithm is to identify which of the remote nodes $\mathbf{r}_b^l$ (which by definition lie inside the overlapped region), also lie inside the local elements $\boldsymbol{\omega}_a^k$ (line 10). This specific task is described in the next section, Local searching.

Once all the remote nodes which lie inside the local elements are found and identified by the local processor (Fig. 4.7 (f)), their identifiers $\mathbf{Id}_{a_c}^{\mathbf{r}_b}$ are shared with the remote processor which owns those detected nodes (line 11). Due to the *SendRecv* instruction and to the fact that Algorithm 1 is executed concurrently in all processors, at this point the local processor will receive the identifiers of all its nodes detected by the remote processors ($\mathbf{Id}_{a_c}^{\mathbf{r}_a}$).

The last step of Algorithm 1 is the assembly of array $\mathbf{ID}_a^k[l]$ (line 12), which contains the main information computed by the algorithm. This array stores the local node and element identificators $\mathbf{Id}_a^k$ and $\mathbf{Id}_{a_c}^{\mathbf{r}_a}$, respectively. The position l in array $\mathbf{ID}_a^k[l]$ represents each one of the remote processors. So, by means of array $\mathbf{ID}_a^k[l]$ each local processor knows: (a) which local nodes lie inside of the subdomain owned by processor l, and (b) which local elements contain remote nodes from processor l. Thus, once the global searching algorithm has finished and given the fact that the global searching is executed in parallel in all processors, the available information at each processor is: (a) a list that maps local nodes with its corresponding remote processor/processors, and (b) the list of local elements that contain remote nodes. Finally, by evaluating $\mathbf{r}_b^l(\mathbf{Id}_{a_c}^{\mathbf{r}_b})$ each processor can compute the coordinates of the remote nodes from remote processor l that are contained by any local element. The list of local elements and the

coordinates of the remote nodes are used to perform interpolation operations between local to remote subdomains.

The list of remote processors $\mathbf{ID}_a^k[l]$ is used to develop a communication scheduling. Such scheduling determines which processors are involved in the coupling and when and how the data should be exchanged between the processors.

4.4.1.1.2 Local searching In this specific task, which is part of the global searching procedure, the identification of all of the remote nodes which lie inside each of the local elements at the overlapped region is done. This is performed by using an octree searching algorithm as a first approximation along with some suitable method to exactly determine whether a node is or not inside a given element. The process of local searching is described in Algorithm 2.

Algorithm 2 Local search/localization

1: $T_b^l = GetOctree(\mathbf{r}_b^l)$
2: **for all** $\mathbf{e}_k \in \boldsymbol{\omega}_a^k$ **do**
3: $\quad q_k = GetQueryBox(\mathbf{e}_k)$
4: $\quad \mathbf{Id}_{a_c}^l = WithinQueryBox(T_b^l, q_k)$
5: $\quad \mathbf{Id}_{a_c}^{\mathbf{r}_b} \mathrel{+}= WithinCells(\mathbf{Id}_{a_c}^l, \mathbf{r}_b^l, \mathbf{e}_k)$
6: **end for**

Once the remote nodes $\mathbf{r}_b^l$ and the local elements $\boldsymbol{\omega}_a^k$ located at the overlapping region Q_{ab}^{kl} have been identified (see previous paragraph, global searching), the next step consists on finding the sub-set of remote nodes which lie inside the sub-set of local elements. Not only the identification but also the pairing between those nodes and elements is done in this process. In order to do that efficiently, an octree search is performed. Such octree T_b^l is created by using the remote nodes $\mathbf{r}_b^l$ (line 1). The first step for the octree construction is the creation of a square in 2D or a box in 3D which encloses all the remote nodes $\mathbf{r}_b^l$. Then a refinement process starts, stopping each time that a *leave* of the octree encloses as much as a sub-set of 3 nodes from the set of remote nodes $\mathbf{r}_b^l$ (Fig. 4.7 (d)).

Next, for each local element $\mathbf{e}_k$ in the sub-set of local elements $\boldsymbol{\omega}_a^k$ (line 2) a *query box* q_k is created (line 3). This query box is basically a bounding box which encloses each element $\mathbf{e}_k$. After the query box is created, the next step is to identify those octree leaves which are overlapped by the query box. A list of those overlapped octree leaves is stored in $\mathbf{Id}_{a_c}^l$ (line 4) (Fig. 4.7 (e)).

The last step consists of identifying which of the remote nodes that lie inside of the octree leaves listed in $\mathbf{Id}_{a_c}^l$ are also inside of the local element $\mathbf{e}_k$ (line 5). For this task, any suitable method to decide whether a point is located inside a given geometry could be used. For instance, homogeneous barycentric coordinates are used in the case of triangles or tetrahedrons. For more general cases, spherical barycentric coordinates can be used. The output of this step is the list $\mathbf{Id}_{a_c}^{\mathbf{r}_b}$ which allows to identify all those remote nodes of the sub-set $\mathbf{r}_b^l$ which lie inside element $\mathbf{e}_k$.

Using octrees provides an efficient way to perform the local searching. This strategy is much more adventageous than other straightforward choices, as the brute force evaluation. Brute force

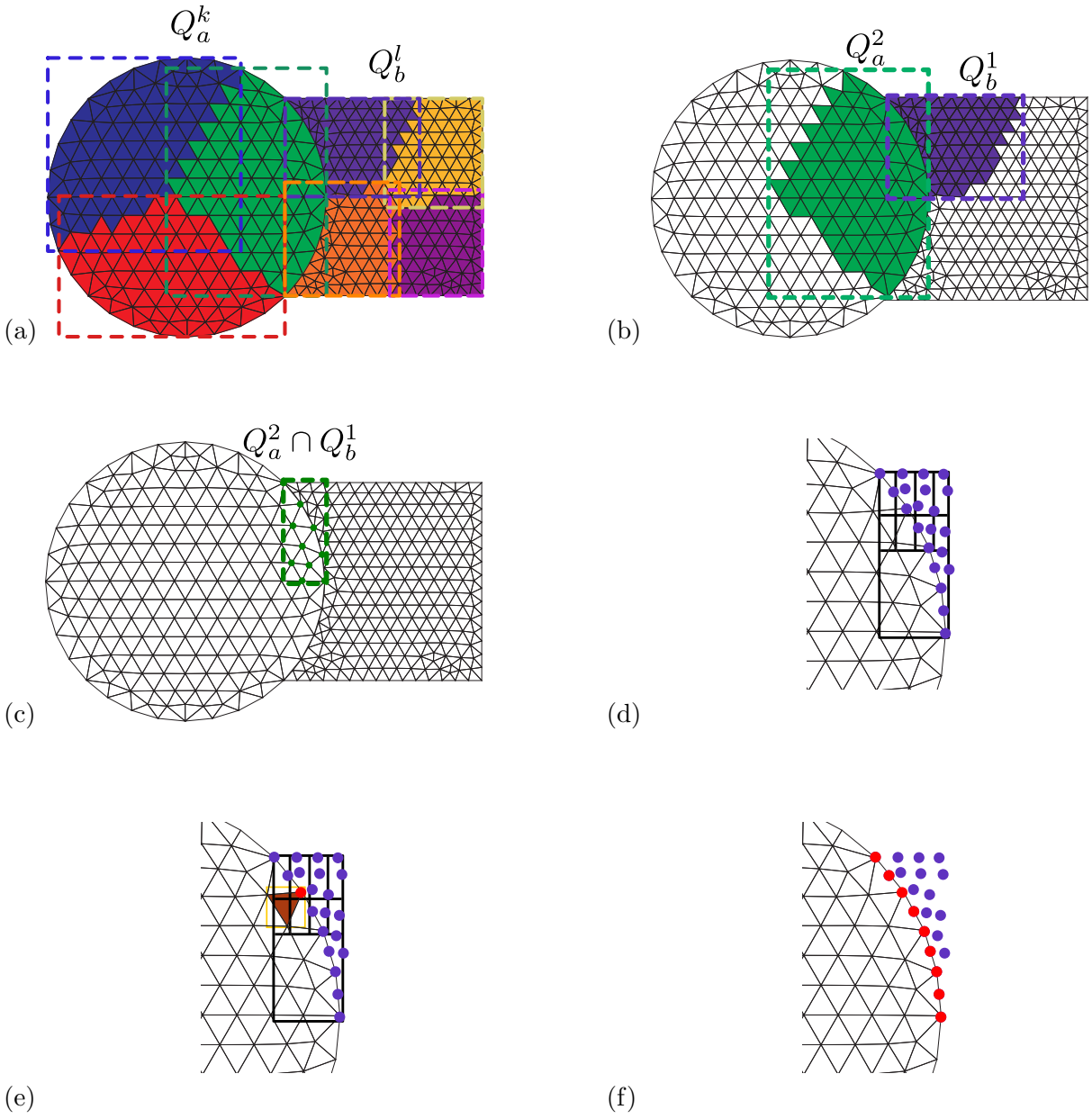

Figure 4.7: (A) Bounding boxes $\mathbf{Q}_a = \{Q_a^1, Q_a^2, Q_a^3\}$ and $\mathbf{Q}_b = \{Q_b^1, Q_b^2, Q_b^3, Q_b^4\}$ are used to find candidate processors to be matched for the coupling. (B) Whether two bounding boxes overlap, the processors are matched for the coupling. (C) Identification of local node coordinates $\mathbf{r}_a^k$ which lie inside the overlapping region. (D) An octree is created using the remote nodes situated in the overlap region $Q_a^2 \cap Q_b^1$. Such octree is used as a first approximation to find the remote nodes that are closest to each local element. (E) When a query box and an octree leave overlaps, barycentric coordinates are used to exactly determine if the remote nodes enclosed by the octree leave are localized inside the local element enclosed by the query box. (F) All the remote nodes which lie inside the local elements are found and identified by the local processor.

evaluation means to check one by one the remote nodes $\mathbf{r}_b^l$ and evaluate if they are inside the local element $\mathbf{e}_k$. This is a very expensive strategy, which cost is considerably reduced by using the octree method.

4.4.1.2 Exchange

The data exchange strategy only considers subdomains of different partitions with common overlapping regions. Since each partition is independently solved, the main operations related to the coupling as communication and interpolation take place locally. Interpolations are performed on each processor, while communications are performed in pairs of processors, by a parallel peer-to-peer communication approach (see Fig. 4.8 and Algorithm 3). On the other hand, it is possible to assume that the workload across the processors has been equally distribuited by a well known domain decomposition method, for instance METIS [78], executed independently on each partition. The set of nodes assigned by METIS to each processor, along with their respective connectivities (i.e. elements), forms the subdomains of each partition.

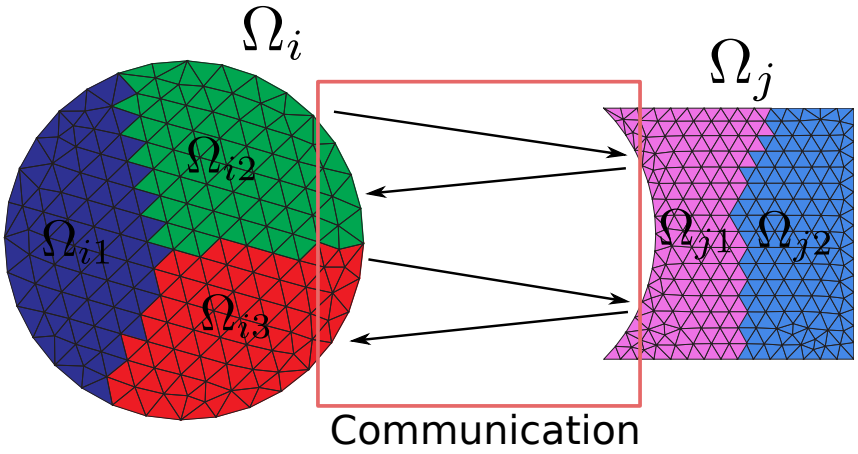

Figure 4.8: Disjoint partitions and subdomains Ω_{ia} and Ω_{jb}. Data is only transferred between overlapping subdomains (Ω_{i2} with Ω_{j1} and Ω_{i3} with Ω_{j1}). Interpolation maps property values $\mathbf{v}_{ia}$ on Ω_{ia} to values $\mathbf{v}_{jb}$ on Ω_{jb} through the coordinates $\mathbf{r}_b^l$ (remote nodes). Exchange is done through the message passing interface.

Algorithm 3 describes briefly the data exchange strategy. The number of communications q_{ij}^a that the subdomain Ω_{ia} stablishes with the partition $\mathbf{\Omega}_j$ (and vice versa) is defined by the number of overlaps between Ω_{ia} with each of the subdomains of partition $\mathbf{\Omega}_j$ (Ω_{jb}). The overlapping surface $\Gamma_{ij} = \mathbf{\Omega}_i \cap \mathbf{\Omega}_j \neq \emptyset$ defines the communication between partitions $\mathbf{\Omega}_i$ and $\mathbf{\Omega}_j$. For the example shown in Fig. 4.8, communication takes place between subdomains Ω_{i2} and Ω_{i3} of partition i and subdomain Ω_{j1} of partition j. Interpolation of local properties $\mathbf{v}_{ia}$ to remote nodes $\mathbf{r}_b^l$ is done locally in each processor (line 3). Then, interpolated property $\mathbf{v}_{jb}$ is communicated to each of the processors that own remote nodes (line 4). This communication is done using the message passing interface (MPI).

Algorithm 3 Data exchange

1: **for** $\mathbf{\Omega}_{jb} = \{\mathbf{\Omega}_{j1}, ..., \mathbf{\Omega}_{jp_b}\}$ **do**
2: **if** $\mathbf{\Omega}_{ia} \cap \mathbf{\Omega}_{jb} \neq \emptyset$ **then**
3: Interpolation$_a(\mathbf{v}_{ia}, \mathbf{r}_b^l) \rightarrow \mathbf{v}_{jb}$
4: Communication$_{ab}(\mathbf{v}_{jb})$
5: **end if**
6: **end for**

4.4.2 Implementation issues

From now on, as we are only interested in unilateral contact problems, we will consider the case were a *rigid* body gets in contact with a *deformable* body. For simplicity, in the rest of this section we will use 2D examples to illustrate the description of the algorithm. Nevertheless, all the ideas introduced here are also applicable to 3D cases. As it was described in Sec. 4.4.1.1, contact detection allows to identify the *contacting nodes* once they have penetrated a given domain (see Fig. 4.5).

At each time step, contact detection is done after the displacements update of the rigid body, but before the resolution loop of the deformable body. In other words, we use the updated mesh of the rigid body as the base mesh for the localization of penetrated nodes of the previous time step configuration mesh of the deformable body. At this instant, both algorithms synchronize and the localization is executed. In Fig. 4.9 we show a temporal representation of this procedure.

The contact algorithm is triggered when at least one boundary node of the deformable body has penetrated inside the rigid body. When this occurs, Algorithm 4 is executed concurrently (i.e. in parallel) in all the processors which belong to the rigid body partition, just after the localization procedure. For each of the *nsend* detected nodes of the deformable body (line 1), the first task is to project each of those nodes to the rigid body's contact boundary (line 2). This projection is done independently by each of the processors of the rigid body partition which has detected at least one penetrated node. So *nsend* variable is local to each processor and represents the number of penetrated nodes that were detected. The *direction* of projection must be given as an input by the user. The output of this computation is a normal-tangent orthonormal basis for each of the penetrated nodes. This orthonormal basis is build in such a way that the tangent direction passes through the projection and is tangent at this point to the contact boundary of the rigid body. The normal distance (i.e. the distance from the point to the normal tangent line) is also computed. This procedure is schematically represented in Fig. 4.10.

Algorithm 4 Rigid body algorithm

Require: Contact detection

1: **for** i = 1,nsend **do**
2: tangent$_i$,normal$_i$,distance$_i$ = projection(direction$_i$)
3: send_to_deformable(tangent$_i$,normal$_i$,distance$_i$)
4: **end for**

Algorithm 5 describes the parallel projection algorithm (i.e. projection function executed

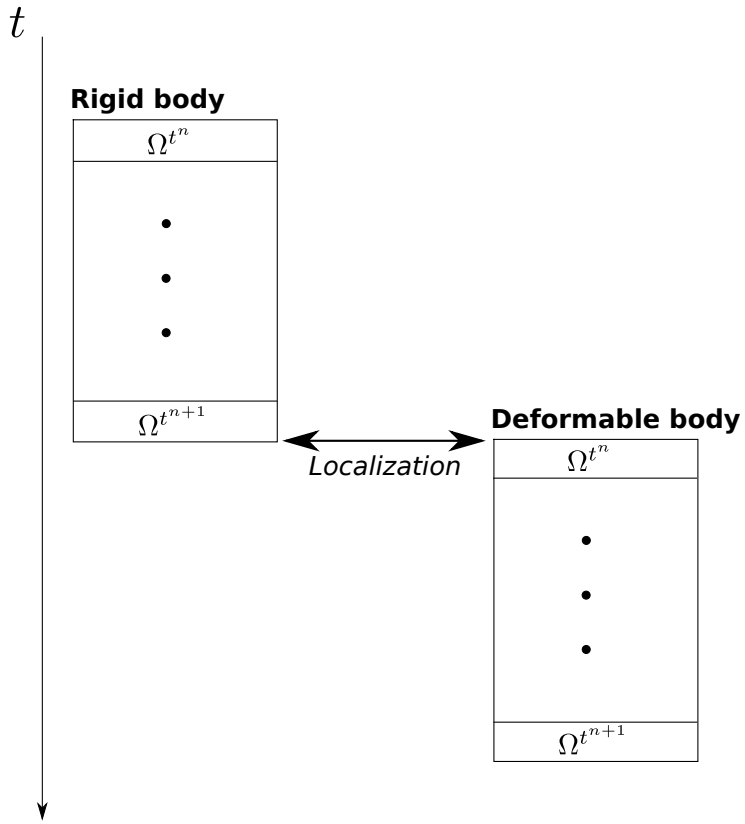

Figure 4.9: Temporal representation of the contact detection. This procedure is repeated at each time step.

on line 2 of Algorithm 4). In a domain decomposition approach, each processor stores only the nodes and connectivities of the associated subdomain, including the boundary information. As each penetrated node is projected to the contact boundary of the rigid body, then each processor must know at least the definition of the boundary segment to which the projection lies (i.e. boundary nodes and its connectivity). The projection algorithm, executed concurrently by each processor of the rigid body, must be general in order to consider the case where the projection lies in a boundary segment of a different processor than the one which owns the detected node (see Fig. 4.11). The strategy followed here is to communicate to all the processors of the rigid body partition the information regarding to the complete contact boundary definition (lines 1 to 4). After line 4 is executed, each processor has a local copy of the coordinates of the boundary nodes and the boundary elements connectivities for the complete contact boundary of the rigid body. Then, for each of the detected nodes i of the deformable body (line 5) the algorithm loops over each boundary element of the contact boundary of the rigid body j (line 6) and builds a plane π_j (or a line, in a 2D case) using the geometrical information of the boundary element (line 7). Then, the algorithm projects the detected node i to the plane π_j in a predefined direction (line 8). Afterwards, the algorithms checks if the projection of node i to plane π_j also lies inside the boundary element j (line 9). If true, the algorithm returns the tangent vector, normal vector and normal distance of node i to the boundary element (i.e. distance from node i to π_j) (lines 10 to 12).

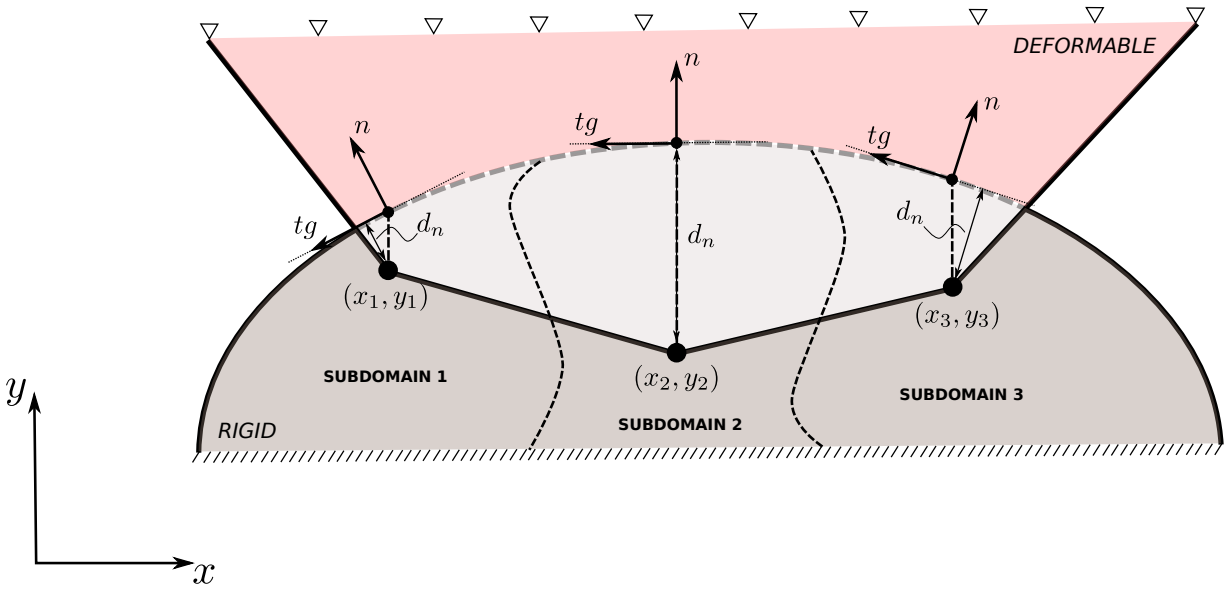

Figure 4.10: Projection operation done by the processors which belong to the rigid body partition. Each of the detected nodes of the deformable body which have penetrated the rigid body are projected to the rigid's body contact surface. The rigid body computes the orthonomal coordinates basis system $n - tg$ at the projection point and the normal distance d_n.

Algorithm 5 Projections algorithm (projection function)

Require: direction$_i$

```
1: communicate local number of boundary elements
2: contactbou_total ← get total number of boundary elements
3: communicate local boundary nodes coordinates
4: bocod_total ← get all boundary nodes coordinates
5: for i = 1,nsend do
6:     for j = 1,contactbou_total do
7:         get plane π_j : ax + by + cz + d
8:         project node i to plane π_j in direction_i
9:         if projection is inside boundary element j then
10:            tangent_i, normal_i ← compute tangent and normal vector of π_j
11:            distance_i ← compute normal distance from node i to π_j
12:            return tangent_i,normal_i,distance_i
13:        end if
14:    end for
15: end for
```

After the rigid body instance has computed all the information required for each penetrated node (orthonormal basis at the projection and normal distance), the next step is to send this data to the deformable body, as stated in line 3 of Algorithm 4. So far, the orthonormal basis and the normal distance computations have been performed by the processors owned by the rigid body,

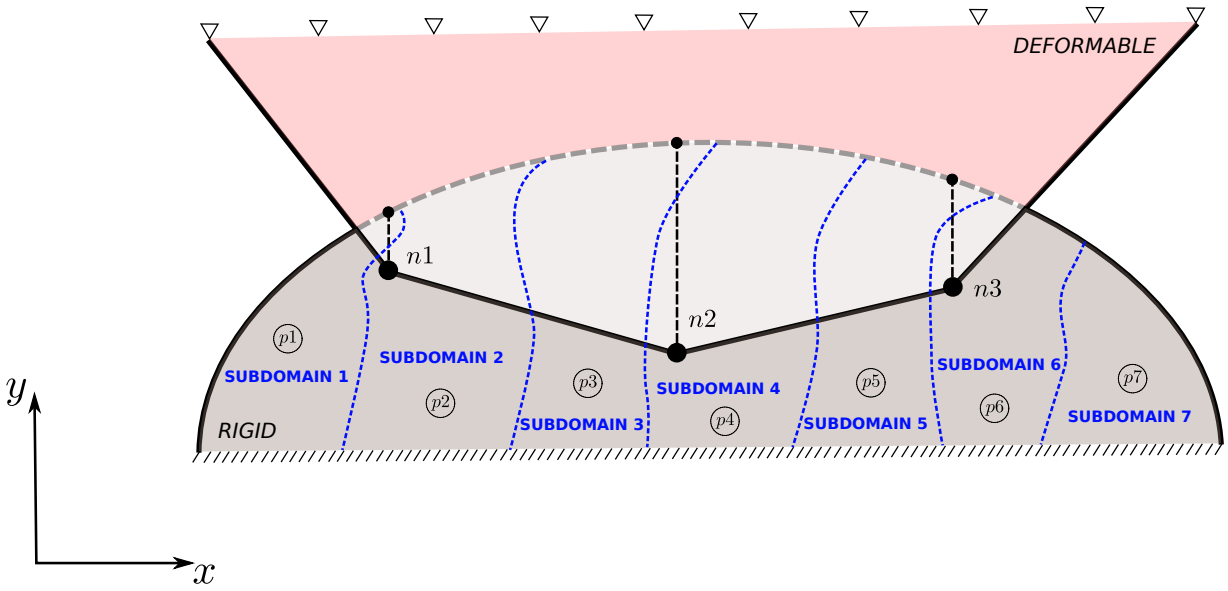

Figure 4.11: Penetrated nodes $n1$, $n2$ and $n3$ are detected by processors 2, 4 and 6 but the projection lies on boundary segments which belong to processors 1, 3 and 5 respectively.

so this information is stored in each of these processors. Given that this information is required by the deformable body, the rigid body must transfer all of the previously computed values. This exchange of information is done via PLE++ tool, using the builtin MPI API, as described in Sec. 4.4.1.2. Each processor of the rigid body that has detected a penetrated node will send the orthonormal basis and normal distance to the processor of the deformable body which owns that node. Fig. 4.12 shows an example where the rigid body is divided in 3 subdomains while the deformable body is divided in 5 subdomains. For the sake of clarity and without loss of generality, we assume that the detected node and its projection are in the same processor of the rigid body partition. Node 1 ($n1$), which belongs to the deformable body's contact surface, is detected by processor 1 (subdomain 1) of the rigid body. Once the orthonormal basis and normal distance are computed, this information is sent to processor 4 (subdomain 1) of the deformable body, as this is the processor/subdomain which owns that node. Same procedure is done with node 2 ($n2$) and node 3 ($n3$). For node 2 and node 3 communication is stablished between processors 2 and 6 and between processors 3 and 8 respectively.

The synchronization point for the exchange of information between both code instances is placed after the execution of Algorithm 4 for the rigid body instance, and after the localization procedure for the deformable body instance. In other words: when the localization procedure is over and after the rigid body has finished the execution of Algorithm 4, is when the exchange of the projection data is produced. This means that after the localization the code instance in charge of the deformable body is on hold waiting for the rigid body instance to finish the execution of Algorithm 4. When this happens, the exchange of data between instances is produced (i.e. the rigid instance sends the data of the projections to the deformable instance). Then, the execution of the rigid body code instance stops and the execution of Algorithm 6, executed by

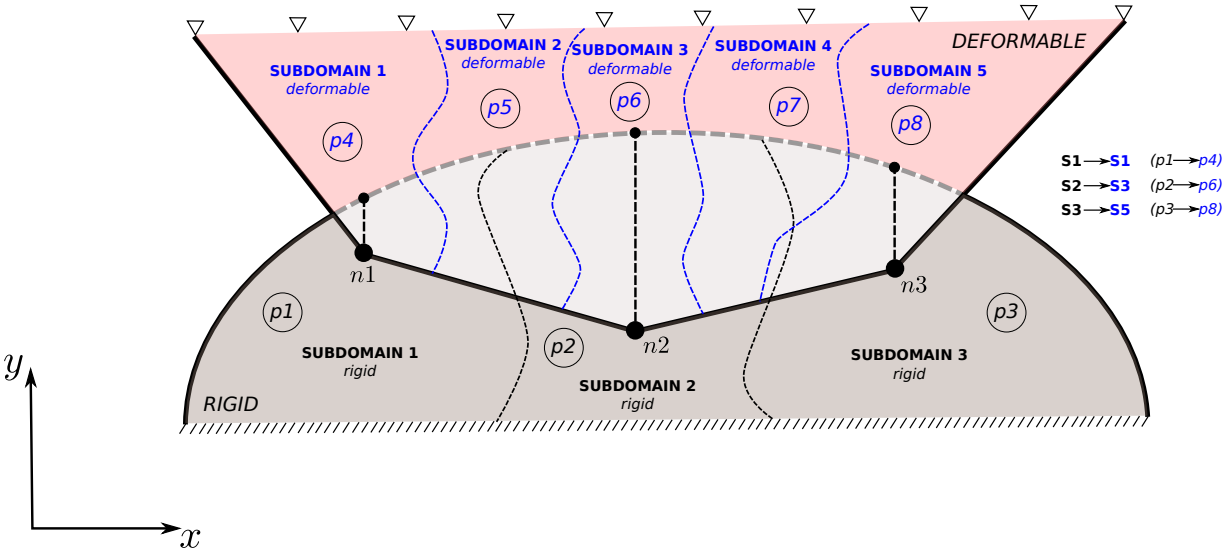

Figure 4.12: Transference of information from the rigid body to the deformable body. Rigid body is divided in 3 subdomains while deformable body is divided in 5 subdomains. Processors 1, 2 and 3 of the rigid body partition send the orthonormal basis and normal distance to processors 4, 6 and 8 of the deformable body partiton respectively.

the deformable body instance, starts. This complete sequence is reproduced in Fig. 4.13.

Algorithm 6 Deformable body algorithm

1: **for** i = 1,nrecv **do**
2: retrieve_from_rigid(tangent$_i$,normal$_i$,distance$_i$)
3: $j \leftarrow$ from_local_to_global(i)
4: tag_contact$_j$ = 1
5: jac_rot$_j$ = create_rotation_matrix(tangent$_i$,normal$_i$)
6: set_displacement$_j$(distance$_i$)
7: **end for**

Algorithm 6 is executed concurrently by each processor of the deformable body partition. Each of these processors loop over all the *nrecv* penetrated nodes they own (line 1). For each penetrated node, they retrieve the normal and tangent vectors which define the orthonormal basis and the normal distance to the tangent plane (line 2). The penetrated nodes detected by PLE++ are a subset of nodes which belong to the set of the totality of nodes which define the deformable body. It becomes necessary to relate the local numbering of penetrated nodes (i.e. from one to the total number of *nrecv* detected nodes that belong to each processor of the deformable body partition) with the global numbering of nodes (i.e. from one to the total number of nodes that conform each subdomain). This relation is automatically created by PLE++ and stored in an array which is used as described in line 3. An array used for identifying all contacting nodes using their global numbering is also constructed for future computations (line 4). Next, a rotation matrix is computed for each of these nodes using the information received by the rigid

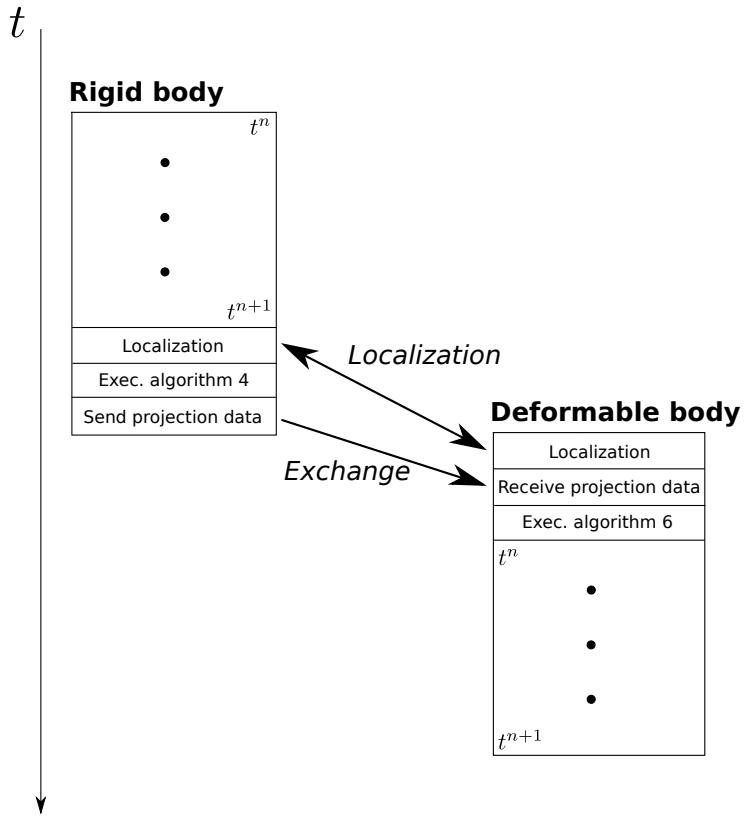

Figure 4.13: Staggered execution of rigid and deformable body algorithms. Identification of the localization and exchange points. This procedure is repeated at each time step.

body (line 5). This rotation matrix will be used for the enforcement of the MPC. Finally, each of the penetrated nodes store in its global numbering the normal distance to the tangent plane (line 6), as this information will also be used for the enforcement of the MPC.

As explained in Sec. 4.3, the PDN method is based on the replacement of the geometrical constraints due to normal and frictional contact by partial Dirichlet-Neumann boundary conditions in the case of unilateral contact with an arbitrary rigid surface. The geometrical constraints due to normal contact are imposed by means of Multi-Point Constraints (MPC) while friction is imposed in the form of a tangential force (Neumann condition), which is applied in the opposite direction of the sliding node. Basically, the general idea of this method is to solve the equilibrium of the deformable body restricting the movement of the contacting/penetrated nodes only in the tangential plane. From a mathematical point of view, the general strategy to solve linear systems of equations with restrictions is the usage of Lagrange multipliers. The major drawback when using Lagrange multipliers is the introduction of extra degrees of freedom to the system of equations which must be solved. For the particular case of contact problems, the number of Lagrange multipliers which must be introduced to the system depends on the number of contacting nodes, which can vary with time. A time-dependent number of degrees of freedom can be very disadvantageous for load balancing when using a parallell computer code. We propose a new strategy for solving the restriction problem without needing to increase the number of degrees

of freedom of the system. This strategy is based on a local rotation of the coordinates system for each of the penetrated nodes. The first step is to associate to each of the penetrated nodes a rotation matrix which is constructed with the normal and tangent vectors received from the rigid body partition (line 5 of Algorithm 6). For a general case, the rotation matrix R_i for the node i is constructed as follows:

$$R_i = \begin{bmatrix} n_x & t_{1,x} & t_{2,x} \\ n_y & t_{1,y} & t_{2,y} \\ n_z & t_{1,z} & t_{2,z} \end{bmatrix}, \tag{4.31}$$

where $\mathbf{n}$ is the normal vector and $\mathbf{t}_1$ and $\mathbf{t}_2$ the tangential vectors associated to node i. In a 2D problem, only one tangent vector is needed.

4.4.2.1 MPC enforcement

From the point of view of the deformable body, an unilateral contact problem solved with the PDN method can be summarized as follow: compute the equilibrium of a deformable body restricting the displacement of some given nodes to pre-defined planes, which can be formulated differently node by node. Fig. 4.14 shows a 2D example of the previous statement. Here, we desire to compute the equilibrium of body $\mathcal{B}$ restricting the displacement of nodes A and B to lines l_1 and l_2 respectively. The PDN method implies that lines l_1 and l_2 must be constructed using the tangent direction of the rigid body's contact surface at the location where the projection of detected nodes lies (for this particular example a vertical projection is used).

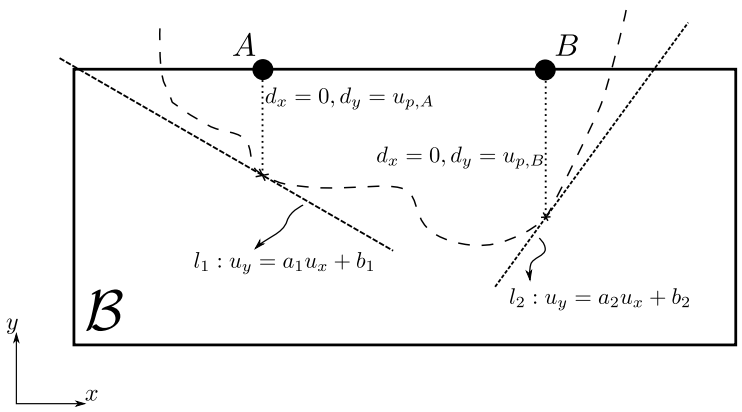

Figure 4.14: Multi-point constraints applied to nodes A and B.

As already mentioned, the most common technique to solve this kind of problems is by means of the Lagrange multipliers method. Nevertheless, introduction of Lagrange multipliers presents several drawbacks for parallel computational codes. The proposed technique is based on a local rotation of the reference frame for each node, and the enforcement of an homogeneous Dirichlet boundary condition along the normal direction. The first step is to *artificially* locate the nodes over each line at the closest point, which would be the normal distance from the point to the line (see Fig. 4.15). This *artificial* displacement is used for the construction and assembly of the finite element matrices for the equilibrium computation of body $\mathcal{B}$.

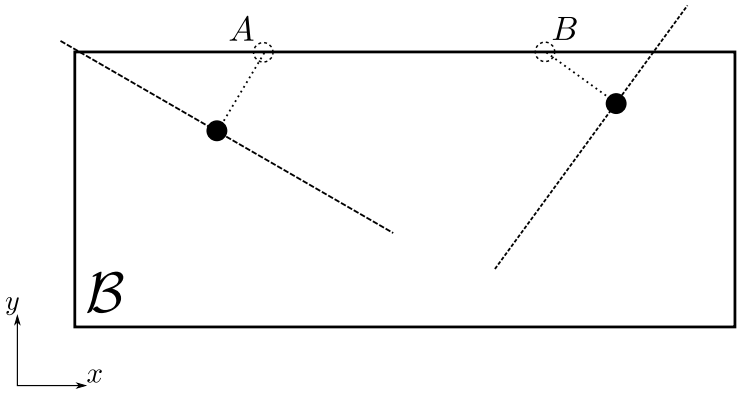

Figure 4.15: Artificial displacement of nodes A and B used for the assembly of finite element matrices.

The next step is to rotate locally the reference frame of the nodes from x, y to n, t using the rotation matrix R_i (see Eq. (4.31)), as shown in Fig. 4.16. Let's suppose that $A\,u = b$ is the original system. R_i is the matrix which rotates the reference frame of a given node i from global to local and $Q_i = R_i^{-1} = R_i^T$ is the matrix which rotates from local to global. Then, to rotate the reference frame of node i in the finite element matrix A, a muliplication by R_i and Q_i must be done in the following way:

$$A^* = \begin{vmatrix} A_{11} & \dots & A_{1j}\,Q_i & \dots & A_{1n} \\ R_i\,A_{j1} & \dots & R_i\,A_{jj}\,Q_i & \dots & R_i\,A_{jn} \\ A_{n1} & \dots & A_{nj}\,Q_i & \dots & A_{nn} \end{vmatrix}, \tag{4.32}$$

which is derived from the following transformation:

$$A\,u = b, \tag{4.33}$$
$$R_i\,A\,u = R_i\,b, \tag{4.34}$$
$$R_i\,A\,(Q_i R_i)\,u = R_i\,b, \tag{4.35}$$
$$R_i\,A\,Q_i\,u^* = R_i\,b, \tag{4.36}$$
$$A^*\,u^* = R_i\,b, \tag{4.37}$$

where u^* represents the unknowns vector in the rotated reference frame. It must be noted that the local rotation represented by Eq. (4.32) should be repeated for each of the contacting/penetrated nodes, using a different rotation matrix for each node.

The next step is to solve the system $A^*\,u^* = R_i\,b$, constraining the displacement of each rotated node in the normal direction by means of an homogeneous Dirichlet condition. Due to this constraint, the displacement of those nodes will only occur in the tangential direction. As a consequence of this procedure, we will obtain a solution that is restricted to the line equations given by the MPC (see Fig. 4.17).

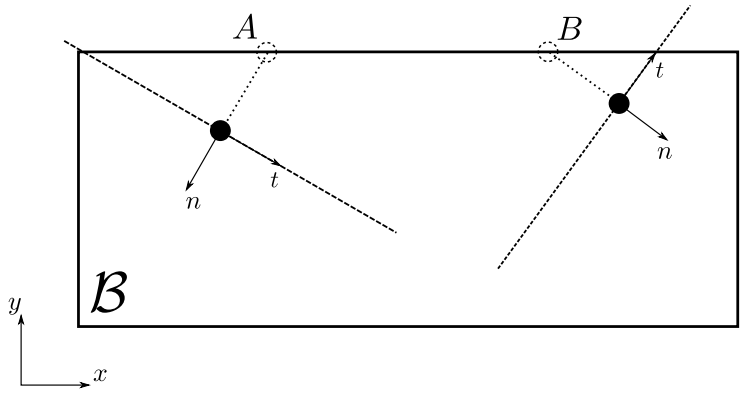

Figure 4.16: Local rotation of the reference frame for nodes A and B.

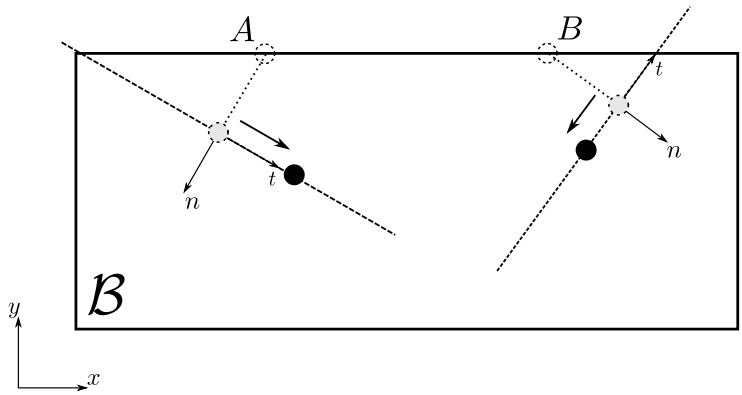

Figure 4.17: Equilibrium positions for nodes A and B.

Once the equilibrium is achieved (the solution for u^* is obtained), the last step is to derotate all the rotated nodes, to transform the solution to the global x-y reference frame. This is done using the relation $u = Q_i\, u^*$.

4.4.2.2 Friction enforcement

The way in which the frictional forces are imposed is based on the idea introduced in Sec. 4.3.2. As explained in the previous section, the enforcement of the MPC is characterized by a local rotation of the coordinate system of each of the penetrated nodes following the rule given by Eq. (4.32). After the MPC are enforced but before the linear system of Eq. (4.37) is solved, the algorithm computes the reaction force at each contacting node and evaluates the condition given by Eq. (4.29). In case of stick, the MPC is removed and a full homogeneous Dirichlet boundary condition is applied to the corresponding node. In case of slip, the frictional force $\underline{\mathbf{F}}^e$ is computed according to Eq. (4.30) and applied to the tangential axis of the node as shown in Fig. 4.18. This force takes the role of a Neumann boundary condition as its value is added directly to the right-hand-side of the linear system at the position which corresponds to the tangential degree of freedom of the node.

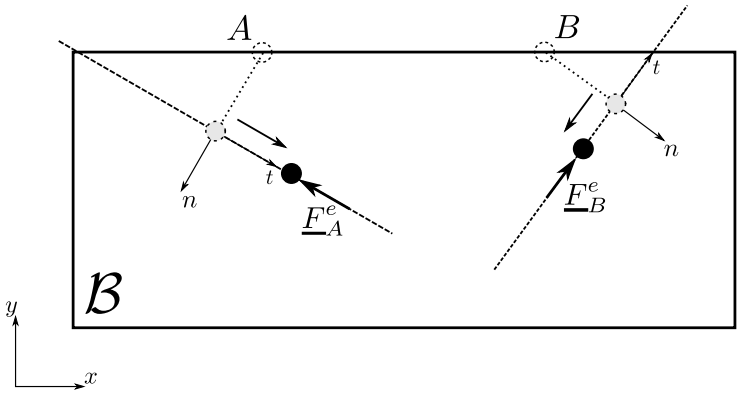

Figure 4.18: Frictional force imposition for nodes A and B.

4.4.2.3 Nodes release

Once the MPC and the frictional forces are applied and the system is solved, the last part of the PDN contact algorithm is intended to check if there is no traction forces in the updated contact interface (see Sec. 4.3.1). If the contact conditions produce artificial traction forces in any of the penetrated nodes, the algorithm must *release* those nodes (i.e. using a *remove contact* tag) and repeat the computation enforcing the MPC and frictional forces only in those nodes where no artificial traction forces were created. This procedure, which allows to determine the active contact zone for each time step, must be repeated until no artifical traction force is present in any of the penetrated nodes.

It must be remarked that the procedure described in the previous paragraph is done *after* the contact searching/localization for a *specific* time step. This means that localization is not repeated while the algorithm is computing the equilibrium of the system and determining the active contact zone. For a general contact problem, the active contact zone can not be predicted a priori, and can be interpreted as an extra result of the total computation. This explains the iterative nature of this procedure.

The algorithm which controls the system resolution and the nodes release for the PDN method in a parallel execution is shown in Algorithm 7. This algorithm is executed concurrently in each processor of the deformable body partition at each simulation time step.

As detailed in Sec. 4.4.2.1, after the contact constraints enforcement the resultant linear system of equations for the deformable body is solved. The result of this procedure is the equilibrium configuration of the deformable body given the MPC and frictional forces imposed by contact (lines 1 to 7 of Algorithm 7). Once the convergence is achieved, reactions are calculated in each penetrated node (line 10). The next step is to check if any of the penetrated nodes is in artificial adhesion (line 11). If this is the case, the multi-point constraint of the node is *released* (line 12) and the system is solved again. This procedure is repeated until all penetrated nodes in artificial adhesion are released.

In general, the nodes which are subjected to artificial adhesion are owned by only a subset of all the processors which own the totallity of the penetrated nodes. As Algorithm 7 is executed

Algorithm 7 Nodes release algorithm

```
1: update boundary conditions
2: assembly of right-hand-side and system matrix
3: set initial guess for inner iterations
4: notconverged ← 1
5: while notconverged == 1 do
6:     call beta-newmark implicit scheme
7:     check convergence outer iterations
8:     if converged then
9:         notconverged ← 0
10:        compute reactions on each contact node
11:        if there are nodes to release (adhesion) then
12:            release nodes
13:            notconverged ← 1
14:        end if
15:    end if
16:    call mpi_sum(notconverged)
17:    if notconverged >= 1 then
18:        notconverged ← 1
19:    end if
20: end while
```

concurrently by all processors, this imply that the processors which own the adhered nodes will continue the execution of the algorithm while the rest will exit the loop as they converged. As it is necessary to keep all processors executing Algorithm 7 once adhesion nodes are detected, it is crucial to synchronize the execution of all processors. This is done by communicating to all the processors the convergence flag (lines 16 to 19). By doing this, it is assured that all processors exit the loop simultaneously when no adhesion node is longer detected.

4.5 Numerical examples

4.5.1 Computational framework

The algorithm described in this chapter was implemented within an environment designed for heterogeneous problems in computational mechanics, which is the multiphysics, multiscale and massively parallel code Alya (see Sec. A.1 from Appendix A).

Taking profit of the flexibility and generality of the algorithm, we use a multicode scheme. Under this scheme, the displacement field of each body (rigid and solid) is solved using different instances of Alya, while the contact detection and the exchange of contact information between computational instances is done by PLE++. This means that for the resolution of the unilateral contact problem we execute two different instances of the Alya code, using two different set of input files, one for each body. Furthermore, as Alya is a parallel code, this scheme allows to parallelize independently each body. Additionally, as we are using different instances of the code and different input files, we can independently define different models for each of the bodies, as if they were in a standalone simulation. This define the black-box characteristic of the proposed

algorithm and is one of its most distinctive features.

In the multicode approach, the parallel simulation of the example depicted in Fig. 4.19 is executed in the following way:

```
$ mpirun -np 3 ./alya ball : -np 5 ./alya block
```

In this example, the code Alya is used for the numerical simulation of both bodies. Though, with a proper implementation, any other simulation tool can be used. So this methodology is not restricted to Alya code. In fact, before its implementation in Alya, the contact algorithm was tested in Ostero (see Sec. A.2 from Appendix A). Ostero is a didactic finite element code for the numerical simulation of solid deformable bodies. It was developed in the frame of this thesis, to use it as a test framework for several mechanical models and problems, as it is a very useful tool to perform proof-of-concept evaluations of contact mechanics algorithms.

On the other hand, as it was mentioned earlier, the multicode approach uses independent input files for each body. The usage of separated input files allows to use different kind of models, from different element types to different material and damage models. The meshes must be generated separately, so the node numbering and element definition is non-correlative. Additionaly, mesh partitioning is also performed separately, which allows to specify independently the number of subdomains to be used.

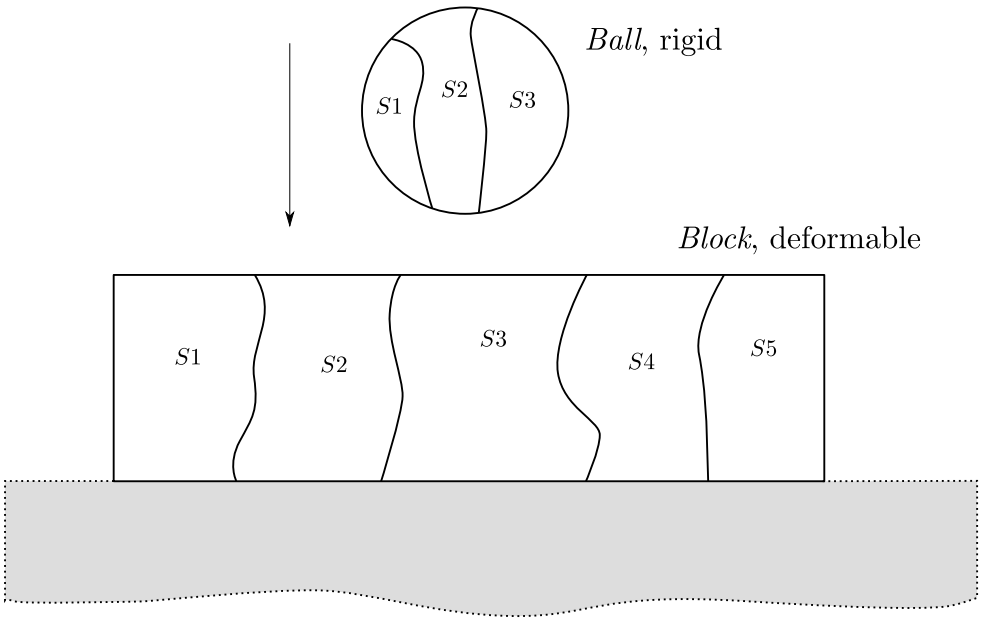

Figure 4.19: Multicode simulation of a parallel unilateral contact problem.

4.5.2 Test cases

We shall now present the results of application of the algorithm presented in this chapter to some 2D and 3D test cases. These test problems were selected to illustrate and validate the behaviour of the proposed algorithm.

4.5.2.1 Signorini problem: cylinder on a rigid foundation - 2D

We first consider a circular cylinder of radius R and length l, resting on a flat foundation, and subjected to an uniform load along its top of intensity F/l. The cylinder is constructed of an homogeneous, isotropic, elastic material with Young's modulus E and Poisson's ratio ν. Taking that $l >> R$, then we can assume a problem of plane strain. No friction is assumed to exist on the contact surface. The physical model of this problem is illustrated in Fig. 4.20.

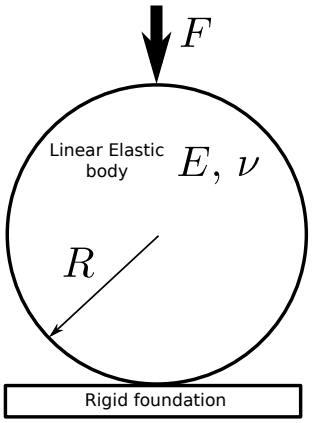

Figure 4.20: Signorini problem - Physical model.

We will compare our numerical results with the Hertz solution (see e.g. [79, 27]), which yields a contact pressure distribution of:

$$P = \frac{2F}{\pi b^2 l}\sqrt{(b^2 - x_1^2)}, \tag{4.38}$$

where F/l is the load per unit length and b is the half-width of contact surface defined by:

$$b = 2\sqrt{\frac{FR(1-\nu^2)}{\pi l E}}. \tag{4.39}$$

For the numerical solution of the physical model shown in Fig. 4.20, we solve an equivalent problem in which we fix the topmost node of the cylinder and move upwards the rigid foundation, as depicted in Fig. 4.21. Taking profit of the symmetry of the problem we use a half-cylinder for the computational domain.

We will assume a cylinder of radius $R = 8\,m$, Young modulus $E = 2000\,N/m^2$ and Poisson's ratio $\nu = 0.3$. The vertical displacement imposed to the rigid foundation is $\delta = 0.081\,m$. Using these values in our computational model, we obtain a contact pressure $P_{max} = 45.6945\,N/m^2$ for node n_0 ($x_1 = 0$, see Fig. 4.21). By combining Eqs. (4.38) and (4.39) we can isolate the variable F/l in order to compute b, which results in $b = 0.333\,m$. The deformed configuration of the body, the mesh used for the numerical solution and the contact zone are shown in Fig. 4.22.

A comparison of the computed contact pressure with the Hertz solution (Eq. (4.38)) is given in Fig. 4.23. We observe a good agreement between analytical and numerical solutions. It is noted that we have not assumed any contact surface and pressure. They are obtained naturally as part of the numerical solution of the problem by means of the algorithm proposed in this chapter.

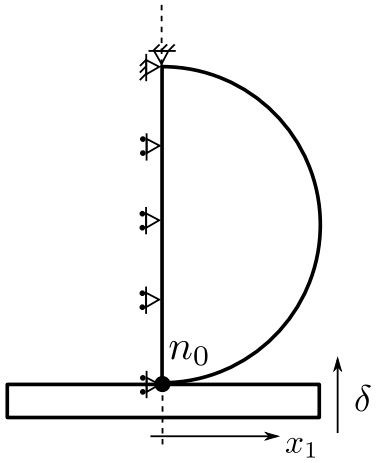

Figure 4.21: Signorini problem - Problem setting for the numerical resolution.

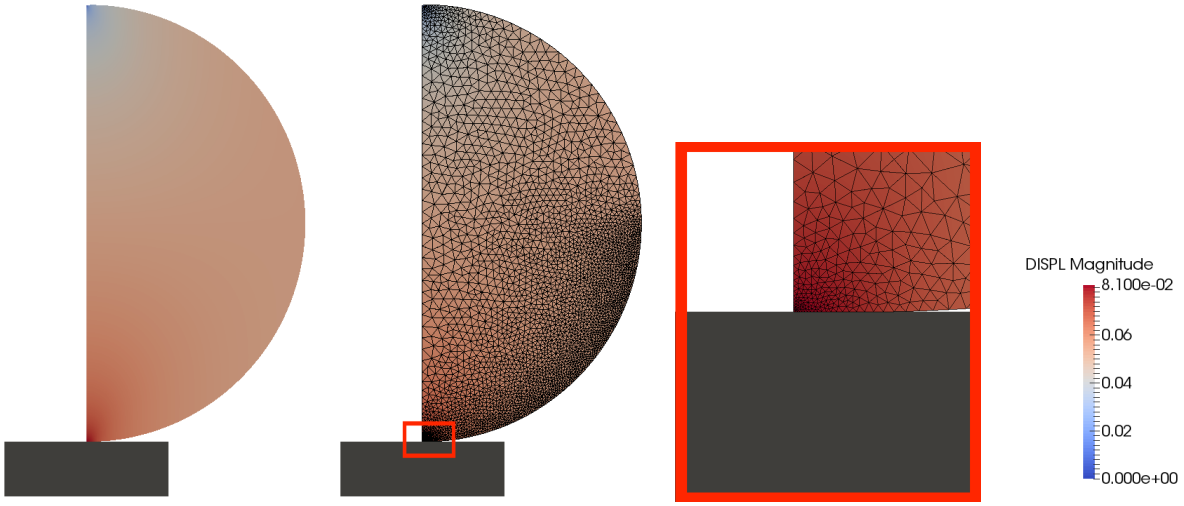

(a) (b) (c)

Figure 4.22: Signorini problem - (a) Deformed configuration. (b) Mesh used for the numerical solution. (c) Zoom in on the contact zone.

Finally, characteristics concerning the convergence of the problem are shown in Fig. 4.24. Specifically, in Fig. 4.24a we show the relative L^2 norm convergence of the displacements increment given by the Newton-Raphson method. Additionally, in Fig. 4.24b we show the convergence of the number of contacting nodes which define the active contact zone. In both figures it can be clearly observed how the algorithm release those nodes which are subjected to an artificial traction.

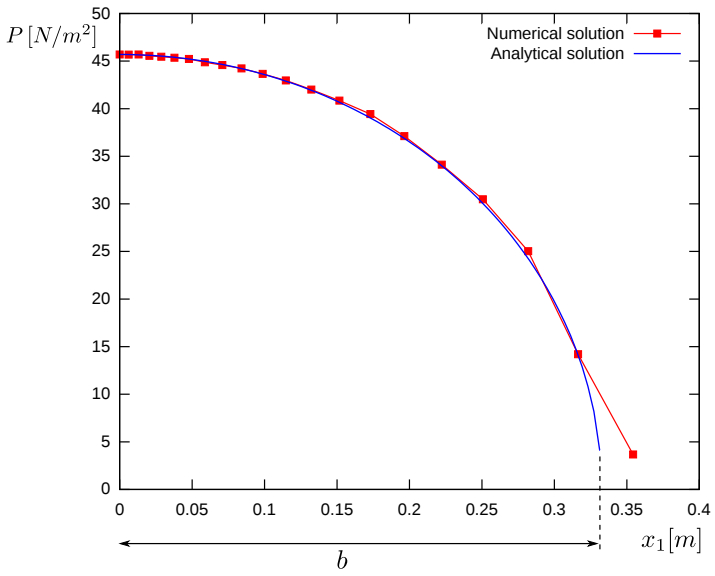

Figure 4.23: Signorini problem - Contact pressure distribution with Hertz solution. Comparison between numerical and analytical solution.

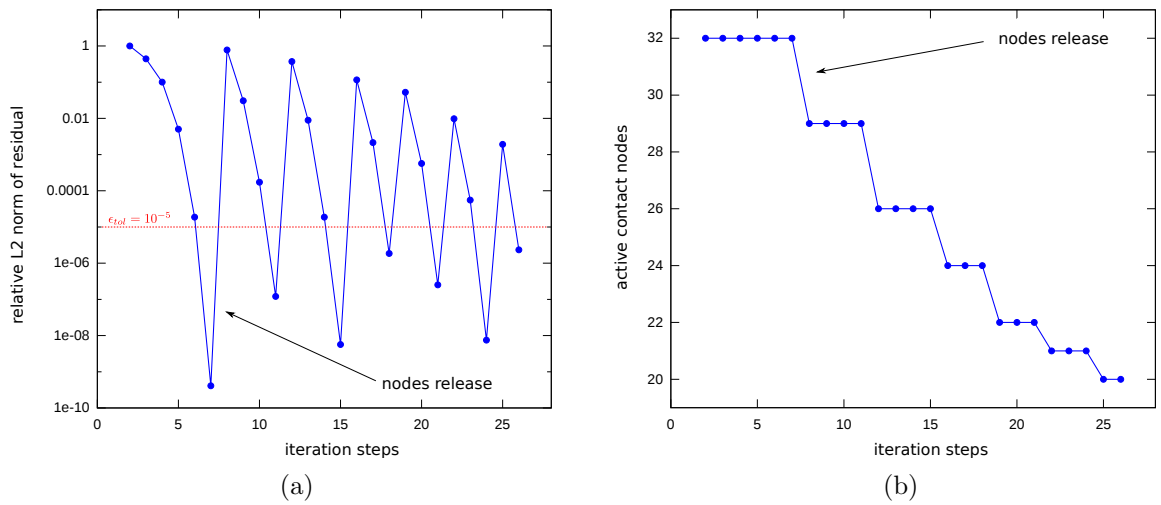

Figure 4.24: Signorini problem - (a) Convergence behaviour of the contact algorithm in terms of the relative L^2 norm of the displacements increment. (b) Convergence behaviour of the active contact zone.

4.5.2.2 Indentation parallel benchmark - 2D

We now solve a 2D frictionless indentation problem which consists of a rounded-head rigid indenter and a deformable square block. The physical model of this problem is shown in Fig. 4.25. The dimensions of the rigid indenter are: $h_i = 0.5\,m$, $w_i = 1.2\,m$ and $r_i = 0.75\,m$, while the vertical displacement imposed to the indenter along the vertical direction is $\delta = 0.15\,m$. The dimensions of the deformable block are $h_b = 0.5\,m$ and $w_b = 1.6\,m$. We consider a Neo-Hookean material model and finite strains for the block, with material properties $E_b = 6.896\,e{+}8\,N/m^2$ and $\nu_b = 0.32$. The relative position of the indenter with respect to the block is given by $a_x = 0.2\,m$ and $a_y = 0.025\,m$. For the bottom of the block, we fix the displacements in all directions.

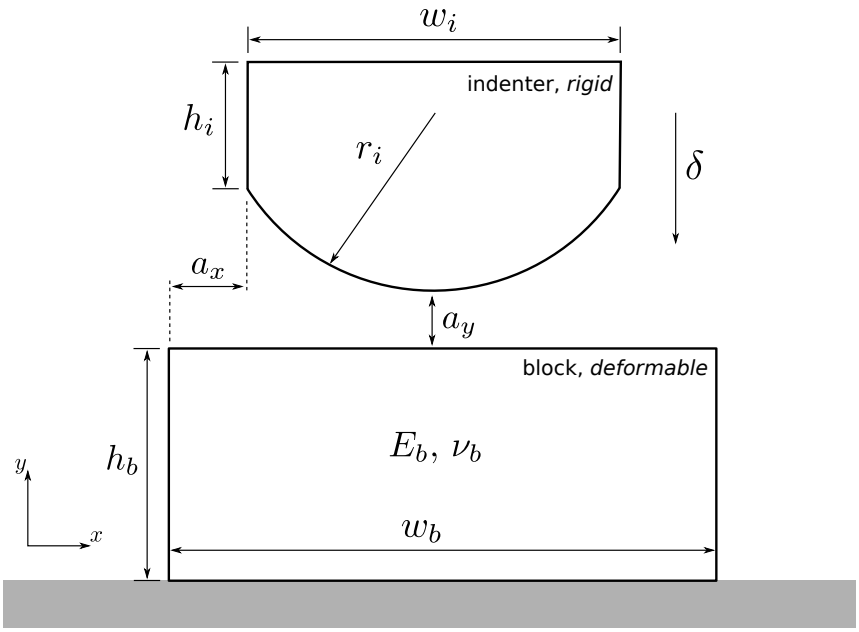

Figure 4.25: 2D INDENTATION PROBLEM - PHYSICAL MODEL.

In order to show that the algorithm is capable of solving unilateral contact problems in parallel, we solve this problem with the Alya code after partitioning the block mesh in eighteen subdomains. The serial execution gives exactly the same results as the parallel execution and therefore won't be considered for the rest of this example. The block mesh and the distribution of subdomains used in this problem are shown in Figs. 4.26a and 4.26b, respectively. To compare the results, we solve the same problem using the same mesh with Code_Aster [31], which is an open source code for civil and structural engineering finite element analysis. It was originally developed as an in-house code by the French company Électricité de France (EDF) and released as free software under the terms of the GNU General Public License in October 2001. Code_Aster uses contact elements derivated from a continuum formulation for the resolution of contact problems, by means of a monolithic scheme. As explained in previous chapters, this is a completely different approach to the one proposed in this thesis. The continuum formulation in which Code_Aster is based is called *Stabilized Lagrangian* [65], which allows to recover the classical cases of the computational contact mechanics literature (penalty, Lagrangian, Augmented Lagrangian) by a

wise choice of its parameters. The contact resolution in Code_Aster has been validated by several test cases, especially by the Hertz problem and the NAFEMS [81] benchmark contact problems. For this particular case, we use the Augmented Lagrangian formulation in Code_Aster.

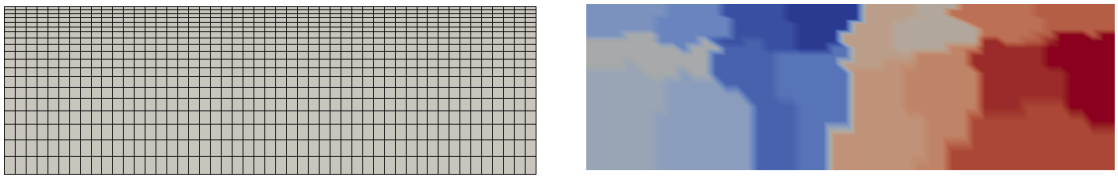

(a) (b)

Figure 4.26: 2D INDENTATION PROBLEM - (a) MESH USED FOR THE NUMERICAL SOLUTION. (b) DOMAIN DECOMPOSITION OF THE MESH USED BY ALYA CODE.

Fig. 4.27a shows the final deformed configuration obtained with Alya. On the other hand, Fig. 4.27b shows a mesh superposition in order to compare the final deformed configurations obtained with both codes. We observe a very good agreement in the results.

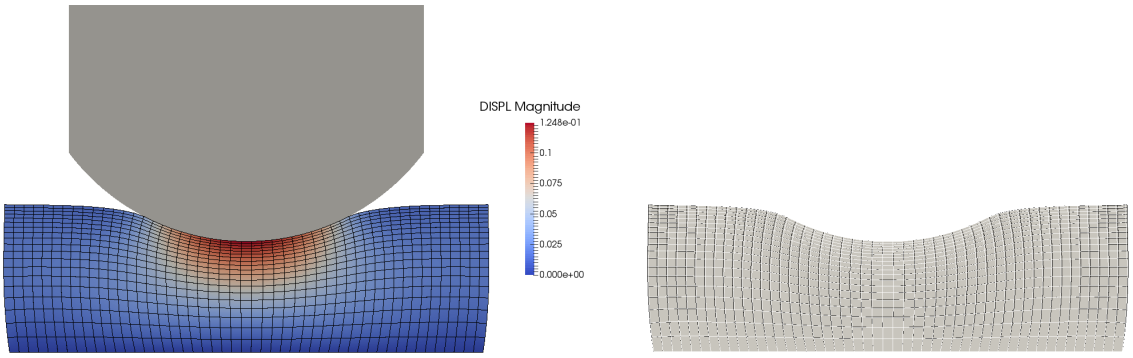

(a) (b)

Figure 4.27: 2D INDENTATION PROBLEM - (a) FINAL DEFORMED CONFIGURATION OBTAINED WITH ALYA. (b) MESH SUPERPOSITION - BLACK LINES: ALYA MESH; WHITE LINES: CODE_ASTER MESH.

In Figs. 4.28a and 4.28b we compare the results of Alya against Code_Aster for the y and x displacement of the contact boundary, respectively. In Fig. 4.28c we show a comparison of the contact forces along the contact boundary. Considering the small scale of the vertical axis in Fig. 4.28b, we can conclude that not only the qualitative behaviour of the contact boundary is very well captured, but also the absolute values are very close between the two models. We would like to emphasize that in this example we are comparing results obtained with two completely different apporaches for the numerical resolution of contact problems. However, the small differences observed in Fig. 4.28c can be associated to the fact that Code_Aster uses the Simo-Miehe model [124] for finite strains, while Alya has implemented a Total Lagrangian formulation based on the principle of virtual displacements (see [29, 9]). Finally, as serial and parallel results obtained with Alya code perfectly match, we validate the parallel implementation of the proposed algorithm.

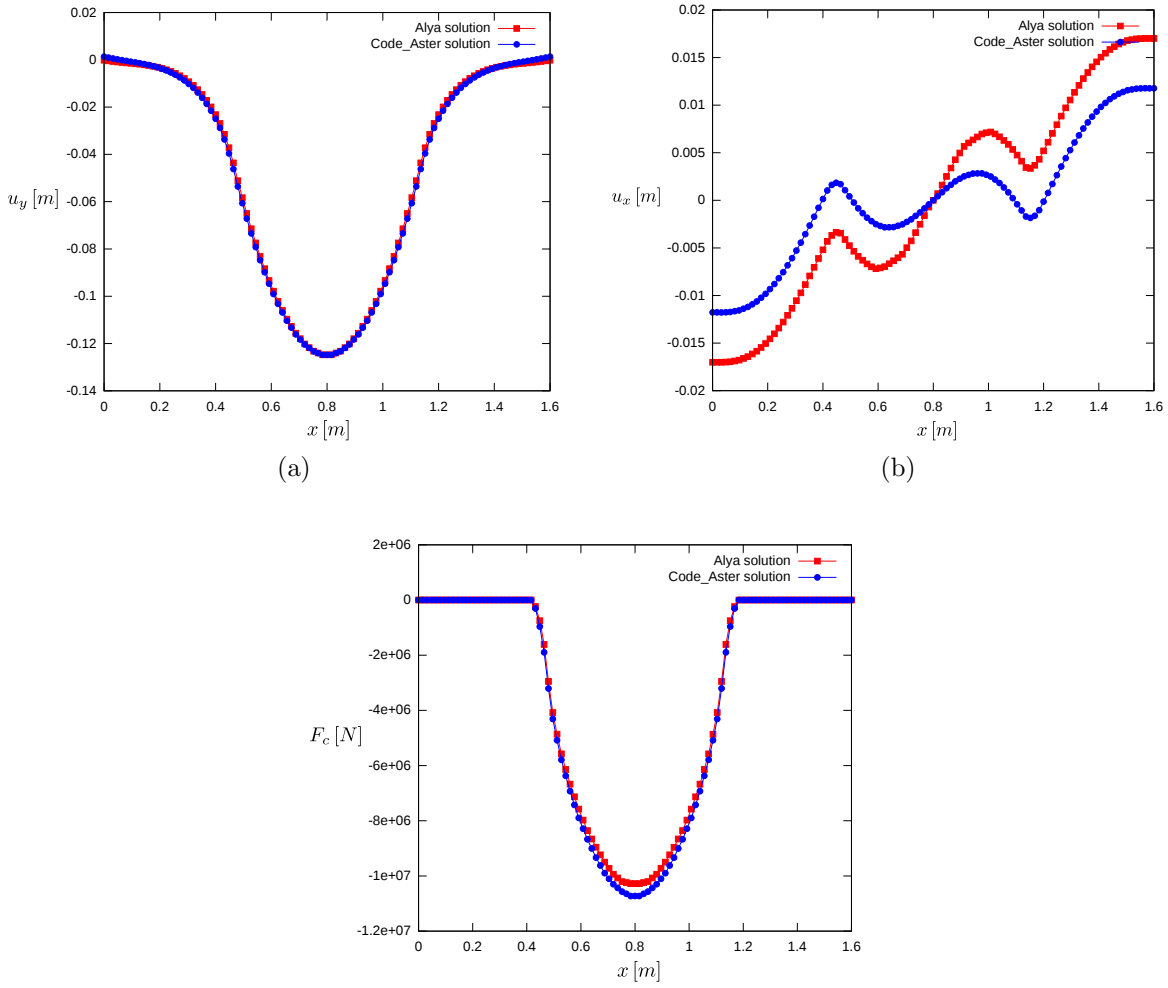

Figure 4.28: 2D INDENTATION PROBLEM - (a) VERTICAL DISPLACEMENT OF NODES ALONG THE CONTACT BOUNDARY. (b) TANGENTIAL DISPLACEMENT OF NODES ALONG THE CONTACT BOUNDARY. (c) CONTACT FORCE ON EACH NODE ALONG THE CONTACT BOUNDARY.

As explained in Sec. 4.4.2.1, the unilateral contact algorithm projects the penetrated nodes of the deformable body to the rigid body's contact boundary in a specific direction. In a quasi-static or dynamic evolution, the projected nodes are those which correspond to the deformed configuration of the previous time step, as Multi-Point Constraints are enforced in the deformed configuration. The direction of projection can be a fixed or a particular value for each node. From a general viewpoint, the sensibility of the algorithm to this value depends mainly on the time step which determines the displacement increments and also, on the curvature and refinement of the contact boundary of the deformable body. In order to evaluate the sensibility of the algorithm to the direction of projection, we solve this example as a quasi-static evolution, in which we apply 40 equispaced displacement increments until reaching the desired total displacement δ. We test three different alternatives for the direction of projection: 0^o, 25^o and 45^o, where these angles are measured with respect to the vertical axis y. These are fixed values for each contacting node. In Fig. 4.29 we show the tangential displacement of nodes along the contact boundary obtained with each of these directions. On the other hand, for the vertical displacement and contact forces

we do not observe any appreciable differences.

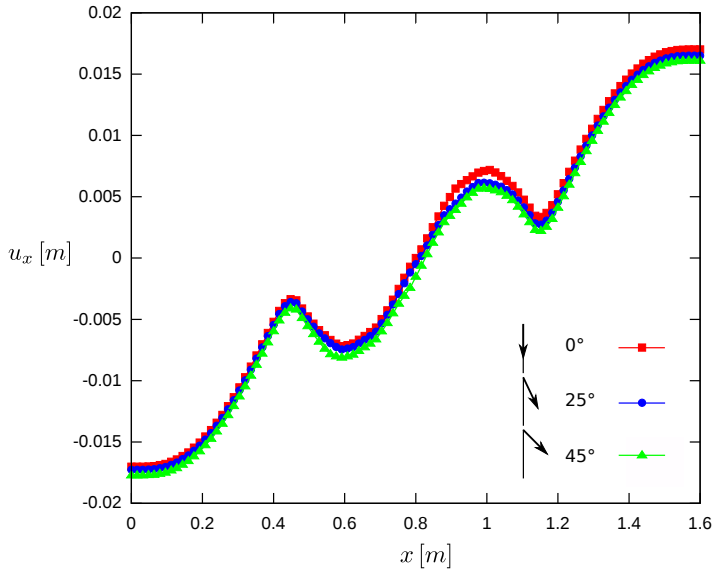

Figure 4.29: 2D INDENTATION PROBLEM - TANGENTIAL DISPLACEMENT OF NODES ALONG THE CONTACT BOUNDARY FOR DIFFERENT DIRECTIONS OF PROJECTION.

4.5.2.3 Frictional case: uniaxial compression test - 2D

In this example we consider a simple 2D frictional problem where a rigid punch compresses a rectangular shaped deformable body. The bottom part of the deformable body is fixed to the rigid foundation. Only its upper part is able to move tangentially along the rigid punch. Fig. 4.30 shows the physical model for this problem.

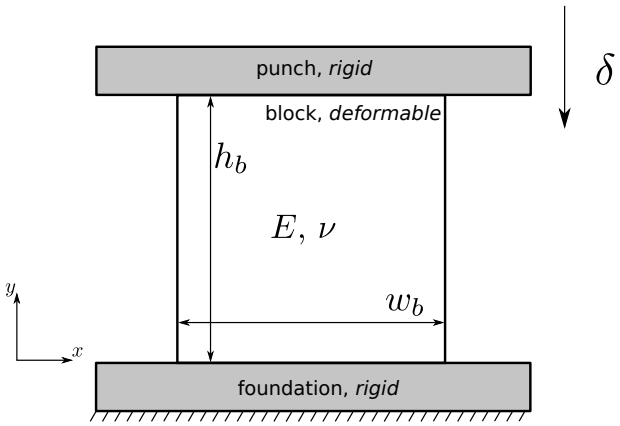

Figure 4.30: Frictional case 2D - Physical model.

We assume an isotropic linear elastic model for the deformable block of dimensions $h_b = 0.5\,m$ and $w_b = 0.4\,m$, and material properties $E = 6.896\,e{+}8\,N/m^2$ and $\nu = 0.32$. The total vertical displacement imposed to the rigid punch is $\delta = 0.09\,m$. We solve this contact problem for four different frictional situations ($\mu = 0.0$, $\mu = 0.08$, $\mu = 0.09$ and $\mu = 0.1$) between the deformable block and the rigid punch. For comparison purposes we solve the same set of problems using Code_Aster.

In Fig. 4.31 we compare the x (tangential) displacement of the nodes located at the contact boundary of the deformable block and the rigid punch. Fig. 4.31a shows the x displacements for a frictionless case ($\mu = 0.0$) and a frictional case with $\mu = 0.08$. On the other hand, Fig. 4.31b shows the x displacement for two different frictional cases with $\mu = 0.09$ and $\mu = 0.1$, respectively.

Finally, in Fig. 4.32 we show the final deformation state for the frictionless case and for a frictional case with $\mu = 0.1$. We note that the contact algorithm implemented in Alya is able to capture the behaviour of the contact boundary with high senstivity, as it is observed in the comparisons of the several frictional cases that were evaluated in this example.

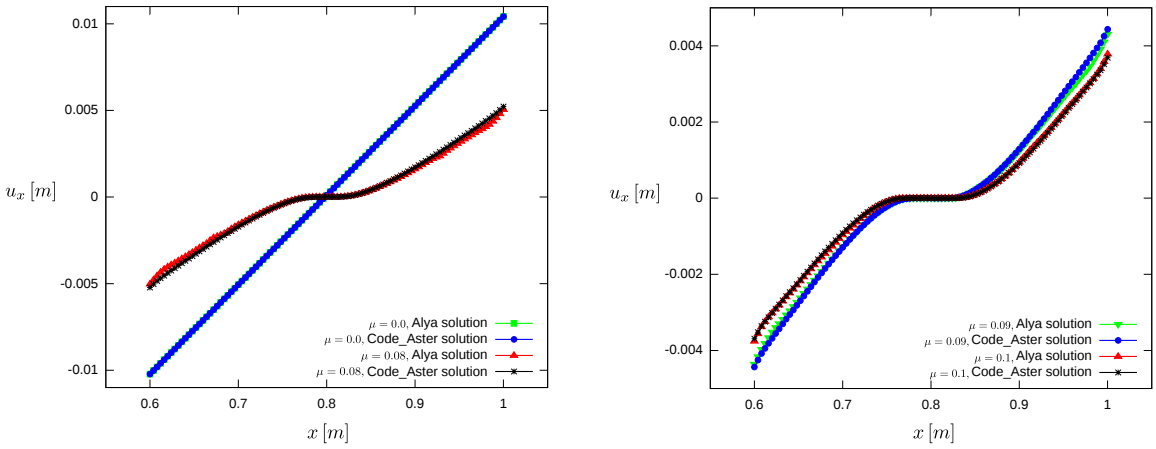

(a) (b)

Figure 4.31: Frictional case 2D - (a) Comparison of tangential displacements along the contact boundary of the frictionless case and a frictional case with $\mu = 0.08$. (b) Comparison of tangential displacements along the contact boundary of two frictional cases with $\mu = 0.09$ and $\mu = 0.1$ respectively.

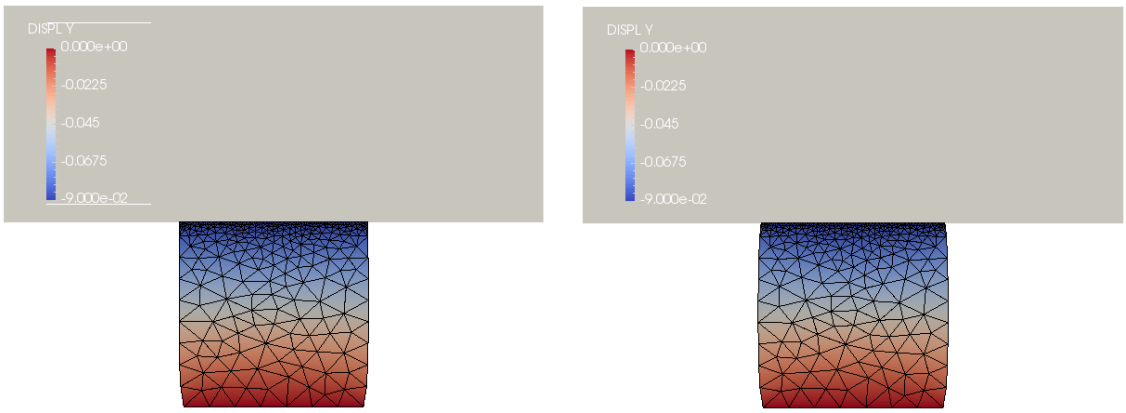

(a) (b)

Figure 4.32: Frictional case 2D - (a) Final deformation state of the frictionless case ($\mu = 0.0$). (b) Final deformation state of the frictional case for $\mu = 0.1$.

4.5.2.4 Hertzian contact: sphere on a flat rigid plate - 3D

In this example we solve the 3D Hertz contact problem which consists of an elastic ball that contacts with a rigid planar foundation. We consider an sphere of radius $R = 8\,m$ and material properties $E = 200\,N/m^2$ and $\nu = 0.32$. The topmost node of the sphere is fixed while an upwards displacement $\delta = 0.05\,m$ is applied to the rigid foundation. As the implementation of the algorithm fully considers all nonlinearities, we choose the magnitude of the displacement imposed to the rigid foundation to be small in order to assume a small deformation hypotesis for the deformable body. The contact interaction is produced at the bottom part of the sphere and is assumed to be frictionless. The physical model for this example is shown in Fig. 4.33. Additionally, the problem setup, an exemplary mesh and an exemplary numerical solution for this problem are illustrated in Fig. 4.34.

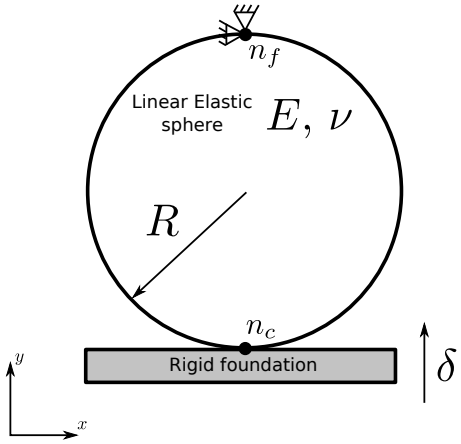

Figure 4.33: Hertzian contact 3D - Physical model.

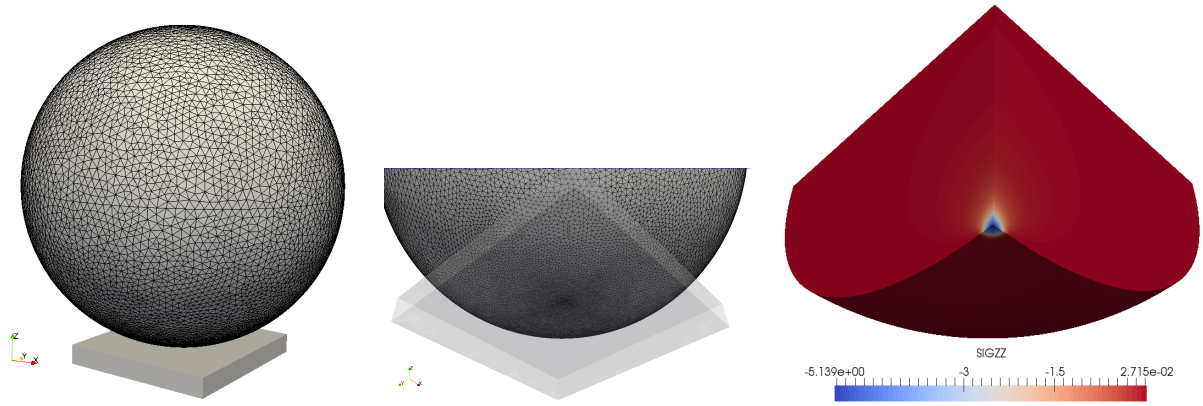

(a) (b) (c)

Figure 4.34: Hertzian contact 3D - (a) Problem setup and exemplary finite element mesh. (b) Exemplary mesh refinement at the contact zone. (c) An eighth of the deformed geometry and schematic normal stresses solution.

Analytical solutions for the contact traction distribution are well-known for Hertzian elastic contact problems. For this particular problem, the analytical solution is characterized via the

contact radius a:

$$a = \sqrt[3]{\frac{3Fd}{8}\frac{(1-\nu^2)}{E}}, \tag{4.40}$$

where F is the reaction force at the fixed node and d is the diameter of the sphere, and the maximum normal contact traction P_{max} given by [27, 13]:

$$P_{max} = \frac{3F}{2\pi a^2}. \tag{4.41}$$

We solve the contact problem and compute numerically the reaction force F at the fixed node n_f (see Fig. 4.33). This result is illustrated in Fig. 4.35 for different mesh sizes. On the x axis we represent the mesh size multiplication factor. The starting point for the resolution of this problem is a reference mesh of 32198 elements while the finer mesh used here has approximately 14.5 times more elements (465603).

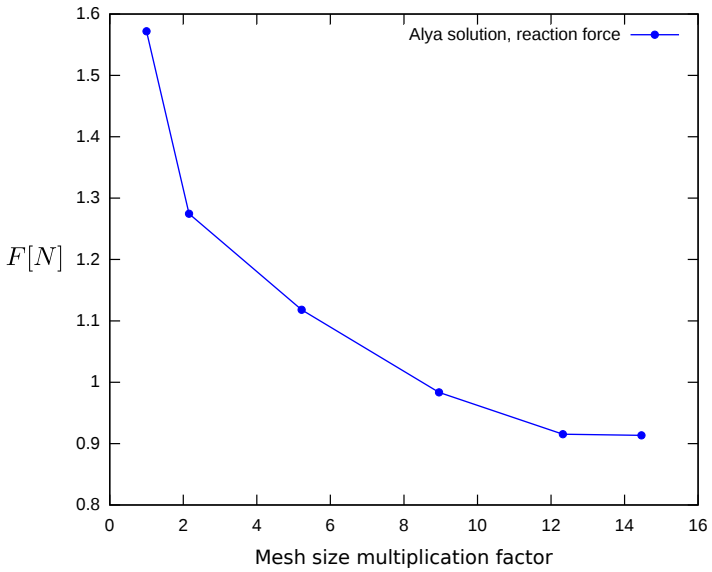

Figure 4.35: HERTZIAN CONTACT 3D - REACTION FORCE F AT NODE n_f FOR DIFFERENT MESH SIZES.

Using the converged value of F ($F = 0.913\,N$) in Eqs. (4.40) and (4.41), we compute the analytical solutions for a and P_{max} to obtain $a = 0.292\,m$ and $P_{max} = 5.11\,N/m^2$. In Fig. 4.36 we graphically compare the analytical solution for the contact radius and the contact zone determined by the simulation with the finer (converged) mesh. Despite the irregular discretization, it can be clearly observed the well-resolved circular shape of the contact zone. Furthermore, a good agreement of the numerical solution with the analytical solution for the contact radius a is visually confirmed.

Finally, in Fig. 4.37 we show the simulated contact pressure distribution at the contact zone for the converged mesh (see Fig. 4.36b). As expected, the point of maximum contact pressure is located at the bottom part of the sphere, on the axis of rotation. The contact pressure at this node gives $P_{sim_{max}} = 5.10\,N/m^2$, which differs from the analytical value in 0.2%.

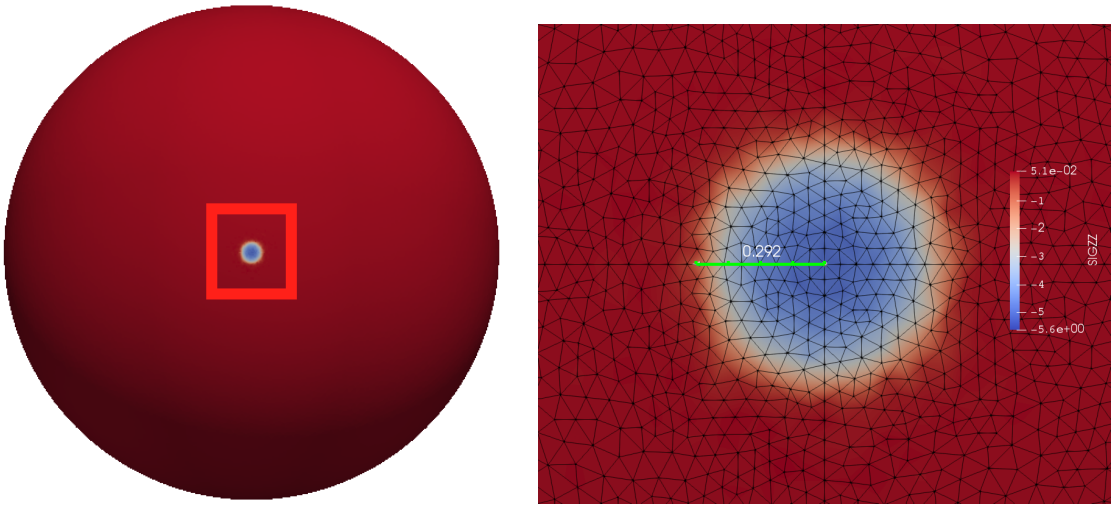

(a) (b)

Figure 4.36: Hertzian contact 3D - (a) Vertical view of the sphere and the zoom area. (b) Zoom in on the contact zone. Comparison of analytical (green line) and numerical solutions for the contact radius a - converged mesh.

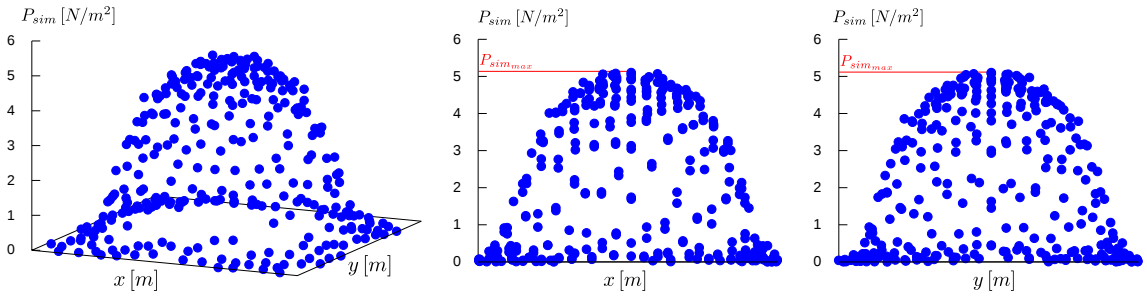

Figure 4.37: Hertzian contact 3D - Simulated contact pressure distribution at the contact zone - converged mesh.

4.5.2.5 Indentation parallel benchmark - 3D

This example problem solves a 3D frictionless indentation test, which consists of a rounded-head rigid indenter and a deformable beam. The physical model for this problem is shown in Fig. 4.38. The rigid indenter is characterized by $r_i = 1\,m$ and $d_i = 0.5\,m$, and the deformable beam by $h_b = 0.25\,m$, $w_b = 1.5\,m$ and $d_b = 0.3\,m$. The relative position of the indenter with respect to the beam is given by $a_x = 0.25\,m$ and $a_z = 0.1\,m$. We consider a Neo-Hookean material model and finite strains for the beam, with material properties $E_b = 6.896\,e{+}8\,N/m^2$ and $\nu = 0.32$. The vertical displacement imposed to the indenter along the vertical y axis is $\delta = 0.1\,m$, while the bottom part of the beam is fixed in all directions. We assume that there is no separation between the indenter and the beam (gap $= 0\,m$) at the beginning of the simulation ($t = 0\,s$).

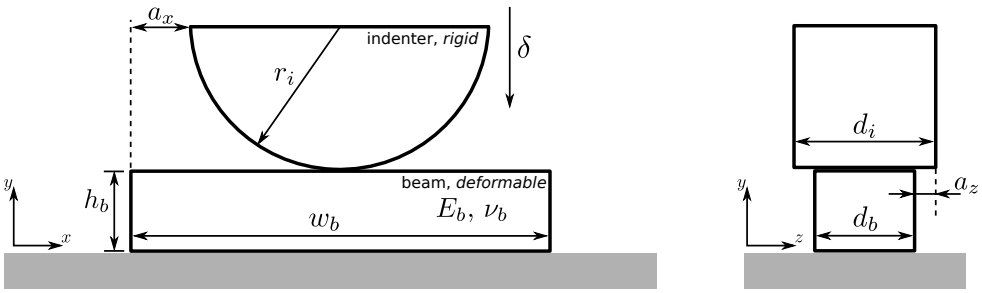

Figure 4.38: 3D indentation problem - Physical model.

To test the 3D parallel behaviour of the algorithm we solve this problem with the Alya code after partitioning the beam mesh in 12 subdomains. These results are equivalent to those obtained in a serial execution, thus showing a proper implementation of the parallel method for the 3D case. The block mesh and the domain decomposition of the mesh are shown in Figs. 4.39a and 4.39b, respectively. It is important to remark that the contact zone shares several subdomains.

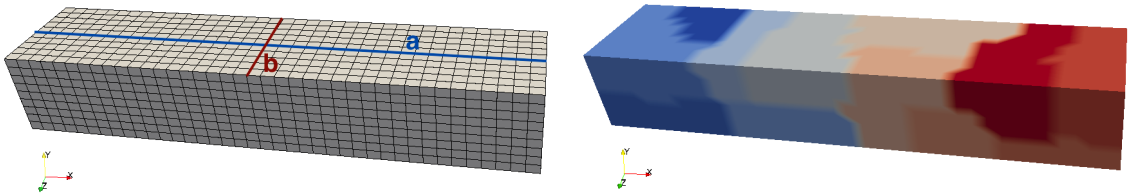

(a) (b)

Figure 4.39: 3D indentation problem - (a) Mesh used for the numerical solution and paths used for post-process of results. (b) Domain decomposition of the mesh used for this problem.

In Figs. 4.40a and 4.40b we show the final deformed configuration computed with Alya.

To compare our results we solve the same problem with Code_Aster. Figs. 4.41a and 4.41b shows a comparison of the vertical and tangential displacement of the nodes located along a path which goes from $(-0.75; -0.02; 0.25)$ to $(0.75; -0.02; 0.25)$, which corresponds to the central

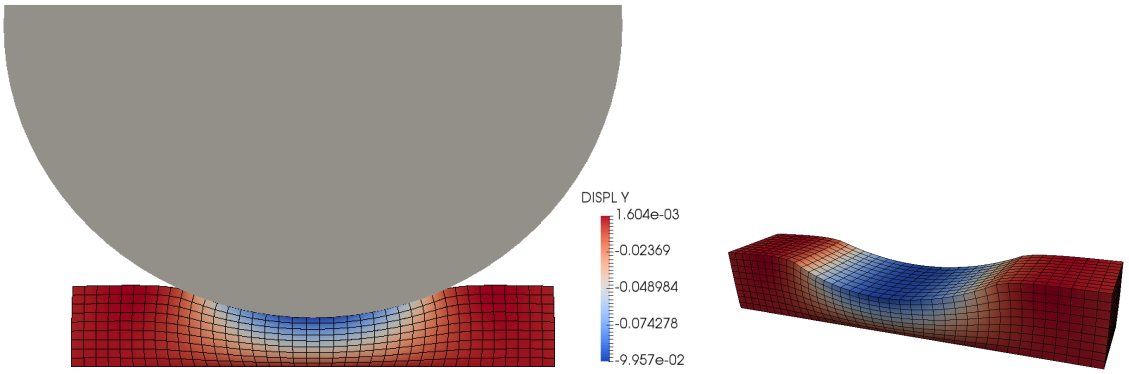

(a) (b)

Figure 4.40: 3D INDENTATION PROBLEM - (a) FINAL DEFORMED CONFIGURATION: BEAM-INDENTER SYSTEM. (b) FINAL DEFORMED CONFIGURATION: BEAM.

longitudinal axis of the beam at the contact surface (path a in Fig. 4.39a). Fig. 4.41c shows a comparison of the contact forces at each node of this path.

On the other hand, Fig. 4.42a shows a comparison of the tangential displacement of the nodes located along a path which goes from $(0.0; -0.02; 0.1)$ to $(0.0; -0.02; 0.3)$ (path b in Fig. 4.39a) while Fig. 4.42b shows a comparison of the contact forces at each node of this path.

In overall, we observe a very good agreement of the results. Taking into account that we are comparing two completely different approaches for the resolution of unilateral contact problems which can explain the small differences observed in Figs. 4.41b and 4.42a, the behaviour of the contact boundary is very well captured with the proposed parallel algorithm. Furthermore, small differences observed in Figs. 4.41c and 4.42b can be associated to the different formulations used in Alya and Code_Aster for finite strains, as mentioned in Sec. 4.5.2.2.

Trace analysis Execution traces are one of the main solutions for measurement and analysis of program performance on parallel computers. Traces are basically space-time diagrams that show how a parallel execution unfolds over time. They are analyzed *post-mortem*, as they are built based on the information gathered during the program execution. In a trace, time lines for different MPI processes are stacked top to bottom. A MPI process activity over time unfolds left to right. Each time line is composed of several colored segments, where each distinct color represent a different procedure, function or subroutine. Space-time visualization of MPI execution traces are very useful for spotting and understanding the temporal behaviour of the program, as they allow to graphically observe the work load balance among the different processors, the idle time for each processor, the time consumed for the execution of a given subroutine, the impact of inter-process communications, etc [129].

In Fig. 4.43 we observe the trace generated with the HPCToolkit [71] suite of an execution on *MareNostrum IV* supercomputer of the indentation parallel problem presented before. For the generation of this trace we have refined the beam mesh up to 224.600 elements. Also, 32 processors were employed for this simulation, each of them executing one MPI task: 1 processor is

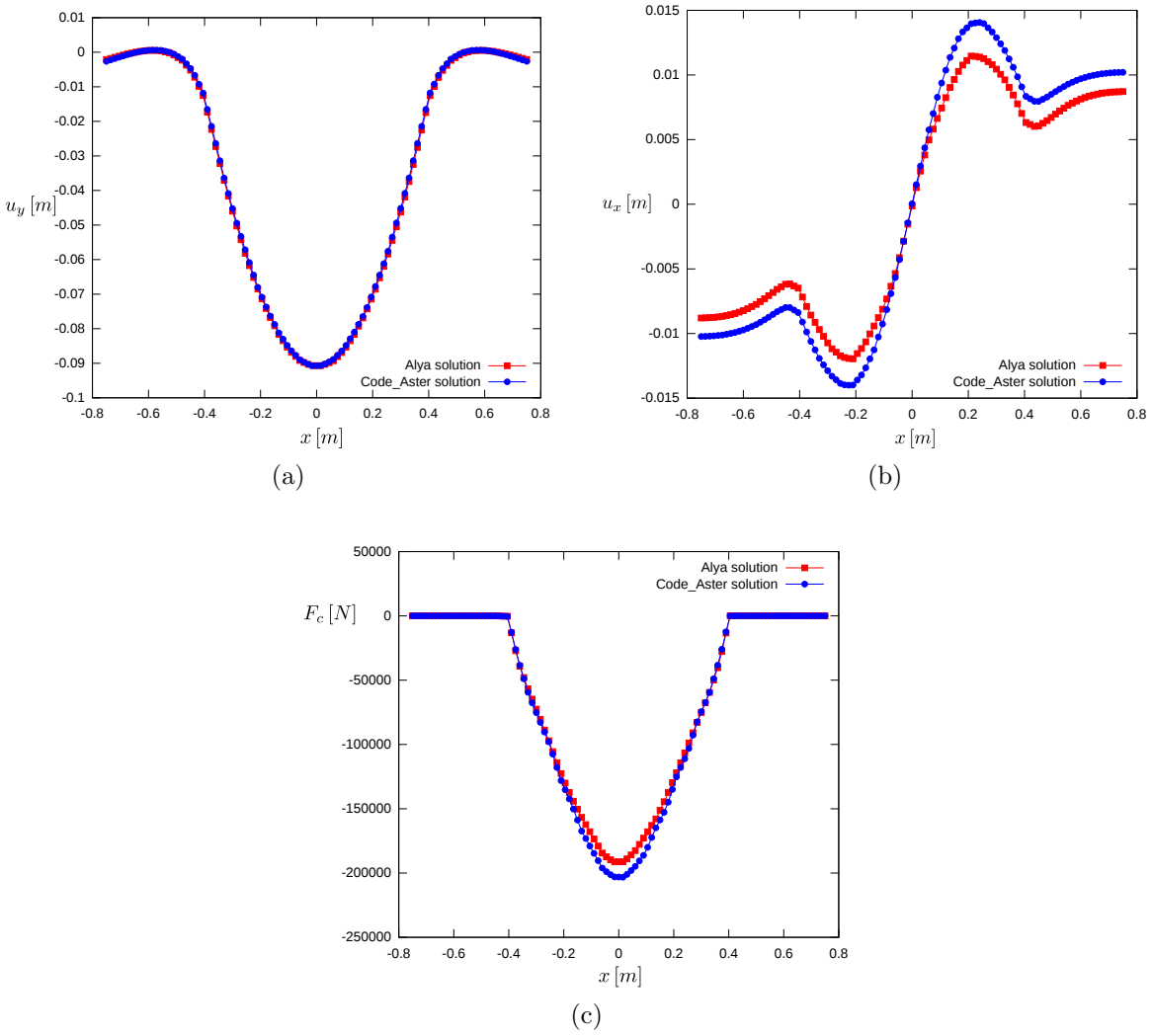

Figure 4.41: 3D INDENTATION PROBLEM - (a) VERTICAL DISPLACEMENT OF NODES AT PATH a. (b) TANGENTIAL DISPLACEMENT OF NODES AT PATH a. (c) CONTACT FORCE OF NODES AT PATH a.

dedicated to the rigid indenter while the 31 remaining processors are dedicated to the deformable beam. 5 time steps complete the full simulation.

Casual inspection of this trace shows five complete repetitons of a pattern, which represents a time step of the simulation. Therefore, matching this observation with the ideas introduced in Sec. 4.4.2 we can deduce that, from bottom to top, the first processor corresponds to the rigid indenter while the rest of the processors correspond to the deformable beam.

The orange color segments observed in the trace represent a running processor. More precisely, this means that the processor is solving the deformation of the body given the boundary conditions for that time step. On the other hand, the green color means that the processor is idle or executing another task non-related to the solution of the finite element problem as, for instance, the contact detection. The block/segregated execution observed in the trace (first the rigid body, then the deformable body) is, in fact, a reproduction of the Gauss-Seidel strategy adopted for the contact algorithm, which forces the processor dedicated to the rigid indenter to

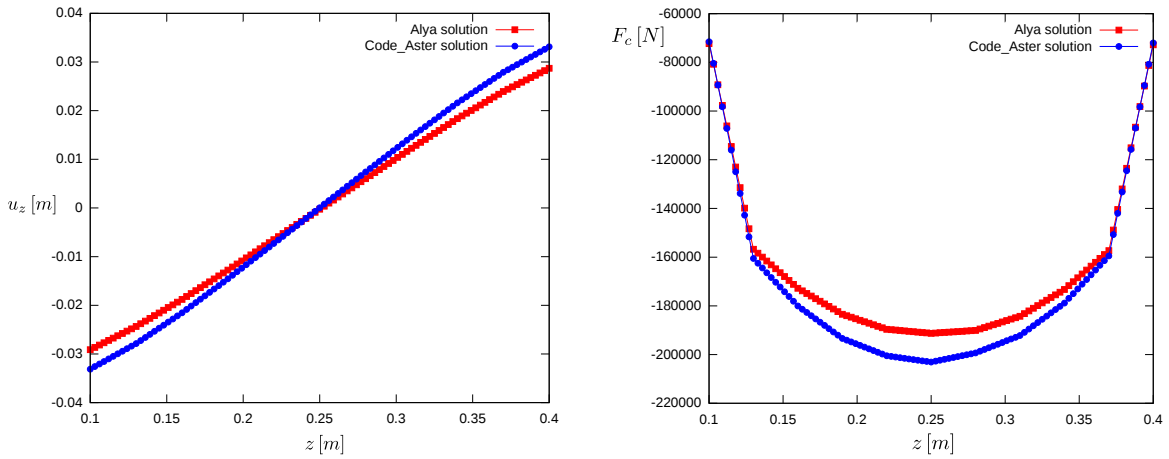

Figure 4.42: 3D INDENTATION PROBLEM - (a) TANGENTIAL DISPLACEMENT OF NODES AT PATH b. (b) CONTACT FORCE OF NODES AT PATH b.

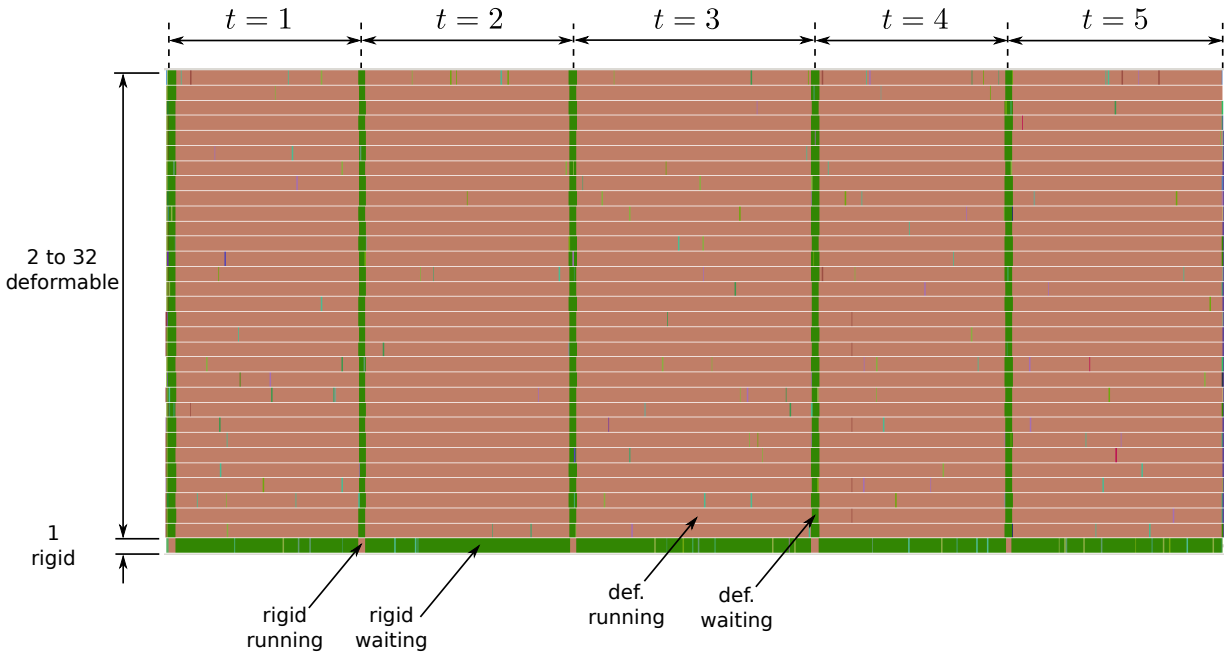

Figure 4.43: 3D INDENTATION PROBLEM - TRACE GENERATED FOR THE FULL SIMULATION (5 TIME STEPS) - 32 PROCESSORS, BEAM MESH OF 224600 ELEMENTS.

be idle when the remaining processors dedicated to the deformable beam are computing, and viceversa. From the observation of the trace we can also deduce that the work load is well balanced among the group of processors which belong to the deformable beam, as they start and finish its execution in a coordinated way. This means that all the computational resources are being used in an efficient way, as there is no waiting or idle time between processors when the deformable beam is computing.

In Fig. 4.44 we show a zoom in on the complete trace restricted to one time step. As mentioned in the previous paragraph, the orange color represents the solution procedure, which

doesn't take into account the localization task for contact detection performed by PLE++. As we can observe in Fig. 4.44, for this particular example the localization task has a small impact in the overall execution time, since the orange lines for the rigid indenter and the deformable beam processors seems to exactly match. Only a zoom in on the interval where the localization occurs allows to distinguish how the localization task affects the execution trace (see Fig. 4.45). As mentioned before, the fact that the localization has a negligible impact in the total simulation time can't be generalized without further analysis and it should be restricted only to the context of this particular example, as this impact strongly depends on the number of used processors. An increase in the number of processors involved in the localization implies more communications and operations, which can affect the execution time of the localization process. How the localization time impacts the overall simulation time as the number of processors increase is a key issue for further analysis.

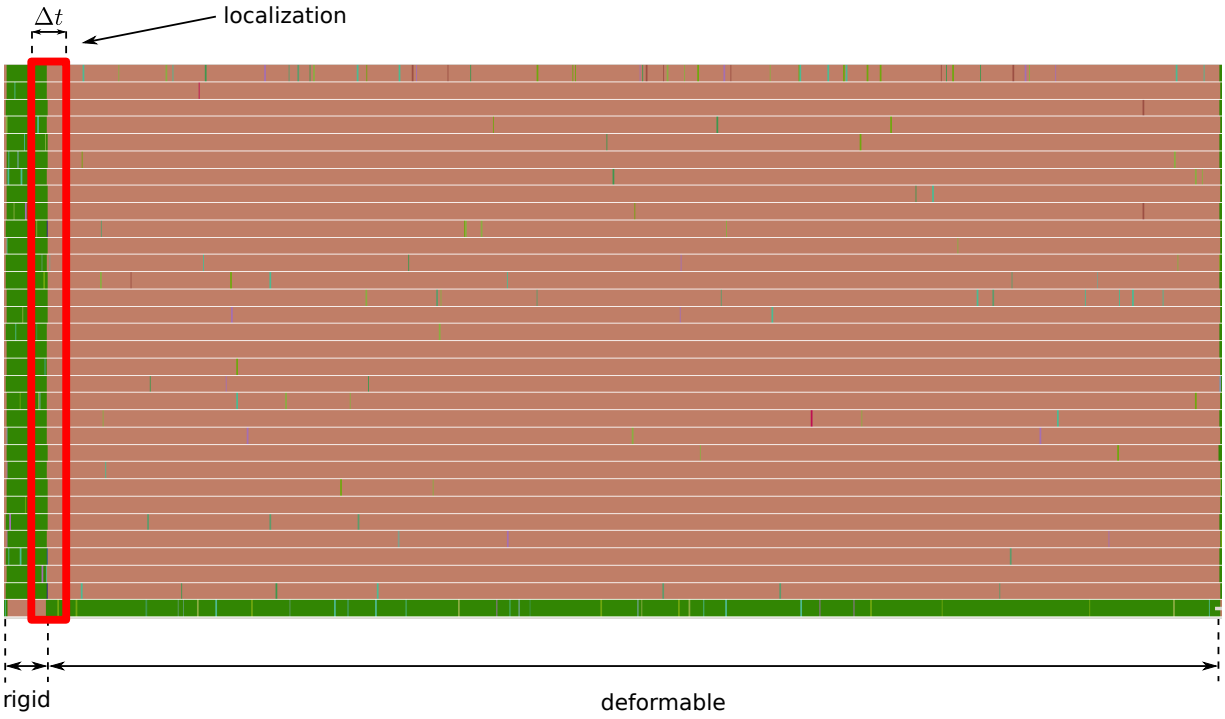

Figure 4.44: 3D INDENTATION PROBLEM - ZOOM IN ON THE TRACE: ONLY ONE TIME STEP IS SHOWN.

Figure 4.45: 3D INDENTATION PROBLEM - ZOOM IN ON THE TRACE: TIME INTERVAL WHERE THE LOCALIZATION OCCURS.

4.5.2.6 Frictional case: sliding of a cube on a rigid plane - 3D

A frictional sliding of a deformable cube on a rigid plane is solved in this example. We assume a Saint Venant-Kirchhoff material model for the deformable cube of side $l = 1\,m$ with material properties $E = 210\,N/m^2$ and $\nu = 0.3$. The physical model and the mesh used for this problem are shown in Fig. 4.46. The cube is moved towards the rigid plane along the vertical axis z and afterwards is moved along the plane, in the x-axis direction. Three different coefficients of friction between the cube and the plane are considered in this example: $\mu = 0.2, 0.5, 0.8$. Boundary conditions applied to the cube are defined by the following relations:

- $\delta_z = -0.05\,m \cdot t$, $0 < t \leq 1$; $\delta_z = -0.05\,m$, $1 < t \leq 3$
- $\delta_x = 0\,m$, $0 < t \leq 1$; $\delta_x = -1/6(t-1)\,m$, $1 < t \leq 3$

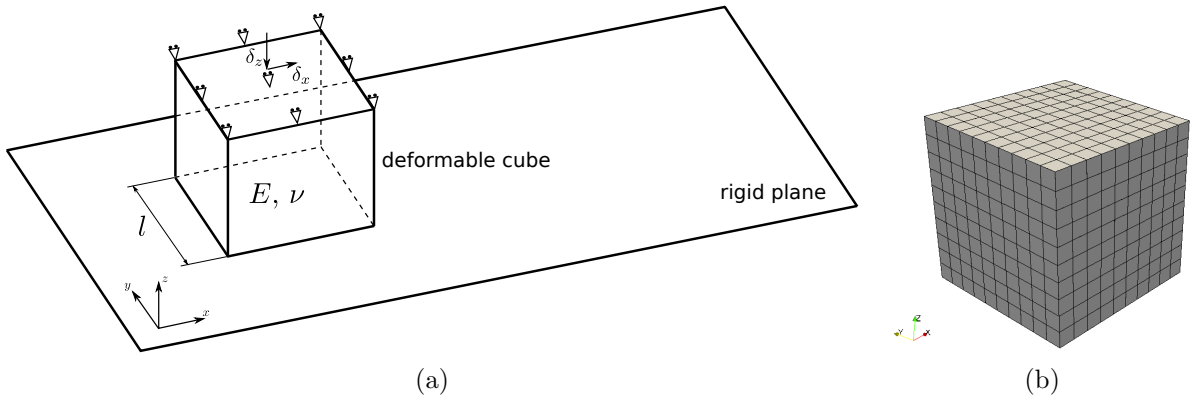

Figure 4.46: Frictional case 3D - (a) Physical model. (b) Cube mesh.

Deformed configurations and the corresponding shear stress σ_{xz} distributions are shown in Fig. 4.47 for the three considered coefficients of friction and time steps $t = 1, 2, 3$. We observe an expected qualitative behaviour, as the shear stresses increase for higher values of μ. Also, we observe further detachment of the contact surface for higher values of coefficients of friction and simulation time, as a consequence of higher frictional forces which oppose to the sliding of the cube. This detachment is observed in Fig. 4.48, where the deformed configuration of the contact surface for the different values of μ at $t = 2$ and $t = 3$ is shown. Finally, in Fig. 4.49 we show the frictional force F_{μ_x} distribution along the path (-0.5;0.0;0.0) – (0.5;0.0;0.0) for $t = 2$ and $t = 3$. We observe here that, as expected, frictional forces increase with the coefficient of friction μ. Additionally, for a given μ, we observe a reduction of the magnitude of the fricional forces as time evolves. This can be interpreted as a consequence of stress redistribution in the contact interface due to detachment.

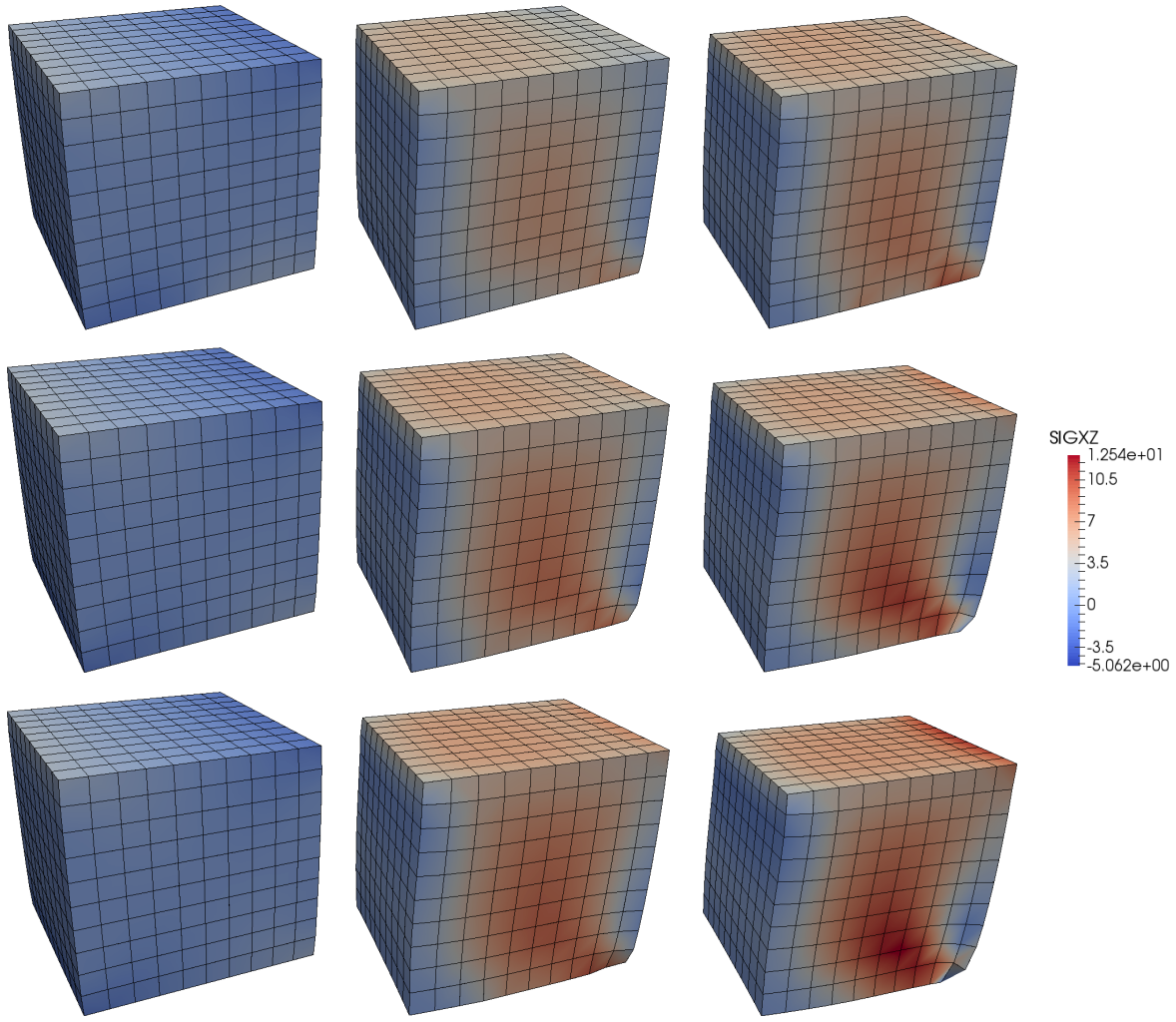

Figure 4.47: Frictional case 3D - Contour plots of shear stress σ_{xz} for different friction coefficients: $\mu = 0.2$ (top), $\mu = 0.5$ (middle), $\mu = 0.8$ (bottom) and time steps: (a) $t = 1$, (b) $t = 2$, (c) $t = 3$.

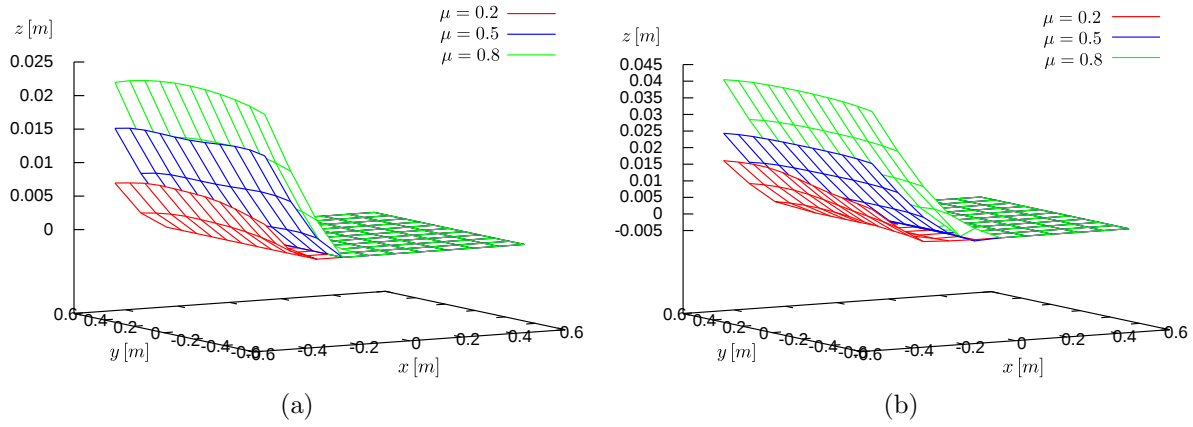

Figure 4.48: Frictional case 3D - Contact surface at (a) $t = 2$, (b) $t = 3$.

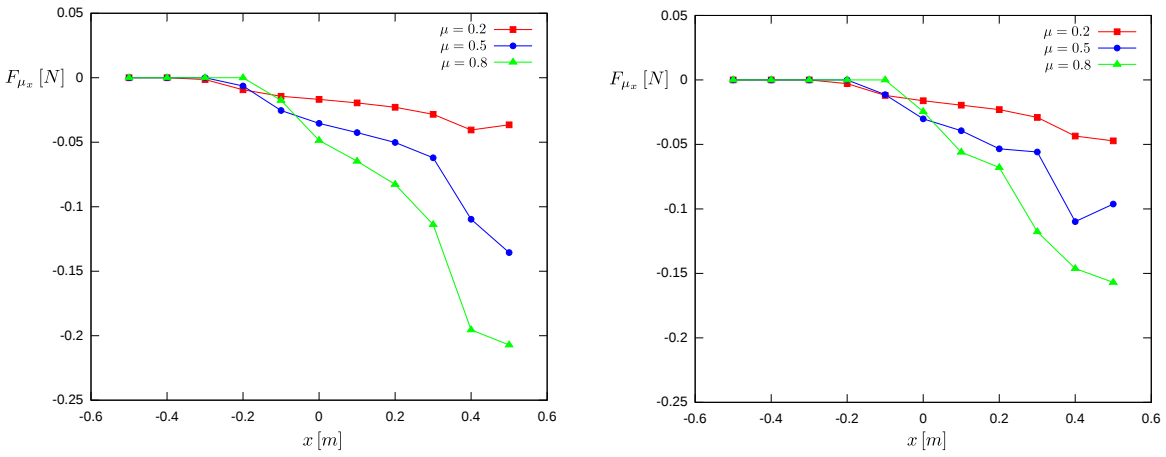

(a) (b)

Figure 4.49: Frictional case 3D - Frictional force along path (-0.5;0.0;0.0) – (0.5;0.0;0.0) at (a) $t = 2$, (b) $t = 3$.

4.5.2.7 Expansion of a tube and a rounded frame - 3D

This last example aims to demostrate that the proposed algorithm is able to manage more complex contact situation and is also able to capture non-constant displacements of the contact interface. The tailor-made example introduced here consists of a tube and a rounded frame, as shown in Fig. 4.50. The tube is fixed in one end while an inner pressure is applied in order to produce its expansion. On the other hand, the frame is situated closer to the non-fixed end of the tube and its base is fixed to the ground. No additional boundary condition is applied to the frame. For this problem we will consider four different scenarios for the contact interface between the tube and the frame: (a) frictionless, (b) $\mu = 0.03$, (c) $\mu = 0.04$ and (d) $\mu = 0.08$. We assume a Saint Venant-Kirchhoff material model for both tube and frame. In order to consider an unilateral contact problem, we suppose that the tube is much more rigid than the frame: $E_t >> E_f$, being E_t and E_f the Young's modulus of the tube and frame respectively. The dimensional parameters which characterize the model are the following: $E_t = 6.896\,e{+}7\,N/m^2$, $\nu_t = 0.32$, $E_f = 210\,N/m^2$, $\nu_f = 0.3$, $p_i = 7.0\,e{+}5\,N/m^2$, $r_t = 1\,m$, $t_t = 0.1\,m$, $h_t = 1.625\,m$, $t_f = 0.12\,m$, $d_{t_1} = 0.2\,m$, $d_f = 0.2\,m$ and $d_{t_2} = 0.6\,m$.

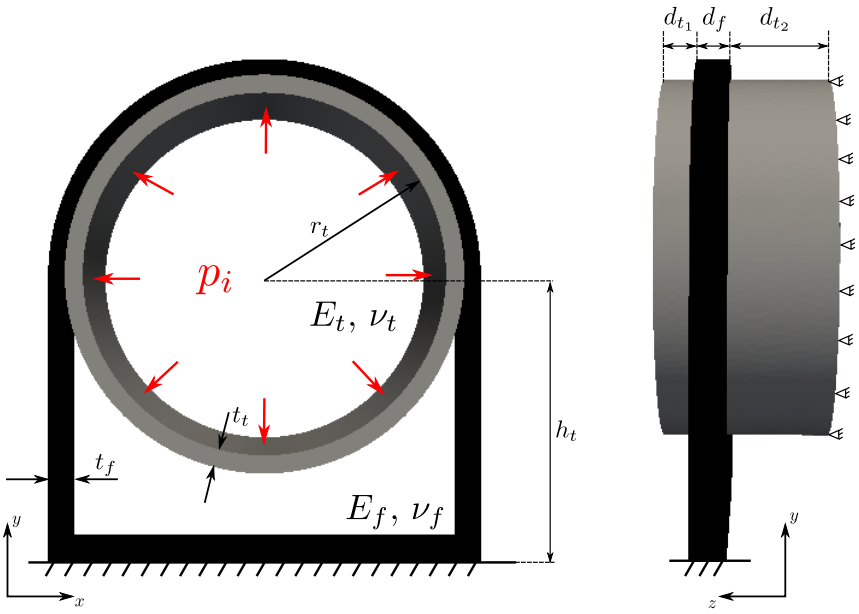

Figure 4.50: Expansion of a tube - Physical model.

In Fig. 4.51 we show the deformed configuration of the tube-frame system for four different time steps assuming a frictionless contact interface. Due to the initial position of the frame with respect to the tube, we observe that the frame slides along the tube while bending backwards. We also observe that this sliding is not constant, reaching its highest rate between $t = 6\,s$ and $t = 10\,s$. Fig. 4.52 shows the displacement along the axial direction (z-axis) of the uppermost nodes of the rounded frame over time for all the frictional situations considered in this example. As expected, we observe that the total sliding/displacement decreases when the coefficient of friction increases. Nevertheless, this relation is not linear. We also observe the sharp change in the rate of sliding mentioned previously between $t = 6\,s$ and $t = 10\,s$. It is worth remarking that the highest sliding rate seems to be equal, instead of smoother, for the frictionless and frictional

cases $\mu = 0.03$ and $\mu = 0.04$ but in different periods of time. We assume that this occurs due to a stress release or redistribution when the frame starts to slide at a higher rate. Finally, we observe that a threshold is reached at $\mu = 0.08$, where small sliding occurs. For bigger values of friction, the frame remains sticked to the tube along the complete simulation.

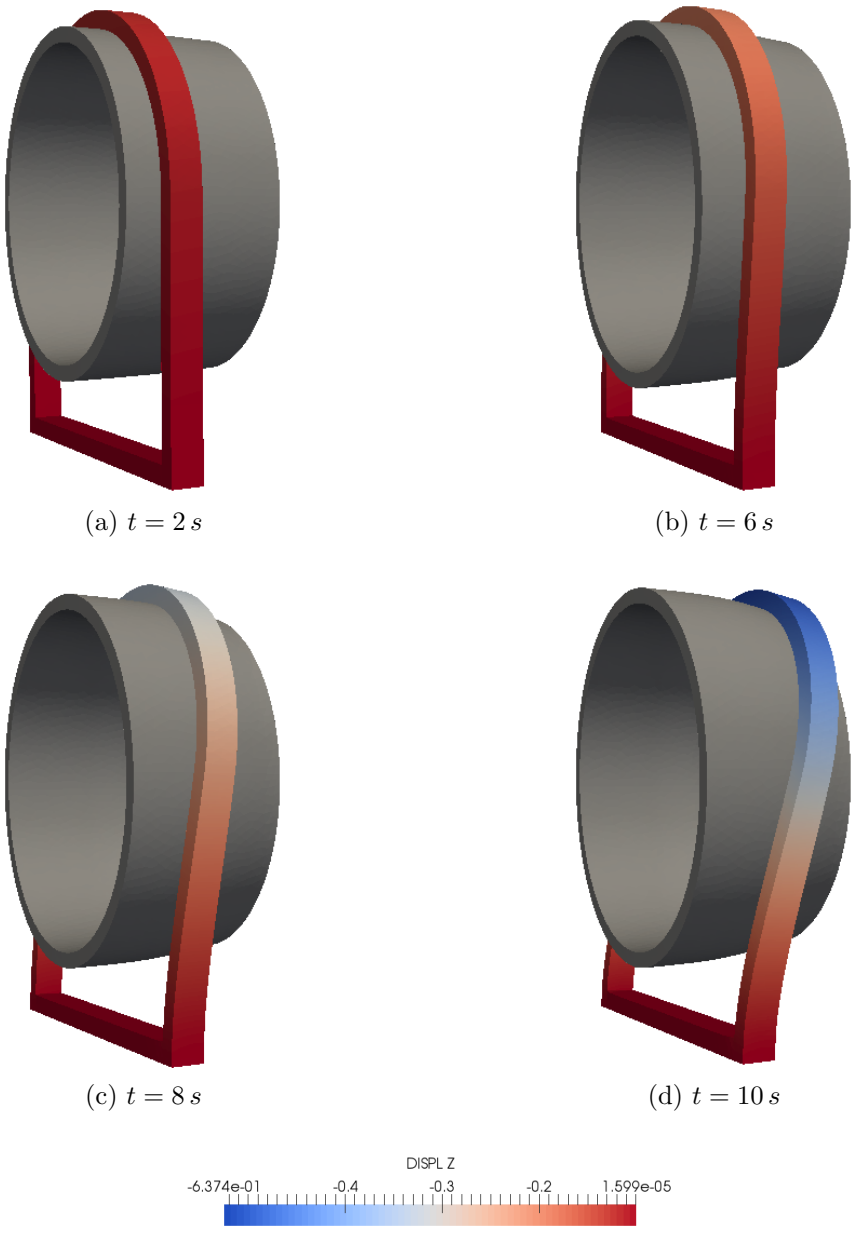

(a) $t = 2\,s$ (b) $t = 6\,s$

(c) $t = 8\,s$ (d) $t = 10\,s$

Figure 4.51: Expansion of a tube - Deformed configuration - Frictionless case.

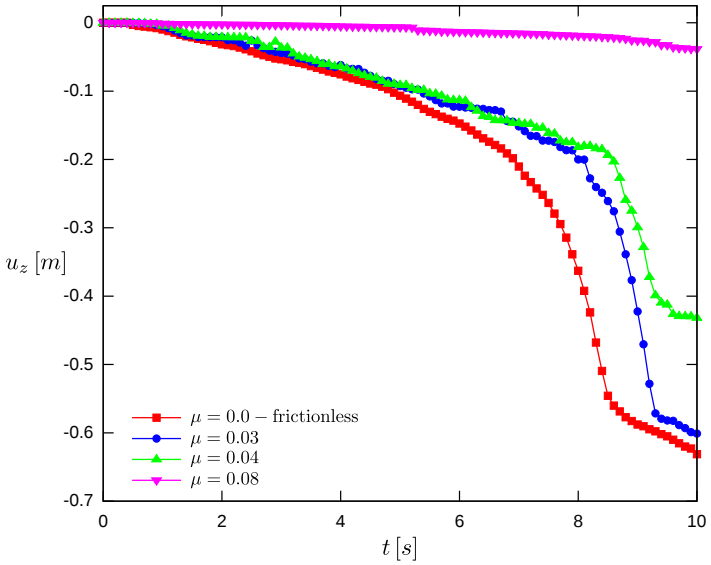

Figure 4.52: Expansion of a tube - Axial displacement of the rounded frame's uppermost nodes vs. time.

Chapter 5

A Parallel Method for the Two-Body Contact Problem

This chapter is devoted to the description of the proposed methodology for the parallel resolution of two-body contact problems and its numerical implementation. This novel methodology for solving contact problems in parallel arises as a combination of the *Method of partial Dirichlet–Neumann boundary conditions (PDN)* proposed in [142] and introduced in the previous chapter, and the *Contact algorithm of Dirichlet-Neumann type (CDN)*, developed in [84] and [85] and commented in [137]. The main idea of the PDN method is to impose partial Dirichlet-Neumann boundary conditions in order to enforce the geometrical and mechanical constraints given by the normal and frictional contact (i.e. contact conditions). Due to its nature, the PDN method can be integrated seamlessly in a parallelized finite element code. On the other hand, the CDN method employs a strategy in which the bodies coming into contact are treated separately. It is based on a nonlinear block *Gauss–Seidel* method as an iterative solver. From the engineering point of view, it can be interpreted as a *Dirichlet-Neumann* algorithm for the nonlinear contact problem. The basic idea in the CDN algorithm is that one applies on one body, which we call $\mathcal{B}^1$, the surface tractions which were computed from a unilateral contact problem for the other body, called $\mathcal{B}^2$, with a fixed deformed state of body $\mathcal{B}^1$. This idea will be further detailed in the following paragraphs.

5.1 Introduction

As explained in Sec. 4.1, the PDN method was introduced as a solution strategy for unilateral contact problems, i.e. a contact between a rigid surface and a deformable body. This method presents one relevant advantage in comparison with the standard formulations that uses penalty, Lagrange multipliers or Augmented Lagrangian method to impose the contact constrains: in the PDN method there is no need to evaluate the residual vectors and the tangent matrices for the implicit resolution scheme. Moreover, Lagrange multipliers and Augmented Lagrangian method increase the number of degrees of freedom by introducing Lagrange multipliers as dual unknowns.

In this sense, another advantage of the PDN method is the reduction of the number of unknowns, even compared with the penalty method, because the nodes over the contact surface are treated as Dirichlet or Newmann boundary nodes, where the boundary conditions are applied.

The CDN method was originally introduced as a new algorithm for the numerical solution of 2D contact problems between linear elastic bodies. The boundary data transfer at the contact zone is essential for the algorithm. In [85] the authors propose to apply a nonlinear block *Gauss–Seidel* method as an iterative solver which can be interpreted as a Dirichlet-Neumann type algorithm for the contact problem. In each iteration step, a linear Neumann problem and a Signorini problem (i.e. unilateral linear elastic contact) are solved (see Fig. 5.1). For the solution of the Neumann problem, the authors propose to use a standard multigrid technique. For the Signorini problem, as linear elasticity and small deformations are considered, the authors propose a novel monotone multigrid method where the boundary stress is formally introduced as a Lagrange multiplier.

The algorithm that we introduce in this chapter is based on a combination of the PDN and CDN methods and it is extended to nonlinear, 3D and parallel problems. Contrary to the strategy proposed in [85], where the authors employ a monotone multigrid method for the solution of the linear elastic Signorini problem, we use the PDN algorithm for the solution of the unilateral contact problem. The Neumann problem is solved using a standard iterative algorithm. Additionally, instead of using a dual basis Lagrange multiplier space for the coupling of the different bodies, we use PLE++ tool for the information exchange between the contacting bodies. This results in a general and robust contact algorithm, capable of solving linear or nonlinear problems and suitable for parallel computing. The use of PLE++ allows to solve each body separately, using different computational instances, as the transference of information is done through MPI. Furthermore, this algorithm can be employed as a black-box strategy, as it allows to solve each body separately even with different computational codes. This last feature allows to use different material models, element technology, damage models, etc, for each contacting body. From the parallel point of view, it avoids dynamic repartitioning due to sliding as no contact elements are used.

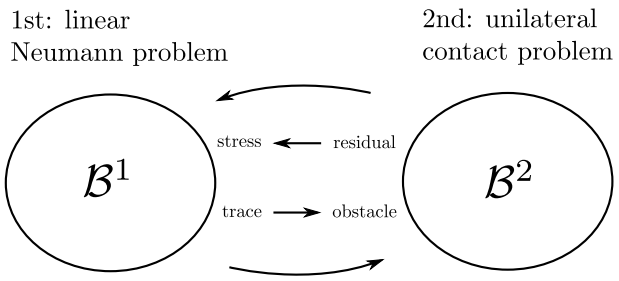

Figure 5.1: Dirichlet-Neumann coupling.

5.2 Contact algorithm of Dirichlet-Neumann type

As shown in Sec. 2.2, the contact problem can be written as a boundary value problem. Eq. (2.12) and the normal contact constraints in Eq. (2.18) can be particularized for the case of linear elasticity in small deformations. Thus, in addition to the equilibrium conditions in $\mathcal{B}^1$ and $\mathcal{B}^2$ and the boundary conditions on $\partial\mathcal{B}$:

$$\begin{aligned} -\sigma_{ij}(u)_{,j} &= f_i && \text{in} \quad \mathcal{B}^1 \cup \mathcal{B}^2, \\ u &= 0 && \text{on} \quad \Gamma_u, \\ \sigma_{ij}(u) \cdot n_j &= \sigma_n(u) = p_i && \text{on} \quad \Gamma_\sigma, \end{aligned} \tag{5.1}$$

we have the linearized normal contact conditions on Γ_c:

$$\begin{aligned} t &\geq (u_1)_n + (u_2)_n, \\ 0 &= ((u_1)_n + (u_2)_n - t) \cdot \sigma_n(u_1), \end{aligned} \tag{5.2}$$

where σ_{ij} is the Cauchy stress tensor, f_i are the external loads, u is the displacements field, p_i represents an external pressure and the function $t : \Gamma_c \in \mathbb{R}^d \to \mathbb{R}$ is the distance between the two bodies in normal direction taken with respect to the reference configuration [22]. Additionally, assuming a frictionless situation, we have the following equilibrium conditions at the contact interface (action-reaction principle or formally Newton's third law):

$$\sigma_n(u_1) = \sigma_n(u_2) \leq 0, \tag{5.3a}$$

$$\sigma_t(u_1) = \sigma_t(u_2) = 0. \tag{5.3b}$$

Eq. (5.3a) enforces the continuity of the projection of the stress tensor in the surface normal direction. On the other hand, Eq. (5.3b) imposes the non-frictional condition.

The discretization of the equilibrium conditions given by Eq. (5.1) for the complete system $\mathcal{B}^1 \cup \mathcal{B}^2$ using the Finite Element Method, gives the following linear system of equations for the nodal displacements $\mathbf{u}$ (see [145] for more details):

$$\mathbf{K}\,\mathbf{u} = \mathbf{P}, \tag{5.4}$$

where $\mathbf{K}$ is the stiffness matrix and $\mathbf{P}$ is the load vector of the system $\mathcal{B}^1 \cup \mathcal{B}^2$.

The contact algorithm of Dirichlet-Neumann type developed in [85] is described in Algorithm 8 for the case of a linear elasticity problem with constant stiffness matrices $\mathbf{K}^1$ and $\mathbf{K}^2$, and given load vectors $\mathbf{P}^1$ and $\mathbf{P}^2$ for bodies $\mathcal{B}^1$ and $\mathcal{B}^2$, respectively. This algorithm is taken as a frame of reference for the methodology introduced in this chapter.

Algorithm 8 Dirichlet-Neumann type contact algorithm

1: set initial values: $\mathbf{v}_0 = 0$, $\mathbf{t}_0 = 0$
2: **for** m = 1,2,..., until convergence **do**
3: solve Neumann problem: $\mathbf{K}^1\,\mathbf{u}^1_{m+1} = \mathbf{P}^1 - \mathbf{t}_m$
4: transfer displacements: $\mathbf{v}_{m+1} = (1-\omega_D)\,\mathbf{v}_m + \omega_D\,\mathbf{Q}\,\mathbf{u}^1_{m+1}$
5: solve unilateral contact problem: $\frac{1}{2}\mathbf{u}^{2\,T}_{m+1}\,\mathbf{K}^2\,\mathbf{u}^2_{m+1} - \mathbf{u}^{2\,T}_{m+1}\,\mathbf{P}^2 \rightarrow MIN$
6: subject to: $\mathbf{N}^1(\mathbf{v}_{m+1})\,\mathbf{u}^2_{m+1} + \mathbf{G}^1_X(\mathbf{v}_{m+1}) \geq 0$
7: compute residual: $\mathbf{R}^2_{m+1} = \mathbf{K}^2_{m+1}\,\mathbf{u}^2_{m+1} - \mathbf{P}^2$
8: transfer boundary tractions: $\mathbf{t}_{m+1} = (1-\omega_N)\,\mathbf{t}_m + \omega_N\,\mathbf{Q}^T\,\mathbf{R}^2_{m+1}$
9: **end for**

In [85] the authors have used fixed parameters for ω_D and ω_N, which represents the damping or relaxation coefficients for the Dirichlet and Neumann parts, respectively. The constraint condition $\mathbf{N}^1(\mathbf{v}_{m+1})\,\mathbf{u}^2_{m+1} + \mathbf{G}^1_X(\mathbf{v}_{m+1}) \geq 0$ for the unilateral contact problem solved in $\mathcal{B}^2$ is formulated with respect to the deformed surface of body $\mathcal{B}^1$. This shows the dependency of $\mathbf{N}^1$ (matrix of normal vectors) and $\mathbf{G}^1_X$ (initial gap vector) on the current displacement $\mathbf{v}_{m+1}$. Matrix $\mathbf{Q}$ transfers the boundary displacement and surface tractions from the surface mesh of body $\mathcal{B}^1$ to the mesh of $\mathcal{B}^2$. The structure of matrix $\mathbf{Q}$ depends on the applied discretization scheme. As the physical correspondence of the residual $\mathbf{R}$ at each contact node is the reaction force (see [130, 69]), this magnitude is transferred from $\mathcal{B}^2$ to $\mathcal{B}^1$ in order to ensure equilibrium condition (5.3a). The iterative behaviour of Algorithm 8 is illustrated in Fig. 5.2.

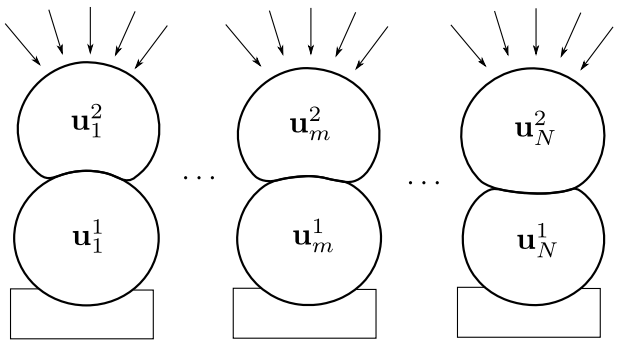

Figure 5.2: Iterative evolution of contact configuration.

5.2.1 Nonlinear parallel extension

Using the ideas and tools introduced in Chapter 4, we can adapt Algorithm 8 to solve nonlinear contact problems in a parallel way. The multicode approach is now used to solve the nonlinear Neumann problem and the unilateral contact problem in finite strains: different code instances are used to solve each problem, while the contact detection and the transference of displacements and boundary reactions are done with PLE++ library. With these concepts in mind we can write the workflow of the proposed algorithm using Algorithm 8 as reference:

Algorithm 9 Multicode Dirichlet-Neumann type contact algorithm

1: **definitions**: $\mathcal{A}^1$: code instance 1, $\mathcal{A}^2$: code instance 2
2: **for** m = 1,2,..., until convergence **do**
3: $\mathcal{A}^1$ receives boundary tractions from $\mathcal{A}^2$.
4: $\mathcal{A}^1$ relaxes (ω_N) and enforces the received boundary tractions to body $\mathcal{B}^1$.
5: $\mathcal{A}^1$ solves Neumann problem for body $\mathcal{B}^1$.
6: $\mathcal{A}^1$ transfers updated mesh position of $\mathcal{B}^1$ to $\mathcal{A}^2$.
7: $\mathcal{A}^2$ receives and relaxes (ω_D) updated mesh position of $\mathcal{B}^1$.
8: $\mathcal{A}^2$ solves unilateral contact problem for $\mathcal{B}^2$ using updated $\mathcal{B}^1$ as rigid body.
9: $\mathcal{A}^2$ computes residual (reactions) for $\mathcal{B}^2$ at the contact interface.
10: $\mathcal{A}^2$ transfers boundary contact tractions of $\mathcal{B}^2$ to $\mathcal{A}^1$.
11: **end for**

Fig. 5.3 graphically shows some iteration steps of Algorithm 9: the transference and enforcement of contact tractions in body $\mathcal{B}^1$ (lines 3 and 4), the solution of the Neumann problem for body $\mathcal{B}^1$ (line 5) and the solution of the unilateral contact problem for body $\mathcal{B}^2$ using the updated configuration of $\mathcal{B}^1$ as a rigid body (line 8). It is important to remark that by *contact tractions* we mean the reaction forces of body $\mathcal{B}^2$ that appear at the contact interface due to the contact interaction.

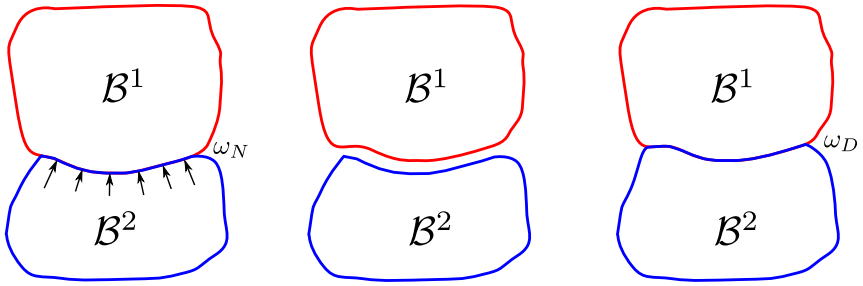

Figure 5.3: Iteration steps of the multicode Dirichlet-Neumann type contact algorithm. (a) Transference and enforcement of contact tractions in body $\mathcal{B}^1$. (b) Solution of the Neumann problem for body $\mathcal{B}^1$. (c) Solution of the unilateral contact problem for body $\mathcal{B}^2$.

With respect to the workflow described in Algorithm 9 some key issues which characterize the originallity of the proposed method are worth remarking. As already mentioned, each code instance can be interpreted as a standalone execution of the code, with its own set of input and mesh files. At this point is important to note that the mesh connectivity is not correlative between instances. In the proposed multicode algorithm, one code instance solves the Neumann problem and the other, the unilateral contact problem. As a result of this approach, the mesh partitioning is done independently in each instance at the beginning of the simulation, as a preprocess task. The transference of information between the instances specified in lines 6 and 10 of Algorithm 9 is done by means of PLE++ library, as explained in Sec. 4.4.1. Algorithm 9 can

also be interpreted as a nonlinear block method used as an iterative solver for the solution of the contact problem. The first block is the Neumann problem (line 5), that is solved for body $\mathcal{B}^1$ by instance $\mathcal{A}^1$. This block uses as input the reaction forces received from instance $\mathcal{A}^2$, which are damped and enforced at the contact interface of $\mathcal{B}^1$ (line 4) together with additional boundary conditions that are imposed to $\mathcal{B}^1$. It should be remarked that the way in which the Neumann problem is solved is only determined by the characteristics of the code instance $\mathcal{A}^1$. If $\mathcal{A}^1$ is a parallel nonlinear solver for solid mechanics (as Alya), this problem can be solved that way. On the other hand, the unilateral contact problem is solved by instance $\mathcal{A}^2$ (line 8). Chapter 4 gives an exahustive explanation on how the resolution of this problem is tackled. The distinctive characteristic here is that the updated configuration of body $\mathcal{B}^1$ is considered as a rigid body for the resolution of the unilateral contact problem for $\mathcal{B}^2$. Also, the algorithm considers the possibility of using a damped/relaxed configuration of body $\mathcal{B}^1$ for the unilateral contact problem. Once the unilateral contact problem is solved, the loop is closed by computing the contact reaction forces at the contact interface of $\mathcal{B}^2$ and transferring that information back to instance $\mathcal{A}^1$. Algorithm 9 is executed at each time step and repeated until convergence in the displacements and forces is reached for bodies $\mathcal{B}^1$ and $\mathcal{B}^2$.

5.2.2 Fixed-point solver analogy - convergence issues

The Dirichlet-Neumann type contact algorithm described in Algorithm 9 can be interpreted and stated as a general fixed-point solver for the solution of interface problems. This generalization allows us to extrapolate techniques that exist in the field of Fluid-Structure Interaction (FSI) regarding convergence ensurance and acceleration [86, 45, 51] to the field of contact problems. Let us assume the existence of an interface operator associated with the Neumann problem solution (line 5) that maps given interface forces $\mathbf{f}_\Gamma^{n+1}$ to the interface displacement $\mathbf{d}_\Gamma^{n+1}$ as follows:

$$\mathbf{d}_\Gamma^{n+1} = \mathrm{NEU}\Big(\mathbf{f}_\Gamma^{n+1}\Big). \tag{5.5}$$

On the other hand, let us assume the existence of an interface operator associated with the unilateral contact problem solution (line 8) that maps a given interface displacement $\mathbf{d}_\Gamma^{n+1}$ into interface forces $\mathbf{f}_\Gamma^{n+1}$ as follows:

$$\mathbf{f}_\Gamma^{n+1} = \mathrm{UNI}\Big(\mathbf{d}_\Gamma^{n+1}\Big). \tag{5.6}$$

Thus, interface operators given by Eqs. (5.5) and (5.6) can be used to define one cycle of Algorithm 9 inside the coupling iteration:

$$\tilde{\mathbf{f}}_{\Gamma,i+1}^{n+1} = \mathrm{UNI}\Big(\mathrm{NEU}\Big(\mathbf{f}_{\Gamma,i}^{n+1}\Big)\Big), \tag{5.7}$$

where i indicates the iteration counter.

In order to ensure and accelerate convergence of the iteration, a relaxation step is needed after each contact cycle (Eq. (5.7)):

$$\mathbf{f}_{\Gamma,i+1}^{n+1} = \mathbf{f}_{\Gamma,i}^{n+1} + \omega_i\, \mathbf{r}_{\Gamma,i+1}^{n+1}, \tag{5.8}$$

with a relaxation parameter ω_i. The magnitude $\mathbf{r}_{\Gamma,i+1}^{n+1}$ is defined as the interface residual:

$$\mathbf{r}_{\Gamma,i+1}^{n+1} = \tilde{\mathbf{f}}_{\Gamma,i+1}^{n+1} - \mathbf{f}_{\Gamma,i}^{n+1}. \tag{5.9}$$

With help of Eq. (5.9) we can rewrite Eq. (5.8) as follows:

$$\mathbf{f}_{\Gamma,i+1}^{n+1} = \omega_i \, \tilde{\mathbf{f}}_{\Gamma,i+1}^{n+1} + (1 - \omega_i) \, \mathbf{f}_{\Gamma,i}^{n+1}. \tag{5.10}$$

Hence, the fixed-point algorithm to solve contact problems consists of the relaxed cycle given by Eq. (5.10) with appropriate relaxation parameters and convergence criteria.

Taking one further step, by means of the interface residual of Eq. (5.9) it is possible to define the interface Jacobian:

$$\mathbf{J}_\Gamma = \frac{\partial \mathbf{r}_\Gamma}{\partial \mathbf{d}_\Gamma}. \tag{5.11}$$

In that case, the relaxation step given by Eq. (5.10) is replaced by the solution of:

$$\mathbf{J}_\Gamma \, \Delta\mathbf{f}_{\Gamma,i+1}^{n+1} = -\mathbf{r}_{\Gamma,i+1}^{n+1}, \tag{5.12}$$

and the update step:

$$\mathbf{f}_{\Gamma,i+1}^{n+1} = \mathbf{f}_{\Gamma,i}^{n+1} + \Delta\mathbf{f}_{\Gamma,i+1}^{n+1}. \tag{5.13}$$

5.2.2.1 Fixed relaxation parameter

The simplest but most ineffective method is to choose a fixed relaxation parameter ω for all iteration steps. The optimal value ω is problem specific and not known a priori. This value has to be small enough to keep the iteration from diverging but large enough to use as much of the new solution as possible and to avoid unnecessary coupling iterations. When the relaxation parameter is fixed, even the optimal value will lead to more iterations than a suitable dynamic relaxation parameter.

5.2.2.2 Aitken dynamic relaxation

FSI problems have already been solved using a Dirichlet-Neumann partitioned approach combined with a fixed-point solver based on the Aitken method [98] . The central idea of Aitken's method is to use values from two previous iterations to improve the current solution, by means of the computation of a new relaxation parameter at each iteration step. This method has proven to be astonishingly simple and efficient. Aitken relaxation method was firstly proposed for computational use in [74]. For a more comprehensive review of this method, including some FSI numerical examples and topics for its numerical implementation, see [86].

5.2.2.3 Quasi-Newton algorithms

As the interface Jacobian given by Eq. (5.11) is not easily available, this value is generally approximated. The different possible strategies for the approximation of the Jacobian are the essence of the so-called quasi-Newton methods. In fact, the Aitken method can be understood as a quasi-Newton scheme where the Jacobian is enforced to be a scalar matrix which is updated at each iteration. On the contrary, using a fixed relaxation parameter would be the same to assume a Jacobian which is equal to a scalar matrix that remains constant the complete simulation. We refer to [21, 91, 19] among others for a more detailed description on quasi-Newton schemes applied to FSI problems and their numerical implementation.

5.3 Computational implementation

Fig. 5.4 shows a block of the iterative scheme of Algorithm 9, which is executed in a staggered way by instances $\mathcal{A}^1$ and $\mathcal{A}^2$. Due to the generality of the algorithm, no differences are made if instances $\mathcal{A}^1$ and $\mathcal{A}^2$ are executed in a serial or parallel way. This block is repeated inside each time step until convergence in displacement and forces is achieved for bodies $\mathcal{B}^1$ and $\mathcal{B}^2$. We can clearly distinguish two parts: one for the unilateral contact problem solution, whose parallel computational implementation was exhaustively explained in Sec. 4.4, and the other for the Neumann problem solution. In the remainder of this chapter we will describe the general parallel algorithm with a focus on the Neumann part. For the case of the unilateral contact problem the ideas introduced in Chapter 4 are directly used here without any modification.

The iterative block starts with the execution of instance $\mathcal{A}^1$, which is in charge of the solution of the Neumann problem for body $\mathcal{B}^1$. Once the instance $\mathcal{A}^1$ has finished with the computation of displacements for body $\mathcal{B}^1$, the unilateral contact part starts. A unilateral contact problem is solved for body $\mathcal{B}^2$ by instance $\mathcal{A}^2$ using the updated geometry of $\mathcal{B}^1$ as if it were a rigid body. This is accomplished by doing the localization after the Neumann problem is solved. Up to this point, no difference is observed with respect to the procedure explained in Chapter 4. When instance $\mathcal{A}^2$ has finished with the computation of the unilateral contact problem, the Neumann part starts. A new localization is the first task of this part, which is done to account for the updated geometry of body $\mathcal{B}^2$. This localization is used to identify the actual contact interface, which is required for the computation, interpolation and transference of the the contact tractions from instance $\mathcal{A}^2$ to $\mathcal{A}^1$. This latter sequence is represented by Algorithm 10, which is executed concurrently by each processor of instance $\mathcal{A}^2$ after the localization procedure.

Algorithm 10 Neumann part, $\mathcal{A}^2$ instance

1: **for** i = 1,nrecv **do**
2: contact_traction_$\mathcal{B}^2_i$ ← compute_contact_traction(i)
3: **end for**
4: **for** j = 1,nsend **do**
5: contact_traction_$\mathcal{B}^1_j$ ← interpolate(contact_traction_$\mathcal{B}^2$,j)
6: **end for**
7: send_to_$\mathcal{A}^1$(contact_traction_$\mathcal{B}^1$)

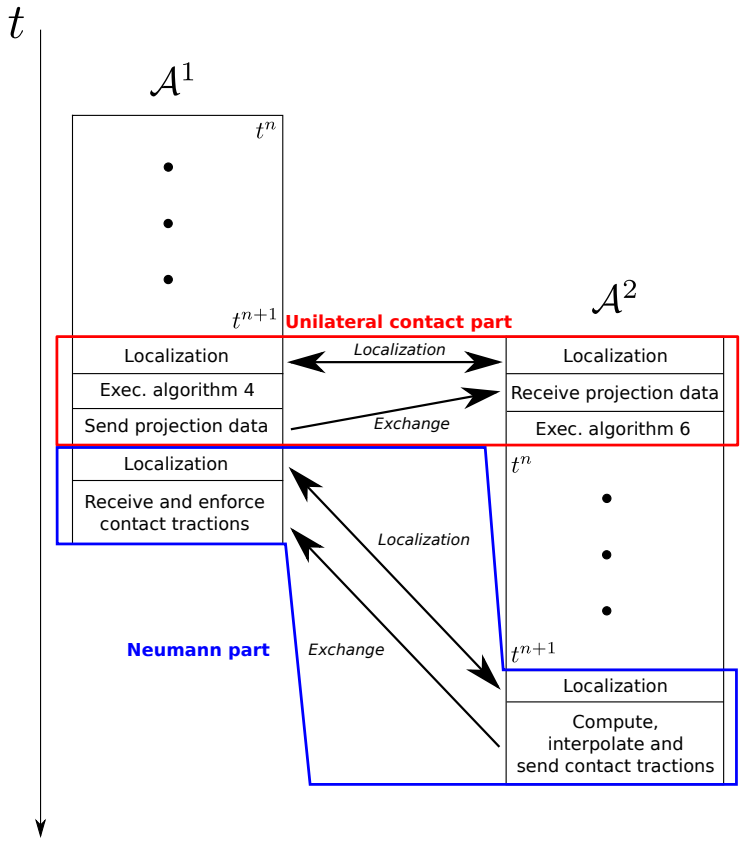

Figure 5.4: Staggered execution of the multicode Dirichlet-Neumann type contact algorithm. Identification of the localization and exchange points. We show here only one block of the iterative scheme. This block is repeated inside each time step until convergence is achieved.

Each processor of instance $\mathcal{A}^2$ who owns boundary nodes located at the contact interface of body $\mathcal{B}^2$ computes the contact tractions for each of those nodes (line 2). The contact tractions, or in other words, the reaction forces at the contact interface, are directly obtained from the residual of the Newton-Raphson iterative scheme, which is used for the solution of the nonlinear Neumann and unilateral contact problems. See Appendix B for a detailed description of this topic. Then, each processor interpolates the contact tractions to the detected nodes that belong to the contact interface of body $\mathcal{B}^1$ (line 5). This procedure is graphically exemplified in Fig. 5.5 for a 2D case. In the next section we give further details on how the interpolations are done.

Finally, those interpolated values are transferred to the corresponding processors of instance $\mathcal{A}^1$ which owns each of the detected nodes (line 7). Fig. 5.6 graphically represents the situation of a 2D case where the processors of instance $\mathcal{A}^2$ ($p1$, $p2$ and $p3$) transfers the interpolated values to the detected nodes owned by instance $\mathcal{A}^1$ (processors $p4$, $p5$, $p6$ and $p7$). The localization and exchange of information is done by means of PLE++ library (see Sec. 4.4.1.1).

On the other hand, the algorithm executed concurrently by each processor of instance $\mathcal{A}^1$ is represented by Algorithm 11. Each processor ($p4$, $p5$, $p6$ and $p7$ in Fig. 5.6) receives the interpolated contact tractions for each of the contacting nodes that it owns (line 1). Finally, for

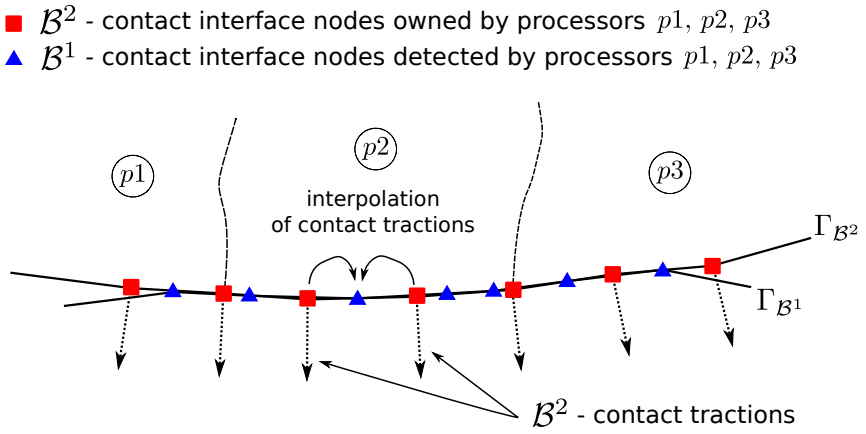

Figure 5.5: Computation and interpolation of contact tractions at the contact interface from body $\mathcal{B}^2$ to body $\mathcal{B}^1$ (2D). This task is performed by instance $\mathcal{A}^2$.

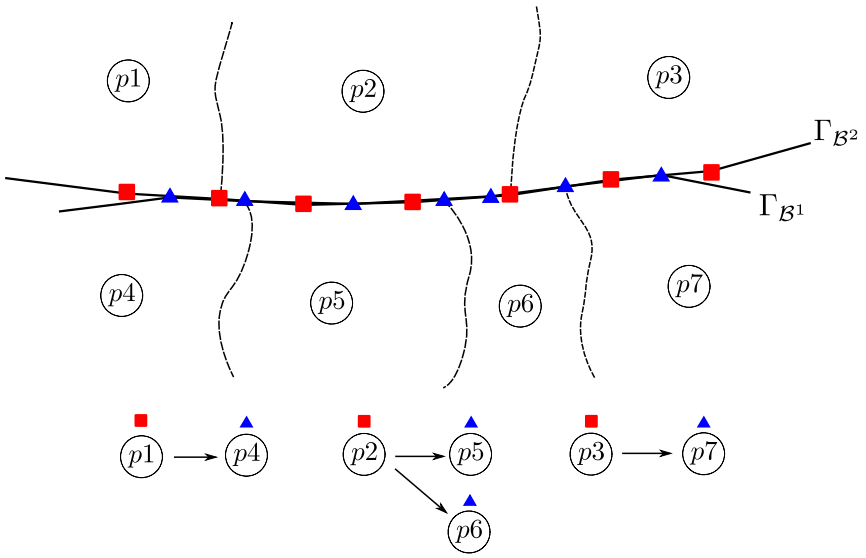

Figure 5.6: Transference of interpolated values from instance $\mathcal{A}^2$ (processors $p1$, $p2$ and $p3$) to instance $\mathcal{A}^1$ (processors $p4$, $p5$, $p6$ and $p7$) - 2D case.

each of those nodes it enforces the received values as a typical Neumann boundary condition for the next iteration of the block (line 3).

Please note that the localization and exchange of information between instances are synchronization points of the algorithm. This means that when any instance reach any of these points, it remains idle until the other instance reaches the same correlative point and the synchronization occurs.

5.3.1 Interpolation of contact tractions. Load transference.

In the 2D examples shown in Figs. 5.5 and 5.6 we considered the most general possible situation in which the meshes of bodies $\mathcal{B}^1$ and $\mathcal{B}^2$ are nonconforming, i.e. that the boundary nodes of both meshes at the contact interface do not match. The same is valid for 3D. An example of this

Algorithm 11 Neumann part, $\mathcal{A}^1$ instance

1: receive_from_$\mathcal{A}^2$(contact_traction_$\mathcal{B}^1$)
2: **for** i = 1,nrecv **do**
3: enforce_Neumann_BC$_i$(contact_traction_$\mathcal{B}^1_i$)
4: **end for**

situation is also shown in Fig. 5.7. This means that for the transference of the contact tractions from the contact surface of body $\mathcal{B}^2$ to $\mathcal{B}^1$ interpolations must be done.

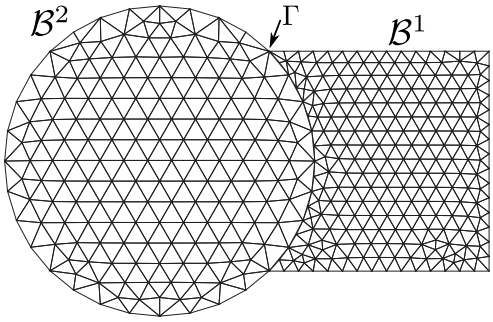

Figure 5.7: 2D EXAMPLE OF TWO NONCONFORMING MESHES AT THE CONTACT INTERFACE: NONMATCHING DISCRETIZATION OF THE SAME PHYSICAL INTERFACE Γ.

As mentioned in the previous section, the interpolation of contact tractions is done by each processor of instance $\mathcal{A}^2$ which owns nodes at the contact interface. In this procedure, the contact tractions at each of these nodes are interpolated to the detected nodes of body $\mathcal{B}^1$ by each of these processors (see Fig. 5.5).

To gather the required information for the interpolations, a new localization is needed at the beginning of the Neumann part. At first, this localization allows instance $\mathcal{A}^2$ to determine which nodes (and the respective owner processors) of body $\mathcal{B}^2$ belong to the contact interface at the current iteration step of the algorithm, i.e. those nodes of $\mathcal{B}^2$ that are in contact with $\mathcal{B}^1$ at that iteration step. Once the localization is finished, $\mathcal{A}^2$ computes for each of those nodes the contact tractions. As a result of the localization procedure, each processor of instance $\mathcal{A}^2$ also knows which are the contacting (detected) nodes of body $\mathcal{B}^1$, its owner processors of instance $\mathcal{A}^1$ and its relative position with respect to body $\mathcal{B}^2$. Then, a linear interpolation using shape functions of elements is performed by the corresponding processors of instance $\mathcal{A}^2$, in which each contacting node of $\mathcal{B}^1$ receives a fraction of the contact tractions from its first neighbours nodes that belong to the contact interface of $\mathcal{B}^2$. Fig. 5.8 schematically shows the interpolation strategy for a 2D case, where the interface variables are interpolated using shape functions of elements. This strategy is also employed for 3D cases.

Finally, once the interpolation has finished, the last step is to transfer the interpolated values of the contact tractions to the corresponding processors of instance $\mathcal{A}^1$, in the way that was explained in the previous section. These values are then directly enforced to the contacting nodes of $\mathcal{B}^1$ following the normal procedure of any typical solid mechanics problem for the enforcement of external loads. As this transference is done at the end of the current iteration

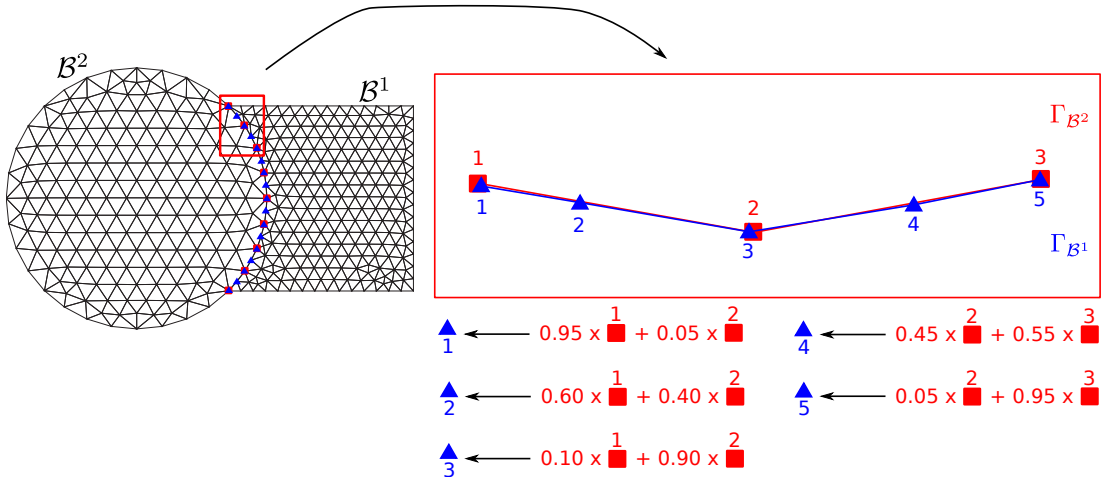

Figure 5.8: Schematic representation of the interpolation procedure - 2D case.

block, the interpolated contact tractions are available to be used at the beginning of the next iteration, when the instance $\mathcal{A}^1$ that solves the Neumann problem starts its execution.

5.4 Numerical examples

5.4.1 Computational framework

The multicode Dirichlet-Neumann contact algorithm described in this chapter was implemented in two stages. In the first stage, the implementation of the Neumann and the unilateral contact problem resolution was done within a simplified finite element code called Ostero (see Sec. A.2 from Appendix A), which was developed in the frame of this thesis. Ostero was coupled with PLE++ library to perform proof-of-concept tests in order to evaluate the feasibility of the contact algorithm. Once its feasibility was confirmed and the algorithm was validated, the second stage consisted on its implementation in the massively parallel code Alya (see Sec. A.1 from Appendix A).

Ostero or Alya can be used for the simulation of contact problems in a multicode scheme, where one instance of the code is in charge of the resolution of the Neumann problem while the other is in charge of the resolution of the unilateral contact problem. Using different code instances, each one of them having its own set of input files, allows to use for each body different mesh types, different material models, different time integration schemes, different types of solvers and preconditioners, different number of subdomains, etc (see Fig. 5.9). For instance, the Neumann problem can be solved explicitly while the unilateral contact problem can be solved implicitly. Even more, the Neumann problem can be solved dynamically using a Conjugate Gradient solver with an Algebraic Multigrid preconditioning, and the unilateral contact problem can be solved implicitly as a quasi-static evolution using GMRES solver with a RAS preconditioner [93, 80]. In summary, this approach allows to solve each body separately, as if they were in a standalone simulation. This is possible because the contact interaction is modelled as a coupled problem, where the coupling of contacting bodies is done by the exchange and enforcement of

Dirichlet and Neumann boundary conditions only at the contact interface.

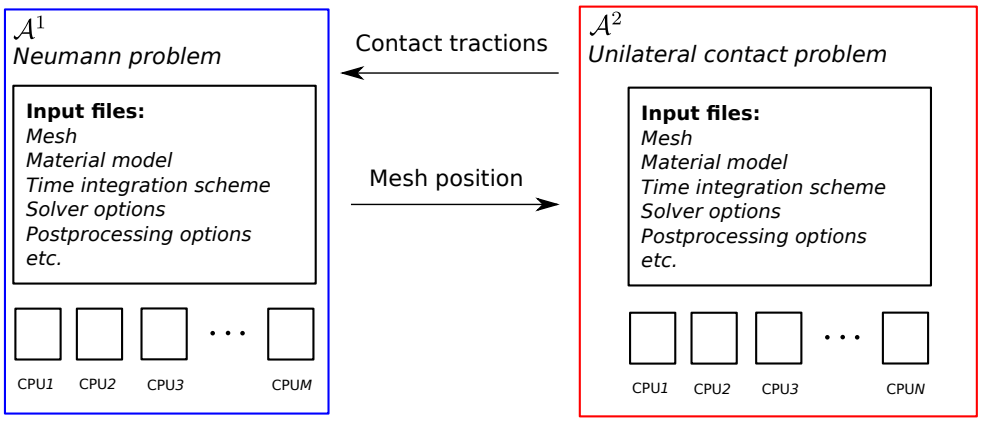

Figure 5.9: Instance composition: each instance is executed as a standalone problem and the connection is done through the transference and enforcement of boundary conditions. Each instance can be parallelized independently and uses independent sets of input files.

Though, this algorithm is not only restricted to Alya and Ostero. With a proper implementation, any other simulation tool can be used. Even more, this multicode scheme and the black-box approach of the proposed algorithm gives the possibility to use and couple different computational codes for the Neumann and unilateral contact problem solution. The contact algorithm can be interpreted and implemented as a black-box that connects same or different computational codes by the transference and enforcement of specific boundary conditions at each contact interface. It must be remarked that for the parallel resolution of both individual problems, parallel codes (as Alya) must be used. As a general aspect of this algorithm, the contact detection and the transference of data between both instances is done by PLE++ (see Sec. 4.4.1). Nevertheless, even this procedure can be replaced by any other suitable tool which has the same functionality.

Let us consider the parallel example problem shown in Fig. 5.10, where both meshes are partitioned in 3 and 5 subdomains, respectively. Similarly to what was explained for the unilateral contact part in Sec. 4.5.1, the multicode simulation of this example and the test cases presented in the following section are done in the following way:

```
$ mpirun -np 3 ./code_instance_1 ball : -np 5 ./code_instance_2 block
```

where `code_instance_1` and `code_instance_2` represents the computational codes used for the solution of the governing equations of the mechanical problem (Ostero, Alya, etc). For this particular case we use 3 processors for the parallel resolution of the ball and 5 processors for the resolution of the block. The assignment of the processors is done with the `-np` instruction.

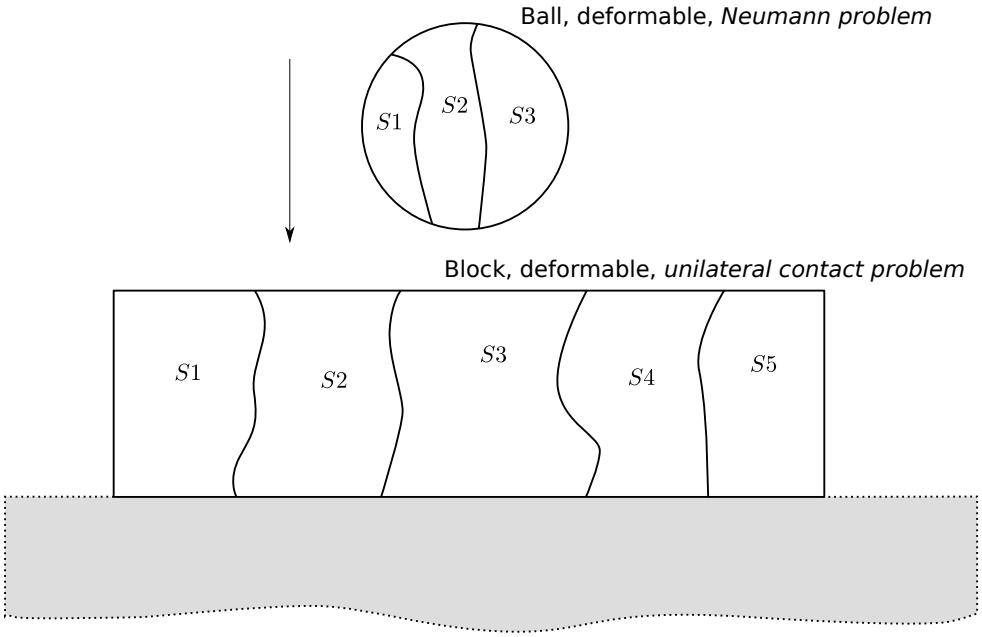

Figure 5.10: Multicode simulation of a two-body contact problem.

5.4.2 Test cases

We shall now present the results of application of the algorithm presented in this chapter to some 2D and 3D test cases. These test problems were selected to illustrate and validate the behaviour of the proposed algorithm. All the results shown below were obtained using Alya code. It is worth mentioning that for each numerical example, in the multicode execution Neumann and unilateral contact parts are solved using exactly the same Alya binary.

5.4.2.1 Hertz contact between two hemispheres - 2D

Hertz problem is often used as a reference for the numerical validation process of contact mechanics algorithms. It consists on the computation of the mechanical state of two infinite long cylinders which contact along their generatrix due to the effect of a concentrated uniform force F, as shown in Fig. 5.11. This problem allows to verify if the resolution method is able to correctly evaluate the contact boundary conditions, even if we only know the boundaries in its approximated form. The analytical solution to this problem, proposed by Hertz in 1882 [62], is only valid if we assume an elastic behaviour of the bodies, no friction at the contact interface, small deformations and a small contact length with respect to the radius of the cylinders.

For the numerical resolution of this example we employ identical cylinders with same dimensions r and material properties E and ν. As the cylinders are infinite long, we consider a 2D simplification under the assumption of plane strain. Furthermore, due to symmetry the problem can be reduced to the modellization of two quarters of cylinders. In order to solve the same problem, we enforce a displacement $\delta/2$ on the boundaries that are parallel to the contact zone. The computational setting for this problem is depicted in Fig. 5.12.

Assuming a frictionless contact and a small contact length b in comparison to the cylinders

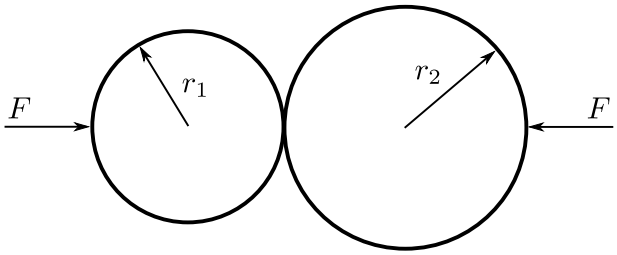

Figure 5.11: Hertz contact - Hertz contact problem, cylinder on cylinder.

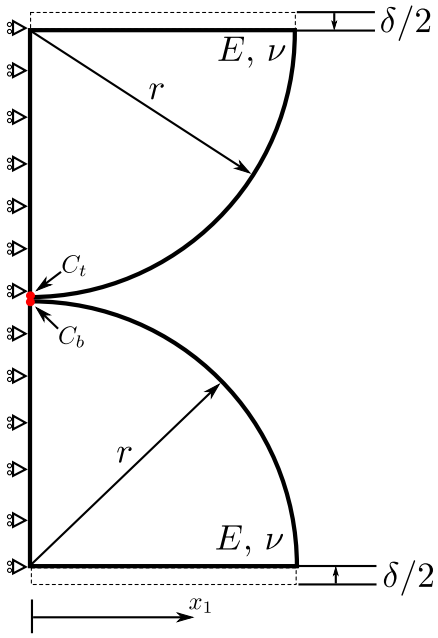

Figure 5.12: Hertz contact - Computational setting.

radius r ($b << r$), the contact pressure distribution at the contact interface is given by [27]:

$$P = \frac{2F}{\pi b^2 l}\sqrt{(b^2 - x_1^2)} = P_{max}\sqrt{\left(1 - \frac{x_1^2}{b^2}\right)}, \tag{5.14}$$

where F/l is the load per unit length. The contact length b can be computed by:

$$b = 2\sqrt{\frac{Fr(1-\nu^2)}{\pi l E}}. \tag{5.15}$$

It is worth to note the equality between Eqs. (5.14) and (4.38) and Eqs. (5.15) and (4.39).

For the numerical solution of this problem we set $E = 20000\,N/m^2$, $\nu = 0.3$, $r = 50\,cm$ and $\delta = 0.767\,cm$. Using these values in our computational model, we obtain for nodes C_t and C_b maximum values of contact pressure equal to $P_{max_t} = 7147\,kPa$ and $P_{max_b} = 7142\,kPa$ respectively. Taking an average value $P_{max} = 7144.5\,kPa$ and by combining Eqs. (5.14) and (5.15) we can isolate the variable F/l in order to compute b, which results in $b = 3.25\,cm$. The deformed configuration of the cylinders, the mesh used for the numerical solution and the contact zone are shown in Fig. 5.13.

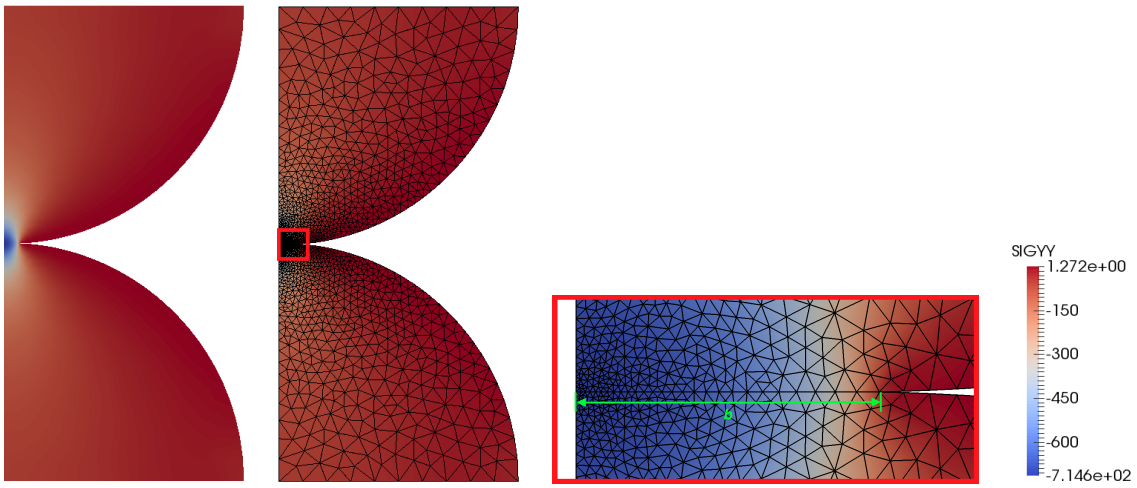

Figure 5.13: Hertz contact - (a) Deformed configuration. (b) Mesh used for the numerical solution. (c) Zoom in on the contact zone.

A comparison of the computed contact pressure distribution for both cylinders with the Hertz solution (Eq. (5.14)) is shown in Fig. 5.14. We observe that contact pressure distribution and contact length are very well captured by the proposed algorithm. This translates into a good agreement between analytical and numerical results. It is noted that we have not assumed any contact surface and pressure distribution. They are obtained naturally as part of the numerical solution of the problem by means of the algorithm proposed in this chapter.

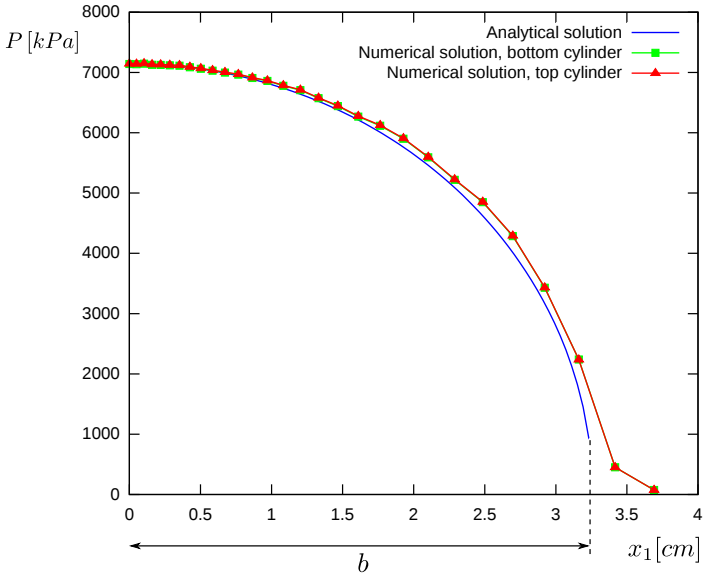

Figure 5.14: Hertz contact - Contact pressure distribution with Hertz solution. Comparison between numerical and analytical solutions for both cylinders.

To evaluate the convergence of the contact algorithm we solve this example as a quasi-static evolution. Small displacement increments are applied at each time step until reaching the desired

total displacement. We analyze two different cases to explore the convergence of the solution: in one of them we solved the problem with a fixed relaxation parameter $\omega = 0.5$ (see Sec. 5.2.2) while in the other we use the Aitken's method [86] to compute a dynamic relaxation factor at each iteration step. In Fig. 5.15a we show the evolution of the coupling residual with respect to the total number of iterations done by the algorithm. The coupling residual is computed as the difference between previous and actual force received by the Neumann body. For visualization purposes we limit to 100 the total number of iterations to display. On the other hand, in Fig. 5.15b we show the total number of coupling iterations for each time step. We observe that in this particular example Aitken's method does not accelerate the convergence of the problem. A simplified statistical analysis shows that the number of average iterations for the fixed relaxation parameter case is $n_{it_{fix}} = 4.69 \pm 1.01$ while for the Aitken's method is $n_{it_{ait}} = 4.73 \pm 1.31$.

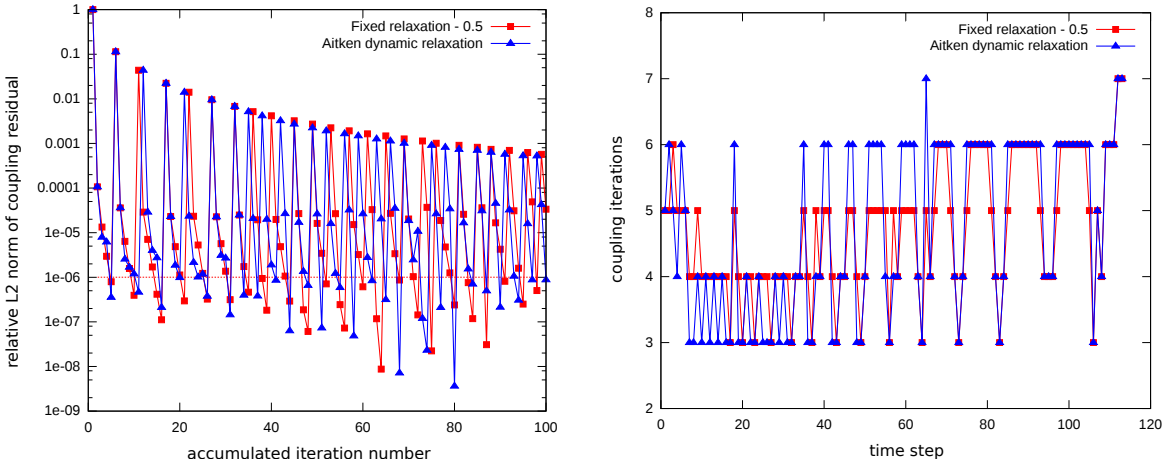

(a) (b)

Figure 5.15: Hertz contact - (a) Convergence behaviour of the contact algorithm in terms of the relative L^2 norm of the coupling residual. (b) Coupling iterations for each time step.

5.4.2.2 Indentation parallel benchmark - 2D

In this example we solve a 2D frictionless indentation problem which consists of a rounded-head deformable indenter and a deformable square block. The physical model of this problem is shown in Fig. 5.16. The dimensions of the indenter are: $h_i = 0.5\,m$, $w_i = 1.2\,m$ and $r_i = 0.75\,m$, while the vertical displacement imposed to the indenter along the vertical direction is $\delta = 0.1\,m$. The dimensions of the block are $h_b = 0.5\,m$ and $w_b = 1.6\,m$. We consider a Neo-Hookean material model and finite strains for the indenter and the block, with material properties $E_i = 6.896\,e{+}9\,N/m^2$, $\nu_i = 0.32$, $E_b = 6.896\,e{+}8\,N/m^2$ and $\nu_b = 0.32$. The relative position of the indenter with respect to the block is given by $a_x = 0.2\,m$ and $a_y = 0.025\,m$. For the bottom of the block, we fix the displacements in all directions.

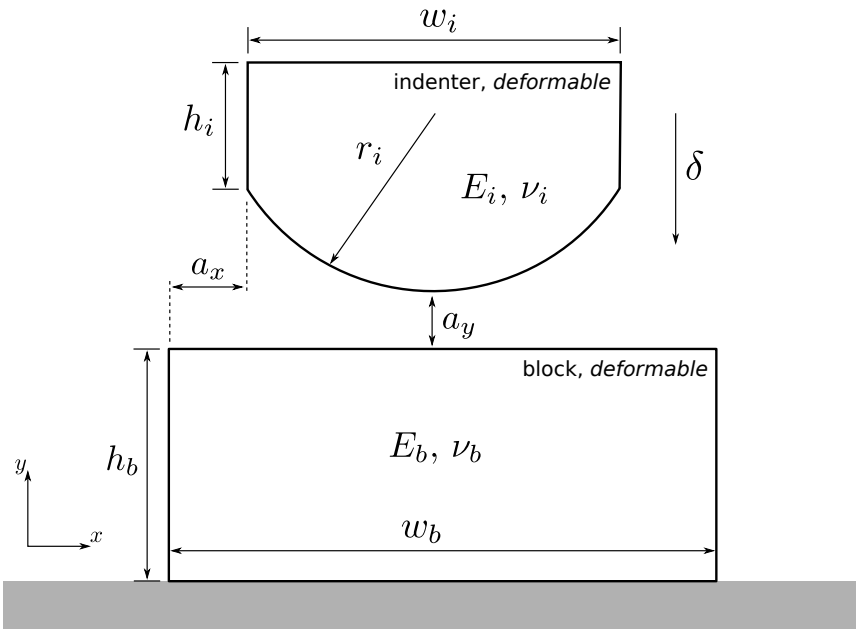

Figure 5.16: 2D INDENTATION PROBLEM - PHYSICAL MODEL.

We solve this problem with Alya code after partitioning the indenter mesh in eight subdomains and the block mesh in eighteen subdomains. Indenter and block meshes and the distribution of subdomains used in this example are shown in Figs. 5.17a and 5.17b, respectively. To compare results, we solve the same problem with Code_Aster [31] using the same meshes and only one domain for the complete system.

Fig. 5.18a shows the final deformed configuration obtained with Alya. On the other hand, Fig. 5.18b shows a mesh superposition in order to compare the final deformed configurations obtained with both codes. We observe a very good agreement in the results.

In Figs. 5.19a and 5.19b we compare the results of Alya against Code_Aster for the y and x displacement of those nodes which belong to the contact boundary of the block, respectively. In Fig. 5.19c we show a comparison of the contact forces along the same contact boundary. Considering the small scale of the vertical axis in Fig. 5.19b, we can conclude that not only the qualitative behaviour of the contact boundary is very well captured, but also the absolute

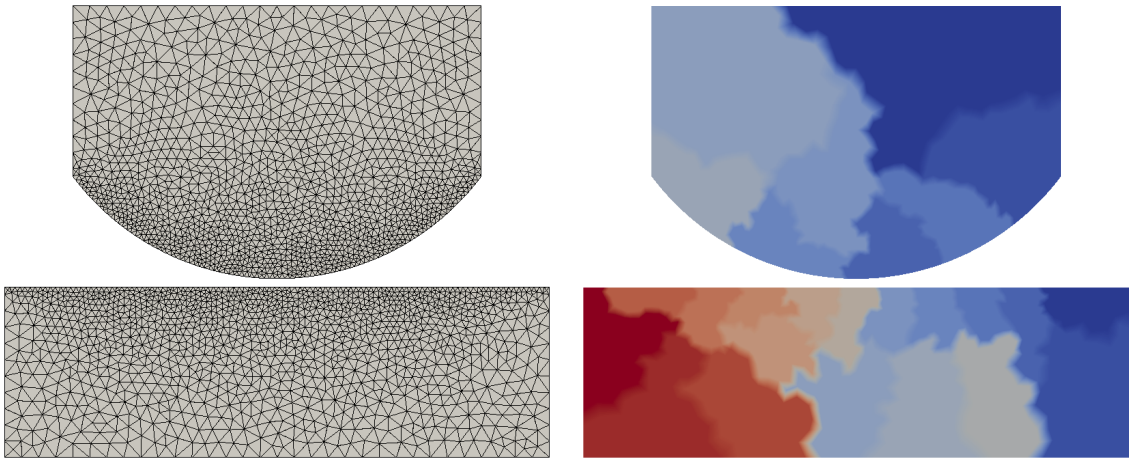

(a) (b)

Figure 5.17: 2D indentation problem - (a) Mesh used for the numerical solution. (b) Domain decomposition of the mesh used by Alya code.

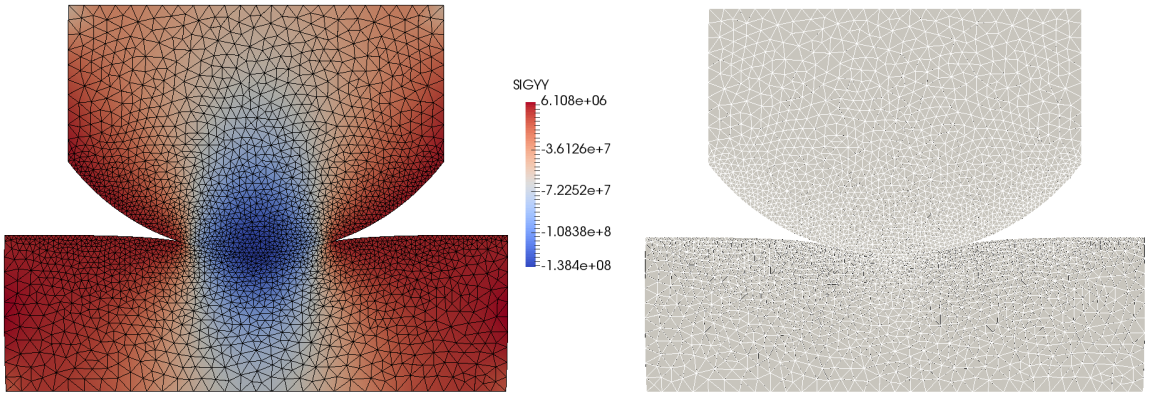

(a) (b)

Figure 5.18: 2D indentation problem - (a) Final deformed configuration obtained with Alya. (b) Mesh superposition - black lines: Alya mesh; white lines: Code_Aster mesh.

values are very close between the two models. We would like to emphasize that in this example we are comparing results obtained with two completely different apporaches for the numerical resolution of contact problems. These results also allow to verify the parallel implementation of the proposed algorithm.

This example is solved as a quasi-static evolution: we apply a small displacement at each time step and solve a static problem until reaching the desired total displacement. For the solution of the linear system of equations resulting at each Newton-Raphson iteration, we employ an iterative GMRES solver with diagonal preconditioning. In this context we evaluate the convergence of the contact algorithm using two sets of values for the relaxation parameter: $\omega = 0.5$ and $\omega = 0.6$, and the Aitken's method. In Fig. 5.20a we show the evolution of the coupling residual with respect to the total number of block iterations. In Fig. 5.20b we show the the total number of iterations for each time step. Finally, in Fig. 5.20c we show the total solver iterations for each

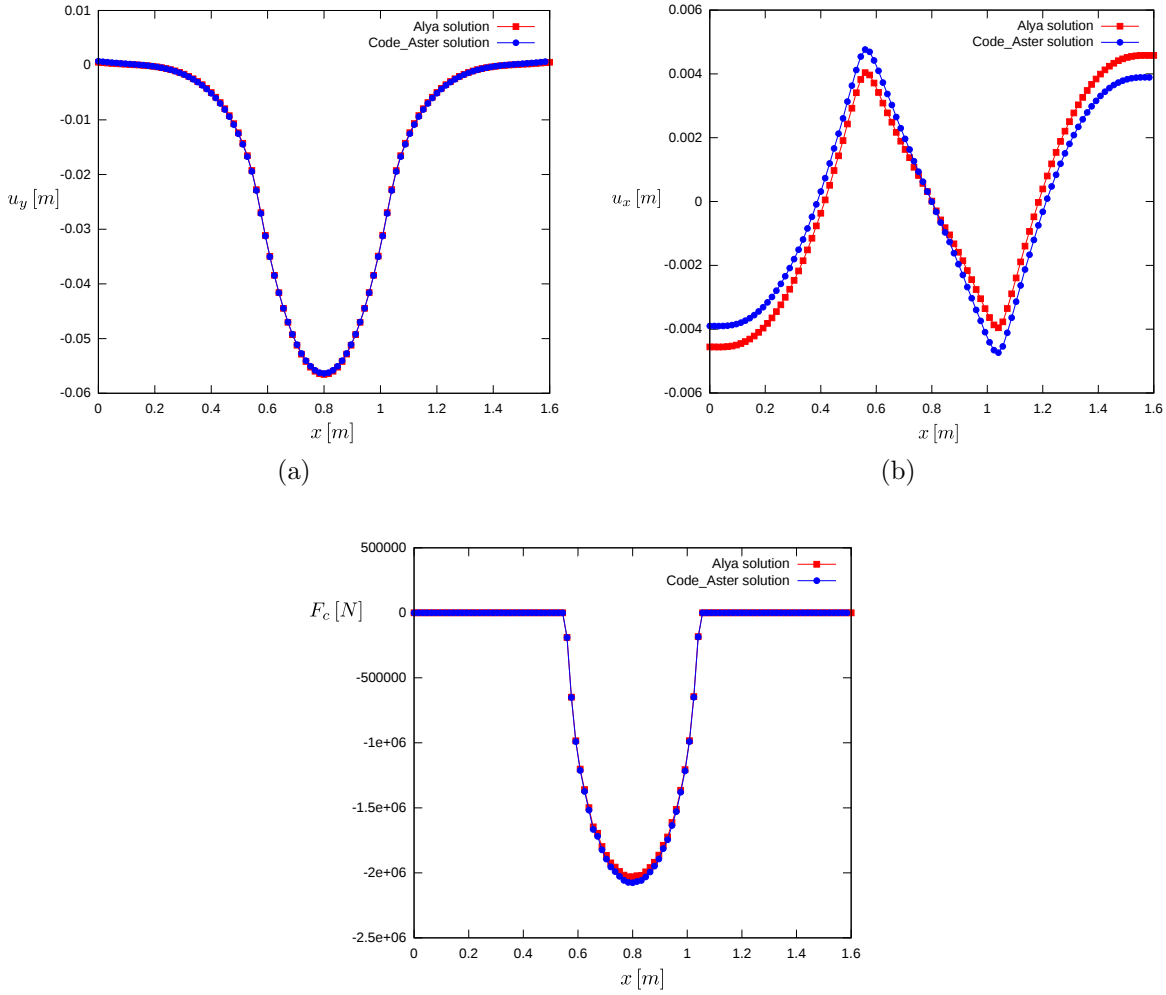

Figure 5.19: 2D INDENTATION PROBLEM - MAGNITUDES ALONG THE CONTACT BOUNDARY OF THE BLOCK: (a) VERTICAL DISPLACEMENT. (b) TANGENTIAL DISPLACEMENT. (c) CONTACT FORCE.

time step. It is clearly observed how the Aitken's method allows to accelerate the convergence of the solution, as the total number of iterations for the complete simulation is reduced. It is worth mentioning that for a fixed relaxation parameter equal to $\omega = 0.9$, the solution diverges. Thus, Aitken's method proves to be a suitable choice to ensure and accelerate the convergence of this problem.

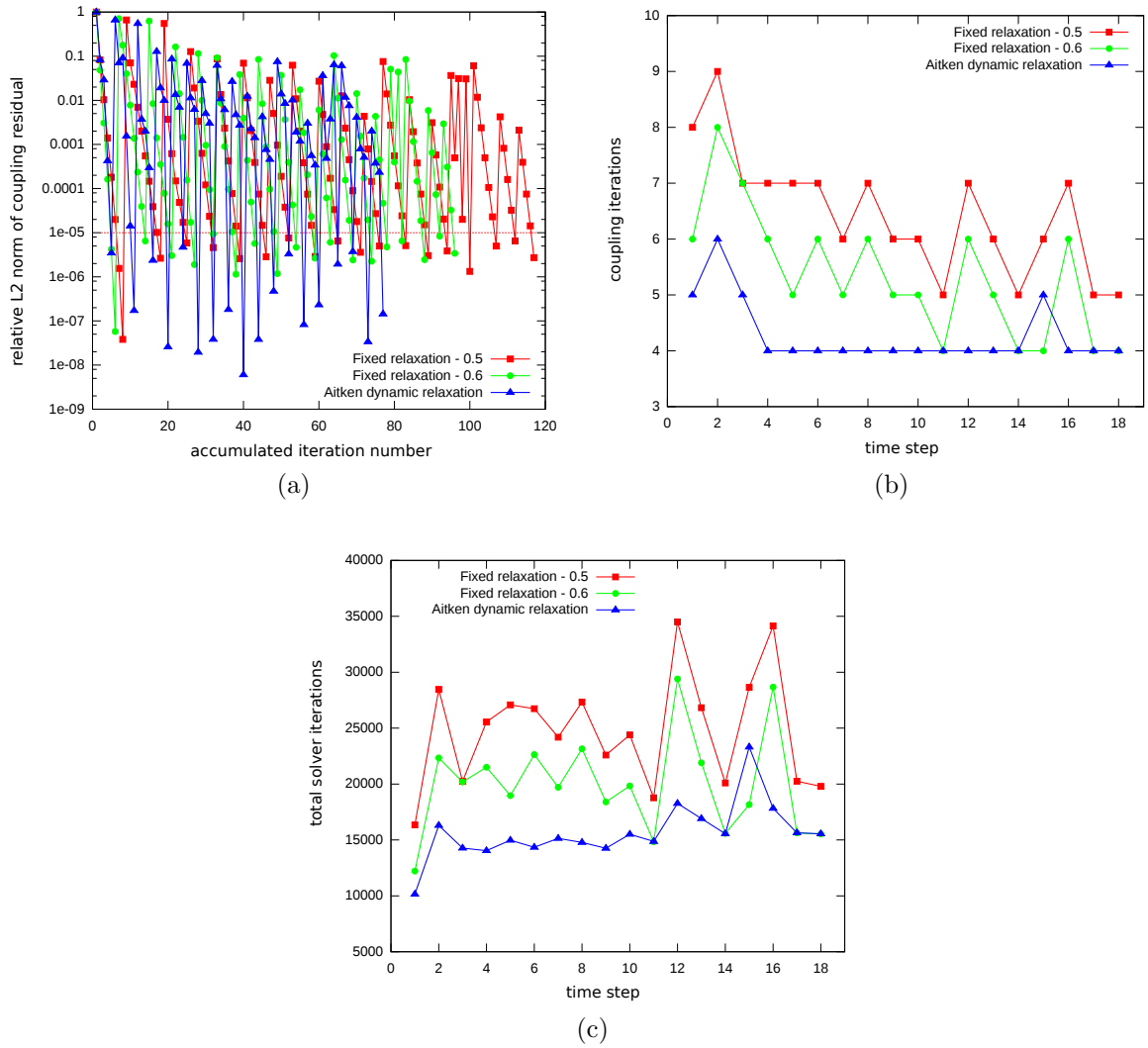

Figure 5.20: 2D INDENTATION PROBLEM - (a) CONVERGENCE BEHAVIOUR OF THE CONTACT ALGORITHM IN TERMS OF THE RELATIVE L^2 NORM OF THE COUPLING RESIDUAL. (b) COUPLING ITERATIONS FOR EACH TIME STEP. (c) TOTAL SOLVER ITERATIONS FOR EACH TIME STEP

5.4.2.3 Bouncing ball - 2D

We solve here a simple problem which consists of a very rigid ball which falls due to gravity and impacts on an elastic deformable membrane, which is fixed at both ends (see Fig. 5.21). We assume an isotropic linear elastic material model and finite strains for the ball and membrane. The physical and material parameters arbitrary chosen for this example are: $r_b = 0.1\,m$, $a_x = 0.5\,m$, $a_y = 0.07\,m$, $h_p = 0.05\,m$, $w_p = 1.2\,m$, $\rho_b = 2.0\,e{+}5\,kg/m^3$, $E_b = 6.896\,e{+}10\,N/m^2$, $\nu_b = 0.32$, $E_p = 6.896\,e{+}8\,N/m^2$ and $\nu_p = 0.32$.

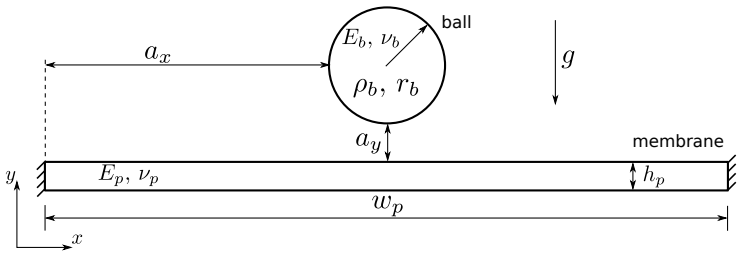

Figure 5.21: Bouncing ball - Physical model.

In order to show the flexibility of the algorithm, we take profit of the low velocity of impact ($\approx 1.2\,m/s$). So, in this example we solve the ball using a transient implicit solver, while the membrane is solved quasi-statically, i.e. we do not consider inertial effects. The mesh used for the numerical solution is shown in Fig. 5.22.

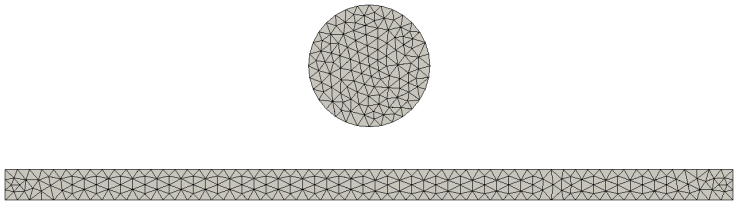

Figure 5.22: Bouncing ball - Mesh used for the numerical solution.

We solve this problem for a real time lapse of $3.2\,s$. Fig. 5.23 shows the evolution of the deformed configuration of the ball-membrane system for four different time steps, while Fig. 5.24 shows a zoom in at the contact interface.

Fig. 5.25 shows the evolution of the total displacement of the rigid ball along the vertical axis y. As we are not considering any source of energy dissipation, the bouncing effect is perfectly elastic.

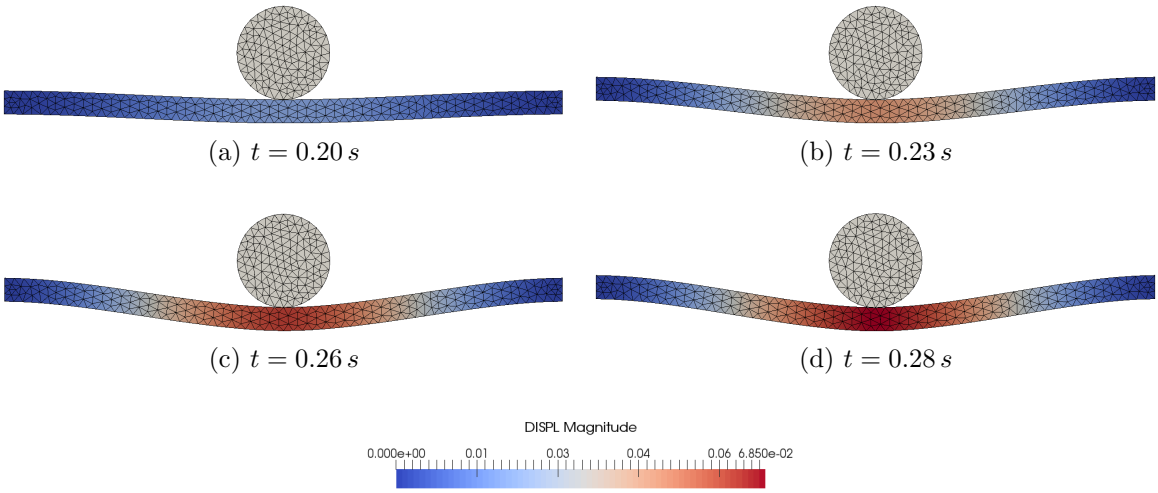

Figure 5.23: Bouncing ball - Evolution of the deformed system.

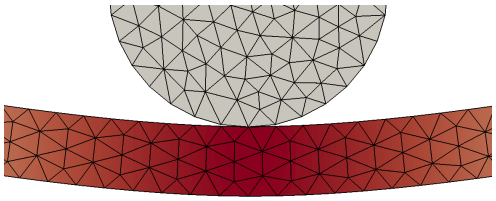

Figure 5.24: Bouncing ball - Zoom in at the contact zone, $t = 0.28\,s$.

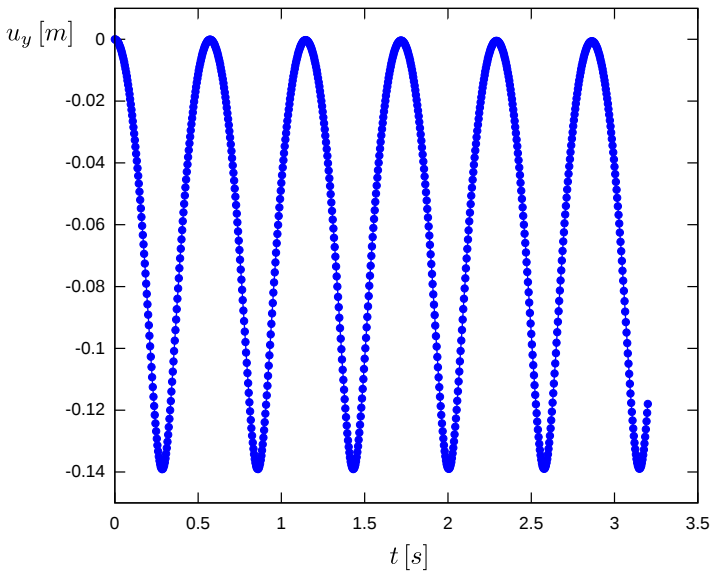

Figure 5.25: Bouncing ball - Total displacement of the rigid ball vs. time.

5.4.2.4 Ironing example - 3D

In this example we study the finite deformation contact of a half-cylindrical elastic die (Neo-Hookean model, $E_d = 1000$, $\nu_d = 0.3$) which is pressed into an elastic beam (Neo-Hookean model, $E_b = 1$, $\nu_b = 0.3$) and then slided over the surface. This problem is commonly referred to as ironing example. Similar analysis using a mortar segment-to-segment contact method have been made in [112, 116], where also further details can be found. The physical model and an exemplary finite element mesh are shown in Fig. 5.26. The geometrical parameters chosen for this example are: $r_d = 3$, $d_d = 5.2$, $w_b = 9$, $h_b = 3$, $d_b = 4$, $a_x = 0.2$ and $a_z = 0.6$. An initial gap of 0.003 between die and beam is considered. The die is first pressed into the beam by prescribing a displacement of -0.9 units in y-direction within 13 quasi-static time steps. Then it slides along the beam 2.6 units in 7 further time steps. Finally, the die returns to its vertical position by moving 0.9 units in y-direction in 10 time steps. The beam is fixed to the ground.

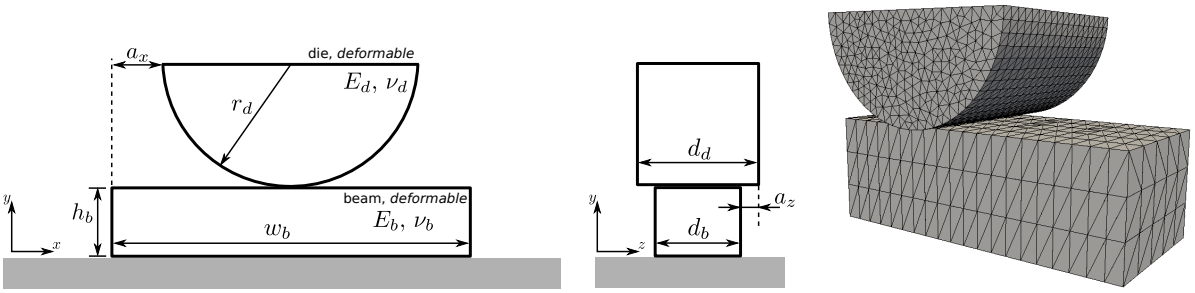

Figure 5.26: Ironing example - Physical model and finite element mesh.

Fig. 5.28 shows the deformation state of the elastic die-beam system for three different time steps. In this example, the numerical efficiency of the proposed contact algorithm in 3D finite deformation situations is evaluated by monitoring the total coupling residual norm during the nonlinear coupling or block iterations. Fig. 5.27a shows the evolution of the coupling residual with respect to the accumulated number of coupling iterations. We observe that for fixed relaxation values of 0.7, 0.9 and 1.0 the simulation diverges at different time steps. Fig. 5.27b shows the number of coupling iterations at each time step for the converged simulation. We observe that only the Aitken dynamic relaxation is able to ensure convergence to the solution for the complete simulation in a reasonable number of coupling iterations.

Trace analysis To study the parallel behaviour of the general contact algorithm we have generated an execution trace of the ironing example using 16 processors for the Neumann part (elastic die, 100k elements) and 32 processors for the unilateral contact part (elastic beam, 70k elements) for 3 time steps. A similar analysis was done in Sec. 4.5.2.5 for the case of an unilateral contact problem. The trace for this example, executed on *MareNostrum IV* supercomputer, is shown in Fig. 5.29. This trace was obtained using the HPCToolkit [71] suite.

Light blue color represents running processors while dark blue color represents idle processors. In Fig. 5.29 we clearly observe the staggered execution of the proposed contact algorithm. Each time step starts with the execution of the code instance assigned to the solution of the Neumann

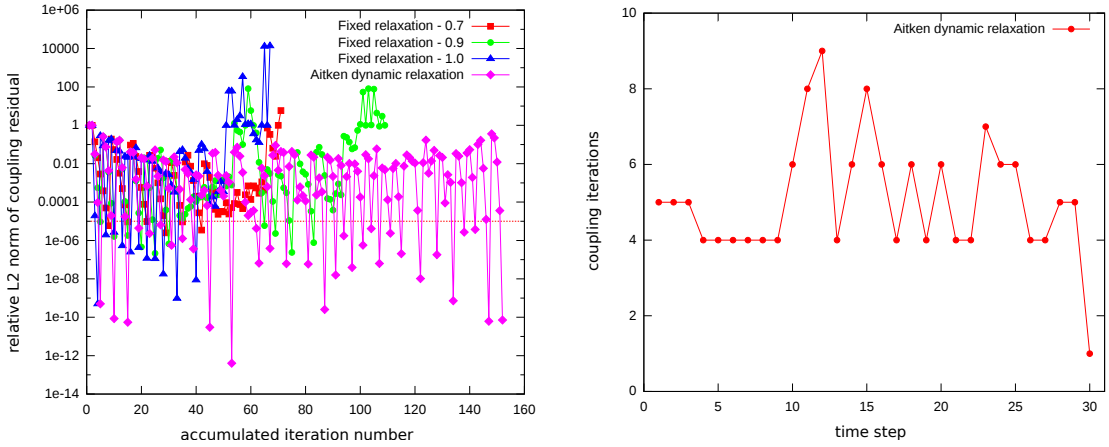

(a) (b)

Figure 5.27: Ironing example - (a) Convergence behaviour of the contact algorithm in terms of the relative L^2 norm of the coupling residual. (b) Coupling iterations for each time step.

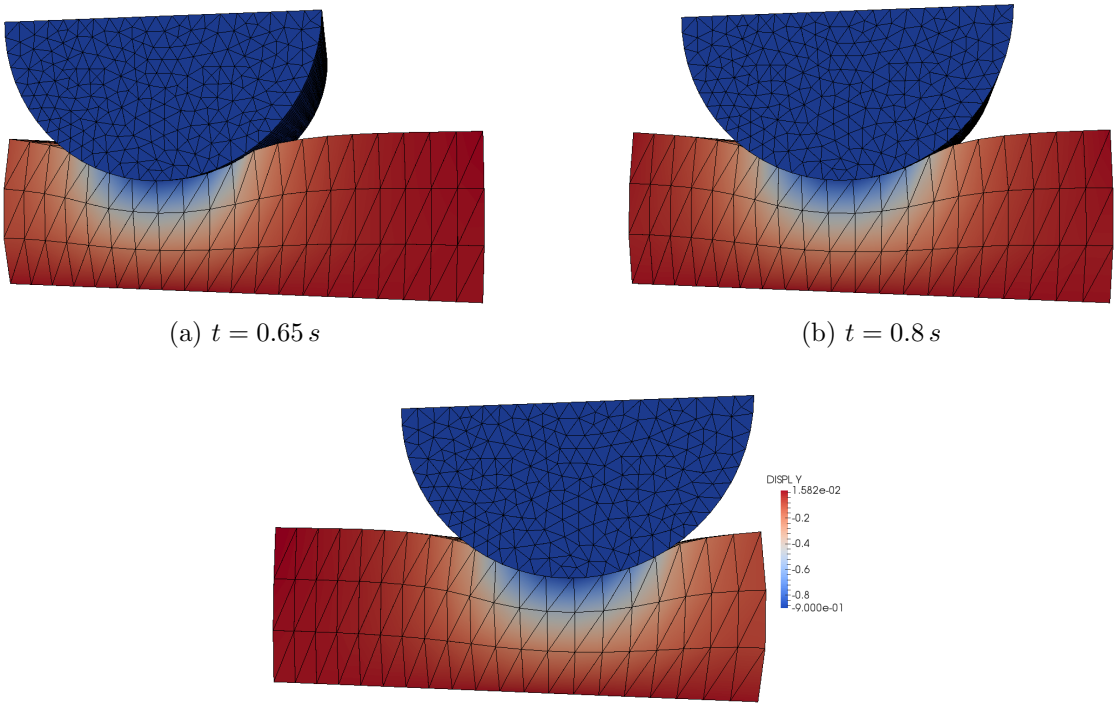

(a) $t = 0.65\,s$ (b) $t = 0.8\,s$

(c) $t = 1\,s$

Figure 5.28: Ironing example - Results for three time steps. The elastic die is fully lowered at (a) and then slid across the beam over the remaining time until (c). For simplicity, a time step of $0.05\,s$ is considered.

problem ($\mathcal{A}^1$). While this instance is running, the processors assigned to the unilateral contact problem (instance $\mathcal{A}^2$) remain idle. Once the solution at $\mathcal{A}^1$ has converged, instance $\mathcal{A}^2$ starts. At this time, while $\mathcal{A}^2$ is running, the processors assigned to $\mathcal{A}^1$ remain idle. This staggered execution represents the coupling or block iteration depicted in Fig. 5.4 and is repeated along the complete simulation. In Fig. 5.29 we also observe that the work load is well balanced among

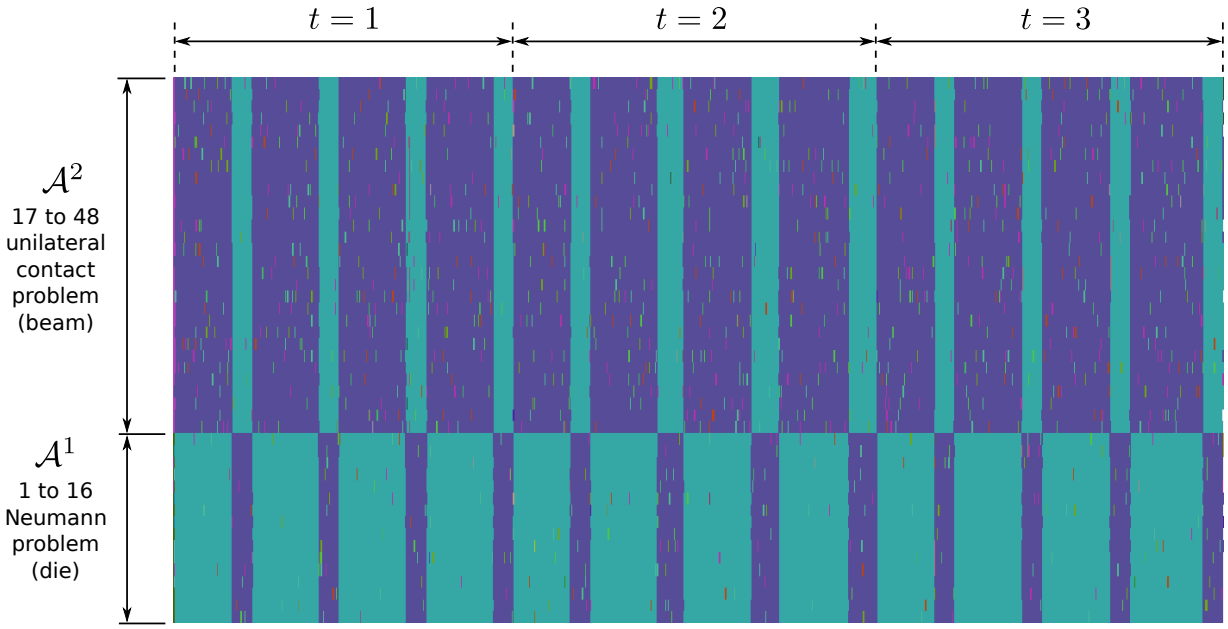

Figure 5.29: Ironing example - Trace generated for the full simulation (3 time steps) - beam mesh of 70k elements, die mesh of 100k elements.

the group of processors of both instances, as they start and finish its execution in a coordinated way. For this particular example we also observe that at each block iteration, instance $\mathcal{A}^1$ takes more than double of time to converge than instance $\mathcal{A}^2$. One reason for this behaviour is that we are using twice of processors for the beam mesh, which is 30% smaller than the die mesh. Moreover, this simplified analysis gives us insight into how we could redistribute the total number of available processors (48) between the two instances in order to improve the performance of the parallel execution. Finally, Fig. 5.30 shows a zoom in on the trace for the first time step, where the coupling iterations can be clearly identified.

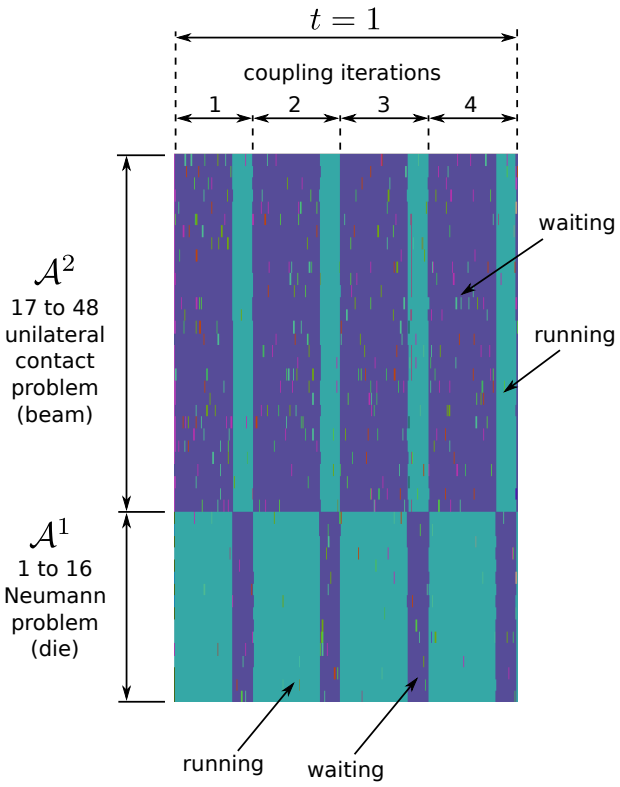

Figure 5.30: Ironing example - Zoom in on the trace: only one time step is shown. Coupling iterations can be clearly distinguished.

5.4.2.5 Impact problem - 3D

In this example we solve a low velocity impact, where a plate is impacted with an hemispherical rigid impactor. We consider an impact energy level of $1.6\,J$. The diameter of the impactor is $16\,mm$ and its mass is $2\,kg$. The dimensions of the plate are $100 \times 150 \times 4.16\,mm$ and it is simply supported ($u_x = u_y = u_z = 0$) along all four edges as shown in Fig. 5.31 (right), leaving an inner region of $75 \times 125\,mm$. The plate is modelled as a T700/M21 unidirectional carbon/epoxy laminate with stacking sequence of $[0_2/45_2/90_2/-45_2]_S$. The material properties of T700/M21 used in this problem were extracted from [2] and are listed in Table 5.1. For the impactor, we assume an isotropic linear elastic material and for the plate, we consider a transversally isotropic material and no damage. The boundary conditions and impact set-up for this problem are based on ASTM D7136/D7136M-05 standard [6]. Similar numerical and experimental analysis have been made in [2, 67].

For the numerical solution of this problem we use a mesh composed of approximately 8k elements for the impactor and 100k elements for the plate. The meshes are generated in order to enforce the best node-matching situation at the contact interface. A global overview of the meshes is shown in Fig. 5.31. We run this problem with Alya code in parallel using 8 processors for the impactor and 40 processors for the plate.

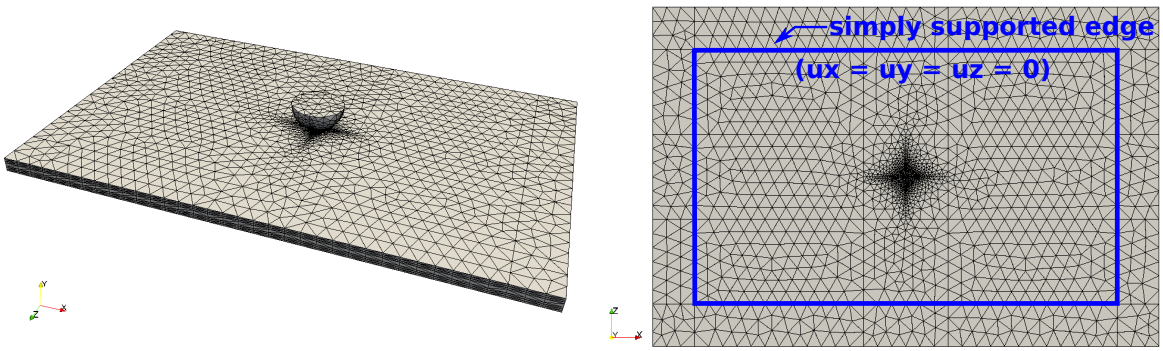

Figure 5.31: Impact problem - Impact set-up: 3D view (left), backview (right).

Property		Values
E_{11}	Longitudinal Young's modulus	$130\,GPa$
$E_{22} = E_{33}$	Transverse Young's modulus	$7.7\,GPa$
$\nu_{12} = \nu_{13}$	Poisson's ratio	0.33
ν_{23}	Poisson's ratio	0.45 (assumed)
$G_{12} = G_{13}$	Shear modulus	$4.8\,GPa$
G_{23}	Shear modulus	$2.655\,GPa$

Table 5.1: Impact problem - Material properties of T700/M21 [2].

For low velocity impact, the inertia effects are relatively small [143], and hence an implicit quasi-static solver can be used to solve such problems. To compare the results obtained with Alya, we solve the same problem using the comercial code Abaqus [1]. Abaqus solves the contact problem using a general implicit dynamic contact algorithm based on the node-to-segment

discretization of the contact interface and the introduction of a penalty parameter for the enforcement of contact constraints. As mentioned in previous chapters, this is a completely different approach that the one proposed in this work.

In Fig. 5.32 we show the typical curves for low velocity impact tests: (a) contact force-displacement, (b) impactor energy-time, (c) contact force-time and, (d) impactor velocity-time. By comparing the results of the present study with the ones obtained with Abaqus, one can note that the qualitative behaviour is very well captured (see Fig. 5.32). At the beginning of the impact, Alya and Abaqus predictions agree well: see Fig. 5.32a until an indentation of $0.4\,mm$ and Fig. 5.32c until a contact time of $0.5\,ms$. However, for larger values of indentation and contact time, the absolute values do not exactly match. From the impactor energy-time curve (Fig. 5.32b) we observe that this magnitude is not perfectly conserved for the solution obtained with our contact algorithm. Based on this matter, qualitative behaviour and quantitative differences in Fig. 5.32 may stem from the fact that, at the beginning of impact, impactor and plate meshes practicaly match at those nodes that are in contact. This conformity results in a good load (reaction forces) transference between plate and impactor. As impact goes on, the meshes lose their conformity, thus affecting the load transference from the plate to impactor. See Appendix C for a more detailed analysis.

It is worth to mention that these are preliminary results, intended to evaluate the impact response of the algorithm for non-conforming meshes and further development is required. This problem evidences the importance of a conservative transference of loads in Dirichlet-Neumann type contact algorithms for impact problems. For fixed interfaces, as in the case of fluid-structure interaction problems, several methods based on conservative load interpolation schemes that can deal with the information transfer between non-matching meshes have been proposed (see [75, 20], among others). However, to the best of our knowledge, the extension of such methods to moving interfaces has not been yet reported, and their implementation in a parallel computational code is not straightforward and requires additional development. This key issue is left for future work.

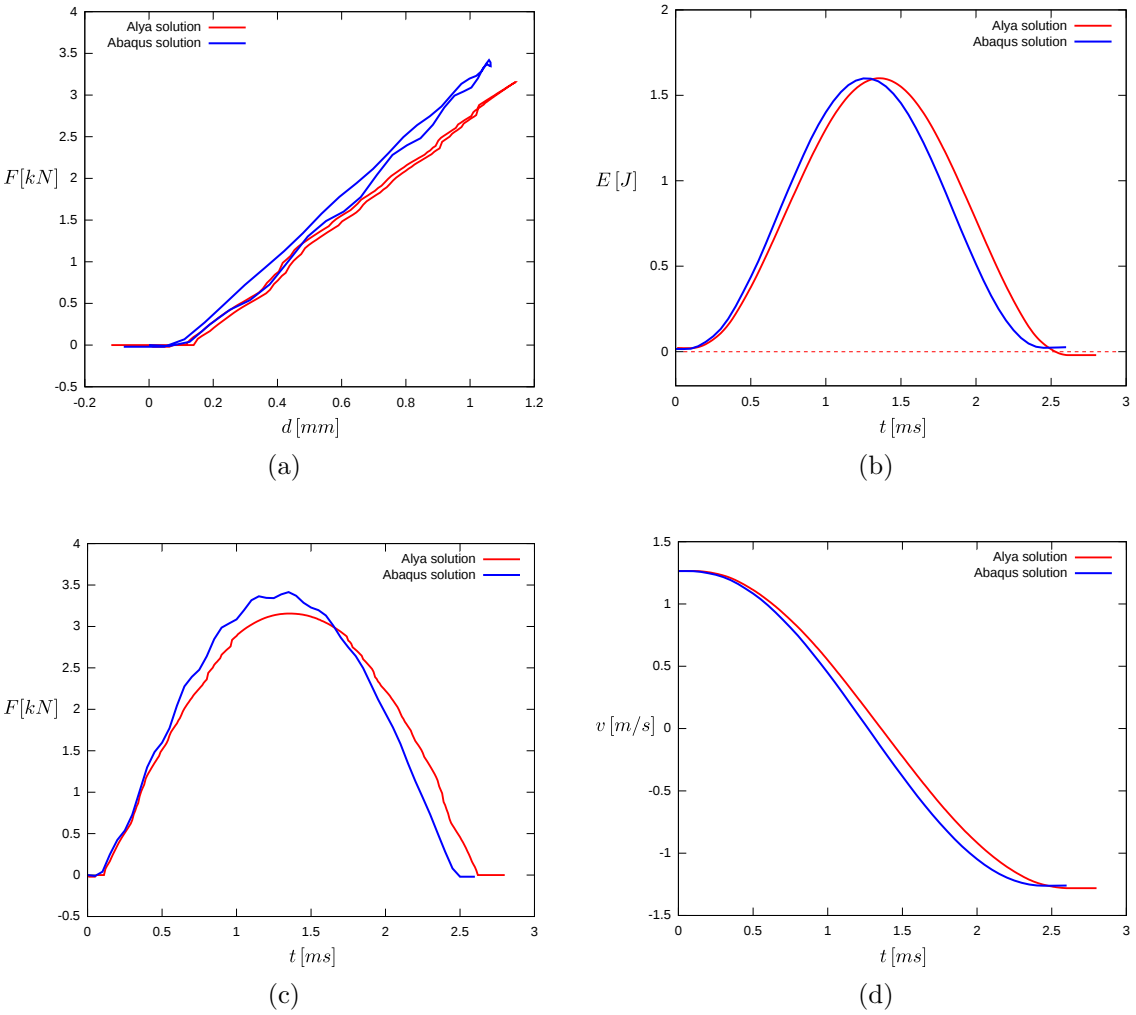

Figure 5.32: Impact problem - (a) Impact force vs. displacement. (b) Impactor energy vs. time. (c) Impact force vs. time. (d) Impactor velocity vs. time.

Chapter 6

Conclusions and Outlook

We dare say that any research work, including a PhD. thesis, is something that never truly ends. Its completion is simply determined by a matter of schedules, solely delimited by time. Nevertheless, summaries are essential as they serve as milestones that help to wrap up all that has been done and to discern which steps should be taken next. In this final chapter we recapitulate all the work done in this thesis, which allows to identify the goals achieved and to establish the potential future lines of development and improvement for this research.

6.1 Summary

This thesis was born by the necessity of solving industrial nonlinear frictional contact problems in parallel, by algorithms capable of executing in HPC-based machines. The computational platform required to be used for the implementation and execution of these algorithms is Alya, which is the Barcelona Supercomputing Center simulation code for multi-physics problems, specifically designed to run efficiently in supercomputers. To reach this objective, several milestones were achieved and passed during the development of this work. It is worth to mention that these milestones were taken as a reference to give structure to this manuscript. In the following list we enumerate in order of accomplishment the most significant of them:

- Reach a comprehensive overview of the state-of-the-art in computational contact mechanics and a clear understanding of the governing equations and the classical methods used for the numerical resolution of these type of problems.
- Understand the workflow of a high-performance parallel computational code as Alya, and the way that domain decomposition is applied for the resolution of parallel nonlinear solid mechanics problems.
- Identify and analyze the strengths and weakness of classical methods in computational contact mechanics, together with the feasibility for they parallel implementation in a high performance computational code, considering the design basis established for such end.

- In response to the fact that standard contact algorithms are not a suitable alternative for efficient parallelization, propose a novel methodology for the parallel numerical resolution of frictional contact problems between deformable bodies, which also suits the design basis previously established.
- Develop from scratch a nonlinear finite element code to be used as a framework for a proof of concept study of the proposed algorithm.
- Describe and implement the parallel contact algorithm in Alya code, for both 2D and 3D frictional contact problems.
- Validate and test the parallel implementation with benchmark test cases and real numerical problems.

6.2 Contributions

Motivated by the fact that standard contact algorithms are not a suitable alternative for efficient parallelization and the lack of scientific literature regarding those issues, the main result of this thesis is the introduction of a novel general parallel contact algorithm based on domain decomposition methods which can run efficiently in HPC-based supercomputers, considering in a unified way: physical, numerical, algorithmic and computational aspects. In this sense, we can remark the three most important contributions of this work: (1) we have idenfied, analyzed and enumerated the drawbacks that standard methods present when they are implemented in parallel environments under a domain decomposition approach, (2) we have proposed a novel methodology for the parallel solution of frictional contact problems, explicitly designed to meet the requeriments of the state-of-the-art HPC-based systems, and (3) we have described in detail the parallel computational implementation of the algorithm, which has been validated and tested with benchmark test cases and real numerical problems.

Several features of the multicode Dirichlet-Neumann type contact algorithm introduced in this work can be highlighted, which define the uniqueness and originality of the proposed method:

- The bodies in contact are treated separately, in a segregated way. From a computational point of view this feature allows to use a multicode apporach, which means to use different computational code instances for each of the contacting bodies.
- It makes use of a completely new approach for the contact detection and for the enforcement of the contact constraints. The contact detection is done by means of a parallel location and exchange library (PLE++), which allows to detect the penetrated nodes even when they are distribuited among different processors.
- The contact is treated as a coupled problem, where the coupling of the contacting bodies is done through Dirichlet and Neumann boundary conditions transfer at the contact zone. The transference of the boundary conditions is also accomplished by the PLE++ library, which relies on the Message Passing Interface (MPI) for parallel communication.

- It can be explained as a black-box parallel solver for frictional contact problems, as it allows to solve each body separately, even with different computational codes. The algorithm can be interpreted as a black-box which detects contact, transfers and enforce the contact boundary conditions at the contact interface of each body.
- In addition, the contact algorithm proposed in this thesis can also be formulated as a general fixed-point solver for the solution of interface problems. This generalization gives us the theoretical basis to extrapolate and implement numerical techniques that were already developed and widely tested in the field of Fluid-Structure Interaction (FSI) problems, especially those related to conservative interpolation schemes and convergence ensurance and acceleration.
- For the enforcement of the Multi-Point Constraints (MPC) which restricts the movement of the node only in the tangential plane, we propose to use a novel solution where we rotate the local frame of reference for each of the contacting nodes, instead of using Lagrange multipliers, which adds extra unknowns to the system.
- The size of the linear system of equations to be solved at each time step remains fixed, since no Lagrange multipliers are used.
- As the algorithm does not rely on contact elements for the discretization of the contact interface, there is no need to update the mesh graph on run time. The mesh partitioning is done at the beginning of the simulation, as a preprocessing task, independently on each body and without restricting the mesh partitioner.
- The multicode approach of the algorithm allows to treat each body independently, as the contact coupling is done only through the transference of boundary conditions at the contact zone. This gives a great flexibility since different inputs files can be used. Different mesh types, material models, damage models, time integration schemes, solvers, preconditioners, etc, can be defined for each body, as if they were in a standalone simulation.

6.3 Future research perspectives

Despite the fact that this work offers a comprehensive solution for the numerical parallel solution of industrial contact problems, is only a first step towards the parallel modelling of this type of problems in a very robust and efficient way. As parallel computing platforms became of general access to the scientific and engineering community only few years ago, there is a considerable lack of scientific literature on parallel contact algorithms. All those years the trend in the computational contact mechanics field seems to have been the adaptation of existing classical methodologies to parallel environments instead of developing from scratch new strategies fully consistent with these new architectures. This thesis intends to take a first step towards this direction. Having said that, a wide range of possibilities for further improvement or development arise as a natural continuation of this work. Based on what we have presented here and the topics which were only marginally covered or not addressed at all, some suggestions for future research lines are presented below:

- We have developed and implemented and algorithm for deformable two-body contact problems. Following the same ideas, the extension to self-contact or multi-body contact problems is an interesting topic to be covered.

- We did not implement a frictional model in the bilateral contact algorithm. Nevertheless, for certain types of bilateral contact problems, friction is crucial and must be considered in the contact resolution. Friction is an interesting but complex phenomena, and an open line of research in the field of computational contact mechanics.

- We have proposed an staggered algorithm, in which one code instance is idle while the other is solving, and viceversa (known as *Gauss-Seidel* scheme). Despite the fact that this apporach is more robust than if the two bodies were executed simultaneously (*Jacobi* scheme), is not optimal in terms of the exploitation of the computational resources. The implementation of a simultaneous scheme and its comparison with the staggered scheme is an interesting task to be performed in order to compare robustness, execution time, efficiency, etc, of both strategies.

- We noted that MPC impact negatively on the speed of convergence to the solution. This becomes more evident as the number of nodes on the active contact zone increase. Motivated by this fact, the issue of tailored iterative solvers or preconditioning techniques that help to accelerate the convergence of the resulting linear system of equations in each solution step has a lot of room for improvement.

- All the implementations and numerical examples in this work has been done with linear elements. Higher order elements, or even the smooth interpolation of contact surfaces with large curvatures will provide improved definition of the contacting surfaces. Among several issues related with the lack of a smooth definition at the contact boundary one may find: inaccurate prediction of the traction distribution or other relevant contact-related quantity, spurious oscillations, inexact contact detection and even convergence problems of the nonlinear solution scheme.

- Load transfer between nonconforming interfaces is one of the key areas of challenges in partitioned approaches as the one presented in this thesis. The level of the accuracy in the load transference have significant impact on the solution of the coupled system. In this thesis we did not evaluate the performance of the algorithm with different load transfer schemes. Due to the impact that this issue has on the performance of the algorithm is worth to be considered for analysis in a next future.

- We have observed that the performance of Dirichlet-Neumann contact algorithm is strongly determined by the relaxation strategy. The calculation of a specific relaxation parameter in each iteration step proved to be crucial. Due to this observations, special emphasis should be put in future works on developing optimal dynamic relaxation strategies. We believe that a deeper analysis in this subject and more comparisons with available Newton field solvers for the interface problem such as Interface Quasi-Newton (IQN) [33] or Broyden [26]

methods are worth to be done in order to gain more insight on efficient techniques for the resolution of contact problems using Dirichlet-Neumann partitioned algorithms.

- The applicability of the developed computational approach to more realistic scenarios has to be proven with further large-scale simulations, including impact analysis considering cohesive materials and damage models.
- Scalability tests in even bigger scenarios are worth to be analyzed and strong efforts for improving the code scalability will have favourable consequences in several aspects which range from faster simulations to efficiency in the exploitation of computational resources.
- Ostero code have proven to be a very useful didactic tool for testing algorithms before they are implemented in more complex computational codes of industrial scale, as Alya. This previous step allows to reduce the source of errors due to the larger input files that bigger codes have and facilitates the debugging of the new segments of code. Ostero is not a finished work, still few improvements must be done. In special, its extension to 3D and parallelization.

Appendix A

Computational Environment

A.1 Alya

The algorithms described in Chapters 4 and 5 were implemented within a computational environment designed for heterogeneous problems in computational mechanics. This framework is called *Alya*. It is fully developed at the Barcelona Supercomputing Center, within the department of Computer Applications for Science and Engineering (CASE). Alya is not a born-sequential simulation code which was parallelized afterwards. Instead, it was designed from scratch as a multi-physics parallel code. The efficient solution of large problems on massively parallel computers was the driving justification behind its development. This section describes its main features.

Alya is a multi-physics, three-dimensional modular code for high performance computational mechanics. It solves discretized partial differential equations (PDEs), prefering variational methods (particularly Finite Elements). It is capable of solving different physics problems, each one with its own modelling characteristics, in a coupled way. Alya runs efficiently in Marenostrum, the most powerful supercomputer in Spain, hosted by the *Barcelona Supercomputing Center*. Alya has shown high parallel efficiency up to several thousands of cores for different physical problems [29, 68, 70, 119]. Its scalability was benchmarked on different architectures such as Intel Nehalem, Sandy Bridge, Xeon Phi and IBM PPC. In Blue Waters, the supercomputer hosted in the National Center for Supercomputing Applications (NCSA), Alya code presented a performance up to 100000 cores, achieving more than 85% parallel efficiency [132].

Alya's architecture is modular, being organized into three main blocks: *kernel*, *services* and *modules*, which can be separately compiled and linked. Each module represents a single set of partial differential equation for a given physical model (e.g. solid mechanics, fluid mechanics, heat transference, etc) and manages the respectively boundary conditions. Therefore, to solve a multi-physics problem, all the required modules must be active and interacting following a well defined workflow. Alya's kernel controls the run: it contains the solvers, the input-output workflow

and all the tools related to the mesh and geometry management. Is responsible for the control of the code's workflow by management of the interconnections between the modules, services and itself. Algorithmically speaking, the most important tasks of the kernel are: reading of the computational mesh and arrangement of the mesh data for domain splitting; construction of the finite element tools to be used by each module (e.g. basis functions) and solving the linear system of equations that results from the finite element approximation. The kernel and the modules allows a given physical problem to be completely solved. The services are supplementary tools, as the parallelization service or the HDF5 format writer. Kernel, modules and services have well defined interfaces and connection points.

The parallelization of Alya is a service implemented in the source code and is based on mesh partitioning (for instance unsing METIS [78]) and MPI tasks, which is specially well-suited for distribuited memory machines and it uses a Master-Slave strategy. Based on the Master-Slave strategy, the master is in charge of reading the mesh, performing the mesh partitioning and writing the output files. Each slave is in charge of an specific subdomain and its main tasks are the construction of the local right-hand side, the local system matrices and the solution of the resulting system. Each slave is administrated by one computational process, thus conforming the relation between slave, subdomain and computational process. In the assembling tasks, no communication is needed between the slaves. Therefore, in this instance, the scalability only depends on the load balance. Due to the necessity of communications, the solution of the linear system the scalability depends on the interfaces (which are minimized by METIS), and the communication scheduling. All the details on the parallelization of Alya can be found in [68].

In Fig. A.1 we show a schematic flowchart for the execution of a parallel simulation using Alya. The tasks executed by the master process are shown on the left side of the same figure with grey background. As explained in previous paragraph, the master performs the first steps of the execution, namely reading the file and partitioning the mesh. Afterwards, the master sends the corresponding subdomain information to the slave processes. Next, the master and slaves enter into the time and linearization loops. Along with the execution of the iterative solvers carried out by the slaves, two types of communications are required to exchange interface information with the neighbour nodes of each subdomain. The exchange of the interface information is performed using the MPI functions `MPI_Sendrecv`, used for the sparse matrix-vector products and `MPI_Allreduce`, used to compute residual norms and scalar products.

A.1.1 Numerical issues - solid mechanics module

The computational solid mechanics problem is solved using a standard Galerkin method for a large deformation framework and a generalized Newmark time integration scheme. This framework is developed in a Total Lagrangian formulation. A large database of element types is available for the solid mechanics module together with explicit and implicit solvers for the non-linearity. The implicit solver is based on the Newton-Raphson method. Well known constitutive equations for large deformation elasticity constitutive models, such as the neo-Hookean or specific hyperelastic models, are also available.

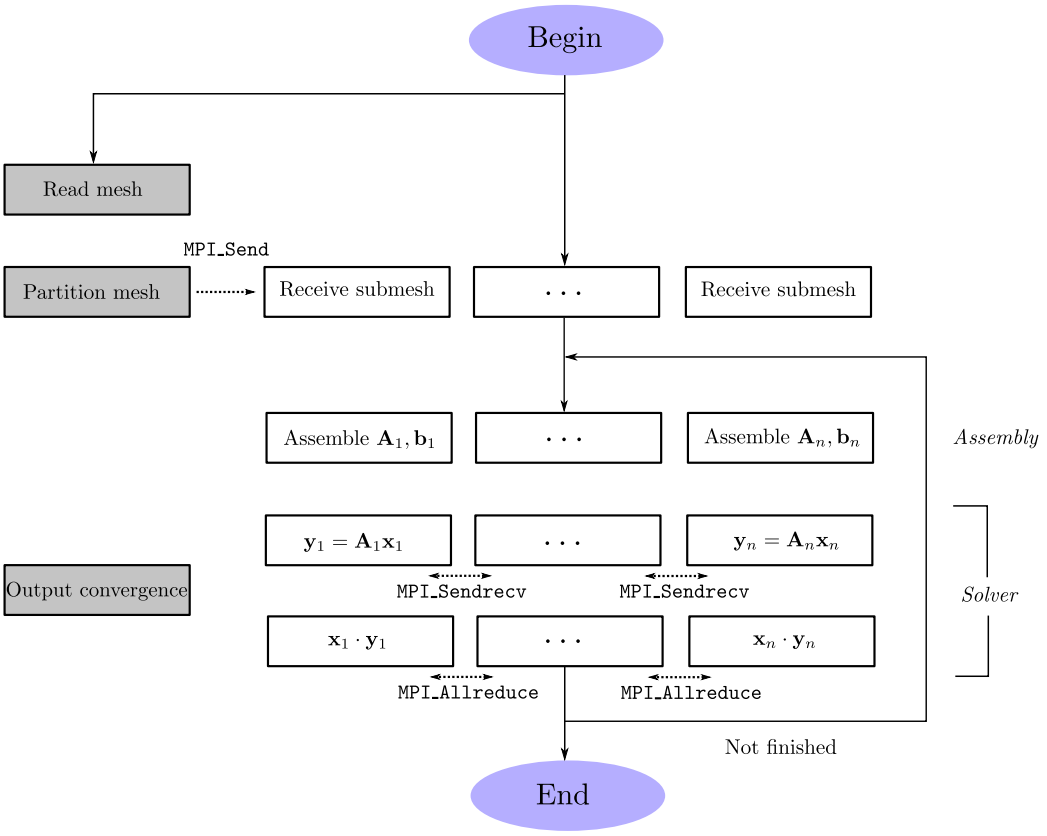

Figure A.1: Parallel flowchart of Alya. Master (grey) and slaves (white).

Fig. A.2 shows a flowchart of the *solidz* module. All the geometrical and physical data of the problem are introduced as input files. Once the input files are read, Alya initializes the computation within the solidz module, either in serial or parallel mode. The parallel service must be specified in the input files.

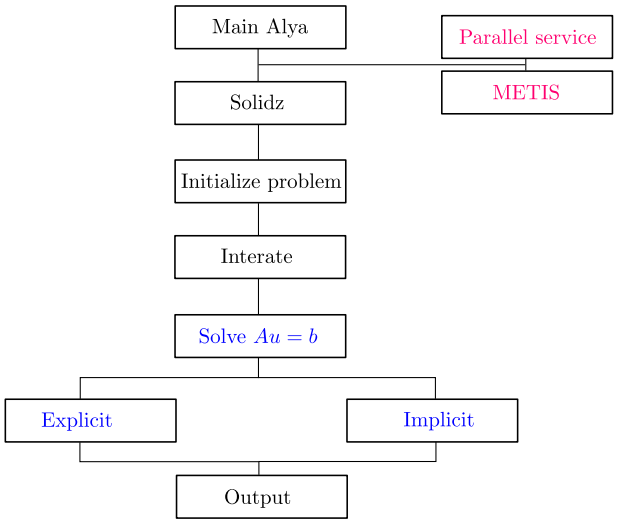

Figure A.2: *solidz* module structure in Alya code.

A.2 Ostero

The aim of this section is to do a briefly presentation of Ostero. Ostero is a didactic finite element code for the numerical simulation of solid deformable bodies. It was developed as part of this thesis, to use it as a test framework for several mechanical models and problems. It is a very useful tool to perform proof-of-concept evaluations of contact mechanics algorithms and damage models before implementing them in the BSC's Alya code, which is a bigger, powerful but more complex code. Ostero was successfully used for the proof-of-concept and *beta-testing* of all of the algorithms proposed in this thesis. Ostero was also succesfully used by PhD. students at the *Barcelona Supercomputing Center* and by BSc. students at the *Universidad de Buenos Aires*. As a general fact, Ostero was designed in order to first: provide the user a clear idea of the structure that usually a finite element code for linear and nonlinear mechanics has, and second: to allow the user to use Ostero as a workbench for personal tests. For further information the reader is refered to the hosting web page of Ostero https://bitbucket.org/matrivero/ostero, where the source code and the user manual are freely available.

A.2.1 Description

Ostero is an open source finite element code that solves the continumm equation which governs the mechanics of a deformable body subjected to external forces, Dirichlet and/or Neumann boundary conditions. In other words, Ostero allows to determine the response of a deformable solid body to an applied external load or displacement. Ostero allows to solve a mechanical problem considering geometric linearity or non-linearity. For geometric non-linearity it uses a Total Lagrangian formulation. For the specific case of the geometrical nonlinear model, Ostero uses an implicit scheme based on the Newton-Raphson method, while the update of tangent matrix is performed at each time step. When a given problem is solved using a geometrically linear setting, the equations of equilibrium are formulated in the undeformed state, and are not updated with the deformation. In some engineering problems, as the deformations are considered small and the deviation from the original geometry is not perceptible, the use of a geometrically linear setting is a very good approximation to the nonlinear model. The mathematical complexity generated by a more realistic theory and the associated increment of the computation time does not compensate the small error introduced by ignoring the update of deformations in the equilibrium equations. But in the engineering field there are also a number of problems where the deformation (large strains and/or large rotations) cannot be ignored. In those cases a geometrically nonlinear model should be used in Ostero to account for the large deformations. It is part of the engineering criteria to choose which model, linear or nonlinear, could be use.

Ostero is based on the solid mechanics module of the Alya code. It can solve quasi-static or transient problems using triangles or quadrilateral linear elements. For the time integration it uses a generalized Newmark integration scheme. The geometrically nonlinear module includes the isolinear (or Kirchhoff) material model and several formulations of the hyperelastic neo-Hookean material model. Recently, a simple damage model was also added to the code.

Ostero intends to be a didactic code, and its main objective is to allow the user to understand

the very basic structure of a linear and nonlinear mechanics finite element code. Also intends to provide a framework for beta testing of different models such as elastic material models, contact, plasticity, fracture, etc.

Ostero was also designed to interact seamlessly with open source meshing and post-processing tools. In that sense, Ostero reads mesh files generated using the open source meshing tool Gmsh, without need of additional conversions to adapt the mesh file format to the input requested by Ostero. On the other hand, Ostero writes outputs in Vtk ASCII format, which can be easily postprocessed using the open source post-processing tool ParaView.

Ostero was written in Python and Fortran to exploit the main advantages and properties of each programming language. The parsing of the input parameters, boundary conditions and other options is done in the main program, coded in Python. The way that Ostero manages the user input is through the usage of dictionaries in Python. For didactic purposes this coding strategy is a convenient choice. From the developer's viewpoint it allows a tidy and understandable programming. On the other hand, from the user perspective, it allows to write very flexible and lexical inputs. The main program also includes the main execution loop, which calls the subroutines that performs the elementary matrix calculations and the assembly operations from the Fortran module. This external Fortran module is imported in the main program as an external library. For the resolution of the linear system of equations resulting from the finite element discretization, Ostero uses NumPy, which is the fundamental package for scientific computing with Python.

Algorithm 12 shows the workflow of Ostero. Next to each task we identify which part of the code is in charge of each operation. For efficiency matters, all those operations such as derivatives computation and matrix assembly which involves a large amount of iterations, are performed by the external pre-compiled Fortran subroutine, while the parsing of the input files and the main loop control is done by the main Python script. The output is written in Vtk format by an external Python function.

Algorithm 12 Ostero workflow

```
read main input file                                   ▷ (main python program)
read mesh file                                         ▷ (main python program)
read boundary conditions file                          ▷ (main python program)
compute jacobian and derivatives                       ▷ (fortran external lib)
for time = 1 to total_time do                          ▷ time loop
    impose boundary conditions                         ▷ (main python program)
    while not converged do                             ▷ nonlinear iterations
        matrix assembly                                ▷ (fortran external lib)
        solve linear system                            ▷ (main python program, Numpy)
    end while
    write output                                       ▷ (vtk python external lib)
end for
```

A.2.2 How to get Ostero

Ostero is hosted in my personal *Bitbucket* space: https://bitbucket.org/matrivero/ostero. The source code and user manual can be downloaded there. Bitbucket is a web-based hosting service for projects that use *Mercurial* or *Git* revision control systems. Bitbucket is similar to *GitHub* (which primarily uses Git), but the main difference is that Bitbucket allows free private repositories, while in GitHub only public repositories are available for free users. Besides being hosted in Bitbucket server, Ostero is under Git revision control, which provides a perfect framework for collaborative development. Git is a free and open source distributed version control system, which allows to manage changes in the code in a very efficient way. Is an essential tool for collaborative projects, but also very useful for individual programmers. Git takes a peer-to-peer approach to version control, as opposed to the client-server approach of centralized systems, as SVN. Rather than a single, central repository on which clients synchronize, in Git each peer's working copy is the complete repository which includes the complete history information of the codebase.

Appendix B

Physical Interpretation of the Newton's Method Residual

The discrete momentum equation at time step $n+1$ in a form applicable to both equilibrium and dynamic problems is:

$$\mathbf{0} = \mathbf{r}(\mathbf{d}^{n+1}, t^{n+1}) = s_D \mathbf{M}\mathbf{a}^{n+1} + \mathbf{f}^{\text{int}}(\mathbf{d}^{n+1}, t^{n+1}) - \mathbf{f}^{\text{ext}}(\mathbf{d}^{n+1}, t^{n+1}), \tag{B.1}$$

where s_D is a switch which is set by: $s_D = 0$ for a static (equilibrium) problem, and $s_D = 1$ for a dynamic (transient) problem. The vector $\mathbf{r}(\mathbf{d}^{n+1}, t^{n+1})$ is called a residual. The discrete equations for both the implicit update of the equations of motion and the equilibrium equations are nonlinear algebraic equations in the nodal displacements, $\mathbf{d}^{n+1}$.

The most widely used and most robust method for the solution of nonlinear algebraic equations is Newton's method. The method is often called Newton-Raphson method in computational mechanics. The solution of Eq. (B.1) by Newton's method is an iterative procedure. The iteration number is indicated by Greek subscript: $\mathbf{d}_\nu^{n+1} \equiv \mathbf{d}_\nu$ is the displacement in iteration ν at time step $n+1$; the time step number $n+1$ will be omitted in the following.

To begin the iterative procedure, a starting value for the unknown must be chosen; usually the solution $\mathbf{d}^n$ for the previous time step is selected, so $\mathbf{d}_0 \equiv \mathbf{d}^n$. A Taylor expansion of the residual about the current value of the nodal displacement $\mathbf{d}_\nu$ and setting the resulting residual equal to zero gives:

$$\mathbf{0} = \mathbf{r}(\mathbf{d}_{\nu+1}, t^{n+1}) = \mathbf{r}(\mathbf{d}_\nu, t^{n+1}) + \frac{\partial \mathbf{r}(\mathbf{d}_\nu, t^{n+1})}{\partial \mathbf{d}} \Delta\mathbf{d} + O(\Delta\mathbf{d}^2), \tag{B.2}$$

where

$$\Delta\mathbf{d} = \mathbf{d}_{\nu+1} - \mathbf{d}_\nu. \tag{B.3}$$

If the terms which are higher order than linear in $\Delta\mathbf{d}$ are dropped, then Eq. (B.2) gives a linear equation for $\Delta\mathbf{d}$:

$$\mathbf{0} = \mathbf{r}(\mathbf{d}_\nu, t^{n+1}) + \frac{\partial \mathbf{r}(\mathbf{d}_\nu, t^{n+1})}{\partial \mathbf{d}} \Delta \mathbf{d}. \tag{B.4}$$

The above is called a *linear model* or *linearized model of the nonlinear equations*. The linear model is tangent to the nonlinear residual function. Note that in the Taylor expansion, the residual is written in terms of the time t^{n+1}. The time-dependence of the residual is usually explicitly given. For example, the tractions and body forces are usually given as functions of time, and any change in the external load forces is due to changes in the nodal displacements. Therefore the residual is ordinarily computed using the load at time t^{n+1} and the latest value of the nodal displacements.

Solving this linear model for the incremental displacements gives:

$$\frac{\partial \mathbf{r}(\mathbf{d}_\nu, t^{n+1})}{\partial \mathbf{d}} \Delta \mathbf{d} = -\mathbf{r}(\mathbf{d}_\nu, t^{n+1}) \quad \Longrightarrow \quad \Delta \mathbf{d} = -\Big(\frac{\partial \mathbf{r}(\mathbf{d}_\nu, t^{n+1})}{\partial \mathbf{d}}\Big)^{-1} \mathbf{r}(\mathbf{d}_\nu, t^{n+1}). \tag{B.5}$$

In the Newton procedure, the solution to the nonlinear equation is obtained by iteratively solving a sequence of linear models given by Eq. (B.5). The new value for the unknown in each step of the iteration is obtained by rewriting Eq. (B.3) as:

$$\mathbf{d}_{\nu+1} = \mathbf{d}_\nu + \Delta \mathbf{d}. \tag{B.6}$$

The process is continued until the solution is obtained with the desired level of accuracy.

In a Total Lagrangian formulation, the residual $\mathbf{r}(\mathbf{d}_\nu, t^{n+1})$ can be expressed in absence of exterior forces using index notation as (see [16]):

$$r_i^b = \int_{\Omega_0} P_{iJ} \frac{\partial N^b}{\partial X_J} \, d\Omega_0, \tag{B.7}$$

where P_{iJ} is the first Piola-Kirchhoff stress tensor, $\partial N^b / \partial X_J$ are the shape function derivatives with respect to the reference frame coordinates and Ω_0 corresponds to the reference domain. From now on we will suppose, without loss of generality and in order to save notation, that the following volumetric integrals are done at the elementary level ($\Omega \to \Omega^e$).

The two-point first Piola-Kirchhoff stress tensor P_{iJ} can be related to the Cauchy's stress tensor σ_{ik}, which is fully expressed in the deformed configuration (see [24]):

$$P_{iJ} = J \sigma_{ik} (F^{-1})_{Jk}, \tag{B.8}$$

where F is the deformation gradient and J the transformation jacobian. Then, we can rewrite Eq. (B.7) using relation of Eq. (B.8) as follows:

$$r_i^b = \int_{\Omega_0} P_{iJ} \frac{\partial N^b}{\partial X_J} \, d\Omega_0 = \int_{\Omega_0} J \sigma_{ik} (F^{-1})_{Jk} \frac{\partial N^b}{\partial X_J} \, d\Omega_0. \tag{B.9}$$

As reference and deformed configurations are related by the transformation $J d\Omega_0 = d\Omega$, then:

$$r_i^b = \int_\Omega \sigma_{ik} (F^{-1})_{Jk} \frac{\partial N^b}{\partial X_J} \, d\Omega. \tag{B.10}$$

Furthermore, as $(F^{-1})_{Jk} = \dfrac{\partial X_J}{\partial x_k}$, then:

$$r_i^b = \int_\Omega \sigma_{ik} \frac{\partial X_J}{\partial x_k} \frac{\partial N^b}{\partial X_J} \, d\Omega, \tag{B.11}$$

which is equivalent to:

$$r_i^b = \int_\Omega \sigma_{ik} \frac{\partial N^b}{\partial x_k} \, d\Omega. \tag{B.12}$$

Please note that Eq. (B.12) allows to compute the residual using only measures which are expressed in the deformed configuration. If we multiply Eq. (B.12) at both sides by the displacements vector u_i^b, then:

$$r_i^b \, u_i^b = \int_\Omega \sigma_{ik} \frac{\partial N^b}{\partial x_k} \, d\Omega \, u_i^b. \tag{B.13}$$

As u_i^b does not depend on the system coordinates, we can include it inside of the integral of Eq. (B.13):

$$r_i^b \, u_i^b = \int_\Omega \sigma_{ik} \frac{\partial N^b}{\partial x_k} \, u_i^b \, d\Omega = \int_\Omega \sigma_{ik} \, \varepsilon_{ik} \, d\Omega, \tag{B.14}$$

where ε_{ik} is the Cauchy's strain tensor. Rewriting Eq. (B.14) in vectorial form gives:

$$(\underline{R}^b)^T \, \underline{u}^b = \int_\Omega \underline{\underline{\varepsilon}}^T \, \underline{\underline{\sigma}} \, d\Omega. \tag{B.15}$$

Right-hand side of Eq. (B.15) represents the work done by the internal forces of Ω. Thus, residual vector $\underline{R}^b$ equals to the forces at each node b of element e. For those nodes subjected to Dirichlet-type boundary conditions these forces correspond to the reactions.

Appendix C

Load Transference Analysis

We apply here a simple methodology to address the accuracy of the interpolation strategy used in this work across similar but non-matching contact interfaces. In the adopted strategy the interface variables (reaction forces) are interpolated using shape function of elements. See Sec. 5.3.1 for further details.

We consider a test set-up, which consists of two blocks with slightly non-matching meshes and a plane contact interface, as shown in Fig. C.1. The upper and lower blocks have dimensions of $3.8 \times 3.8 \times 2.85$ and $6 \times 6 \times 2$ units, respectively. We assume a frictionless contact.

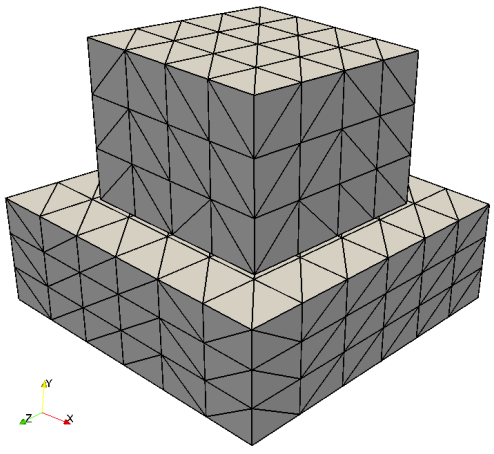

Figure C.1: Finite element meshes used in this analysis.

We employ a Neo-Hookean material law for both bodies. For the upper block we assign a Young's modulus $E = 10000$ and Poisson's ratio $\nu = 0.3$, while for the lower block we assign $E = 100$ and $\nu = 0.3$. In this tailor-made test the lower block is fixed in all directions at its bottom surface, while a total vertical displacement of -0.5 units (y-direction) is applied to the top surface of the upper block. This problem is solved as a quasi-static evolution using 20 time steps. The final deformed state for both bodies is shown in Fig. C.2.

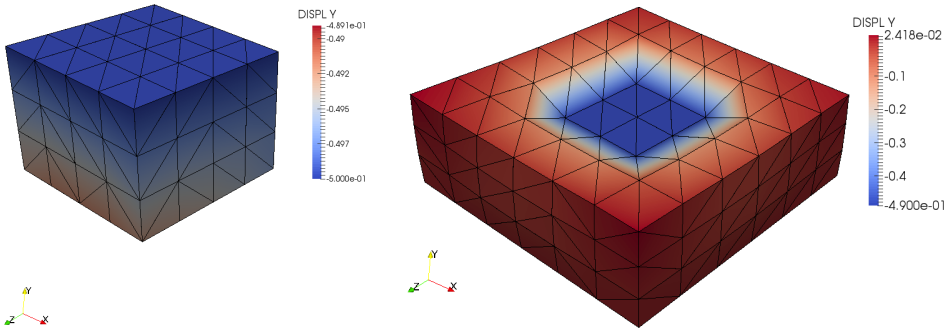

(a) (b)

Figure C.2: Deformed state at last time step. (a) Upper block. (b) Lower block.

To evaluate the load transference due to contact, we compute at each time step the total reaction force at the top surface of the upper block and at the bottom surface of the lower block. Due to Newton's third law, in the case of a perfect load transference both total reaction forces should be exactly equal at each time step. Fig. C.3 shows a comparison of the computed magnitudes for all the simulation time. We observe that curves exactly match at the beginning. However, they apart as the simulation advances, which indicates that at those instants of time forces are not exactly transferred. This can be explained due to the effect of loss of conformity between meshes. At the beginning, meshes are slightly non-matching. Nevertheless, as time advances, the lower block suffers a bigger deformation than the upper block, which affects the initial configuration of the meshes at the contact interface. As meshes lose their similarity, the effects of the non-conservativeness of the load transference become relevant.

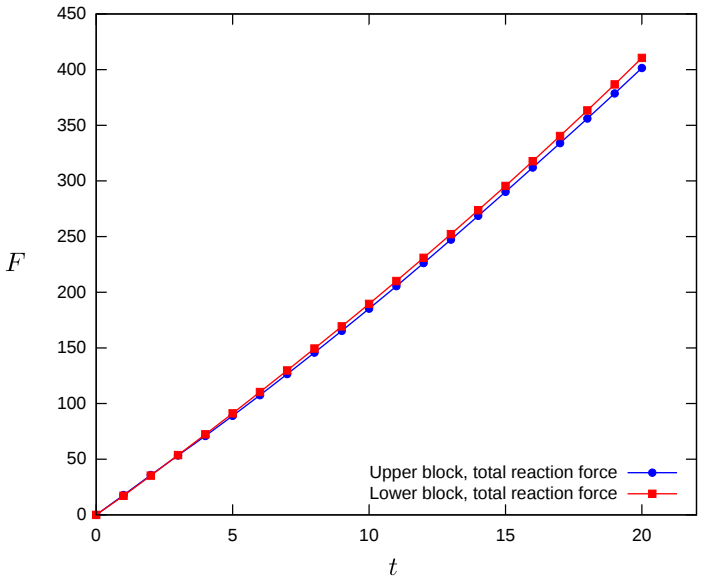

Figure C.3: Total reaction force at each time step. Forces are measured at the top surface of upper block and at the bottom surface of lower block.

Bibliography

[1] *Abaqus unified FEA*. URL: https://www.3ds.com/products-services/simulia/products/abaqus/.

[2] M. R. Abir et al. "Modelling damage growth in composites subjected to impact and compression after impact". In: *Composite Structures* 168 (2017), pp. 13–25.

[3] *ADINA – Finite element analysis software*. URL: http://www.adina.com/.

[4] P. Alart and A. Curnier. "A mixed formulation for frictional contact problem prone to Newton like solution methods". In: *Computer Method in Applied Mechanics and Engineering* 92 (1991), pp. 353–375.

[5] *ANSYS Structures*. URL: http://www.ansys.com/products/structures.

[6] *ASTM D7136/D7136M-05, Standard Test Method for Measuring the Damage Resistance of a Fiber-Reinforced Polymer Matrix Composite to a Drop-Weight Impact Event*. Standard. ASTM International, 2005.

[7] S. W. Attaway et al. "A parallel contact detection algorithm for transient solid dynamics simulations using PRONTO3D". in: *Computational Mechanics* 22.2 (1998), pp. 143–159.

[8] K. J. Bathe and A. Chaudhary. "A solution method for planar and axisymmetric contact problems". In: *International Journal for Numerical Methods in Engineering* 21 (1985), pp. 65–88.

[9] K.-J. Bathe, E. Ramm, and E. L. Wilson. "Finite element formulations for large deformation dynamic analysis". In: *International Journal for Numerical Methods in Engineering* 9 (1975), pp. 353–386.

[10] G. Bayada, J. Sabil, and T. Sassi. "Algorithme de Neumann-Dirichlet pour des problèmes de contact unilatéral: résultat de convergence". In: *Comptes Rendus Mathematique* 335 (2002), pp. 381–386.

[11] G. Bayada, J. Sabil, and T. Sassi. "A Neumann-Neumann domain decomposition algorithm for the Signorini problem". In: *Applied Mathematics Letters* 17 (2004), pp. 1153–1159.

[12] G. Bayada, J. Sabil, and T. Sassi. "Convergence of a Neumann-Dirichlet algorithm for two-body contact problems with non local Coulomb's friction law". In: *Mathematical Modelling and Numerical Analysis* 42 (2008), pp. 243–262.

[13] F. P. Beer and E. R. Johnston. *Mechanics of materials*. 2nd ed. McGraw-Hill, 1992.

[14] F. Ben Belgacem. "The mortar finite element method with Lagrange multipliers". In: *Numerische Mathematik* 84 (1999), pp. 173–197.

[15] F. Ben Belgacem, P. Hild, and P. Laborde. "The mortar finite element method for contact problems". In: *Mathematical and Computer Modelling* 28 (1998), pp. 263–271.

[16] T. Belytschko, W. K. Liu, and B. Moran. *Nonlinear finite elements for continua and structures*. 1st ed. Wiley, 2006.

[17] D. J. Benson and J. O. Hallquist. "A single surface contact algorithm for the post-buckling analysis of shell structures". In: *Computer Methods in Applied Mechanics and Engineering* 78 (1990), pp. 141–163.

[18] C. Bernardi, Y. Maday, and A. T. Patera. "A new nonconforming approach to domain decomposition: the mortar element method". In: *Nonlinear partial differential equations and their applications*. Ed. by H. Brezis and J. Lions. Wiley, 1994, pp. 13–51.

[19] D. Blom et al. "A review on fast quasi-Newton and accelerated fixed-point iterations for partitioned fluid-structure interaction simulation". In: *Y. Bazilevs, K. Takizawa (eds) Advances in Computational Fluid-Structure Interaction and Flow Simulation. Modeling and Simulation in Science, Engineering and Technology.* (2016), pp. 257–269.

[20] A. de Boer, A. H. van Zuijlen, and H. Bijl. "Review of coupling methods for non-matching meshes". In: *Computer Methods in Applied Mechanics and Engineering* 196 (2007), pp. 1515–1525.

[21] A. E. J. Bogaers et al. "Quasi-Newton methods for implicit black-box FSI coupling". In: *Computers Methods in Applied Mechanics and Engineering* 279.1 (2014), pp. 113–132.

[22] P. Boieri, F. Gastaldi, and D. Kinderlehrer. "Existence, uniqueness, and regularity results for the two-body contact problem". In: *Applied Mathematics and Optimization* 15.1 (1987), pp. 251–277.

[23] E. G. Boman et al. "The Zoltan and Isorropia parallel toolkits for combinatorial scientific computing: Partitioning, ordering and coloring". In: *Scientific Programming* 20.2 (2012), pp. 129–150.

[24] J. Bonet and R. D. Wood. *Nonlinear continuum mechanics for finite element analysis*. 2nd ed. Cambridge University Press, 2008.

[25] F. Brezzi and M. Fortin. *Mixed and hybird finite element methods*. Springer Verlag, 1991.

[26] C. G. Broyden. "A class of methods for solving nonlinear simultaneous equations". In: *Mathematics of Computation* 19 (1965), pp. 577–593.

[27] R. Budynas and K. Nisbett. *Shigley's mechanical engineering design*. 8th ed. McGraw-Hill, 2008.

[28] L. T. Campos, J. T. Oden, and N. Kikuchi. "A numerical analysis of a class of contact problems with friction in elastostatics". In: *Computer Methods in Applied Mechanics and Engineering* 34.1-3 (1982), pp. 821–845.

[29] E. Casoni et al. “Alya: Computational solid mechanics for supercomputers”. In: *Archives of Computational Methods in Engineering* 22.4 (2015), pp. 557–576.

[30] J. H. Cheng and N. Kikuchi. “An analysis of metal forming processes using Lagrange deformation elastic-plastic formulations”. In: *Computer Methods in Applied Mechanics and Engineering* 49 (1985), pp. 71–108.

[31] *Code_Aster Open Source – General FEA software*. URL: http://www.code-aster.org.

[32] A. Curnier and P. Alart. “A generalized Newton method for contact problems with friction”. In: *Journal de Mécanique Théorique et Appliquée. Special issue: Numerical Methods in Mechanics of Contact involving Friction* (1988), pp. 67–82.

[33] J. Degroote, K-J. Bathe, and J. Vierendeels. “Performance of a new partitioned procedure versus a monolithic procedure in fluid-structure interaction”. In: *Computers and Structures* 87 (2009), pp. 793–801.

[34] Z. Dostál, A. Friedlander, and S. A. Santos. “Solution of coercive and semicoercive contact problems by FETI domain decomposition”. In: *Contemporary Mathematics* 218 (1998). conforming mesh, elastic frictionless, pp. 82–93.

[35] Z. Dostál, D. Horák, and D. Stefanica. “A scalable FETI-DP algorithm with non-penetration mortar conditions on contact interface”. In: *Journal of Computational and Applied Mathematics* 231 (2009), pp. 577–591.

[36] Z. Dostál, F. A. M. Gomez Neto, and S. A. Santos. “Solution of contact problems by FETI domain decomposition with natural coarse space projections”. In: *Computer Methods in Applied Mechanics and Engineering* 190 (2000). conforming mesh, elastic frictionless, pp. 1611–1627.

[37] Z. Dostál et al. “A scalable TFETI algorithm for two-dimensional multibody contact problems with friction”. In: *Journal of Computational and Applied Mathematics* 235 (2010), pp. 403–418.

[38] Z. Dostál et al. “A theoretically supported scalable TFETI algorithm for the solution of multibody 3D contact problems with friction”. In: *Computer Methods in Applied Mechanics and Engineering* 205 (2012), pp. 110–120.

[39] Z. Dostál et al. “Scalable FETI algorithms for frictionless contact problems”. In: *Domain Methods in Science and Engineering XVII. Lecture Notes in Computational Science and Engineering (LNCSE)*. ed. by U. Langer et al. Vol. 60. Springer, 2008, pp. 263–270.

[40] Z. Dostál et al. “Scalable TFETI algorithm for the solution of multibody contact problems of elasticity”. In: *International Journal for Numerical Methods in Engineering* 82 (2009), pp. 1384–1405.

[41] G. Duvaut and J. L. Lions. *Inequalities in mechanics and physics*. Springer, 1976.

[42] C. Eck and B. Wohlmuth. “Convergence of a Contact-Neumann iteration for the solution of two-body contact problems”. In: *Mathematical Models and Methods in Applied Sciences* 13 (2003), pp. 1103–1118.

[43] C. Farhat and F. X. Roux. "A method of finite element tearing and interconnecting and its parallel solution algorithm". In: *International Journal for Numerical Methods in Engineering* 32 (1991), pp. 1205–1227.

[44] *FEAP – Finite element analysis program.* URL: http://projects.ce.berkeley.edu/feap/.

[45] M. A. Fernández and M. Moubachir. "A Newton method using exact jacobians for solving fluid-structure coupling". In: *Computers & Structures* 83.2–3 (2005), pp. 127–142.

[46] K. A. Fischer and P. Wriggers. "Mortar based frictional contact formulation for higher order interpolations using the moving friction cone". In: *Computer Methods in Applied Mechanics and Engineering* 195 (2006), pp. 5020–5036.

[47] Y. Fournier. *Parallel location and exchange.* Tech. rep. Électricité de France (EDF), 2014.

[48] A. Francavilla and O. C. Zienkiewicz. "A note on numerical computation of elastic contact problems". In: *International Journal for Numerical Methods in Engineering* 9.4 (1975), pp. 913–924.

[49] J. Frohne, T. Heister, and W. Bangerth. "Efficient numerical methods for the large-scale, parallel solution of elastoplastic contact problems". In: *International Journal for Numerical Methods in Engineering* 105.6 (2016), pp. 416–439.

[50] F. J. Gallego and J. J. Anza. "A mixed finite element model for the elastic contact problem". In: *International Journal for Numerical Methods in Engineering* 28 (1989), pp. 1249–1264.

[51] J.-F. Gerbau, M. Vidrascu, and P. Frey. "Fluid-structure interaction in blood flows on geometries based on medical imaging". In: *Computers & Structures* 83.2–3 (2005), pp. 155–165.

[52] P. E. Gill, W. Murray, and M. H. Wright. *Practical Optimization.* Academic press, 1981.

[53] G. M. L. Gladwell. *Contact problems in the classical theory of elasticity.* Springer, 1980.

[54] R. Glowinski and P. Le Tallec. *Augmented Lagrangian and operator-splitting methods in nonlinear mechanics.* Vol. 28. 1989, pp. 1249–1264.

[55] W. Gropp, E. Lusk, and A. Skjellum. *Using MPI: Portable parallel programming with the message-passing interface.* The MIT Press, 2014.

[56] G. Hager and G. Wellein. *Introduction to high performance computing for scientists and engineers.* CRC Press, 2011.

[57] J. O. Hallquist, G. L. Goudreau, and D. J. Benson. "Sliding interfaces with contact-impact in large-scale Lagrangian computations". In: *Computer Methods in Applied Mechanics and Engineering* 51 (1985), pp. 107–137.

[58] J. Har and R. Fulton. "A parallel finite element procedure for contact-impact problems". In: *Engineering with Computers* 19 (2003), pp. 67–84.

[59] S. Hartmann et al. “A contact domain method for large deformation frictional contact problems. Part 2: Numerical aspects”. In: *Computer Methods in Applied Mechanics and Engineering* 198 (1992), pp. 2607–2631.

[60] J. Haslinger, R. Kúcera, and T. Sassi. “A domain decomposition algorithm for contact problems: analysis and implementation”. In: *Mathematical Modelling of Natural Phenomena* 4 (2009), pp. 123–146.

[61] J. Haslinger et al. “A domain decomposition method for two-body contact problems with Tresca friction”. In: *Advances in Computational Mathematics* 40 (2014), pp. 65–90.

[62] H. Hertz. “Über die Berührung fester elastischer Körper”. In: *Journal für die reine und angewandte Mathematik* 92 (1881), pp. 156–171.

[63] M. R. J. Hestenes. “Multiplier and gradient methods”. In: *Journal of Optimization Theory and Applications* 4.5 (1969), pp. 303–320.

[64] P. Hild. “Numerical implementation of two nonconforming finite element methods for unilateral contact”. In: *Computer Methods in Applied Mechanics and Engineering* 184 (2000), pp. 99–123.

[65] P. Hild and Y. Renard. “A Stabilized Lagrange multiplier method for the finite element approximation of contact problems in elastostatics”. In: *Numerische Mathematik* 115.1 (2010), pp. 101–129.

[66] D. A. Hills, D. Nowell, and A. Sackfield. *Mechanics of elastic contact*. Elseiver, 1993.

[67] N. Hongkarnjanakul. “Modélisation numérique pour la tolérance aux dommages d’impact sur stratifié composite: de l’impact à la résistance résiduelle en compression”. PhD thesis. Université de Toulouse, 2013.

[68] G. Houzeaux et al. “A massively parallel fractional step solver for incompressible flows”. In: *Journal of Computational Physics* 228.17 (2009), pp. 6316–6332.

[69] G. Houzeaux et al. “Domain decomposition methods for domain composition purpose: chimera, overset, gluing and sliding mesh methods”. In: *Archives of Computational Methods in Engineering* 24.4 (2017), pp. 1033–1070.

[70] G. Houzeaux et al. “Hybrid MPI-OpenMP performance in massively parallel computational fluid dynamics”. In: *Parallel Computational Fluid Dynamics. Lecture Notes in Computational Science and Engineering (LNCSE)*. ed. by D. Tromeur-Dervout et al. Vol. 74. Springer, 2008, pp. 293–297.

[71] *HPCToolkit performance tools*. URL: http://www.hpctoolkit.org.

[72] T. J. R. Hughes et al. “A finite element method for a class of contact-impact problems”. In: *Computer Methods in Applied Mechanics and Engineering* 8.3 (1976), pp. 249–276.

[73] T. R. J. Hughes, R. L. Taylor, and W. Kanoknukulchai. “A finite element method for large displacement contact and impact problems”. In: *Formulations and Computational Algorithms in FE Analysis*. Ed. by K. J. Bathe, J. T. Oden, and W. Wunderlich. MIT-Press, 1977, pp. 468–495.

[74] B. M. Irons and R. C. Tuck. “A version of the Aitken accelerator for computer iteration”. In: *International Journal of Numerical Methods in Engineering* 1 (1969), pp. 275–277.

[75] R. K. Jaiman et al. “Conservative load transference along curved fluid-solid interface with non-matching meshes”. In: *Journal of Computational Physics* 218 (2006), pp. 372–397.

[76] K. L. Johnson. *Contact mechanics*. Cambridge University Press, 1985.

[77] J. J. Kalker. *Three-Dimensional elastic bodies in rolling contact*. Springer, 1990.

[78] G. Karypis and V. Kumar. “A fast and high quality multilevel scheme for partitioning irregular graphs”. In: *Proceedings of the 1995 International Conference on Parallel Processing*. Ed. by D. P. Agrawal. CRC Press, 1995, pp. 113–122. ISBN: 9780849326189.

[79] N. Kikuchi and J. T. Oden. *Contact problems in elasticity: A study of variational inequalities and finite element methods*. 1st ed. SIAM, 1988.

[80] J. Koldan et al. “Algebraic multigrid preconditioning within parallel finite-element solvers for 3-D electromagnetic modelling problems in geophysics”. In: *Geophysical Journal International* 197.3 (2014), pp. 1442–1458.

[81] A. Konter. *Advanced finite element contact benchmarks*. NAFEMS, 2006.

[82] R. Kornhuber. *Adaptive monotone multigrid methods for nonlinear variational problems*. B.G. Teubner, 1997.

[83] R. Kornhuber and R. Krause. “Adaptive multigrid methods for Signorini’s problem in linear elasticity”. In: *Computing and Visualization in Science* 4 (2001), pp. 9–20.

[84] R. Krause. “Monotone multigrid methods for Signorini’s problem with friction”. PhD thesis. FU Berlin, 2001.

[85] R. Krause and B. Wohlmuth. “A Dirichlet-Neumann type algorithm for contact problems with friction”. In: *Computing and Visualization in Science* 5 (2002), pp. 139–148.

[86] U. Küttler and W. A. Wall. “Fixed-point fluid-structure interaction solvers with dynamic relaxation”. In: *Computational Mechanics* 43.1 (2008), pp. 61–72.

[87] T. A. Laursen. *Computational contact and impact mechanics*. 1st ed. Springer, 2003.

[88] T. A. Laursen. “Formulation and treatment of frictional contact problems using finite elements”. PhD thesis. Department of Mechanical Engineering, Stanford University, 1992.

[89] T. A. Laursen. “The convected description in large deformation frictional contact problems”. In: *International Journal of Solids and Structures* 31 (1994), pp. 669–681.

[90] T. A. Laursen and J. C. Simo. “A continuum-based finite element formulation for the implicit solution of multibody, large deformation frictional contact problems”. In: *International Journal for Numerical Methods in Engineering* 36 (1993), pp. 3451–3485.

[91] F. Linder et al. “A comparison of various quasi-Newton schemes for partitioned fluid-structure interaction”. In: *Proceedings of 6th International Conference on Computational Methods for Coupled Problems in Science and Engineering. Venice* (2015), pp. 1–12.

[92] D. G. Luenberger and Y. Ye. *Linear and nonlinear programming*. 3rd ed. Springer, 2008.

[93] F. Magoules, F. X. Roux, and G. Houzeaux. *Parallel scientific computing*. Wiley - ISTE, 2015.

[94] J. G. Malone and N. L. Johnson. "A parallel finite element contact/impact algorithm for non-linear explicit transient analysis: Part II–Parallel implementation". In: *International Journal for Numerical Methods in Engineering* 37.4 (1994), pp. 591–603.

[95] J. G. Malone and N. L. Johnson. "A parallel finite element contact/impact algorithm for non-linear explicit transient analysis: Part I–The search algorithm and contact mechanics". In: *International Journal for Numerical Methods in Engineering* 37.4 (1994), pp. 559–590.

[96] T. W. McDevitt and T. A. Laursen. "A mortar-finite element formulation for frictional contact problems". In: *International Journal for Numerical Methods in Engineering* 48 (2000), pp. 1525–1547.

[97] *METIS: Family of graph and hypergraph partitioning software*. URL: http://glaros.dtc.umn.edu/gkhome/views/metis.

[98] D. P. Mok and W. A. Wall. "Partitioned analysis schemes for the transient interaction of incompressible flows and nonlinear flexible structures". In: *W. A. Wall, K.-U. Bletzinger, K. Schweitzerhof (eds) Trends in Computational Structural Mechanics, CIMNE, Barcelona, Spain* (2001).

[99] J. J. Moreau. "On unilateral constraints, friction and plasticity". In: *New Variational Techniques in Mathematical Physics*. Springer Berlin Heidelberg, 2011, pp. 171–322.

[100] J. T. Oden and E. B. Pires. "Algorithms and numerical results for finite element approximations of contact problems with non-classical friction laws". In: *Computers & Structures* 19 (1984), pp. 137–147.

[101] J. T. Oden and E. B. Pires. "Nonlocal and nonlinear friction laws and variational principles for contact problems in elasticity". In: *Journal of Applied Mechanics* 50 (1983), pp. 67–76.

[102] J. T. Oden and E. B. Pires. "Numerical analysis of certain contact problems in elasticity with non-classical friction laws". In: *Computers & Structures* 16 (1983), pp. 481–485.

[103] J. Oliver et al. "A contact domain method for large deformation frictional contact problems. Part 1: Theoretical basis". In: *Computer Methods in Applied Mechanics and Engineering* 198 (2009), pp. 2591–2606.

[104] P. Pacheco. *An introduction to parallel programming*. MK - Elseiver, 2011.

[105] P. Papadopoulos and R. L. Taylor. "A mixed formulation for the finite element solution of contact problems". In: *Computer Methods in Applied Mechanics and Engineering* 94 (1992), pp. 373–389.

[106] H. Parisch. "A consistent tangent stiffness matrix for three-dimensional non-linear contact analysis". In: *International Journal for Numerical Methods in Engineering* 28.8 (1989), pp. 1803–1812.

[107] F. Pellegrini. “Distillating knowledge about SCOTCH”. in: *Combinatorial Scientific Computing*. Ed. by Uwe Naumann et al. Dagstuhl Seminar Proceedings 09061. Schloss Dagstuhl - Leibniz-Zentrum fuer Informatik, Germany, 2009.

[108] P. Persson. “Parallel numerical procedures for the solution of contact-impact problems”. PhD thesis. Linköpings Universitet, Sweden, 1996.

[109] G. Pietrzak. “Continuum mechanics modelling and Augmented Lagrangian formulation of large deformation frictional contact problems”. PhD thesis. Département de Génie Mécanique, École Polytechnique Fédérale de Lausanne, 1997.

[110] G. Pietrzak and A. Curnier. “Large deformation frictional contact mechanics: continuum formulation and Augmented Lagrangian treatment”. In: *Computer Methods in Applied Mechanics and Engineering* 177 (1999), pp. 351–381.

[111] S. Plimpton et al. “Parallel transient dynamics simulations: Algorithms for contact detection and smoothed particle hydrodynamics”. In: *Journal of Parallel and Distributed Computing* 50 (1998), pp. 104–122.

[112] A. Popp. “Mortar methods for computational contact mechanics and general interface problems”. PhD thesis. Lehrstuhl für Numerische Mechanik, Technische Universität München, 2012.

[113] A. Popp et al. “Improved robustness and consistency of 3D contact algorithms based on a dual mortar approach”. In: *Computer Methods in Applied Mechanics and Engineering* 264 (2013), pp. 67–80.

[114] M. J. D. Powell. “A method for nonlinear constraints in minimization problems”. In: *Optimization*. Ed. by R. Fletcher. Academic Press, 1969, pp. 283–298.

[115] W. H. Press et al. *Numerical recipes in C: The art of scientific computing*. 2nd ed. Cambridge University Press, 1992.

[116] M. A. Puso and T. A. Laursen. “A mortar segment-to-segment contact method for large deformation solid mechanics”. In: *Computer Methods in Applied Mechanics and Engineering* 193 (2004), pp. 601–629.

[117] M. A. Puso and T. A. Laursen. “A mortar segment-to-segment frictional contact method for large deformations”. In: *Computer Methods in Applied Mechanics and Engineering* 193 (2004), pp. 4891–4913.

[118] M. A. Puso, T. A. Laursen, and J. Solberg. “A segment-to-segment mortar contact method for quadratic elements and large deformations”. In: *Computer Methods in Applied Mechanics and Engineering* 197 (2008), pp. 555–566.

[119] V. Puzyrev et al. “A parallel finite-element method for three-dimensional controlled-source electromagnetic forward modelling”. In: *Geophysical Journal International* 193.2 (2013), pp. 678–693.

[120] A. Quarteroni and A. Balli. *Domain decomposition methods for partial differential equations*. Clarendon Press - Oxford, 1999.

[121] *SCOTCH: Software package and libraries for sequential and parallel graph partitioning.* URL: http://www.labri.fr/perso/pelegrin/scotch/.

[122] A. Signorini. "Sopra alcune questioni di statica dei sistemi continui". In: *Annali della Scuola Normale Superiore di Pisa - Classe di Scienze, Serie 2* 2 (1933), pp. 231–251.

[123] J. C. Simo and T. A. Laursen. "An Augmented Lagrangian treatment of contact problems involving friction". In: *Computers & Structures* 42 (1992), pp. 97–116.

[124] J. C. Simo and C. Miehe. "Associative coupled thermoplasticity at finite strains: Formulation, numerical analysis and implementation". In: *Computer Methods in Applied Mechanics and Engineering* 98.1 (1992), pp. 41–104.

[125] J. C. Simo, P. Wriggers, and R. L. Taylor. "A Perturbed Lagrangian formulation for the finite element solution of contact problems". In: *Computer Methods in Applied Mechanics and Engineering* 50 (1985), pp. 163–180.

[126] D. Stefanica. *Domain decomposition methods for mortar finite elements.* Courant Institute of Mathematical Sciences. New York University, 1999.

[127] *The MPI standard.* URL: http://mpi-forum.org.

[128] *The OpenMP API specification for parallel programming.* URL: http://www.openmp.org.

[129] J. Torres. *Understanding supercomputing with Marenostrum supercomputer in Barcelona.* 1st ed. Lulu Press, Inc, 2016.

[130] A. Toselli and O. B. Widlund. *Domain decomposition methods - algorithms and theory.* Springer, 2005.

[131] M. Tur, F. J. Fuenmayor, and P. Wriggers. "A mortar-based frictional contact formulation for large deformations using Lagrange multipliers". In: *Computer Methods in Applied Mechanics and Engineering* 198 (2009), pp. 2860–2873.

[132] M. Vázquez et al. "Alya: Multiphysics engineering simulation toward exascale". In: *Journal of Computational Science* 14 (2016), pp. 15–27.

[133] V. Vondrák et al. "A FETI domain decomposition method applied to contact problems with large displacements". In: *Domain Methods in Science and Engineering XVI. Lecture Notes in Computational Science and Engineering (LNCSE).* ed. by O. B. Widlund and D. E. Keyes. Vol. 55. Springer, 2007, pp. 771–778.

[134] C. Walshaw and M. Cross. "JOSTLE: Parallel multilevel graph-partitioning software – An overview". In: *Mesh Partitioning Techniques and Domain Decomposition Techniques.* Ed. by F. Magoules. Civil-Comp Ltd., 2007, pp. 27–58.

[135] B. Wohlmut and R. Krause. "Monotone multigrid methods on nonmatching grids for nonlinear multibody contact problems". In: *SIAM Journal on Scientific Computing* 25 (2003), pp. 324–347.

[136] B. Wohlmuth. *Discretization methods and iterative solvers based on domain decomposition.* Springer, 2001.

[137] P. Wriggers. *Computational contact mechanics.* 2nd ed. Springer, 2006.

[138] P. Wriggers and J. C. Simo. "A note on tangent stiffness for fully nonlinear contact problems". In: *Communications in Applied Numerical Methods* 1.5 (1985), pp. 199–203.

[139] P. Wriggers, J. C. Simo, and R. L. Taylor. "Penalty and Augmented Lagrangian formulation for contact problems". In: *Proceedings of the NUMETA 1985 Conference*. Ed. by J. Middleton and G. N. Pande. Elseiver, 1985, pp. 97–106.

[140] P. Wriggers, T. Vu Van, and E. Stein. "Finite element formulation of large deformation impact-contact problems with friction". In: *Computers & Structures* 37.3 (1990), pp. 319–331.

[141] V. Yastrebov. "Computational contact mechanics - geometry, detection and numerical techniques". PhD thesis. École Nationale Supérieure des Mines de Paris, 2011.

[142] V. Yastrebov. *Numerical methods in contact mechanics*. 1st ed. ISTE, Wiley, 2013.

[143] A. S. Yigit and A. P. Christoforou. "Limits of asymptotic solutions in low-velocity impact of composite plates". In: *Composite Structures* 81.4 (2007), pp. 568–574.

[144] G. Zavarise and P. Wriggers. "A segment-to-segment contact strategy". In: *Mathematical and Computer Modelling* 28 (1998), pp. 497–515.

[145] O. C. Zienkiewicz and R. L. Taylor. *The finite element method: Solid mechanics*. Butterworth-Heinemann, 2000.